ABSTRACT

ZIMMER, MATTHEW DALY. Vertical Two-Phase Flow Regime Transition Study Using Interface Resolved Simulations (Under the direction of Dr. Igor A. Bolotnov).

Two-phase flow regime transitions represent a significant change in flow properties, such as momentum transfer, heat transfer, and pressure drop. Transient three-dimensional interface capturing direct numerical simulations (DNS) of the two-phase flows is an exciting field that, due to recent advancements in computing power, has become capable of simulating phenomena previously not achievable due to the extremely expensive spatial and temporal resolution requirements. Two-phase flow regime transitions are an excellent example of such phenomena. Performing fully resolved interface capturing DNS of two-phase flow regime transition simulations could be valuable to contributing to the understanding of the involved physics. However, studying two-phase flow regime transitions using interface capturing DNS currently has nearly no committed body of research evaluating how feasible and accurate such a simulation is. Determining the important physics of two-phase flow regime transitions and quantifying the associated computational mesh resolution has yet to be done for this type of simulation.

Bubble breakup and coalescence, interfacial shear, thin film dynamics, and turbulent-interface interactions are all events unique to two-phase flow with significantly small length and time scales. This work will discuss these length scales and quantify the mesh resolutions necessary to accurately simulate slug to churn and slug to bubbly two-phase flow regime transitions while maintaining a reasonable computational expense for modern machines. In this way a standard is created for future research in the area of interface capturing DNS of two-phase flow regime transitions. Validation is also a focus of this work in order to further support the code's simulation capabilities. Following these studies, first of their kind two-phase flow regime transition studies are performed and analyzed using techniques designed specifically for these simulations.

Slug flow was accelerated to reach churn-turbulent and bubbly flow, followed by their decelerations back to slug flow. The simulations were designed to isolate the effects of individual flow parameters in order to understand their contributions to the transition. The high fidelity numerical data provided by the simulations yield a detailed view of the flow characteristics, and their temporal development. By analyzing the similarities and differences in the results, such as local turbulent kinetic energy (TKE), interfacial shear profiles, and interfacial area, associated with each isolated parametric study, an understanding of what induces the flow regime transition and how it develops can be formulated. Analysis shows there is a competition between turbulence-induced large interfacial instabilities and shearing at the tail in driving the breakup of the Taylor bubble. The deceleration also experiences a competition between coalescence and TKE decay that prevents the transitions from being fully reversible. The interfacial shear was identified as the vehicle for energy transfer from liquid to the interface. By relating the total energy transferred to the turbulent energy in the flow, a transition criterion was formulated as a universal predictive capability for slug flow transition.

Vertical Two-Phase Flow Regime Transition Study using Interface Resolved Simulations

by
Matthew Daly Zimmer

A dissertation submitted to the Graduate Faculty of
North Carolina State University
in partial fulfillment of the
requirements for the degree of
Doctor of Philosophy

Nuclear Engineering

Raleigh, North Carolina
2020

APPROVED BY:

_____	_____
Dr. Igor A. Bolotnov Committee Chair	Dr. William Kevin Cope External Member
_____	_____
Dr. Nam Dinh	Dr. J. Michael Doster
_____	
Dr. Hong Luo	

DEDICATION

This work and dissertation are dedicated to my parents

BIOGRAPHY

Matthew (Matt) Daly Zimmer was born alongside his identical twin, Joshua (Josh) Thomas Zimmer, on June 5th, 1993, to Margaret (Peggy) and John. He spent most of his childhood in Harvard, a small town in central Massachusetts. As Matt matured his interest in skiing, backpacking, and the outdoors in general deepened. In the summer of 2010 Matt attended Philmont for the first time. He loved it so much he would return to Philmont four more times, once as a participant in the Rayado special trek, and three times on staff (twice as a Ranger and once as a Ranger Trainer). Matt's time at Philmont as well as the friends he made there are something he will cherish forever. However, despite his extensive time spent backpacking, skiing will always be his first and foremost true passion, and the primary reason why he considers himself an adopted Vermonter and true New Englander. He is excited to return to the Northeast after graduating and get back to the real winters.

In August of 2015 Matt began his schooling at Rensselaer Polytechnic Institute (RPI) where he would initiate his Nuclear Engineering education. Thanks to the direction of Dr. Dillon Shaver and Dr. Michael Z. Podowski he would find interest in computational fluid dynamics and would eventually be introduced to Dr. Igor Bolotnov, his now Ph.D. advisor. Matt's time at RPI would also lead to many great friendships and opportunities to learn and grow from.

Matt lives by two life mottos. The first is a lyric from "Hang Loose", a song from the legendary band The Alabama Shakes: "let the ocean worry about being blue." This is a reminder for Matt to focus on how fortunate he is and all the good things there are to enjoy in the world. There are a million things to worry and stress about and absorbing all of them would take an ocean to do so. So be positive, focus on the good stuff, and do not try to be a turbulent blue ocean. The second, "shred the gnar," is an adopted and transformed saying from the skiing community. Matt takes this

in two ways, first, due to those who say it genuinely often being the subject of ridicule and mockery, this is Matt's reminder to not take one's self too seriously and not get tied up with worrying about what others think. Second, shred the gnar is often yelled at someone about to do something "gnarly," risky, and gutsy. So Matt uses it to make sure he isn't always taking the safe road. He has learned that some of the greatest things in his life have come from pushing his comfort zone and/or taking a risk. With the hopes of this upward trajectory continuing, he continues to shred the gnar.

ACKNOWLEDGMENTS

I would first like to thank my advisor, Dr. Igor Bolotnov for the guidance, advice, and encouragement throughout my time at NCSU. It all has proven invaluable and massively contributed to my research and career. I was fortunate to be able to work with and take classes from him, and I look forward to keeping in touch on both a professional and personal level once I leave North Carolina. I would also like to thank my committee, composed of Dr. Cope, Dr. Dinh, Dr. Doster, and Dr. Luo, for their time and contributions. In particular, I would like to recognize Dr. Cope for working through the public utterance process on my papers and for serving as an excellent Rickover Fellowship mentor.

I would like to thank the Rickover Fellowship program for funding me through graduate school. In particular, Nancy Carder and Nicole Hutchet, who made the logistics of the Rickover Fellowship, like travel, renewal, forms, etc., effortless on my part. I would also like to acknowledge the many folks I met during my practicum, Trip Dacus, Dart Strayer, Tara Gallaway, Brian Waite, Dave Hjelmar, and many more, that made my time at Knolls Atomic Power Laboratory highly enjoyable and an incredible learning opportunity. I am very excited to return and work with them.

Thank you to Dillon Shaver for first introducing me to the field of thermal hydraulics and being a friend over the years. If he had not convinced me to perform undergraduate research with him then I would almost certainly not be in the place I am today. I would also like to thank Dr. Michael Z. Podowski, whose group I performed the undergraduate research in. Dr. Podowski's guidance helped teach me what it meant to be a researcher.

Each and every member of my research group has been excellent over the years and provided valuable insight and contributed to my work. I also need to recognize the many other graduate students in my department that I have befriended. Thank you for your ongoing support.

I of course need to thank the many friends I have made during my time in North Carolina because I could not have done it without them. Thank you to Jean Mosher and Kirby Culbertson for being the best neighbors in all of Raleigh, and Mark Lisanti for being the person that finally convinced me I was missing out on fixed gears. Thank you to Ben Perryman, Jane Gribble, and Jacques Louhier for the fond memories and meaningful discussions during the, sometimes long, nights at the pool hall. My sincere gratitude goes to all my climbing friends, particularly Audrey Stephan, Mike Vinsel, and Greg Gavitt, who have kept me sane during my withdrawal from skiing. My barista and bakery friends also need recognition for fueling me and providing a smiling face on the days I need an extra cup of coffee or a baked good to start the day off. And above all, my dearest thanks goes to Dex, who has been the smiling face that excitedly greets me every single day.

Finally, I would like to acknowledge my family for being incredibly supportive. My mom, dad, and brother (Josh, identical twin) are all wonderful people who are friends I could count on whenever I might need them. Josh is the only person my age I have ever maintained a friendship with my whole life, so thank you for putting up with a copy of yourself. Mom and Dad, thank you for letting me spend these years in North Carolina in order to pursue my degree. Mom, I know you would move mountains for me and Josh, and I truly appreciate everything you have done for me. Dad, you have given me much of your wisdom over the years and served as a role model to look up to.

TABLE OF CONTENTS

LIST OF TABLES

LIST OF FIGURES

CHAPTER 1. INTRODUCTION

1.1 Overview and Motivation

Several different methods of simulating single and two-phase flows exist, each with different resolution and modeling requirements. Some of the more common flow simulation methods are systems level codes, subchannel codes, Reynolds Averaged Navier-Stokes (RANS), large eddy simulation (LES), and direct numerical simulation (DNS). Rather than being in competition for the same task, each of these methods are best suited to different applications. A DNS code, for example, would not be used to analyze nuclear reactor operation. A system level code would be best in this situation. Vice versa, a systems level code would not be appropriate for small scale simulation. Even though all the methods can model two-phase flow, different scales of physics and levels of fidelity are captured in each. The multiphase computational fluid dynamics (M-CFD) RANS and subchannel approaches rely heavily on empiricism to provide closure to their models since they are not capable of resolving many physical flow features. In contrast, DNS solves the Navier-Stokes equations directly and requires no turbulence closures. The computational requirements of lower resolution codes tend to be smaller, making them popular for system/component design applications. In these circumstances, a large number of simulations may be required to analyze all possible operating conditions, making a high resolution and computationally expensive method such as DNS not feasible.

As computational power has improved over time, DNS has increased in popularity for model development applications. DNS allows for the detailed exploration of complex phenomenon without the need for monetarily expensive experimental equipment or extensive modeling. Since DNS does not rely on as numerous a set of models, the phenomenological domain is larger. A model is limited in its application to the system it was designed for, but a two-phase DNS code, in

theory, is limited by the computational power available. Therefore, flows ranging from single phase pipe flow to two-phase convective boiling flows in a reactor subchannel all lie within DNS's grasp. This allows verified and validated DNS to explore the true physics on a fundamental level. These simulations can be used to formulate new models that are implemented in the lower resolution codes. Nuclear engineers employ nearly all scales of computational fluid dynamics (CFD) in their research to improve reactor performance and safety. Given the importance of safe and efficient reactor performance, the requirement for accurate modeling is crucial. The models must be carefully formulated to be representative of real world phenomena. To do so, experiments are commonly used to replicate the physics of a nuclear reactor and generate empirical correlations. However, boiling water reactor (BWR) and pressurized water reactor (PWR) prototypic experimental equipment is difficult to manufacture and come with a sacrifice to measurement resolution. The high temperature and pressure conditions are preventative for many common high-resolution measurement methods such as conductivity probes and particle image velocimetry (PIV). DNS's limits are computational rather than physical, and simulating high pressure and temperature fluid properties and complex geometries is not an issue with modern solvers. In addition, DNS allows for data collection at time and spatial resolutions many experimental methods cannot achieve, even at atmospheric conditions. Numerical data can come from every computational point at every time step, producing terabytes worth of data. With such an immense volume of numerical data, a challenge is knowing how to analyze it while maximizing its utility.

Single-phase DNS has already been shown to accurately capture flow behavior for a wide range of Reynolds numbers, $\mathrm{Re} = 11{,}000 - 500{,}000$ [1, 2, 3]. Given BWR flows approach $\mathrm{Re} \approx 300{,}000$ [4], single-phase DNS has already reached and surpassed reactor relevant turbulence conditions. These DNS studies simulated flow between parallel plates and DNS was shown to

agree very well with what has been observed experimentally. Results from single phase DNS studies show that these methods accurately predict both small scale, such as the hairpin vortices structure in shear flow [5], and large scale, such as the inverse relationship between wave number and pre-multiplied energy spectra density at extremely high Reynolds number [1], without any supplied physical knowledge. A significant proportion of the fluid dynamics research community has accepted single phase DNS-based data as the valid benchmark to theoretically study and understand the turbulence at the same level as the high-quality experimental data. However, in a nuclear reactor core the turbulent flows are more complex and two-phase flows are encountered. As far as Reynolds number range, two-phase DNS lags behind single-phase due to the extra complexity of tracking the interfaces. However, as shown by Fang et al. [6], this gap is closing annually. Additionally, research has proven the reliability of two-phase DNS and its potential as a powerful tool [7, 8, 9, 10] for flow analysis and understanding. Specifically, DNS's utility is highlighted by Feng & Bolotnov [11] where a single bubble, held static in space (impossible experimentally), was subjected to different levels of turbulence. The bubble-induced turbulence (BIT) was then measured, providing insight to how a single bubble contributes to turbulence enhancement.

In BWRs, the vapor volume fraction, or void fraction, enters the core at zero value and peaks at around 0.75 [4]. The axially dependent void fraction leads to axial macro-interface topology changes. As boiling begins near the bottom of the core small bubbles will first be produced due to nucleate flow boiling phenomenon. As more bubbles are produced they begin to collide and coalesce, forming larger interfacial structures that can further grow or become too large to support itself and break apart. This process of coalescence and breakup is continuous along the length of the subchannels and is extremely complex. Flow properties such as local heat transfer coefficient

and pressure drop are dependent on the interfacial structure [12, 13, 14], necessitating knowledge of the local void location and two-phase flow pattern. The void distribution in the core is consequential to the neutronics as well since water is the primary neutron moderator. To fully describe the physics involved in such a flow, several ***two-phase flow regimes*** have been defined. Each regime is defined by a classical interface shape most prevalent in the domain. These are a convenient way to categorize flows with similar behavior and interface topology. The macro-interface topology changes that occur along the length of the core are therefore named ***two-phase flow regime transitions***. As mentioned, depending on the structure of the interface the turbulence, heat transfer, momentum transfer, and critical heat flux (CHF) of the flows can be different. This variation in properties makes the knowledge of where each regime exists in the BWR core important for predictive capabilities of coolant flow behavior. Unfortunately, the two-phase flow regime transitions are not well understood by the scientific community, making accurate predictions of their location difficult. Flow regime maps implemented in some codes can be as simple as a linear relationship between void fraction and flow rate. Experiments can explore individual steady state two-phase flow regimes, but capturing the transition between the regimes can be very challenging due to their time-dependent nature and non-trivial identification. The two-phase flow regime transition process represents an excellent candidate for a DNS study. The study would require high spatial and temporal resolution for the data collection techniques, something DNS excels at, and producing new models that better capture the physics would be beneficial for two-phase flow modeling. Additionally, studying such a complex phenomenon in fine detail can reveal the physical mechanisms behind the transitions and inform the scientific community on why the transition occurs. Despite flow regime transitions being a strong candidate for an interface resolved DNS study, no DNS researchers have committed significant effort to the field. This is

partly due to the relatively small DNS community, but also due to the extremely high computational expense that is expected from high flow rate simulations with highly deformed interfaces. With limited high-performance computing facilities available, most time has been dedicated to singular two-phase flow regime simulations.

This work aims to begin to fill this gap by being the first research to tackle two-phase flow regime transitions using interface capturing simulations. Specifically, slug to churn-turbulent, slug to bubbly, churn-turbulent to slug, and bubbly to slug transitions will be focused on. The selected code is PHASTA, which will be fully explained in CHAPTER 2, and uses the level set method for interface capturing. Beginning research into a new area requires evaluation of computational limitations and development of novel data analysis techniques that may not have been necessary previously. An obvious example of new requirements is the need to resolve the Kolmogorov scale in a DNS but not in lower fidelity codes. Therefore, part of this work, as well as the literature review, will focus on determining new computational requirements, limitations, and data analysis techniques that are necessary to simulate the previously mentioned two-phase flow regime transitions using PHASTA.

In this report the DNS study of vertical two-phase flow regime transitions will be summarized. First, the knowledge of two-phase flow regimes and their transitioning will be discussed. A short summary of the numerical methods used in this study will be provided. Some important computational considerations specific to this study will also be described. Using simulations that were designed from experiments, new resolution requirements for simulating the transitions will be discussed and presented. Some data analysis tools that were developed specifically for this work will also be explained. Then the results from the transition simulations will be presented and analyzed. In order to provide confidence in the DNS code as a useful tool for studying such a

complex flow, validation was an important part of this research. Both theoretical and experimental validation studies whose quantities of interest ranged from globally averaged to local and instantaneous were examined. Due to their suspected importance to the flow regime transitions, geometry, gas viscosity, and surface tension were varied to observe their effect on the transition. The goal of this study was to identify prominent mechanisms for two-phase flow regime transitions, determine what causes these mechanisms to be the driver for the transition, and how these causal effects can be characterized in models required in lower resolution codes.

1.2 Literature Review

Historically, a primary focus of two-phase flow regime transition research was the production of a tool to accurately predict which regime exists under what flow conditions and when the regimes transition from one to another. Experimental, theoretical, and computational tools have all been used in this research, and the presented literature review will discuss all of them. The structure of the literature review is as follows: (1) two-phase flow regime definitions; (2) methods for identifying flow regimes; (3) methods for predicting flow regime transitions through experimental and computational means; (4) a discussion of computational efforts to model flow regime transitions; (5) a brief history of high-resolution interface resolved two-phase flow regime transition research. The history of two-phase flow regime transition research is quite extensive and while this discussion covers enough to provide the major structure, it does not claim to be a fully exhaustive review.

1.2.1 Two-Phase Flow Regimes

As discussed, two-phase flow regimes are defined by the major liquid-gas interfacial structure observed in the flow. In nuclear engineering, the four common vertical two-phase flow regimes are bubbly, slug, churn-turbulent, and annular flow [15], as shown in Figure 1.1.

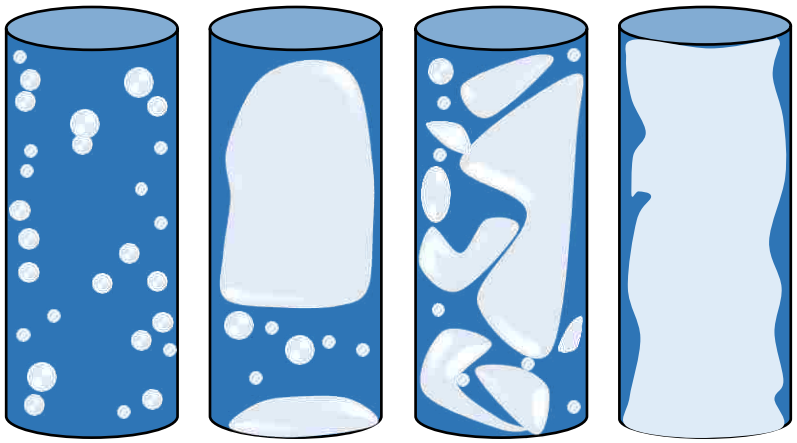

Figure 1.1: The common two-phase flow regimes: bubbly (a), slug (b), churn-turbulent (c), and annular (d).

Bubbly flow (Figure 1.1 (a)) is characterized by small bubbles dispersed throughout the liquid. Generally, the bubbles remain relatively spherical as surface tension remains dominant and they are either not numerous enough to coalesce and form larger structures or turbulent forces are too strong to allow for larger bubbles. Slug flow (Figure 1.1 (b)) is characterized by long smooth bubbles that occupy the entire flow area other than a liquid film on the wall, called Taylor bubbles, separated by slugs of liquid. It is common to have smaller bubbles dispersed within the slugs. Depending on the flow conditions both the liquid slugs and Taylor bubbles can be very long, being tens of conduit diameters in length. Churn-turbulent flow (Figure 1.1 (c)) is a relatively high void flow where large and small interfacial structures are mixed throughout. The interfaces are not smooth and the axial void distribution is chaotic, occurring at high flow rates. There is no single coherent structure that characterizes this regime, instead it is a culmination of heavily deformed interfaces at high void fractions. Annular flow (Figure 1.1 (d)) sustains a continuous column of gas in the center of the conduit with a film of liquid on the walls. While the phases are primarily in their continuous regions, dispersed liquid and gas is possible as well (e.g. small liquid droplets in the vapor core and small gas bubbles in the liquid film). The liquid film thickness typically varies spatially as well, a result of the interfacial shear forming waves in the film. Other regimes,

such as cap-bubbly, froth, annular-mist, and annular-wavy, have been proposed but are essentially variations or sub-categories of the four main discussed above.

In other disciplines, such as chemical engineering, and even within nuclear engineering, horizontal and different vertical flow regimes are often identified [15]. Horizontal two-phase flow regimes include plug, which is characterized by larger bullet shaped bubbles that are still smaller than a Taylor bubble. When the plug bubbles become large enough they form horizontal slug flow, which is similar to vertical slug flow but buoyancy forces the bubble closer to the top wall. Horizontal stratified flow is where gravity completely separates the phases and they form two layers with a flat interface between them. As the flow rate increases the interface between the phases becomes wavy, a regime appropriately known as wavy flow. Horizontal flow also allows for the annular regime if gas flow rates are high enough. Annular flow, at all inclinations, can be even further categorized into falling film and wispy. Falling film annular flow occurs when the liquid film flows downward, against the flow of gas (so-called counter-current flow conditions). Wispy annular flow is characterized by finely dispersed droplets in the gas core. Other regimes that have been identified are froth flow, which is considered to be close to churn-turbulent but is composed of smaller bubbles, cap-bubbly, a regime between bubbly and slug flow, and mist, where only small dispersed droplets are flowing amongst continuous gas. Vertical regimes will remain the focus of this work because both typical PWR and BWR cores are oriented vertically.

As mentioned, each regime behaves differently, which is why they have each been distinguished with a name. To fully simulate two-phase flow using a M-CFD approach each regime has its unique set of models to describe its mass, momentum, and energy transfer. To apply these models, the flow regime must be identified at every location in the simulation. As will be described

in the next section, two-phase flow regime identification is not always trivial, yet has a profound effect on modeling results.

1.2.2 Flow Regime Identification

The interfacial topology of a certain flow can closely resemble more than one regime. Therefore, for an experimentalist capturing data intended for creating a correlation, different correlations may be produced from the same data depending on how the flow regimes are identified. A computationalist implementing a flow regime heat transfer correlation may find a different solution depending on how the code determines when a flow regime transition occurs. Two-phase flow regime identification was first visual [16] but due to natural variability in human behavior this is subject to human error. Pressure signal [12, 13] and void distribution [17] based methods were developed as a more quantitative means of interpreting the data. Researchers would use tools to measure signals for the respective parameter and would bin the regime based on the more quantitative signal. While effective, this often still requires human eyes to bin each flow condition based on the recorded signals. Machine learning provides the means to eliminate the need for human classification and has been implemented in several two-phase flow regime studies [17, 18, 19]. Machine learning requires large volumes of data for training purposes but, once trained, can classify two-phase flow regimes more consistently than a human. Using experimental measurements and machine learning is the most rigorous method of classifying experimental flow regimes available.

The next step after classifying individual regimes is compiling this into a database that summarizes under what conditions a certain regime exists. A 2D map is often constructed for this characterization. The axes are most commonly the superficial liquid and gas velocity. Superficial velocity is defined as

$$j_i = \alpha_i u_i \quad (1.1)$$

where subscript i refers to phase, α is the volume fraction, and u is the mean flow velocity. Therefore, maps using superficial velocities only take into account flow rate and volume fraction, an inherent flaw in flow regime maps. The map is either created from a series of experimental data points that are numerous enough to define the regime boundaries, or theoretical criteria that determine for what superficial velocities the transition occurs. The experimental maps allow for interpolation between measured flow conditions and define the flow regime transition boundaries. Knowing precisely when one regime transitions to another is important for applying the correct correlations and therefore predicting system behavior. Because of this predictive capability, flow regime maps can be a valuable tool when designing new systems.

1.2.3 Predicting Flow Regime Transition

While two-phase flow regime maps are a useful tool and are applied in many codes, they do not provide a completely accurate representation of the flow regime transition phenomenon. Flow regime maps commonly use lines to indicate the point one regime suddenly transitions to another. In reality, the transition process is continuous, with no sudden jump. This is reminiscent of the Reynolds number, in which there is a transition region between the laminar and turbulent single-phase regimes. It is at these transitions that the aforementioned non-trivial classification situations exist as well, allowing flow regime maps to be different even if they were developed for very similar conditions.

Two common methods of producing flow regime maps are experimentally, by collecting a set of data for many different flow conditions, and theoretically, where transition criteria are postulated by the researcher and a map is created from these conditions. The benefits and downsides of each of these are discussed next.

1.2.3.1 Experimentally Based Regime Boundaries

There is a plethora of experimental flow regime maps, for many different conditions and geometries, available in the literature [19, 20, 16, 21, 22]. The reason for this is also the largest downside to experimental flow regime maps. A 2D flow regime map only directly applies to the precise conditions it was created from, so for each new practical application a new map needs to be generated. The alternative is extrapolating from an existing map and potentially losing accuracy. Different temperatures, pressures, geometries, fluids, etc. prevent flow regime maps from being widely applicable because the physics is dependent on each of these variables and extrapolating from one flow regime map may inaccurately predict behavior. Creating a complete flow regime map, for just a BWR subchannel geometry, would require equipment that can stand BWR temperatures and pressures and a measurement technique appropriate for the experimental setup. Another problem with experimental flow regime maps is that they are created using steady state flow conditions. Researchers employ very long test sections to allow the two-phase flow to fully develop and reach its appropriate flow regime before observations are made and data taken. In reality, the boiling in BWRs prevents the flow from ever reaching a fully developed condition. Therefore, a flow regime map for BWR prototypic conditions still only determines the flow regime for conditions that do not occur in the core of a BWR. It is entirely feasible to have flow conditions that visibly resemble bubbly flow, but are predicted to be slug flow and would reach slug flow given a development length. On the other hand, experimentally based flow regime maps are excellent because they capture the full physics. The experimental data comes directly from the phenomenon and no simplifications or assumptions are made. With the proper tools, a flow regime map could be very accurate for its appropriate application. For example, Williams and Peterson Jr. [23] used a high pressure setup capable of boiling to study two-phase flow regimes in a 4×1 rod

bundle. The work produced flow regime maps that reflected the physics in a BWR closer than many other studies could.

An excellent example of a rod bundle flow regime map study are the maps developed by Ren et al. [21]. The researchers not only identified classic flow rate dependency of flow regime, but also the spatial dependency. Three different subchannel classes in the rod bundle were focused on: the corner, the side, and the inner subchannels. One flow regime map produced from this study is shown in Figure 1.2.

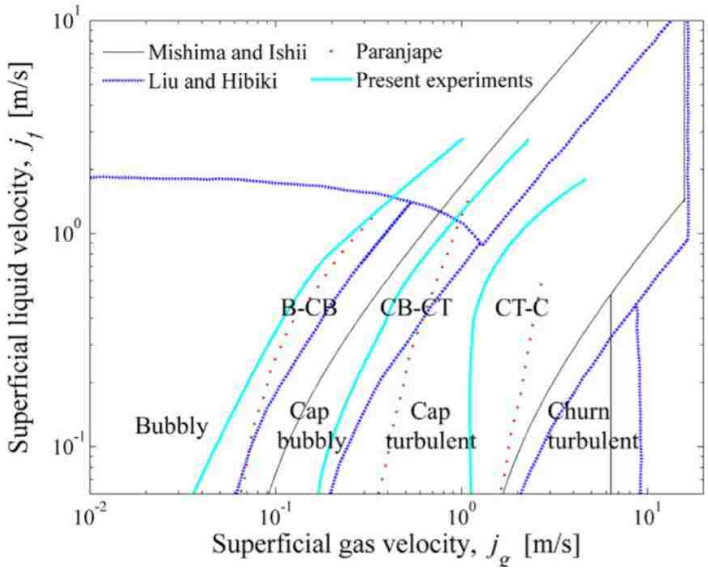

Figure 1.2: Flow regime map developed by Ren et al. *[21]* for an inner subchannel in a rod bundle.

As seen in Figure 1.2, Ren et al. also compared their results to several other flow regime maps [24, 25, 26]. The maps all follow the same trend, but it is clear that there is still variation despite nearly all these maps being developed for the same conditions. To determine the precise reason for the variation and coalesce to a single map is extremely difficult due to the multiple sources of uncertainty, including both human and machine, existing in the studies.

1.2.3.2 Theoretically Derived Regime Boundaries

The first step in creating a theoretical two-phase flow regime map is deciding what physics contribute to each flow regime transition. This hypothetical cause must then be formulated into an expression that can be used to build a flow regime map. Theoretically derived two-phase flow regime maps are advantageous as they can be adjusted to accommodate a wider variety of flow conditions. The fluid properties can be altered to accommodate different fluids, temperatures, and pressures, and the transition lines will respond accordingly. Where these maps fall short is the difficulty in capturing the full physics involved with something as complex as a two-phase flow regime transition. Even if the most dominant effects are taken into account, small inaccuracies may exist. Because theoretical flow regime maps represent the most prominent effort to characterize the physical mechanisms behind two-phase flow regime transitions several different theoretical maps will be discussed. This will demonstrate how such a map is created as well as what researchers consider to be major contributing factors in each transition. The maps that will be discussed are the Mishima & Ishii [24], Taitel et al. [27], and Barnea [28] maps. Note that the most recent of these papers was published in 1987. There is little recent work committed to theoretically deriving transition criteria. Instead, research has been focused on developing more advanced experimental flow regime maps for specific fluids, geometries, and conditions. The literature review found only one recent theoretically produced map. Liu & Hibiki [26] derived a flow regime map for flow in a vertical rod bundle in 2017.

1.2.3.2.1 The Mishima & Ishii Maps

The Mishima & Ishii [24] maps consider steady state upward vertical pipe flow, meaning even theoretical maps are still limited in application. Below a void fraction of 30% bubble flow was assumed to always exist. This was based on sphere packing theory, a denser packing efficiency

and the bubbles coalesce to form slug flow. This single void fraction is not enough to form a map using the conventional superficial velocities space. To do so, the following expression was formulated using a drift flux model [29].

$$\frac{j_g}{\alpha} = C_0 j + \sqrt{2}\left(\frac{\sigma g \Delta\rho}{\rho_l^2}\right)^{\frac{1}{4}}(1-\alpha)^{1.75} \quad (1.2)$$

where j_g is the gas superficial velocity, α is the void fraction, σ is surface tension, ρ_l is the liquid density, $\Delta\rho$ is the difference in liquid and gas densities, g is acceleration due to gravity, and C_0 is a drift-flux parameter. The slug to churn transition was postulated to occur when the void fraction in the entire domain exceeds that of just the Taylor bubble segment. This can also be interpreted as the point at which the liquid slug is no longer discernable due to redistribution of void. Through analysis of the flow dynamics this criterion was translated into the following expression:

$$\alpha \geq 1 - 0.813\left(\frac{(C_0-1)j + 0.35\sqrt{\frac{\Delta\rho g D}{\rho_l}}}{j + 0.75\sqrt{\frac{\Delta\rho g D}{\rho_l}}\left(\frac{\Delta\rho g D^3}{\rho_l \nu_l^2}\right)^{\frac{1}{18}}}\right)^{0.75} \quad (1.3)$$

where ν_l is the liquid kinematic viscosity and D is the pipe diameter. The final transition, from churn to annular was considered to occur via two different mechanisms: flow reversal in the liquid film around the Taylor bubbles, or destruction of the liquid slugs by gas entrainment or interfacial deformation. Two new expressions, similarly based on a drift-flux model, were derived for these conditions.

$$j_g = \sqrt{\frac{\Delta\rho g D}{\rho_g}}(\alpha - 0.11) \quad (1.4)$$

$$j_g \geq \left(\frac{\sigma g \Delta\rho}{\rho_l^2}\right)^{\frac{1}{4}} N_{\mu l}^{-0.2} \quad (1.5)$$

where $N_{\mu l}$ is a parameter to characterize onset of entrainment for film flow.

1.2.3.2.2 The Taitel et al. Maps

The Taitel et al. [27] maps are also applicable only to upward steady state two-phase flow in vertical pipes. Similar to the Mishima & Ishii maps, Taitel et al. define the transition from bubble to slug to occur at 25% void fraction. This is also based on spherical packing theory but some experimental data was cited for support of the lower value. To create an expression for this criterion, Taitel et al. consider conditions at which turbulent dispersion forces are dominant. If turbulent dispersion properties are not dominant, then the bubbles can coalesce and form slug flow.

$$j_l = 3.0 j_g - 1.15 \left(\frac{g \Delta \rho \sigma}{\rho_l^2} \right)^{\frac{1}{4}} \quad (1.6)$$

If turbulent dispersion forces are dominant, then a Taylor bubble will not form. The following expression defines these flow rates.

$$j_l + j_g = 4.0 \frac{D^{0.429} \left(\frac{\sigma}{\rho_l} \right)^{0.089}}{\nu_l^{0.072}} \left(\frac{g \Delta \rho}{\rho_l} \right)^{0.446} \quad (1.7)$$

The last condition for bubbly flow defined by Taitel et al. stated the void fraction must be below 52%. Note that those values are cross-section averaged, and even in the bubbly flow one would expect a lateral variation of void fraction. The authors also considered pipe geometry and decided there is a lower limit on pipe diameter that bubbly flow will not exist for and slug flow will persist.

$$\left(\frac{\rho_l^2 g D^2}{\Delta \rho \sigma} \right)^{\frac{1}{4}} \leq 4.36 \quad (1.8)$$

The slug to churn transition was theorized to occur when the liquid slugs are too short to maintain a turbulent velocity profile, resulting in trailing bubbles overtaking the one ahead of it. They consider churn to be an entrance phenomenon and use characteristic lengths and velocities to

determine when this churn state occurs. The resulting expression only requires the mixture velocity to be known and depends strongly on pipe dimensions.

$$\frac{l_E}{D} = 40.6\left(\frac{j}{\sqrt{gD}} + 0.22\right) \quad (1.9)$$

where l_E is the churn entrance length. Taitel et al. determined annular flow only exists when the drag of the gas flow against the droplets is sufficient to support the droplets, otherwise they would fall and accumulate, segmenting the gas core. By estimating the drag coefficient Taitel et al. arrived at this expression for the transition to annular flow.

$$\frac{j_g \rho_g^{1/2}}{(\sigma g \Delta\rho)^{1/4}} = 3.1 \quad (1.10)$$

1.2.3.2.3 The Barnea Maps

The Barnea [28] maps are more universal and provide transition criteria for all pipe sizes at all inclinations for steady state flows. Because of the additional flow regimes that exist at non-vertical angles, there are more equations to model each transition. Therefore, in this report the equations are not presented and only the theory for each transition will be discussed.

The Barnea maps postulate that bubbly flow exists when the Taylor bubble velocity exceeds the small bubble velocity. Additionally, bubbly flow exists when the angle of inclination is large enough to prevent bubble migration to a single wall, i.e. preventing coalescence due to proximity to other bubbles. Finally, bubbly flow will not exist below a critical pipe diameter. Note that these conditions are not sufficient on their own to relate the flow rates of each phase. Therefore, Barnea uses the 25% void fraction as a transition criterion as well. This condition comes from experimental observations and packing theory.

Barnea makes a distinction between bubbly flow and dispersed bubble flow. Bubbly flow occurs at lower flow rates and dispersed bubbly flow occurs at high flow rates where turbulent

dispersion forces prevent coalescence to form large bubbles. By approximating the turbulence necessary to break up bubbles, Barnea created a criterion for dispersed bubbly flow as well. The condition for dispersed bubbly flow only specifies the gas superficial velocity for transition. To obtain a liquid superficial velocity, packing theory is again applied, where the maximum allowed void fraction is 52%.

The stratified (which can be stratified smooth or stratified wavy) to non-stratified (elongated bubble, slug, churn, or annular) transition occurs only in horizontal/low angle pipes. Barnea decided the historically used Kelvin-Helmholtz instability is the best predictor for the transition out of the stratified regime. When the energy of the Kelvin-Helmholtz instabilities that develop on the interface between the two phases is enough to overcome the decay caused by gravity, a transition occurs. It was found that this criterion was applicable to all pipe inclinations. The other criterion determines what regime the flow transitions to when leaving stratified flow. At steep pipe inclinations, the stratified regime region disappears due to other regimes being predicted to exist at those conditions.

Barnea determined that the transition mechanism for stratified to annular (annular or wavy annular) depends on the inclination of the pipe. At steep downward angles when the void fraction is large enough, and when the liquid flow rate is high enough, small droplets separate from the stratified liquid and deposit on the other side of the pipe. This process forms a liquid film covering the entire pipe circumference, creating annular flow.

The annular to intermittent (elongated bubble, slug, or churn) transition was theorized to occur when the gas core of the annular flow becomes blocked by the liquid. This could occur via either instabilities in the liquid film growing until they bridge the pipe, or the flow rate of the liquid film being large enough to supply enough liquid to a region to block the gas core. From these two

mechanisms a criterion that characterizes the instability of the liquid film and a criterion that models the flow rate in the liquid film were created.

Barnea breaks the intermittent regime into elongated bubble, slug, and churn regimes. Elongated bubbly flow is flow with Taylor bubbles and liquid slugs where there are no bubbles in the slug. Slug flow is the same but with bubbles in the slug. To define the transition between these three regimes Barnea uses a single expression which defines the holdup (another term for void fraction) in the liquid slug. When the holdup is predicted to be zero, elongated bubble exists. When the void fraction is 52% or more, holdup is predicted in the slug and churn exists. Between these conditions slug flow exists.

The stratified regime is also segmented into stratified smooth and stratified wavy. The names refer to the shape of the interface between the phases and the transition between the two is also defined by when these waves occur. To formulate an equation Barnea considered the wind effect, which is a means of estimating the shear at the interface. Flow is not necessary in the gas for this condition to predict a transition.

1.2.4 Two-Phase Flow Regime Transition Modeling

Lower resolution codes modeling two-phase flow regime transitions rely heavily on flow regime maps to predict when a flow regime transition occurs. A subchannel code, for example, can use 1/1.5D mass, momentum, and energy transfer equations to predict void fraction and flow rates. The code then refers to a flow regime map to check what regime region the flow lies in. The code selects the appropriate regime and the correlations associated with that regime calculate parameters such as relative velocity and heat transfer coefficient. When the calculated superficial velocities cross a flow regime boundary on the map, the flow regime transitions. Underlying problems with this method include the assumption that the flow regime transition is a sudden and

distinct event, and the flip between correlations may result in discontinuities if a smoothing function is not applied. Finally, the accuracy of these models is inherently tied to the fidelity of the flow regime map. Uncertainty can be produced from using a map created from different geometries, pressures, or oversimplification. An example of an oversimplified flow regime map that is used by the subchannel code CTF [30] is shown in Figure 1.3.

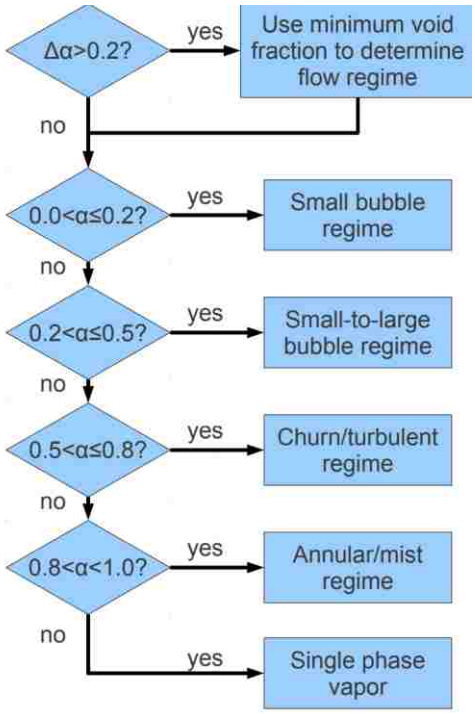

Figure 1.3: COBRA-TF flow regime map *[30]*.

While this map does provide some guidance, void fraction is the only parameter considered for all transitions. As was shown in Section 1.2.3.2 Theoretically Derived Regime Boundaries, this is not consistent with what many researchers consider to be the primary flow regime transition criteria. Updating CTF with a more accurate map could improve the accuracy of the code.

The current state of RANS, unsteady RANS (URANS), and large eddy simulation (LES) codes, while more resolved than subchannel codes, are not capable of modeling all flow regimes. As explained by Bestion [31], some RANS, URANS, and LES codes do implement interface

capturing methods but do not fully resolve all scales of the two-phase flow. These methods decompose the two phases into continuous liquid, continuous gas, dispersed liquid, and dispersed gas. This two-fluid four-field model can capture bubbly, annular, and droplet flow regimes, but not cap-bubbly, slug, and churn-turbulent. The issue is time and space averaging, or filtering, are not compatible with intermittent flows where bubble sizes are highly variable and complex interfacial structures exist. Codes employing this method do not account for different flow regimes. Instead, eight different combinations of continuous liquid/gas and dispersed liquid/gas can be identified at each computational point in the domain. The mass, momentum, and energy transfer equations are solved to track the distribution of each of the four fields. Since the void distribution is part of the solution, these codes do not rely on flow regime maps. A significant challenge of two-phase modeling is capturing the effects of sub-grid turbulence and interfaces. An accurate two-phase model can predict where and when interface-interface (e.g. a small dispersed bubble encounters a continuous phase) and interface-turbulence interactions occur while conserving mass, momentum, and energy. Due to the complexity, a model proven to accurately capture any void distribution and interfacial topology has yet to be widely recognized in the M-CFD community. This task requires advanced models to predict where large and small bubbles will exist and account for their interactions with each other and the liquid [31].

1.2.5 The Interfacial Area Transport Equations

The interfacial area transport equations [32], when proper coalescence and breakup models are applied, are a means of simulating two-phase flow while avoiding the need to characterize the flow as any regime. Instead, the equations directly calculate the interfacial structure, without the naming system. The equations can be applied to the two-fluid model [33], which uses a pair of mass, momentum, and energy conservation equations, one for each phase. In each of these equations a

respective interfacial mass, momentum, and energy transfer term appears. The interfacial area transport equations are used to close these terms due to their strong dependence on the interfacial area concentration. The interfacial area transport equations are given below.

$$\frac{\partial n}{\partial t} + \frac{d}{dz}\left(n v_p\right) = \left(\phi_B - \phi_C\right) + \left(\phi_{PN} - \phi_{PC}\right) \quad (1.11)$$

$$\frac{\partial a_i}{\partial t} + \frac{d}{dz}\left(a_i v_i\right) = \frac{1}{3\psi}\left(\frac{\alpha}{a_i}\right)^2 \left(\left(\phi_B - \phi_C\right) + \left(\phi_{PN} - \phi_{PC}\right)\right) + \left(\frac{2a_i}{3\alpha}\right)\left(\frac{\partial \alpha}{\partial t} + \frac{d}{dz}\left(\alpha v_i\right)\right) \quad (1.12)$$

where n is the bubble number density, t is time, v_p is the average bubble velocity, z is the axial position along the flow direction, a_i is the interfacial area concentration, v_i is the interfacial velocity, α is the void fraction, and ψ is a bubble shape factor. ϕ_B, ϕ_C, ϕ_{PN}, and ϕ_{PC} are the rates of change in bubble number density due to breakup, coalescence, nucleation, and collapse, respectively. Extensive modeling is needed to further define these rate of change terms. In total, there are seven closure relations needed for this model, and include definitions for maximum particle volume, breakup frequency, coalescence frequency, and more [32]. Still, these models do not require flow regimes to calculate the interfacial area concentration and can come from both experimentation and theory. When compared to experimental data the equations are capable of capturing the correct interfacial area distribution to within 10% error but can exceed 20% [34], depending on the experiment. An issue with the interfacial area concentration transport equations, as presented, becomes apparent when considering their dependent variables. The shown equations are area averaged in the streamwise direction, z. Three-dimensionality is a possibility but requires many more models as well as experimental data that can match this level of detail. This is important when considering flow in a nuclear reactor because where the distribution of void is important to convective heat transfer properties. An issue with the equations is that they were originally developed for the bubbly flow regime. The origin of the interfacial area transport equations comes

from the Boltzmann transport equation, which describes discrete particle distribution. Therefore, the interfacial area transport equations assume spherical or slightly deformable bubbles. Accounting for flow regimes with highly deformed interfaces has been a research focus in the community but involves significantly more closure relationships [35, 34].

1.2.6 High-Resolution Two-Phase Flow Regime Simulations

High-resolution two-phase flow simulations are still a relatively recent focus in the scientific community. Experiments cover a larger area in the space of two-phase flow phenomenon but, as will be discussed, simulation continues to demonstrate its utility. Some very enlightening DNS studies have been performed. Early work by Esmaeeli and Trygvasson [36, 37] studied bubbly flows to observe the dynamics of small rising clusters of bubbles. A combination of 2D and 3D simulations were performed with only eight bubbles in the 3D simulations. Later, Lu and Tryggvason [9] studied how the deformability of bubbles affects turbulent channel flow. These simulations increased the number of simulated bubbles to 21. The results showed bubble deformability determines the void distribution. Bolotnov [38] performed a similar study, this time using the bubbly channel flow to conclude bubbles improve turbulence isotropy for low Reynolds number flows. Elghobashi [39] reviewed the DNS work on how bubbles and droplets behave in turbulence. The review covers research on bubbles and droplets smaller and larger than the Kolmogorov scale and several different interface capturing methods. The review found most methods are restricted to viscosity and density ratios of about 0.01, a limitation not experienced by PHASTA. Some smaller scale simulations focused on analyzing individual bubbles to determine bubble induced turbulence and drag coefficients [40, 11]. While possible, an experimental study of individual bubbles encounters statistical and resolution challenges that are easier for a simulation to overcome. Simulations with more complex geometries, PWR

subchannels with spacer grids, have recently been performed [8, 41], this time with hundreds of bubbles being simulated and information specific to individual bubbles being collected in-situ. Due to the large number of bubbles and complex geometry, these simulations require extremely large meshes and powerful computational resources. The tradeoff for such an expense is obtaining flow information that is highly detailed and directly relevant to the nuclear industry. Moving beyond the bubbly flows, Behafarid et al. [7] studied Taylor bubble motion in a pipe. The rise velocity and shape of a Taylor bubble is relatively well described, thanks largely to Dumitrescu [42], allowing for validation of the DNS. Rodriguez [43] simulated annular flow and was able to capture the major physics associated with annular flow (liquid film thickness, large wave formation, and bubble carry-under). By using advanced analysis techniques, the dispersed liquid and gas phases were both tracked during the simulation, allowing for four-field information to be collected and analyzed. The possibility to collect this numerical data in various ways highlights a major advantage of DNS.

So far, only simulations of statistically steady state flows have been discussed. Only recently has the focus of a high-fidelity two-phase flow simulation been a two-phase flow undergoing a major topology change [10, 44, 45, 46]. In this work spherical bubbles were placed in a channel and were allowed to coalesce over time. In addition to observing how various parameters develop over time, the series of papers investigates the effect of surface tension and void fraction on the development and eventual steady state flow. Numerical data was collected to analyze how the topology change affected the flow over time. Lu and Tryggvason found the void distribution and topological structure was strongly related to both the surface tension and void fraction. An important distinction of this work is that the observed transient is a consequence of the initial bubble distribution, rather than some outside forcing factor that drives the flow from one steady

state to another. Therefore, this study is distinctly different from nuclear reactor flows where the initial condition is single phase liquid and flow regime transitions are forced by void addition through boiling.

Similarly, but on a smaller scale, Mohammadi et al. [47] studied the coalescence of two water droplets in oil. This study examined the effect of surface tension, collision velocity, and how off-center the bubbles collided with each other on the coalescence process. The code was first validated and proven to agree very well with experiments. The results showed how each of the aforementioned parameters affects the coalescence process, which is very important for flow regime transitions.

Another recent paper used DNS to study two-phase flow in both 2D and 3D inclined pipes [48]. This work first solved for a steady state light fluid only solution and then injected stratified heavy fluid into the pipe. The results were compared to flow regime maps in order to show agreement between the code and experiments. Both the 2D and 3D simulations agreed with the flow regime maps. The researchers also used the simulations to compare how the 2D and 3D flows differ and concluded that the dynamics is only slightly different between them.

After an extensive literature review, a study using high-fidelity simulations to analyze the transition between one stable two-phase flow regime state to another stable flow regime state has not been found. The lack of simulation on this topic represents a gap in the field that is commonly explored through experimentation. The objectives of the research presented in this report include addressing this research gap by using the PHASTA code to simulate two-phase flow regime transitions. Due to the challenge of simulating highly turbulent transient two-phase flows, a significant focus of the work is to determine computational requirements for simulating such a flow as well as assess PHASTA's ability to accurately simulate these flows. In addition, important

data analysis techniques that are needed to analyze the computational data will be discussed. This creates a framework for future researchers to follow when developing their studies. A series of flow regime transition simulations will also be discussed. DNS produces volumes of numerical data that are not matched by that of other numerical methods or experiments. This ability provides the opportunity to extensively analyze and elucidate the physics of the two-phase flow regime transition phenomena. This contribution aims to bring a physical understanding to a largely empirically based field.

1.2.7 Interface Capturing Simulations Validation

Validation of interface capturing simulations is a difficult task due to the challenge of obtaining accurate experimental data that can match the length and time scales resolved by such simulations. Even single-phase DNS relies on time averaged quantities to validate their simulations. The single phase DNS of Lee & Moser [1] and the multiple single phase DNS studies reviewed in [49] all compare time averaged quantities, such as velocity, Reynolds stresses, wall shear, and vorticity with experimental data. Ideally, since DNS can resolve individual eddies, validation would occur at the eddy level. As discussed in [50, 51], single phase DNS has been able to accurately simulate the horseshoe structure of wall bounded turbulence in the viscous sub-layer. However, the current practice is to trust the eddies are modeled accurately if the velocity and Reynolds stresses agree with experiments. Two-phase DNS has the added challenge of capturing the behavior and interactions of the interface. The interface adds a new scale of resolution because during coalescence important physics occur on the fraction of micrometer scale [52]. In addition, bubbles can both induce and suppress turbulence, necessitating the interface capturing method accurately recreates this turbulence generation and suppression. Experimental data for such phenomena does exist. Using techniques like particle image velocimetry (PIV), instantaneous velocity and vorticity

measurements of the rise of a single bubble in stagnant liquid are possible [53, 54]. These experiments are even capable of 55 μm resolution [53], more than fine enough to compare to a two-phase DNS. Unfortunately, even when simulations attempt to reproduce the exact test of a bubble rising in a stagnant liquid, only parameters like terminal bubble velocity are compared to experiments for the validation [55].

A common validation technique for two-phase DNS is to measure the interface location because in complex flows this can be more easily measured experimentally than turbulence (it would be difficult to experimentally measure highly resolved instantaneous turbulence in bubbly or churn flow conditions). For example, Lahey [56] used the classic 2D dam break problem to validate PHASTA. The front location and the height of the liquid is measured over time and compared to experiments. Mohammadi et al. [47] compared the shape and location of bubble interfaces as they coalesced in viscous oils and Xie et al. [48] made subjective flow regime classifications and ensured their code's predictions matched flow regime maps. None of these validation studies capture the finest resolved scale of the respective simulations. To the best of the author's knowledge no two-phase DNS researcher has used the single eddy scale to validate their simulations. As mentioned, the reason for this is the difficulty in experimentally measuring and observing these scales. At the moment the best option is to find experiments as detailed and relevant to the research and use the available experimental data to validate the predictive capabilities of the same selected quantities for which experimental data is available.

1.3 Research Objectives

Using high-fidelity computational data to inform the knowledge base of two-phase flow is a continuous objective for researchers. Two-phase flow regimes offer an excellent opportunity for furthered understanding but the complexity of two-phase flow regime transitions necessitates that

computationalists pay extra attention to preparing a simulation. Considering interface capturing two-phase flow regime transition DNS is a new field, the computational requirements, both pre and post-simulation, have yet to be fully outlined by the CFD community. This dissertation presents a foundation for simulating two-phase flow regime transitions by: (a) Identifying limiting scales for resolving the flow and proposes computational requirements for ensuring accuracy; (b) Proposing and completing a validation hierarchy, based on the work contributed by Oberkampf [57, 58, 59] to the CFD field, for flow regime transitions; (c) Developing data collection and analysis tools that can take advantage of the wealth of computational data. The presented tool is designed for flow regime transitions as it captures interfacial area, a parameter often used to analyze flow regimes; (d) Performing simulations and analyzing their associated data to determine the driving physics of the two-phase flow regime transitions. These simulations are the first of their kind and simulate forward transitions, which are common to the field, and reverse simulations, which are explored less often.

This dissertation is structured as follows. The PHASTA's governing equations and the level set method for interface capturing are explained and a validation history is provided in CHAPTER 2. Despite having a robust flow solver available for this work, very little research has been committed to studying transient two-phase flows. Therefore, CHAPTER 3 is dedicated to determining the necessary components for successful interface resolved two-phase flow regime transition DNS. This includes discussing new meshing requirements specific to two-phase flow and data collection and analysis tools. CHAPTER 4 provides details on how the simulations are prepared (meshing, geometry, boundary conditions, etc.) and CHAPTER 5 details how we trust PHASTA to be capable of simulating this complex problem (validation). CHAPTER 6 presents and analyzes all the simulations prepared for this research. There is a focus on determining the mechanisms for

transition and what properties differ between each mechanism. A flow regime transition criterion is also presented and tested to ensure its validity. CHAPTER 7 provides the major conclusions drawn from this dissertation and CHAPTER 8 proposes some recommendations for future work.

CHAPTER 2. NUMERICAL METHODS

The open source PHASTA code is the primary tool used in this work. PHASTA is a Parallel, Hierarchic, higher-order, Adaptive, Stabilized (finite element method-based (FEM)), Transient Analysis flow solver capable of simulating compressible and incompressible flows on structured (hexahedrons) and unstructured meshes (tetrahedrons). PHASTA uses the level set method for capturing the interface between two immiscible fluids. PHASTA is highly parallelizable and has been shown to scale well up to 768×1024 processors on the IBM Blue Gene/Q Mira System (at Argonne National Laboratory). Detailed descriptions of PHASTA and its implementation can be found in [60, 61, 62, 63]. PHASTA's capability of using unstructured meshes allows for simulation of complex geometries.

PHASTA has a strong history of two-phase flow simulations including: studying the effect a single bubble has on turbulence [11], examining full bubbly flow with hundreds of bubbles where both the liquid turbulence and individual bubble information is collected and analyzed [38, 8], using Taylor bubble flow to verify and validate the code [7], simulating the complexities of annular flows [43], and demonstrating the capability to simulate implosions and plunging jets [56]. The body of work behind PHASTA has shown its value to analyzing two-phase flows.

2.1 Governing Equations

PHASTA solves the strong form of the incompressible Navier-Stokes (INS) equations [64]:

Continuity:
$$u_{i,i} = 0 \tag{2.1}$$

Momentum:
$$\rho u_{i,t} + \rho u_j u_{i,j} = -p_{,i} + \tau_{ij,j} + f_i \tag{2.2}$$

where ρ is the density, u_i is the i component of velocity, p is dynamic pressure, τ_{ij} is the viscous stress tensor, and f_i is the i component of the body force vector (which includes gravity, surface tension, and driving pressure gradient). In a periodic domain where gravity is oriented parallel to

the flow direction, an additional value equal to the hydrostatic pressure gradient is added to the pressure gradient. This value is a simple multiple of density and gravity and it supports the weight of the fluid mixture, preventing it from falling downward due to the gravity forces. The spatial and temporal discretization of these equations are given in [64]. The viscous stress tensor is

$$\tau_{ij} = \mu S_{ij} = \mu\left(\frac{\partial u_i}{\partial x_j} + \frac{\partial u_j}{\partial x_i}\right) \quad (2.3)$$

where μ is dynamic viscosity and S_{ij} is the strain rate tensor.

2.2 Level Set Method

PHASTA implements the level set method for interface capturing [65, 66, 67]. In the level set method a signed distance field, φ, is overlaid on the entire domain. The fluid-gas interface is located at the zero level set value in the distance field (i.e. the interface is located at $\varphi = 0$) and the liquid is in the positive distance field and gas in the negative distance field. The interface is advected exactly with the fluid, prescribed by

$$\frac{\partial \varphi}{\partial t} + \mathbf{u} \cdot \nabla \varphi = 0 \quad (2.4)$$

where $\boldsymbol{u}$ is the fluid velocity vector. To allow a continuous transition from liquid to gas properties, the interface is assumed to have some thickness, 2ε. Typically, ε is at least 1.2 computational elements in size. The property transition follows the smooth Heaviside function, given by

$$H_\varepsilon(\varphi) = \begin{cases} 0, & \varphi < -\varepsilon \\ \frac{1}{2}\left(1 + \frac{\varphi}{\varepsilon} + \frac{1}{\pi} sin\left(\frac{\pi\varphi}{\varepsilon}\right)\right), & |\varphi| < \varepsilon \\ 1, & \varphi > \varepsilon \end{cases} \quad (2.5)$$

Hence, fluid properties are defined by

$$\rho(\varphi) = \rho_l H_\varepsilon(\varphi) + \rho_g\left(1 - H_\varepsilon(\varphi)\right) \quad (2.6)$$

$$\mu(\varphi) = \mu_l H_\varepsilon(\varphi) + \mu_g\big(1 - H_\varepsilon(\varphi)\big) \quad (2.7)$$

This method is not limited in the number of gas and/or liquid regions allowed, meaning continuous liquid, continuous gas, dispersed liquid and dispersed gas flows are all possible. While solving Eq. (2.4) the far distance field can become distorted by the fluid velocity. To maintain an accurate distance field, a redistancing operation is performed by solving

$$\frac{\partial d}{\partial \tau} = S(\varphi)(1 - |\Delta d|) \quad (2.8)$$

where d is a scalar that represents the corrected distance field and τ is the pseudo time over which the equation is solved [66, 67]. $S(\varphi)$ is defined as

$$S(\varphi) = \begin{cases} -1, & \varphi < -\varepsilon_d \\ \left(\frac{\varphi}{\varepsilon_d} + \frac{1}{\pi}\sin\left(\frac{\pi\varphi}{\varepsilon_d}\right)\right), & |\varphi| < 1 \\ 1, & \varphi > \varepsilon_d \end{cases} \quad (2.9)$$

Where ε_d is the distance field interface half-thickness which can be different from ε previously defined. Notice that $\frac{\partial d}{\partial \tau}$ is zero at the interface, meaning the interface location is not changed during redistancing. Figure 2.1 plots this property transition.

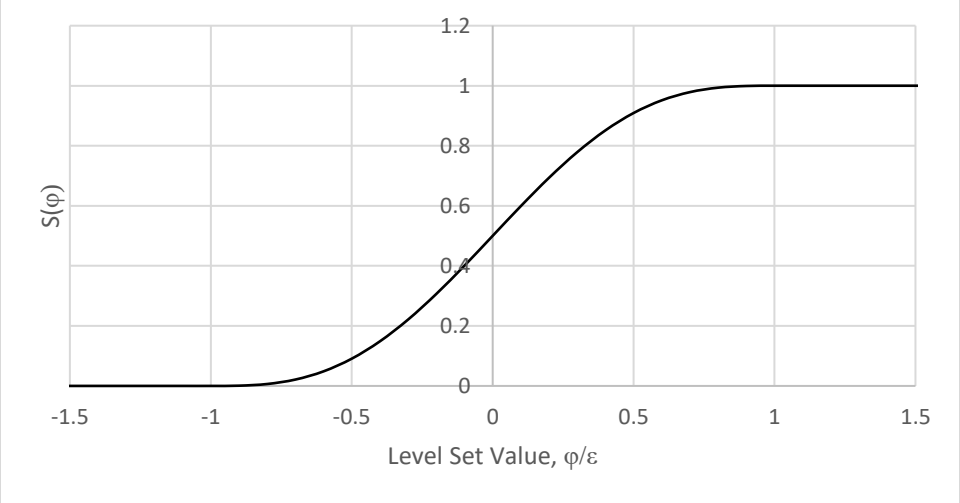

Figure 2.1: Depiction of the property transition across the interface.

2.3 Code Validation

This section will expand on PHASTA's validation in order to provide a basis for the validation discussion that occurs in CHAPTER 5. A significant amount of effort has been placed in validating PHASTA and it begins with single phase simulations in a parallel plate channel. Trofimova et al. [3] designed simulations of two different friction Reynolds numbers, 180 and 395, that matched the simulations performed by Moser et al. [2]. Three different meshes, ranging from 66,500 to 9,500,000 computational elements in size were designed for each flow condition. For both flows all the meshes met the typical requirements for single phase DNS (discussed in depth in Section 3.1 Single Phase Flow Resolution Requirements) at the wall but the bulk resolution varied between meshes. Only the finest mesh met the DNS standard for resolution. Statistics ranging from mean velocity (Figure 2.2 left) to the decomposed energy spectra (Figure 2.2 right) were compared to the Moser et al. [2] numerical data. The code used by Moser et al. has been extensively validated against high Reynold number experiments. The code has also shown to predict high Reynolds numbers phenomena that had never been observed computationally before. Therefore, this code-to-code comparison is utilizing a robust code. The comparison showed that for the sufficiently refined meshes (the finest mesh in the study), PHASTA was capable of accurately predicting the turbulent flow behavior.

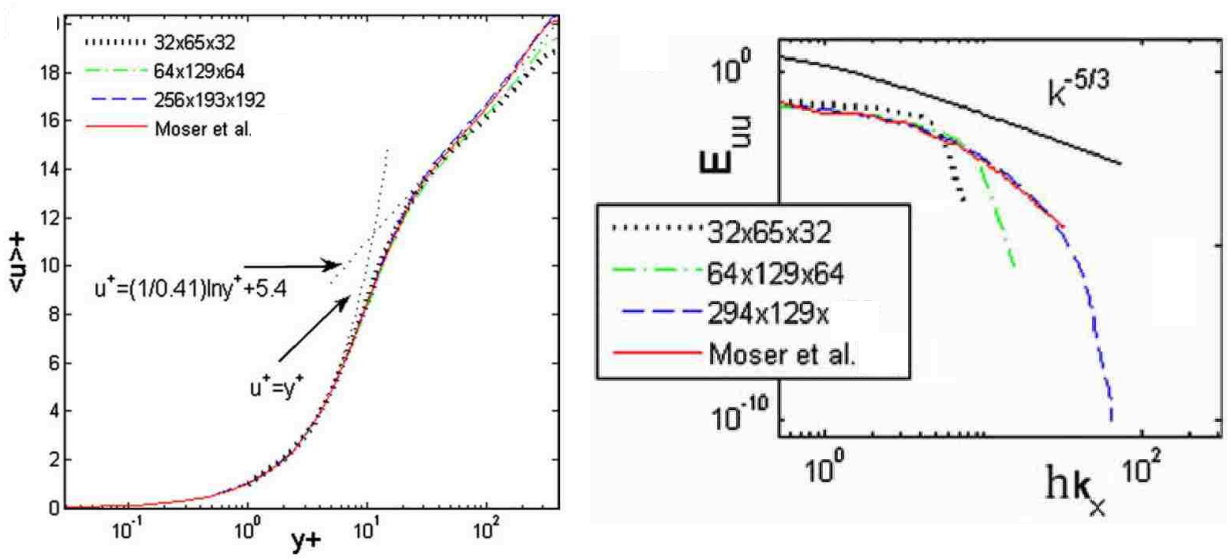

Figure 2.2: Images from Trofimova et al. *[3]* showing the mean streamwise velocity (left) and streamwise energy spectra (right) PHASTA data compared to Moser et al. *[2]*.

Lahey [56] presents PHASTA's results for the classic dam break problem. A 2D column of water, held by an imaginary dam, is initialized and allowed to flow as if the dam holding it suddenly disappeared. The liquid height and leading edge location is tracked and can be compared to experimental data. The results show that PHASTA can accurately predict the liquid's behavior even for a relatively coarse mesh. Just before the liquid hit the wall on the opposite side of the domain in the simulation, the liquid height differed by about 10% and the liquid front location differed by about 8% (see Figure 2.3).

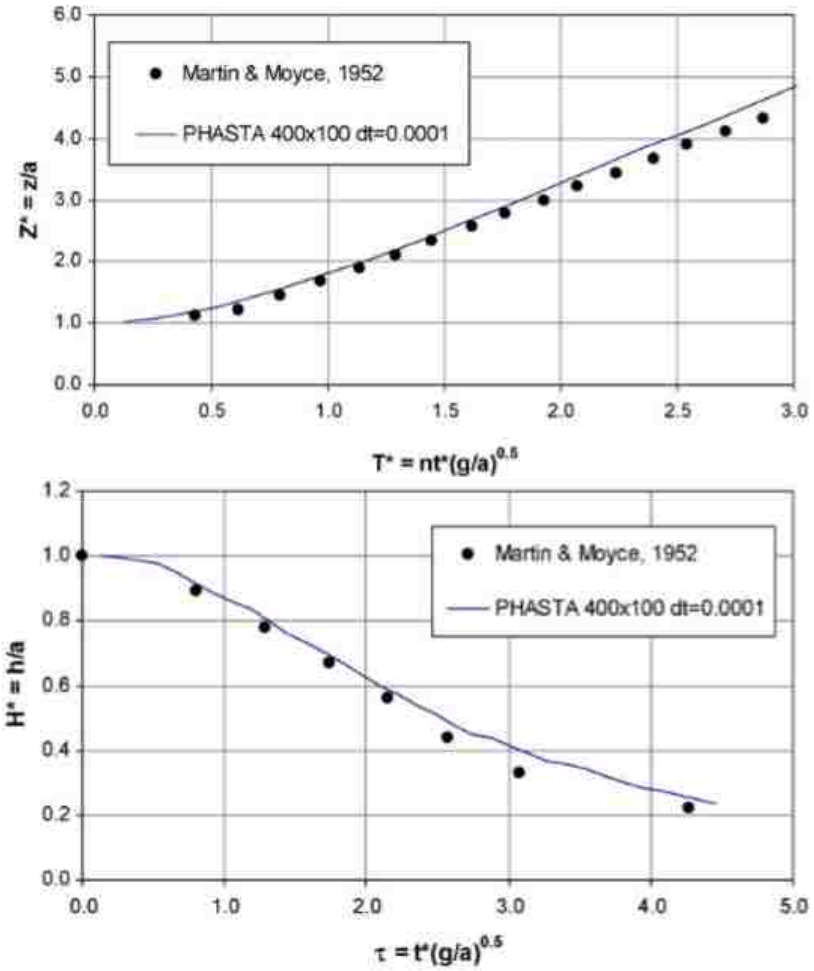

Figure 2.3: Images from Lahey *[56]* showing the results from the dam break front location (top) and height (bottom) compared to experiments.

Thomas et al. [68] performed a validation study of a single bubble in laminar flow. The drag force on the bubble was extracted and compared to correlations. The comparison showed excellent agreement with the Tomiyama et al. [69] correlation at the lower Reynolds number (see Figure 2.4).

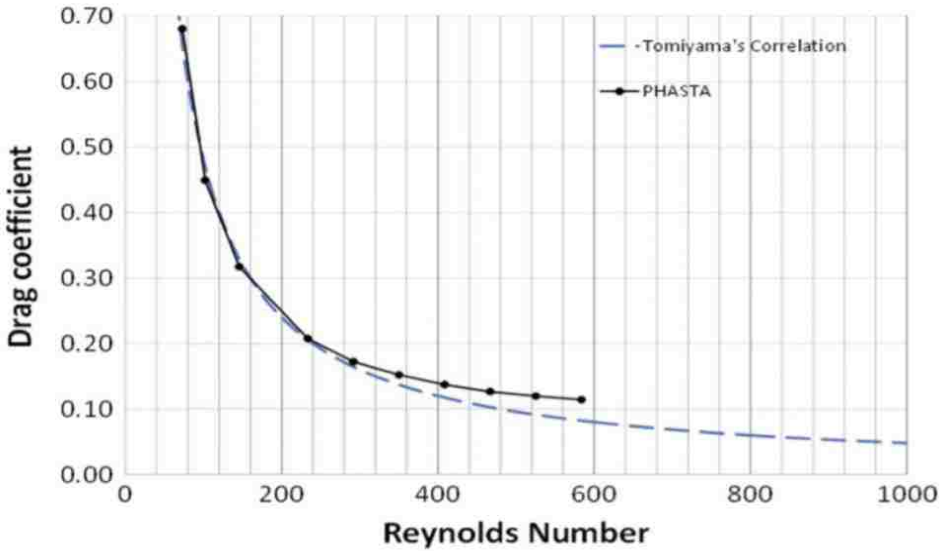

Figure 2.4: An image from Thomas et al. *[68]* showing how the PHASTA drag coefficient predictions compare to the Tomiyama correlation.

At the larger Reynolds numbers the PHASTA bubble deformed slightly from spherical, varying the results from the Tomiyama correlation, which assumes spherical bubbles. Experimental data for the drag coefficient on a bubble in turbulent flow was not available in this study. However, when the calculated drag coefficient was compared to the prediction from a simple force balance using the relative velocity, the results compared well. This work shows that PHASTA is able to predict the drag coefficient, which depends largely on the interfacial shear, of a bubble in both laminar and turbulent flow.

Feng & Bolotnov [11] extended the single bubble studies to examine bubble-induced turbulence. In this work the turbulence in front of and behind a bubble was examined. Using dimensional analysis the factors contributing to turbulence suppression and enhancement were isolated. This study also did not have experimental data to compare to, due to the difficulty of experimentally isolating a single bubble's turbulence generation. However, a study was performed to ensure the interface capturing method was not artificially affecting the turbulence. It was found

that given a fine enough resolution and an appropriate interface half thickness, the level set method only changed the turbulence intensity by 2%, at most.

Taking these results one step further leads to bubble channel flow simulations, which were performed by Bolotnov et al. [70]. In this work comparisons to experimental data were not performed, but the simulation predicted the wall peaked bubble distribution that is expected in bubbly flow where the bubbles are not deformable. The work also examined flow of a large deformable bubble in a channel and found the bubble remained in the center, as is expected.

Behafarid et al. [7] performed a simulation of a Taylor bubble rising in a pipe of stagnant liquid. A common correlation for the rise velocity of a Taylor bubble, u_T, that has been proven to be accurate, takes the form of the following:

$$u_T = C\sqrt{gD} \tag{2.10}$$

C is a coefficient determined from fluid properties and geometry, *g* is gravity, and *D* is the pipe diameter. Behafarid et al.'s simulation Eq. (*2.10)* predicted a rise velocity of 16.88 cm/s while PHASTA predicted 16.44 cm/s, only a 2.6% difference. This result is relevant to the accurate prediction of both interfacial shear and Taylor bubble shape predictions and is particularly relevant to the work presented here.

CHAPTER 3. BUILDING A FRAMEWORK FOR SIMULATING FLOW REGIME TRANSITIONS

Due to the lack of research in this area it is important to establish a standard for future researchers to reference when developing their own interface resolved flow regime transition simulation research. This Chapter will cover some well-established single phase DNS meshing requirements, as well as introduce new two-phase considerations originally developed for flow regime transition simulations, but are applicable to any two-phase flow simulation. Additionally, important computational considerations will be discussed and some data analysis tools useful to transient two-phase flow regime transitions will be presented.

3.1 Single Phase Flow Resolution Requirements

Amongst the DNS community, it is generally accepted that a fully resolved DNS mesh has a bulk mesh fine enough to capture the Kolmogorov scale and a wall boundary layer mesh that resolves the steep velocity gradients in the viscous sublayer [51]. The Kolmogorov scale is the smallest scale of turbulence in the flow that carries energy before dissipating it into heat. Therefore, in order to be fully resolving the turbulent flow, a DNS needs to capture this scale, otherwise the momentum transport is incorrect. Very close to the wall viscous forces dominate. Therefore, as the fluid approaches zero velocity, due to the no slip condition, the velocity profile approaches a straight line (e.g. constant gradient). Designing the wall boundary layer mesh to have at least one point in this linear region is important to resolve the wall shear. This shear is what ultimately produces eddies in turbulent flow, making its resolution also very important to DNS. To quantify the resolution Δy^+ at the wall and in the bulk are typically referenced. Δy^+ is a nondimensional distance,

$$\Delta y^+ = \frac{\Delta y u_\tau}{\nu} \quad (3.1)$$

where Δy is the absolute length (in meters), ν is the liquid kinematic viscosity, and u_τ is the friction velocity, defined as

$$u_\tau = \sqrt{\frac{\tau_w}{\rho_l}} \quad (3.2)$$

where τ_w is the wall shear. For a fully resolved DNS, $\Delta y^+_{wall} \leq 1$ and $\Delta y^+_{bulk} \leq 12$ are the generally accepted criteria [1, 51].

3.2 Two-phase Flow Resolution Requirements

Formulating two-phase resolution requirements has been previously addressed by Fang and Bolotnov [8] who determined at least 20 computational points across the diameter of a bubble are required to simulate a bubble which can properly deform during the flow solution. This requirement was formulated to tackle more than one important consideration to bubble dynamics. First, the 20 point resolution minimizes the mass conservation issue that the level set method experiences. Second, the 20 point criterion ensures the curvature of the bubble, even when it deforms, is properly resolved, which allows for the surface tension force to be accurately calculated. Therefore, this criterion does not address flow physics such as how thick the interface is relative to gradients or turbulent structures in the fluids. Additionally, for slug flow the Taylor bubble is so large the 20 point minimum is practically not a concern until it begins to break up. To ensure the transitions are fully resolved different two-phase factors were considered.

3.2.1 Interfacial Shear

The interfacial shear, the shear between the liquid and the gas, is extremely important in these accelerating flows, as will be shown in future discussion. Interfacial shear plays a role in

determining the relative velocity, bubble breakup, and BIT. Additionally, the single phase DNS resolution requirements are built around the wall shear, making the interfacial shear an excellent place to start for two-phase resolution considerations. To understand how well DNS resolves interfacial shear, a series of simulations were designed based on the simple shear flow experiments performed by Karam and Bellinger [71]. In these experiments, two highly viscous fluids were used to form a continuous phase and a single droplet between two parallel plates moving in opposite directions. This forms a linear shear flow that deforms the droplet but does not move it laterally. The droplet deformation occurs because the continuous phase applies a shear force that stretches the bubble in opposite directions. This makes this experiment an excellent candidate to test the resolution requirements corresponding to interfacial shear. Properties for the fluids used are shown in Table 3.1.

Table 3.1: Experimental properties from *[71]* used to design simulations

Fluid	**Density [kg/m^3]**	**Viscosity [kg/m-s]**	**Surface Tension [N/m]**	**Shear Rates [1/s]**
Continuous	998	3.11	0.0027	0.4174, 17.53, 25.45
Droplet	920	0.203		

Due to the high viscosity and relatively small density difference, buoyancy is practically insignificant and the droplet is held almost perfectly in place for multiple seconds. Previous single bubble studies performed in PHASTA [11] required the use of the partial-integral-derivative (PID) controller [68]. The PID controller detects the forces acting on a bubble and applies equal and opposite forces to hold the bubble in place. Therefore, measurements of lift force acting on the bubble, or bubble-induced turbulence behind the bubble, could be made. By choosing a study using an extremely viscous liquid and small density difference, there is no need to use the PID controller because the bubble is naturally held in place. This allows for simulations with PHASTA without

the PID controller, eliminating the concern of inaccuracies introduced by it. Karam and Bellinger measured droplet deformation and the angle of the deformation relative to the centerline plane parallel to the plates. Deformation, D, is defined by

$$D = \frac{L - B}{L + B} \qquad (3.3)$$

where L is the length of the bubble along its major axis and B is the length of the droplet along its minor axis. Figure 3.1 shows a diagram of the deformed bubble with L, B, and the measured angle shown.

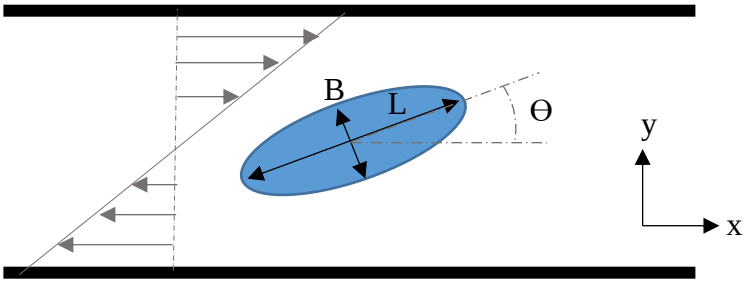

Figure 3.1: A diagram showing the layout for the experiment performed by Karam and Bellinger *[71]*. The velocity profile of the continuous phase is shown. Not to scale.

Three different shear rates were chosen, shown in Table 3.1. All three shear rates remain fully laminar due to the extremely high viscosity of the continuous fluid. Three different meshes were also designed for the simulations. The mesh sizes were 60, 30, and 15 μm, which corresponds to 8.5, 17, and 34 points across a 0.5 mm diameter droplet, respectively. The series of nine simulations were run until the bubble no longer changed shape and measurements were taken in Paraview [72]. Note that the finest mesh could not converge in the lowest shear simulation. The reason for this is not clear but may be a result of the dominant viscous forces, highly resolved mesh, and the method by which the finite element method in PHASTA is stabilized coming together to form an unstable solution. Nonetheless, the summary of the results from these simulations is presented in Table 3.2.

Table 3.2: Results from the simple shear simulations

Shear Rate [1/s]	Mesh Size [μm]	D_{sim}	D_{exp}	Error in D [%]	Θ_{sim}	Θ_{exp}	Error in Θ [%]
0.4174	60	0.63	0.46	37.0	18	N/A	N/A
	30	0.51		10.8	26		N/A
	15	N/A		N/A	N/A		N/A
17.53	60	0.42	0.33	27.2	30	27	11.1
	30	0.38		15.2	32		18.5
	15	0.36		9.1	32		18.5
25.45	60	0.66	0.39	69.2	26	21	23.8
	30	0.58		48.7	23		9.5
	15	0.53		35.9	25		19.0

As Table 3.2 shows, as the simulations are further resolved the agreement generally improves with respect to D. It is worth noting that the experiment used droplets about 0.5 mm in diameter and the measurement tools were only capable of measuring to 0.1 mm accuracy. This means there could be significant uncertainty in the reported D values, especially when the B dimension can be as thin as 0.3 mm. Using the two higher shear rates, the grid convergence index (GCI) and the order of convergence, *p*, can be calculated. GCI is a measurement that estimates the discretization error present in the finest simulation [73]. Here *p* is defined as

$$p = \frac{1}{ln(r_{21})}\left|ln\left|\frac{\varepsilon_{32}}{\varepsilon_{21}}\right| + q(p)\right| \quad (3.4)$$

where r_{21} is the ratio of the middle mesh to the finest mesh size (larger than one), ε_{32} is the difference between the solutions for the coarsest and middle mesh, ε_{21} is the difference between the solutions for the middle and finest mesh, and $q(p)$ is defined as

$$q(p) = ln\left(\frac{r_{21}^{p} - s}{r_{32}^{p} - s}\right) \quad (3.5)$$

where r_{32} is the ratio of the coarsest mesh to the middle mesh size (larger than one), and *s* is

$$s = 1 \cdot sgn\left(\frac{\varepsilon_{32}}{\varepsilon_{21}}\right) \quad (3.6)$$

GCI is defined as

$$GCI = \frac{1.25 e_a^{21}}{r_{21}^p - 1} \quad (3.7)$$

where $e_a^{21}$is

$$e_a^{21} = \left| \frac{\varphi_1 - \varphi_2}{\varphi_1} \right| \quad (3.8)$$

where φ corresponds to the solution for the quantity of interest for the mesh indicated by the subscript.

The order of convergence in the 17.53 and 25.45 1/s shear rate cases was 1.63 and 0.74, respectively. This aligns with the first order convergence that was expected. The GCI in these cases was 2.4% and 17.4%, respectively. The higher shear rate having a larger GCI is logical. A GCI for the lowest shear rate could not be directly calculated due to there being only two measurements. However, if p is assumed to be one, then the GCI can be estimated to be 29.4% for the middle mesh. Presumably, if the finest simulation were capable of numerically converging, this error would become significantly smaller. Together, this suggests that the finest mesh used in these simulations is required to resolve the interfacial shear.

As mentioned earlier, interfacial shear is similar in concept to the wall shear that determines the y^+ meshing resolution requirements. However, this flow is so viscous that even if the largest interfacial shear were used to calculate y^+ values (about 100 N/m^2), the supposed necessary mesh size would be on the order of the distance between the plates. Therefore, this method for calculating meshing requirements was not considered. To better determine when the simulation becomes fully resolved, measurements of interfacial shear were taken on the inner and outer sides of the interface, as well as on the top and bottom sides of the droplet. Paraview was used to extract this information

using the method described in Section 3.4 Interfacial Shear Data Collection. Using this information the interfacial shear for each mesh and shear rate simulation was plotted, shown in Figure 3.2.

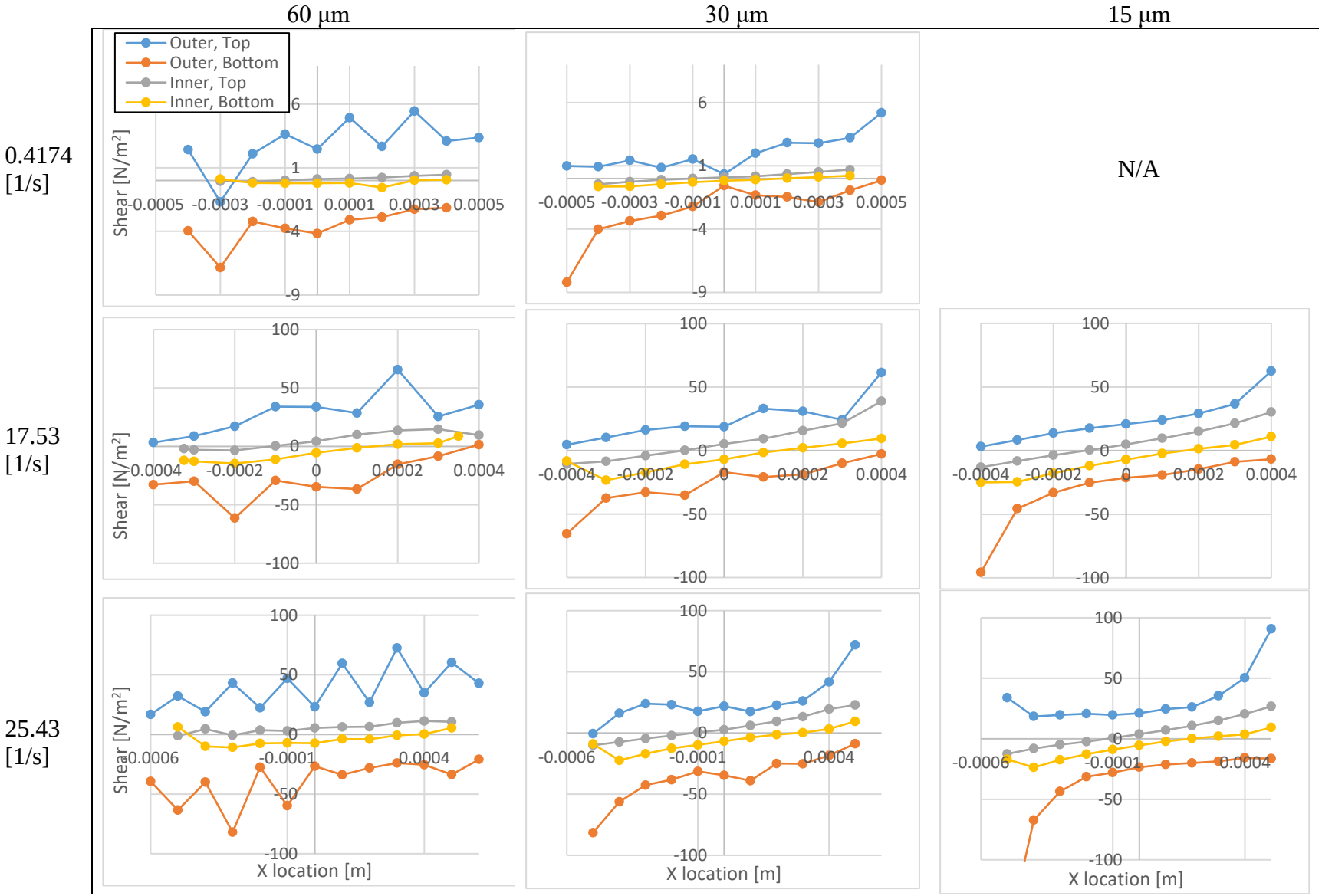

Figure 3.2: Interfacial shear profiles for the droplet deformation simulations.

As can be seen in Figure 3.2, the top and bottom shear profiles for both the inner and outer sides of the droplet are nearly mirror images of each other, which is expected due to the symmetry of the flow. The coarsest meshes produce a saw tooth pattern, which somewhat persists in the middle mesh, but has completely disappeared in the finest mesh. This is true for all the shear rates, except the smallest where the finest mesh did not converge, despite their values differing by a factor of about 60. Similarly, the magnitude of the interfacial shear in each case varies by a factor of about 10. Despite this variability in the shear rate and interfacial shear, each simulation becomes resolved at the same mesh. If the finest mesh is assumed to fully resolve the shear then this suggests that interfacial shear, or magnitude of velocity gradient at the interface, is not the primary factor determining if the mesh is fine enough. Instead the determining factor must be a parameter that is approximately constant in every simulation. The same droplet size, 0.5 mm diameter, is used in each simulation, making it a possible contender. In their work Karam and Bellinger [71] have cited the important role that the recirculation within the droplet or bubble in a simple shear flow may play in determining the shape of the droplet/bubble. Given a strong enough recirculation the interface is supported and can resist deformation to the point where larger shear rates deform the droplet less. Additionally, the recirculation within the droplet helps determine the interfacial shear because very close to the interface the two fluids must have the same velocity. There must be a conservation of momentum across the interface, which is why the shear flow drives the recirculation in the droplet. However, if the recirculation cannot be resolved then the velocity profile in the droplet will change, also changing the gradient at the interface and the momentum transfer across the interface. Therefore, it is theorized that resolving the recirculation inside the droplet is important. Figure 3.3 shows images of the streamlines inside the droplet for each mesh in the 25.45 1/s shear rate simulations.

(a)

(b)

(c)

Figure 3.3: Images from the 25.45 1/s shear rate case showing the recirculation inside the droplets in the coarse (a), intermediate (b), and fine (c) meshes. The interface is shown as the transparent grey contour and the streamlines are the white lines.

As is clear from Figure 3.3, as the mesh becomes finer the recirculation becomes stronger, more defined, and the streamlines become smoother. The stronger recirculation supports the droplets, causing it to become less deformed for the finer meshes. Additionally, as the mesh becomes finer the interface thickness becomes thinner as well. The shorter distance over which the property transition occurs in the finer meshes minimizes its effect on the recirculation. The property transition clearly interferes with the coarse mesh's recirculation. The higher viscosity dampens the recirculation, visible by the region inside the droplet close to the interface where no streamlines

exist. This observation is important because it indicates that the addition of a droplet into a simple shear flow is enough to make the simulation under resolved. The single phase shear case would be fully resolved at the coarse mesh and the solution would not change as the mesh is refined. However, by adding the droplet (or a bubble), a confined recirculating flow is formed in the domain. An analogy can be drawn between this confined recirculation and a single turbulent eddy that is somehow held in place. With this addition, the resolution requirements suddenly jump to meet the recirculation. As shown, if this recirculation is not properly resolved the interfacial shear and droplet deformation will be incorrect.

Considering this observation, the conclusion is the mesh must be fine enough to resolve the circulation in the fully deformed droplet and further capture the velocity gradients at the interface. As has been demonstrated, due to the "eddy" that can be formed inside the droplet this requirement may be more stringent than the classic single phase DNS requirements. Quantitatively, the B length is the smallest dimension of this recirculation flow in the droplet. In the 25.45 and 17.53 1/s fine mesh simulations the B length, without the half interface thickness, corresponded to 0.274 mm and 0.331 mm, respectively. This equates to 18.3 and 22.1 points across the length, respectively. Given the middle mesh had a mesh size equal to two times the fine mesh size, more than 10 points across the B dimension are required to resolve the recirculation and 18 is sufficient. This is very similar to, but slightly less demanding than, the 20 points across the diameter criterion determined by Fang and Bolotnov [8] if the bubble remains spherical. Deformed bubbles need to maintain this new criterion, which for highly deformable bubbles may be very demanding. It is also possible, especially for large Taylor bubbles, turbulent structures form that do not occupy the entire volume of the bubble. In these circumstances, the structures will also need to satisfy some resolution requirements in case they collide with the interface. In flows where the eddy scale is smaller than

the bubble diameter the y^+ units become relevant because if eddies are generated in the bubble they likely start at the interface. The comparison between a wall and an interface is not perfect because the interface does not hold a no-slip condition, but a shear layer is still formed between them. A viscous sub-layer may not be formed, but the y^+ information generated from using the interfacial shear can inform the eddy generation and ensure the mesh meets the standard DNS requirement of 12 y^+ units. Therefore, in these cases standard y^+ units will determine if the flow inside the bubbles is fully resolved. Moving forward, in slug flow simulations the Taylor bubble's interfacial shear will likely rely on y^+ calculations since the bubble is too big for a single recirculating flow to form. The criterion for when a single recirculation occupies the entire bubble will likely apply when small bubbles are being torn off the Taylor bubble. The interfacial shear, and therefore the process of tearing the bubble off, will only be resolved for a certain minimum bubble size, corresponding to at least 10 and ideally 18 element lengths.

This study also revealed PHASTA's inability to simulate extremely large viscosity ratios. As cited in literature [39], most interface capturing DNS codes can only simulate viscosity ratios of 0.01 before the property transition across the interface causes numerical problems. PHASTA has been used to simulate the same viscosity ratio, but when attempting to recreate the experiments in Müller-Fischer et al.'s work [74], which used a highly viscous liquid continuous phase and standard air for the bubble instead of a lighter liquid, problems arose. The buoyant force would still only drive the bubble at 0.1 mm/s, making it practically still. However, it became quickly clear that the sudden viscosity change across the interface, a ratio of $6.393 \cdot 10^{-6}$, prevented the code from reaching numerical convergence. This ratio is an order of magnitude smaller than the smallest viscosity ratio, 0.0001, tested by DNS. Instead of reaching numerical convergence, extremely large velocities in the gas phase and large artificial jumps in pressure would occur around the interface.

This is likely due to the mesh being unable to resolve the extremely large velocity gradient that would need to be on the gas side of the interface in order to reconcile the large shear force on the liquid side. So instead, the momentum equation calculated that this shear force induced large velocities in the gas.

3.2.2 Liquid Film Resolution

The liquid film between the Taylor bubble and the wall can be quite thin while still maintaining a velocity profile. The velocity in the film must be well defined in order to capture the interfacial shear on the bubble and the interaction between the liquid leaving the film, also known as liquid film jets, and the wake behind the Taylor bubble. Due to how thin and close to the wall the liquid film is, the liquid is typically laminar, meaning the velocity profile takes up a parabolic profile. One side of the parabola has a zero velocity, at the wall, and the other moves with the interface of the bubble. Due to the fast moving Taylor bubble, the liquid film often has an average negative velocity for low flow conditions and a slower velocity if the flow rate is high enough. This approximate parabolic velocity profile has been observed experimentally [75, 76] and other measurements have shown how the liquid film can be less than a millimeter thick [77, 78]. Given the parabolic nature of the velocity profile, at least six points will be required to resolve the film. At least three points are required to define a curve so the 6 point resolution provides three points per side of the parabola. Ideally, the mesh would provide more than six points. This resolution requirement will be discussed further in the mesh design section.

3.2.3 Taylor Bubble Breakup Events

The bubbles that breakup from the main body of the Taylor bubble will either enter the wake of the Taylor bubble or depart the wake into the main body of the slug. Due to their influence on the flow dynamics, capturing a realistic distribution of these daughter bubbles is important to

resolving slug flow as well as the breakup of the Taylor bubble leading to new regimes. Additionally, capturing accurate bubble size distributions in the wake suggests the simulations are accurately capturing the physics of slug flow. There is very little research focused on determining size distributions of bubble breaking off from Taylor bubbles. However, there are studies that focus on tangentially related flows.

Evans et al. [79] performed an experimental study where the bubble distribution behind a ventilated cavity in downward pipe flow (creating what resembles a static cap bubble) was measured. Water and air at atmospheric pressure were used. In this experiment air is continuously pumped into downward flow, forming a gas cavity that stays in place and resembles a very large cap bubble or very short Taylor bubble. This forms a short liquid film region and a recirculation region, or wake, behind the cavity very similar to slug flow. The distribution of bubbles coming off the cavity are then measured. The diameter of the pipe is 5.0 cm, considerably larger than the pipe used in this work. The experiments found that the bubbles coming off the cavity were almost never smaller than 0.5 mm in diameter and typically averaged around 1-2 mm in diameter.

Experiments by Lehr et al. [80] performed a similar study, but for bubble columns. Air and water at atmospheric pressure were also used in this study. They found similar results where bubbles rarely were smaller than 0.5 mm in diameter and averaged around 2-4 mm in diameter, depending on flow conditions. This is promising for the flow regime transitions because these bubbles are well within the resolution capability available to this work.

An experiment performed by Sun [81] found that bubbles shearing off of large cap bubbles typically averaged at 0.5 mm and were as small at 0.2 mm. This is considerably smaller than the previous studies. An explanation for this may be the very high flow rates associated with this research, $j_l = 2.839$ and $j_g = 0.995$ m/s. At these flow rates the Reynolds number approaches

100,000. This exceeds the Reynolds number expected to be encountered in this study, meaning the bubbles are likely to be broken into smaller sizes by the more energetic turbulence. Even still, for a fully resolved flow of a Reynolds number equal to 100,000, the mesh would likely be capable of resolving these bubbles by approximately 10 points across the diameters.

3.3 Virtual Probe Data Collection

To collect the instantaneous local numerical data, the static probe approach was used. The tool places a network of static probes aligned along a plane, or planes, in the domain. The probe locations are chosen so that, for a pipe, there are many layers of probes that are all equidistant from the pipe wall and they align along radial lines extending from the center. The plane is static and collects data at every time step. Figure 3.4 shows the probe setup used for all the pipe simulations.

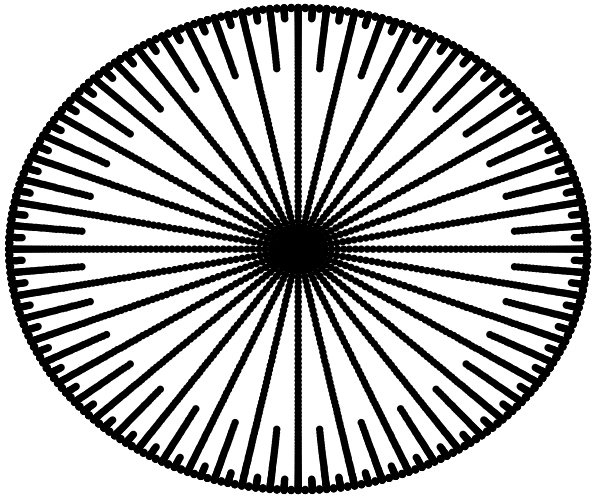

Figure 3.4: Numerical data collection probe locations used for the pipe flow simulations.

There are 5120 probes distributed among 75 layers. Each profile generated from analysis contains 75 radial data points. The point closest to the wall is well within the $\Delta y^+_{wall} \leq 1$ region for all times steps in the simulations. At each time step the velocity components, pressure, and level set values are collected at each probe. The user can time average this information for any timespan to

calculate the mean profile for many different quantities of interest. For example, mean u-velocity, void fraction, and $\langle v'w' \rangle$ Reynolds stress are all possible. Eqs. (*3.9*) and (3.10) show examples of how mean velocity and $\langle v'w' \rangle$ would be calculated.

$$U(t) = \frac{1}{N_r} \sum_{m=1}^{N_r} \left(\frac{1}{N_s} \sum_{j=1}^{N_s} u^i(t + t_j) \right) \quad (3.9)$$

$$\langle v'w' \rangle(t) = 1/N_r \sum_{m=1}^{N_r} \left(\frac{1}{N_s} \sum_{j=1}^{N_s} \Big(v(t + t_j) - V(t) \Big) \Big(w(t + t_j) - W(t) \Big) \right) \quad (3.10)$$

Here N_r is the number of ensemble runs performed (always one here), N_s is the number of time samples, t is the current time, and t_j is the time of a particular data sample. Important to note is that the static probe tool cannot collect information in wedge shaped mesh elements. The boundary layer mesh is by default wedge shaped, so typically they are tetrahedronized before beginning the simulation. This was not done for the one simulation (10 cm long pipe, M2 case), so no data from the boundary layer elements from this case are presented. Most of the important information regarding the flow regime transition occurs in the bulk of the flow, so this was not a major obstacle to overcome.

The time averaging tool was originally developed for channel flow, where wall perpendicular and parallel directions do not change relative to the Cartesian coordinate system. For a pipe, this does not hold true and averaging all the y and z velocities at each distance from the wall would not produce meaningful results. To account for this a new script was produced to translate the Cartesian coordinate velocities to cylindrical velocities. In this system the velocity vector is composed of streamwise, wall parallel (u_Θ), and wall perpendicular (u_r) velocities.

Another challenge with static probe tool unique to this two-phase flow regime transition study is the change of calculating mean flow rate over time. The tool calculates the local mean velocity

from all points and all time steps at that particular radial location. This mean velocity is then used to calculate the fluctuations at each time step. Due to the acceleration, the true mean velocity at the first time step in the window is smaller than the calculated mean. Incorrect mean velocity calculations contribute significant error to the velocity fluctuations, particularly for the streamwise direction. To compensate for this, the mean velocities for multiple sequential time windows are calculated and a linear interpolation line is calculated from the midpoint of each time window. To illustrate this process, *u* velocity (streamwise) data at a single point was extracted from the flow. The slug was broken into seven time windows and the interpolation process was applied. Figure 3.5 shows the results of this analysis.

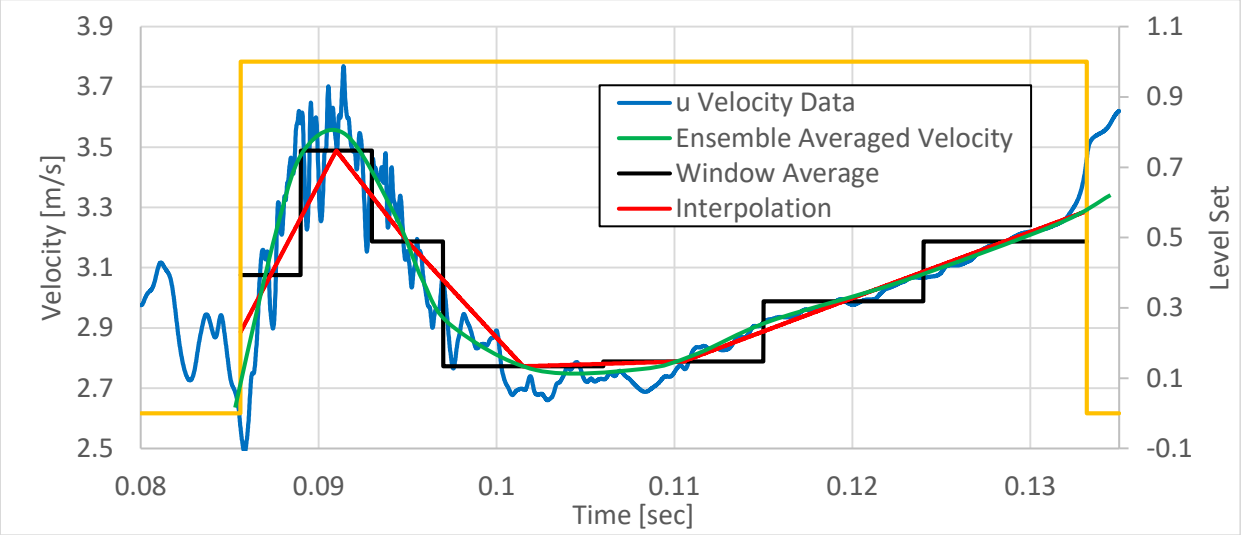

Figure 3.5: A hypothetical dataset showing how the mean velocity is interpolated to generate a more accurate dependent mean velocity.

The yellow line is the level set value where zero indicates gas and one indicates liquid. Only liquid data was processed for this demonstration. The varying mean velocity is clearly visible in both the wake region and the liquid slug. Ideally, the velocity fluctuation calculations would come from a mean velocity trace similar to the green line. Instead, this modification calculates the velocity fluctuations from the red line, which is a significant improvement to the constant mean velocity (black line). This improvement is especially clear in the region far from the wake. The acceleration

is nearly linear in this region and the interpolated mean velocity agrees well with the expected ensemble average. To validate the code, an accelerating single phase laminar flow case was created. Zero TKE is expected but the standard static probe tool would calculate a non-zero value. TKE measures the energy coming from the velocity fluctuations. In a cylindrical coordinate system, the TKE is defined by the following.

$$TKE = \frac{1}{2}(\overline{u'u'} + \overline{u_r'u_r'} + \overline{u_\theta'u_\theta'}) \quad (3.11)$$

The superscript indicates a velocity fluctuation measurement. As Figure 3.6 shows, the correction brings the mean TKE profile much closer to zero.

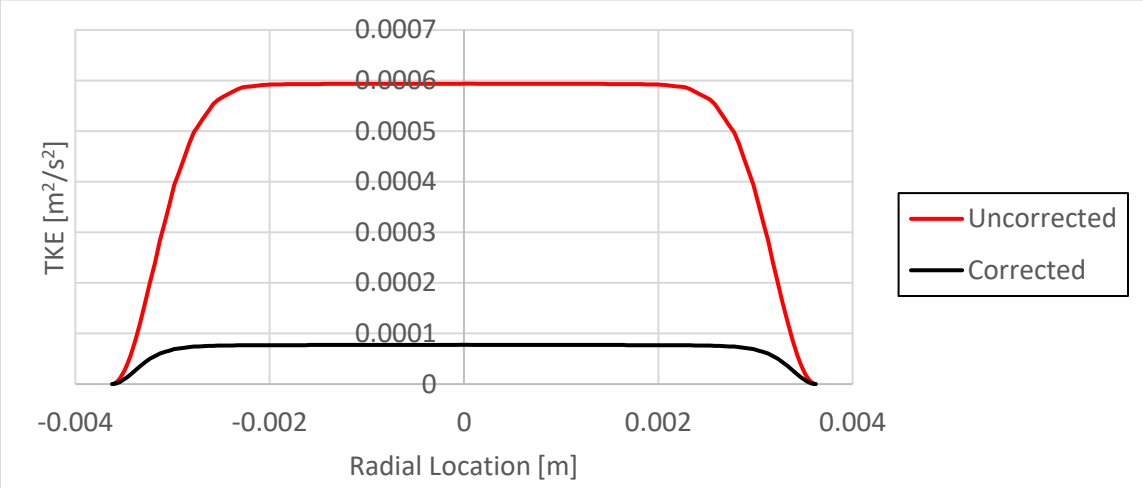

Figure 3.6: Results from an accelerating laminar flow case demonstrating the reduction in error the interpolation method provides.

The TKE calculation is still not zero, revealing that the flow does not accelerate perfectly linearly. Paraview has also proven to be a valuable data collection method. Multiple quantities of interest are difficult to obtain via the static probe tool due to its immobile probe locations and lack of information regarding the points where probes are not located. Paraview can analyze a single time step for any and all points in the domain. Turbulent structures, interfacial shape, and interfacial shear are examples of numerical data that static probe tool cannot calculate but Paraview can. The major disadvantage of Paraview is averaging in time is difficult because data at every time step is

not saved and loading the numerical data from each time step into Paraview is extremely time consuming.

3.4 Interfacial Shear Data Collection

The interfacial shear on the bubbles will be discussed extensively, and has already been analyzed in Section 3.2.1 Interfacial Shear. This section will quickly explain how the interfacial shear is calculated. The process is entirely performed in Paraview by first choosing a thin slice of the domain, perpendicular to the streamwise direction. In the pipe flow simulations this slice is typically 1 mm thick. This slice is then contoured twice at the one interface half thickness, 1.0ε, and 1-1/3 interface thickness, 1.33ε. An image of this contouring is provided in Figure 3.7.

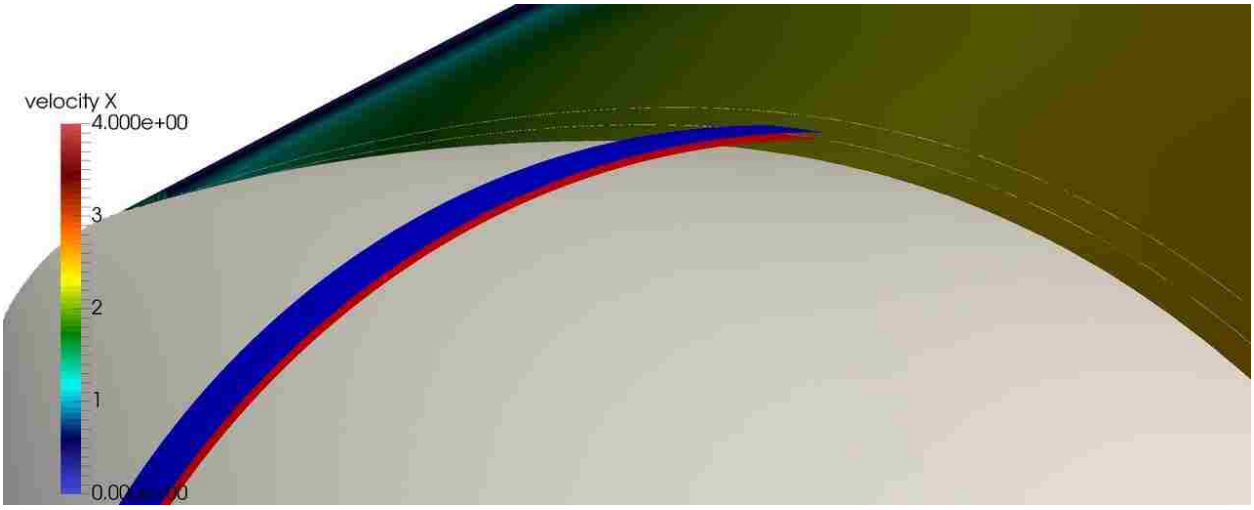

Figure 3.7: An image illustrating how the interfacial shear is calculated on a Taylor bubble. Red and blue surfaces show the level set contours velocity is averaged over.

The grey contour is the bubble interface and the red and blue planes shows the 1.0ε and 1.33ε contours that velocity is averaged over, respectively. The locations of the 1.0ε and 2.0ε level set contours are shown on the velocity plane by the white lines. The velocity parallel to the level set contour is then calculated from the contour normal:

$$u_{par} = \boldsymbol{u} - \boldsymbol{n} \cdot \boldsymbol{u} \tag{3.12}$$

where $\boldsymbol{u}$ is the velocity vector and $\boldsymbol{n}$ is the contour normal. u_{par} is averaged over the entire contour and the shear is calculated from the gradient between these averages

$$\tau_i = \mu \frac{u_{par,1.33\varepsilon} - u_{par,1\varepsilon}}{0.33\varepsilon} \quad (3.13)$$

where τ_i is the interfacial shear and μ is the viscosity. This operation can be performed for both the liquid side and gas side of the interface. The slice of the domain is then adjusted to a new location and a new interfacial shear is calculated.

3.5 Interfacial Area Concentration Data Collection

Interfacial area concentration is a quantity commonly measured and calculated in order to describe the state of the two-phase flow [82]. PHASTA did not have the capability to measure the interfacial area concentration during simulation, preventing quantitative analysis of the interfacial area information during the transitions. To analyze the interface structure as the flow develops during the transition, a tool was developed to collect the interfacial area information throughout the entire domain at every time step. This section discusses this tool and the analysis that it allows to be performed.

3.5.1 Tool Description

To collect the interfacial area concentration information, the user must first define a pseudo grid that is overlaid on the domain. This grid can have any dimensions but should be coarser than the computational mesh. As the simulation runs, the total interfacial volume is collected in each element of the pseudo grid. Since the level set method simulates the interface as a volume, with a thickness of 2ε, directly collecting interfacial area is not possible. Instead, the code calculates the interfacial volume, V, and divides by the interface thickness to find the interfacial area.

$$A_i = \frac{V}{2\varepsilon} \qquad (3.14)$$

As long as the grid is fine enough relative to the curvature of the interface, this interfacial area calculation will be accurate. The interfacial area information is collected locally on each processor and later compiled together to form a single matrix of interfacial area in each element of the pseudo grid. The user can then find the interfacial area information, for every time step, in a dedicated output file.

3.5.2 Method Verification

To verify that this tool correctly calculates the interfacial area, a simple case with just two 1.0 m diameter bubbles in 3.0 m cube was designed. The code should calculate 6.28 m^2. In actuality, the code calculated 5.44 m^2, a 13.4% error. This error is significant and likely comes from the method used to calculate the interfacial area, Eq. (3.14), rather than the collection method. Figure 3.8 shows an instant in time from a simulation and the associated interfacial area information shown on a semi-transparent 3D grid.

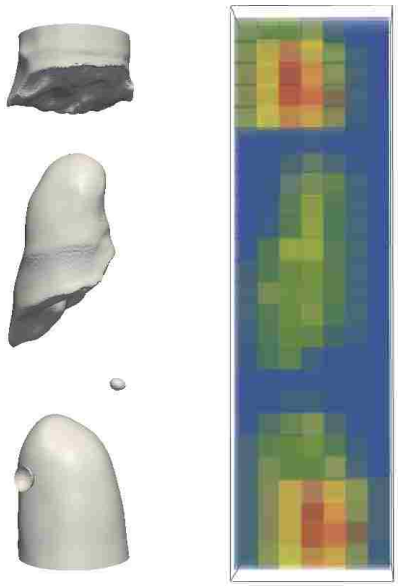

Figure 3.8: An image of the air-water interface (left) and the associated interfacial area concentration information (right). The interfacial area grid is 3D and semi-transparent.

Figure 3.8 shows that the interface shape measured from the interfacial area collection code matches the simulation.

Turning this capability on is inexpensive, increasing the run time by about 1.1% over 40 time steps on the Argonne BGQ machines. Therefore, users can either continuously collect data or run single select time steps to collect data at representative instances. However, for large pseudo grids, the interfacial area output file can become gigabytes in size if collecting at every time step. The Matlab script that analyzes this data becomes extremely slow when inputting files this large. It is recommended that single time steps are collected at a time. Appendix A.1 shows the Fortran routine that calculates the interfacial area. Other pieces of code, like MPI commands, that are scattered among other PHASTA subroutines are not included.

3.5.3 Data Analysis

To analyze the data collected by this newly developed tool, a Matlab script was generated. Since the code collects interfacial and gas volume information at every time step and at every point in the domain, a wide range of parameters can be calculated. The script is capable of identifying the major structures in the flow, namely the nose of the Taylor bubble, and calculating parameters like Sauter mean diameter, defined below, at different distances from the nose (see Figure 3.9).

$$D_s = \frac{6V}{A_i} \qquad (3.15)$$

Here V is the total volume of gas and A_i is the total interfacial area.

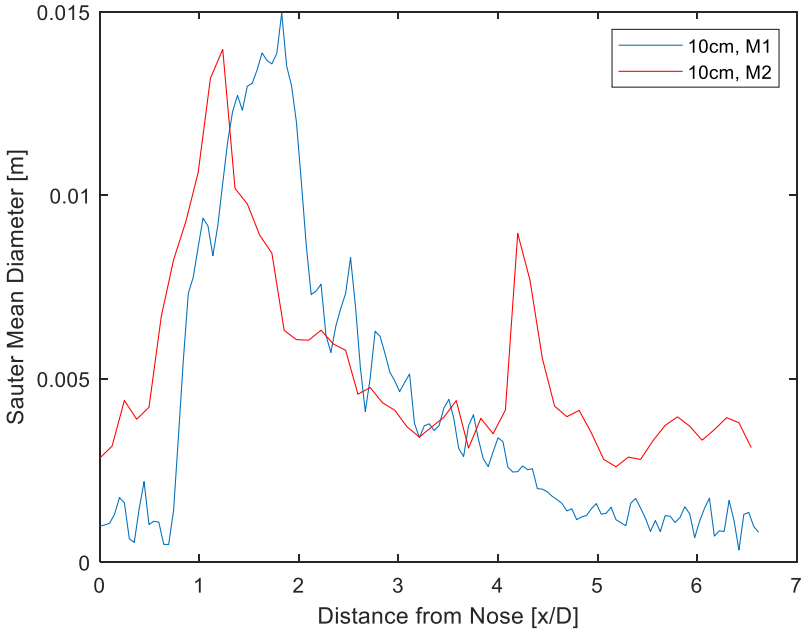

Figure 3.9: Sauter mean diameter information for two different meshes at the same time instance.

The script also can spatially average across the whole domain, or a specified region if desired. This allows for the temporal progression of interface void location to be understood, allowing for possible future model development and comparison. Figure 3.10 gives a short example of this temporal progression and shows radial profiles for the mean interfacial area in the domain at two different time steps in the 20 cm long pipe.

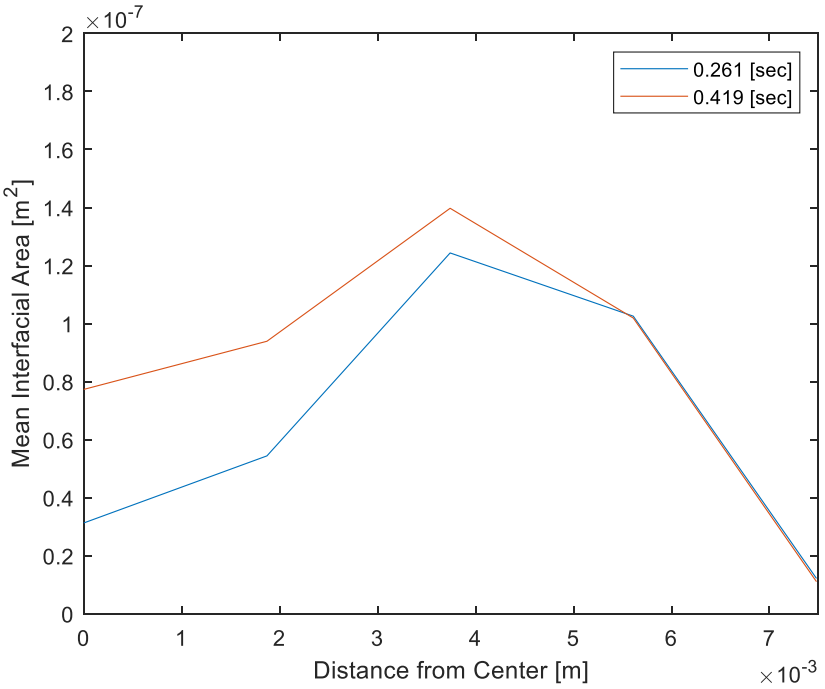

Figure 3.10: Spatially averaged interfacial area information for two different points in time of the 20 cm long pipe simulation.

The script would also allow similar plots for void fraction and Sauter mean diameter. This capability is similar to the wire mesh sensor used in experiments. The difference is that this method is unobtrusive and allows for data collection over a volume rather than just a plane. Appendix A.2 contains the Matlab code for this tool.

CHAPTER 4. PROBLEM SETUP

Simulating flow regime transitions using interface resolved methods has never been the primary research project focus of other computational studies using similar interface resolved methods. This Chapter details the considerations that were necessary for creating these first of their kind simulations that can accurately predict flow regime transitions while remaining computationally affordable and relevant to the available literature. An explanation of all the information needed to recreate these flow regime transition simulations will be included.

4.1 Boundary Conditions

All presented flow regime transition simulations use no-slip conditions on the walls and periodic boundaries on the ends of the pipes. The long development length required by flow regime transitions required the periodic boundary conditions. Otherwise, a domain multiple meters long would be necessary. This simulation would be prohibitively expensive at the necessary mesh resolution. The consequence of applying periodic boundaries will be discussed in Section 4.2.2 Domain Length Study.

4.2 Domain Design

All the domains are oriented vertically and x is the streamwise direction. A pipe was chosen as the primary geometry because of the large body of research already committed to studying both single and two-phase flow in pipes. Before analyzing complex geometries, such as the BWR subchannel, simpler geometries should be studied in order to provide confidence in the code's ability and understand the physics of the simpler flows.

4.2.1 Dimensions

The three different pipe geometries are summarized in Table 4.1.

Table 4.1: Summary of the three primary domains used in this work.

	Length [cm]	Diameter [mm]
Pipe 1	10.0	15.0
Pipe 2	20.0	15.0
Pipe 3	4.0	2.4

The two diameters were both chosen due to their similarity to relevant experimental research [24, 83, 84]. Additionally, these sizes are expected to highlight specific physics of interest. The 15.0 mm pipe is close to the size of a BWR subchannel, implying similar phenomenon and dominant forces will be observed. The 2.4 mm pipe, or minichannel, offers the opportunity to perform validation studies due to the dominant surface tension and viscous forces that make the flows easier to characterize. Minichannel/microchannels have been the studied extensively and their behavior is well documented [84, 85, 86].

4.2.2 Domain Length Study

A major consideration for each periodic domain is its length. Unlike other two-phase flow regimes, slug flow is intermittent. Bubbly and churn-turbulent flow regimes look approximately similar spatially, and especially in the axial direction two arbitrary segments are nearly indistinct. In contrast, slug flow is composed of two distinct segments, the liquid slug and the Taylor bubble. The length scale of slug flow is therefore the length of the slug and bubble together. Choosing a computational domain whose length is not an integral length of the slug flow length scale would be unphysical. A simple example would be a periodic pipe so short it forces annular flow. Fortunately, several studies have focused on measuring liquid slug lengths behind a Taylor bubble [87, 88, 89, 90]. These experiments find that the slug length is highly variable and can be as little as 3 pipe diameters to greater than 40 pipe diameters. Higher flow rates and smaller diameter pipes tend to decrease the expected slug length as well.

A study was performed to examine if pipes 1 and 2 produced realistic flows. A 6.0 cm and 24.0 cm domain, 15.0 mm in diameter were created. For both cases the mean liquid flow rate was 0.2 m/s and the void fraction was 40%. At this condition slug flow is expected. The simulations were allowed to reach steady state and the resulting flows were observed (see Figure 4.1).

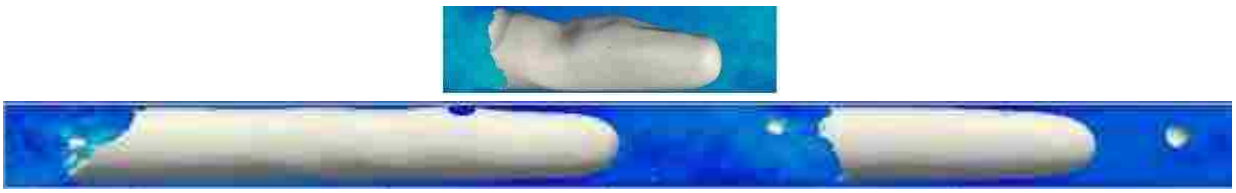

Figure 4.1: Stables conditions for the 60 mm (top) and 240 mm (bottom) domains used in the domain length study.

As Figure 4.1 shows, the interface in the 6.0 cm domain is perturbed, causing large fluctuations in the local liquid film thickness, and the interfaces in the 24.0 cm domain are smooth. The perturbations are caused by the wake of the bubble self-interfering through the periodic stream-wise boundary. A Taylor bubble experiencing this phenomenon would not be a stable condition and the trailing Taylor bubble would accelerate and merge with the leading bubble. The liquid slug in this flow is less than two diameters long, an unlikely condition according to relevant experiments [87, 90]. The Taylor bubbles in Figure 4.1 (bottom) are smooth and they survive without merger. To achieve this flow the computational expense would become too large at the finer mesh resolutions due to how long the pipe is. Therefore, the 10.0 cm long pipe domain (that is used in future simulations) was modeled after the shorter liquid slug/Taylor bubble pair in Figure 4.1 (bottom), where the liquid slug is about three diameters long. The 20.0 cm long domain was chosen to extend the slug length, to about 10 diameters, and characterize how the slug length affects the transition.

4.3 Mesh Design

Three different meshes, M0, M1, and M2, were designed (see Table 4.2, Table 4.3, and Table 4.4). Starting at M0, the coarsest mesh, the mesh size is halved in each direction. This uniform refinement increases the number of computational elements by about a factor of $\mathbf{2^3}$. Using a drift-flux model [29], the Δy^+ values were estimated for the high flow rates at which slug flow has been predicted to undergo a transition [24]. At these conditions the Reynolds number is expected to be about 60,000 in the 15.0 mm diameter pipes.

Table 4.2: Description of the computational meshes for the 10.0 cm long, 15.0 mm diameter pipe.

	Base/M0	1st Refinement/M1	2nd Refinement/M2
Wall Mesh [mm]	0.0700	0.0385	0.0154
Bulk Mesh [mm]	0.2360	0.1230	0.0615
Wall Δy^+	14	7	3
Bulk Δy^+	46	24	12
Smallest Resolvable Bubble Diameter [8] [mm]	4.72	2.46	1.23
Smallest Bubble Diameter for Resolving Interfacial Shear [mm]	4.25	2.21	1.11
Number of Elements [millions]	8	57	430

Table 4.3: Description of the computational meshes for the 20.0 cm long, 15.0 mm diameter pipe.

	1st Refinement/M1	2nd Refinement/M2
Wall Mesh [mm]	0.0154	0.0075
Bulk Mesh [mm]	0.123	0.0615
Wall Δy^+	3	1.5
Bulk Δy^+	24	12
Smallest Resolvable Bubble Diameter [8] [mm]	2.46	1.23
Smallest Bubble Diameter for Resolving Interfacial Shear [mm]	2.21	1.11
Number of Elements [millions]	140	1117

Table 4.4: Description of the computational meshes for the 40 mm long, 2.4 mm diameter minichannel.

	Base Mesh/M0	1st Refinement/M1
Wall Mesh [mm]	0.010	0.005
Bulk Mesh [mm]	0.04	0.02
Wall Δy^+	0.027	0.014
Bulk Δy^+	0.110	0.055
Smallest Resolvable Bubble Diameter [8][mm]	0.80	0.40
Smallest Bubble Diameter for Resolving Interfacial Shear [mm]	0.72	0.36
Number of Elements [millions]	36	291

M0 was not applied to the 20 cm long pipe because, as will be discussed, the M0 mesh could not fully resolve the flow. The 10 cm long simulations also indicated that the boundary layer mesh should be finer. Knowing this, the 20 cm long domain boundary layers were adjusted to be finer. The smallest resolved bubble diameter is calculated from the criteria developed by Fang & Bolotnov [8] stating the level set method requires 20 points across the diameter of a bubble. The smallest resolvable bubbles according to the criterion developed in Section 3.2.1 Interfacial Shear is also shown. The Δy_w^+ shown in Table 4.2, Table 4.3, and Table 4.4 refer to a single instance, the highest velocity condition, when the flow is at steady state. However, because the flow regime transition is a transient phenomenon, the necessary mesh resolution is also changing with time. Therefore, each mesh may be appropriate at different times in the simulation. Using Eqs. (3.1) and (3.2) and wall shear information from the 20 cm long pipe flow, the necessary wall resolution at different time steps was calculated and compared to the wall mesh size of the different meshes (Figure 4.2).

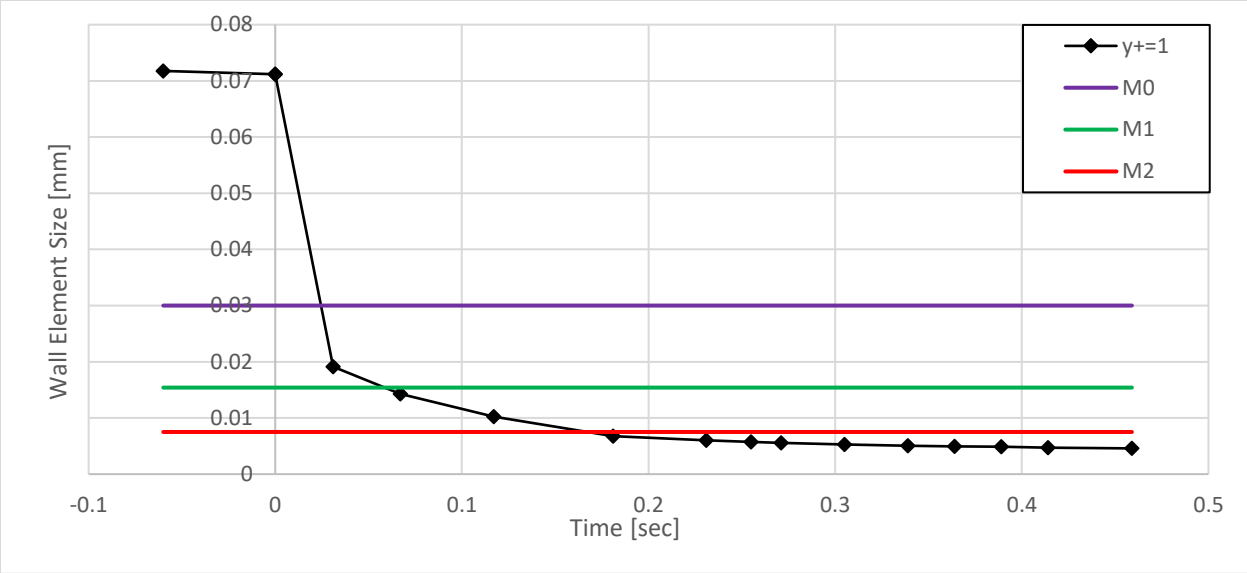

Figure 4.2: The wall mesh size necessary to fully resolve the flow. The three horizontal lines refer to the actual wall mesh size used in the 20 cm long pipe simulations. The data for wall shear comes from flow in the 20 cm long pipe.

As Figure 4.2 shows M0 quickly loses $\Delta y_w^+ < 1$ qualification. Even the M2 mesh becomes under resolved according to this criterion. An M3 mesh would be necessary to meet this criterion at all time steps. This mesh would be about 8 billion elements in size and a single flow through in the 10cm pipe would require about 50 million CPU-hours. Fortunately, it has been observed that the flow regime transition begins while M2 still fully resolves the flow. Additionally, the Δy_w^+ of M2 never becomes larger than 2 and remains close to 1.5 (which has been shown to be satisfactory resolution in bubbly turbulent channel flow simulations). To observe the effect the mesh has on the TKE, Figure 4.3 compares the TKE in the liquid slug from the M1 and M2 simulations at five different time windows in the 20 cm long pipe.

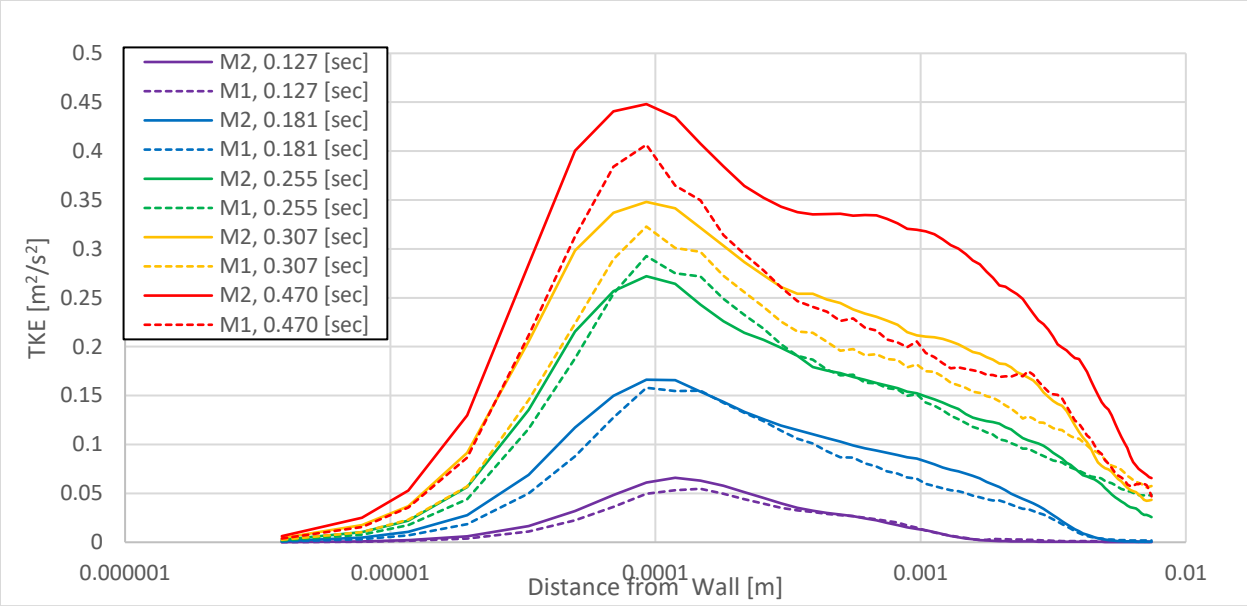

Figure 4.3: Comparing M1 and M2 liquid slug TKE profiles at different instances in time. Time refers to time since the pressure gradient was increased.

As Figure 4.3 shows, the TKE is only slightly different between each mesh for earlier time instances. Some difference is acceptable because there is uncertainty from sampling and in the TKE calculation (see Section 3.3 Virtual Probe Data Collection). For the times when the meshes agree on TKE, the peaks, although slightly different in magnitude, are consistently located at the same location as well. The TKE calculations only begin to differ after 0.3 seconds, which corresponds to six flow throughs of the Taylor bubble. As seen in Figure 4.2 M1 and M2 would be expected to become inaccurate after about 0.05 and 0.15 seconds, respectively. These results suggest that even when the classic $\Delta y_w^+ < 1$ criterion is not met, the results from an "under resolved" mesh can still match a fully resolved mesh. Altogether, initially in the transient, it seems the discretization uncertainty is relatively insensitive to the Reynolds number. The M1 mesh can still be used to approximate the TKE even when it no longer meets the $\Delta y_w^+ < 1$ condition. This will be important for when M2 is too computationally expensive but other tests are still desired using M1. Additionally, this suggests M2 is accurate past the time it no longer satisfies the $\Delta y_w^+ < 1$ condition.

While Δy^+ is an appropriate measurement for single-phase DNS resolution, two-phase DNS meshing requirements may be just as, or more, limiting. Using the criterion developed in Section 3.2.1 Interfacial Shear, the interfacial shear data at two different time instances were chosen to determine the interface Δy^+ dimensions. Time steps early and late in the transient were chosen in order to observe the shear for a laminar and turbulent liquid film. Profiles of the interfacial shear on the gas and liquid side are shown in Figure 4.4.

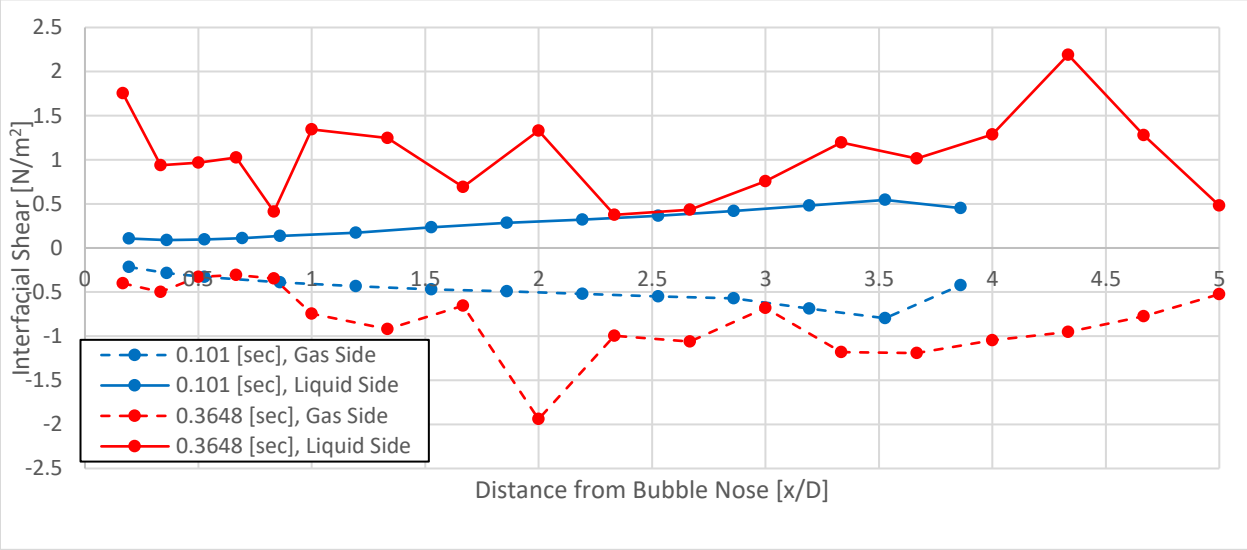

Figure 4.4: Interfacial shear profiles on the liquid side (solid line) and gas side (dotted line) of the interface of the Taylor bubble at two different time steps.

At the earlier time step, the Taylor bubble's interface is still smooth and the nose does not encounter a significant amount of turbulence. The flow in the later time step is fully turbulent and the interface is very perturbed. Taking the maximum interfacial shear value from both sides of the interface, the Δy^+ units of each bulk mesh, for liquid and gas were calculated. The elements in M1 were 5.87 Δy^+ units in the liquid and 3.32 Δy^+ units in the gas. The elements in M2 were 2.93 Δy^+ units in the liquid and 1.66 Δy^+ units in the gas. Therefore, the meshes are both still resolving the interfacial shear of the Taylor bubbles. However, the bubbles in the wake of the Taylor bubble can be very small, just a couple elements across the diameter. These are not well resolved but since

they are so small do not have a significant effect on the flow. The majority of the bubbles in the wake were millimeters in diameter. The M2 mesh meets the interfacial shear criterion for these bubbles.

As was discussed in Section 3.2.2 Liquid Film Resolution, for slug flow, the liquid film around the Taylor bubble was considered to be one of the smallest scale two-phase phenomenon that would be important to the flow regime transitions. In Figure 4.5, images from the M0, M1, and M2 simulations show a zoomed in view of the liquid film (the region above the thick white line) with an overlay of the computational mesh. In these images the thick white line is the bubble interface (the zero level set contour), the blue lines outline the mesh, and the thin white lines are the integral values of half interface thickness (ε) level set contours (see Figure 2.1 for reference).

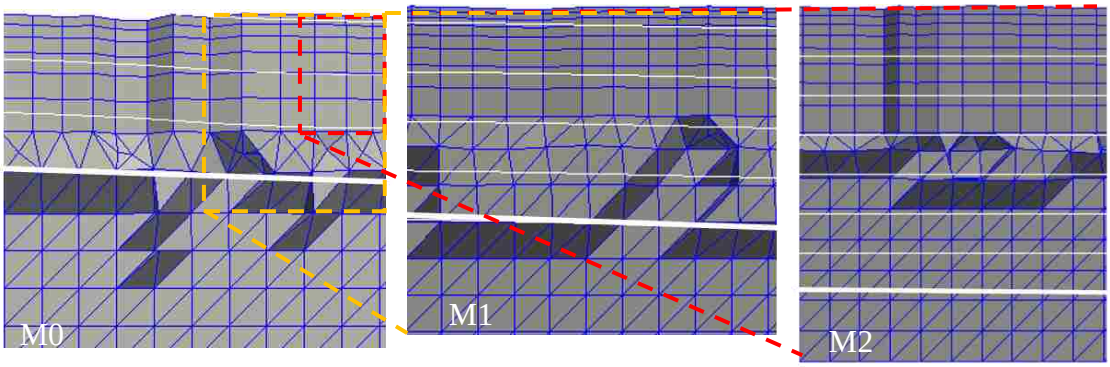

Figure 4.5: Images showing how well each mesh resolved the liquid film. The top of each image is the pipe wall. The blue lines show the computational mesh. The thick white line is the interface and the thin white lines are half interface level set contours.

Figure 4.5 (left) clearly shows that the fully liquid properties region of the liquid film (above the first thin white line) is only resolved by five or six points in M0. Considering one of these points is the boundary, this is not a well resolved flow. As discussed, at least six points are required to form the parabolic velocity profile expected in the liquid film region. In fact, the simulations show that hardly any down coming liquid is being ejected from the film into the wake of the bubble. As the mesh is refined the liquid film becomes thinner, from about 1.0 mm to 0.7 mm, further suggesting M0 is too coarse. At M1 and M2 the film thickness is approximately the same and it is

resolved by, at a minimum, 10 and 13 points, respectively. Since M0 has been shown to not resolve the flow in the 15.0 mm diameter pipe it will not be further considered in other simulation.

The importance of testing the two-phase resolution of the mesh is highlighted in the minichannel flow when considering the liquid film. Even though the Δy^+ values indicate the mesh is very well resolved, $\Delta y_w^+ = 0.027$, for M0, the liquid film is only resolved by four points. A researcher only considering single phase factors would assume this was fully resolved, when in fact important liquid film phenomena are lost.

Unfortunately, determining how well PHASTA predicts the size of bubbles being torn off the Taylor bubble, referring to the discussion in Section 3.2.3 Taylor Bubble Breakup Events, is difficult. PHASTA's bubble tracking capability [91] cannot yet accurately track new bubbles being produced so rapidly. Therefore, the only alternative to determine the size of these bubbles is to measure individual bubble volumes in Paraview and calculate Sauter mean diameters using either Paraview or the interfacial area tracking code developed for this work. As Figure 4.6 shows, the interfacial structure behind the Taylor bubble can be very complex.

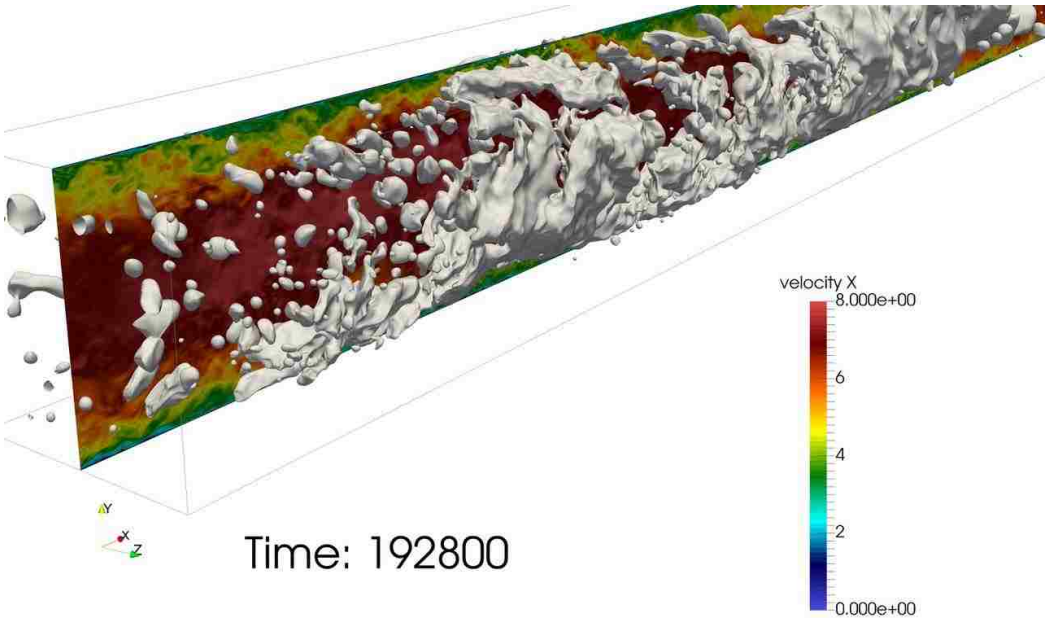

Figure 4.6: A snapshot showing the complex interface topology in the wake of the Taylor bubble.

The size of the smallest visible bubbles was measured and the Sauter mean diameter in the wake was measured. Two different time instances were chosen and both M1 and M2 were investigated. One time is right after bubbles began to shear off the Taylor bubble and the second is late in the transient when the wake has many bubbles in it. Results from this study are reported in Table 4.5.

Table 4.5: Data from measuring the bubble sizes in the wake of the Taylor bubble at two different time instances for both M1 and M2.

	Mesh Size [mm]	Early Time		Late Time	
		Sauter Mean Diameter [mm]	Equivalent Diameter of Smallest Observed Bubbles [mm]	Sauter Mean Diameter [mm]	Equivalent Diameter of Smallest Observed Bubbles [mm]
M1	0.123	2.94	0.248	3.86	0.494
M2	0.065	2.66	0.252	2.52	0.456

The equivalent diameter is calculated from the volume of the bubble.

$$D_{eq} = 2\left(\frac{V3}{4\pi}\right)^{\frac{1}{3}} \quad (4.1)$$

This result compares well to the experimental results measuring similar quantities [79, 80]. For both meshes, at both time instances, the mean diameters fell within the range of what was expected, about 2-4 mm. Additionally, at the early time step, M1 and M2 have a very similar Sauter mean diameter. M1 is only 10.5% different from M2. Later in the simulation, the two meshes differ considerably, but this is expected since M1 is not fully resolving the turbulence. In both meshes the smallest observed bubbles are only a few grid points across. It is unclear if these bubbles are remnants of bubbles suffering from the level set method's mass conservation issues or if this is the size they broke into. Interestingly, the size of these small bubbles does not change appreciably between M1 and M2. This suggests they are physical because M2 would have bubbles half as small if their size was primarily dependent on the mesh size. If this is true, then they are in approximate agreement with the scale of the smallest bubbles observed in experiment. The

maximum size is not comparable in these cases because the experimental geometry in both papers was considerably bigger than the pipes in this work.

4.4 Inducing a Flow Regime Transition

Having the capability to induce a flow regime transition without misrepresenting the physics is an important consideration for this study. Experiments are fortunate to have valves that individually control the flow rates of each phase (effectively setting the superficial velocities for each phase). The researchers can hold the liquid flow rate constant while independently changing the gas flow rate, and vice versa. Some experiments can even add void via boiling. The periodic boundary conditions prevent the use of techniques involving valves and the boiling capability is still being developed [92]. Therefore, a new method for inducing a flow regime transition must be created.

One possible method that was initially considered focused on changing the void fraction. As the flow went past a certain region of the domain the code would change the level set field just within this region to increase the void fraction. This interface moving method is not physical however, so it was not chosen. Instead, the transitions were induced by increasing the driving pressure gradient, one of the input parameters. Using this method, both the liquid and gas flow rates will increase, moving diagonally across a superficial velocity based flow regime map. Since the pressure gradient is included in the INS, this method does not alter the physics and every single computational node will observe the change in pressure gradient simultaneously. When the pressure gradient is suddenly increased, the flow begins to accelerate because there exists an imbalance in the wall shear force and driving pressure gradient force. Consequentially, the flow accelerates until these two are balanced. Figure 4.7 shows this temporal progression.

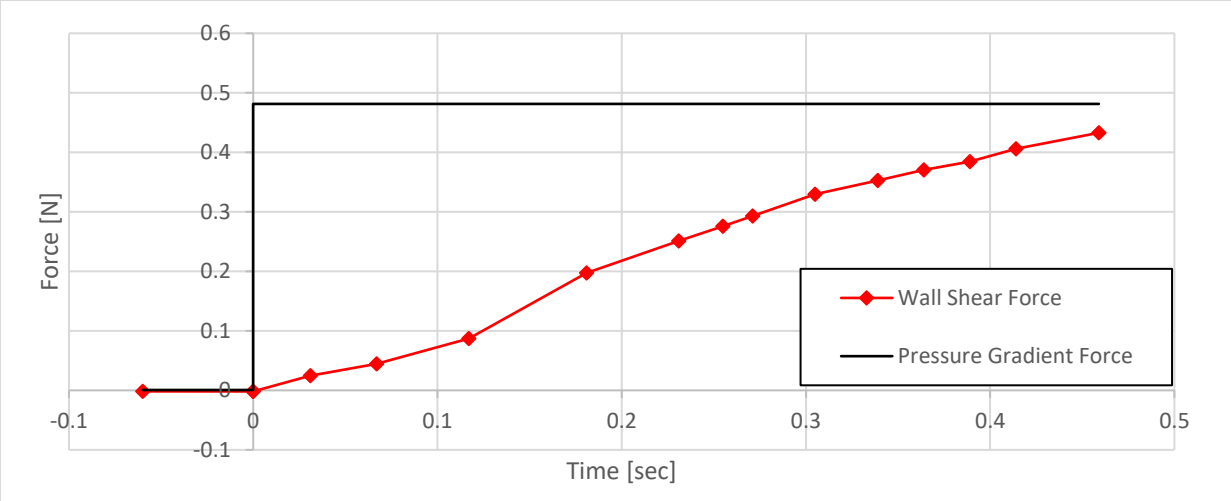

Figure 4.7: An example of how the wall shear responds when the pressure gradient is step increased. The wall shear data comes from the 20 cm long pipe, at the M1 resolution.

The time period that this transient occurs over allows for detailed data analysis as the flow develops and a two-phase flow regime transition occurs.

4.5 Fluid Properties and Flow Conditions

Depending on the purpose of the simulation, different fluid properties and flow conditions were chosen. For the 15.0 mm diameter pipe, the same density and viscosity properties were used for most of the simulations. The surface tension was typically the STP value but it was varied for some cases and will be specified when necessary. These properties are given in Table 4.6 and the pressure gradient values are given in Table 4.7.

Table 4.6: Fluid properties used in the simulations. Properties at BWR and atmospheric conditions are given for reference.

	Density [kg/m^3]			**Viscosity [kg/m-s]**			**Surface Tension [N/m]**	
	Simulation	**BWR**	**STP**	**Simulation**	**BWR**	**STP**	**BWR**	**STP**
Liquid	758.15	758.15	997.00	8.54E-4	8.54E-5	8.72E-4	0.014	0.0714
Vapor	30.83	30.83	1.17	2.86E-4	1.86E-5	1.20E-5		

Table 4.7: The pressure gradient values, and their names, used in the simulations.

Pressure Gradient [Pa/m]
P0: 17.5
P1: 1017.5
P2: 15047.5

The densities chosen correspond to what would be found in a BWR. The viscosities were inflated in order to allow for high flow rates while maintaining reasonable time step sizes and meshing requirements. The pressure gradients were calculated from a drift-flux model [29], where smooth slug flow is expected at P0 and P1, and a transition out of slug flow is expected for P2. The minichannel fluid properties correspond to atmospheric conditions because experiments use primarily atmospheric conditions. The void fractions of the 10 cm long, 20 cm long, and minichannel domains are 40%, 20%, and 50%, respectively. The 10 and 20 cm long domains have the same volume of gas. This volume was chosen to allow for a single Taylor bubble to form in the 10 cm long domain. The minichannel's void fraction was chosen by estimating the void in the experiments that the simulation will be designed from [84].

Using the properties from Table 4.6, bubble size information from Table 4.5 and flow rate information, the range of Reynolds number (Re),

$$Re = \frac{\rho U D}{\mu} \tag{4.2}$$

Weber number (We),

$$We = \frac{\rho u_r^2 l}{\sigma} \tag{4.3}$$

and Eötvös number (Eo),

$$Eo = \frac{\Delta \rho g l^2}{\sigma} \tag{4.4}$$

are provided in Table *4.8*. In these equations l refers to the bubble diameter.

Table 4.8: Non-dimensional number information for the transition simulations

Number	10 cm Long Pipe	20 cm Long Pipe
Reynolds	2700-54,000	3,200 - 74,200
Weber	0.11 - 5.85	
Eötvös	0.006 - 16.88	

Ranges are provided for the transient because the two-phase flow regime transitions are changing in flow rate and produce bubbles of different sizes, especially in the churn-turbulent regime. The largest Weber and Eötvös numbers refer to the Taylor bubble. As the new regimes develop it is expected that the Taylor bubbles breakup and the Weber and Eötvös numbers both decrease. The Reynolds number range, initially beginning in the transition region, ends at the value corresponding to the liquid flow rate from the 20 cm long pipe at the end of the transition. This high Reynolds number arises after the transition has already begun. For comparison, in the 10 cm long pipe the two-phase flow regime transition began when the Reynolds number was about 40,000. Additionally, the Reynolds number range in Table *4.8* uses the mean liquid velocity. Using the mean velocity in the film, the film Reynolds number before the acceleration is found to be 674. Since the velocity in the film is negative prior to acceleration, this Reynolds number would initially decrease as the film velocity approaches zero. The Reynolds number would then increase as the film velocity becomes positive. To calculate the Weber number, the relative velocity of the Taylor bubble at the low pressure gradient condition was calculated exactly. However, the relative velocity of the bubbles in the wake was not directly measured, so an assumption of 0.2 m/s was used. Note that the largest Weber and Eötvös correspond to the observed Taylor bubbles. The range of Weber and Eötvös shows that both spherical bubbles, where surface tension is dominant, and deformable bubbles, where liquid inertial effects are more prominent, exist in these flows. In

particular, the large values indicate that the Taylor bubble is prone to instabilities and deformation due to the interface's interaction with the liquid.

4.6 Initialization

At time zero all locations in the domain have the same velocity, 0.1 m/s. To initialize the gas in the domain small bubbles are randomly placed within the domain until the desired void fraction is reached (see Figure 4.8).

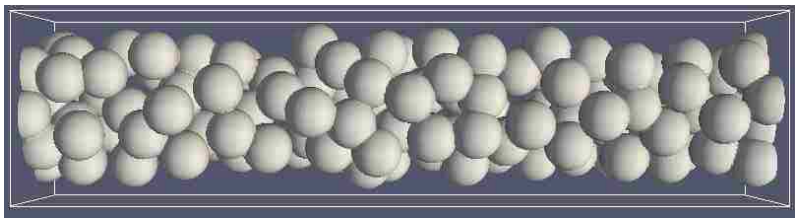

Figure 4.8: An example of the void initialization.

In the first time steps the bubbles will rapidly coalesce into one large Taylor bubble, forming slug flow. The rapid coalescence is chaotic, and generates some turbulence. This is not a concern however because once the Taylor bubble is formed, it is allowed to complete at least two flow-throughs of the domain. During these flow-throughs the liquid is entering the thin film and then being ejected into the wake. This process of reaching a laminar flow in the film, where the Reynolds number is about 400, and then becoming turbulent in the wake is considered to erase information regarding the initial condition. Following these flow-throughs the transitions will initiate, meaning all forward transitions in this work begin with slug flow.

CHAPTER 5. VALIDATION EFFORTS

Validation is important to all CFD codes. William L. Oberkampf is the premier expert on CFD validation and has committed significant time to laying out a framework for scientific verification and validation. In his writings Oberkampf has detailed his frustration with the CFD community's general lack of proper validation: "Common practice has been that if the computational results generally agree with the experimental data over the range of measurements, the model is commonly declared 'validated.' Comparing computational results and experimental data on a graph, however, is only incrementally better than making a subjective comparison." [57]. This point is especially important when considering the subjective nature of flow regime transition classification. Additionally, the nuclear engineering community commonly uses a single piece of data to validate a multiphysics problem. For example, due to the limited amount of data available, researchers using nuclear reactor system codes will validate their code using the reactor pressure vessel pressure and core water level data from the Fukushima accident. Upon claiming the code is validated, the same code will be used to predict parameters such as pressure vessel failure time, isotope release, core relocation, and hydrogen generation [93, 94, 95]. The intention of pointing out this practice of low data validation is not to highlight weaknesses, but rather draw parallels between reactor system code validation and DNS validation (in particular two-phase DNS). In both cases, directly applicable data that is on the scale necessary for validation is limited. So far an extensive method to validate codes that experience this problem has not been developed. Instead, this Chapter will attempt to follow Oberkampf's methods, specifically the validation hierarchy, to prove PHASTA is capable of simulating two-phase flow regime transitions using the pressure gradient jump method discussed in Section 4.4 Inducing a Flow Regime Transition. This Chapter

should also provide confidence in the accuracy of the numerical data created from the developed simulations.

5.1 The Validation Hierarchy

The validation hierarchy proposed by Oberkampf and Trucano [59] provides a path for validating a code designed for simulating extremely complex processes, such as an airplane, race car, or two-phase flow system. In the paper [58], Oberkampf and Trucano use the example of a cruise missile. The hierarchy shows how the problem is decomposed to different levels of complexity and how each level relates to each other. The hierarchy breaks down the main physics into different levels of complexity: system, subsystem, benchmark, and unit problem. Identifying the correct components to each level is not always obvious but is extremely important for a complete validation process. In general, the system level breaks the entire problem up into the major components that make it up (physical structure, fluids, electrical components, etc.). While all the systems are related and interact with one another, they operate on different principles and physics from each other. The subsystem level is composed of the classes of physics that each system encounters (electrodynamics, thermal hydraulics, structural mechanics, etc.). The benchmark level puts forth individual problems that no longer are directly derivative of the initial problem, but are test pieces for the physics mentioned in the subsystem level. An example would be convective boiling in a pipe being a benchmark problem of a nuclear reactor. The unit problem level is the simplest in terms of physics, but still very important because all of the components of this level must capture the physics of the entire problem on the simplest level. For example, simple geometry single phase laminar and turbulent flow problems and individual bubble flows would be included here.

This hierarchy provides an order of operations when performing a code validation. Simulations described in the unit problem level must be performed first. These unit problems are designed to test a single piece of physics, such as single phase turbulence in a parallel plate channel, or drag on a single bubble. Unit problems generally have experimental data to directly compare to as well. Once the code is shown to be accurate for each unit problem then the code is said to be validated for these phenomena. If all the problems at the unit level are validated then the code can be used to predict phenomena at the benchmark level, such as bubbly flow in a parallel plate. In turn, if the code can be validated for all the benchmark problems, then it can be confidently used to perform simulations at the subsystem level, such as convective boiling flow in a complex geometry (like a BWR channel). If all the pieces at the subsystem level are then validated, then the code can be extended to the system level. Finally, if the code is validated at the system level then it can be extended to predict behavior of the total problem. Therefore, even though the code has not been validated against experiments at the total problem level, since the problem is a combination of simpler problems that the code has been validated for, researchers can conclude the code can make accurate predictions of the total problem behavior.

Fully validating a code by this method is quite a demanding task, especially for the example given of a cruise missile, and would take considerable time. Fortunately, the problem of two-phase flow regime transitions is not as interdisciplinary as a cruise missile and the entire problem likely already falls under the subsystem level. Figure 5.1 shows the novel validation hierarchy that was created for two-phase flow regime transitions.

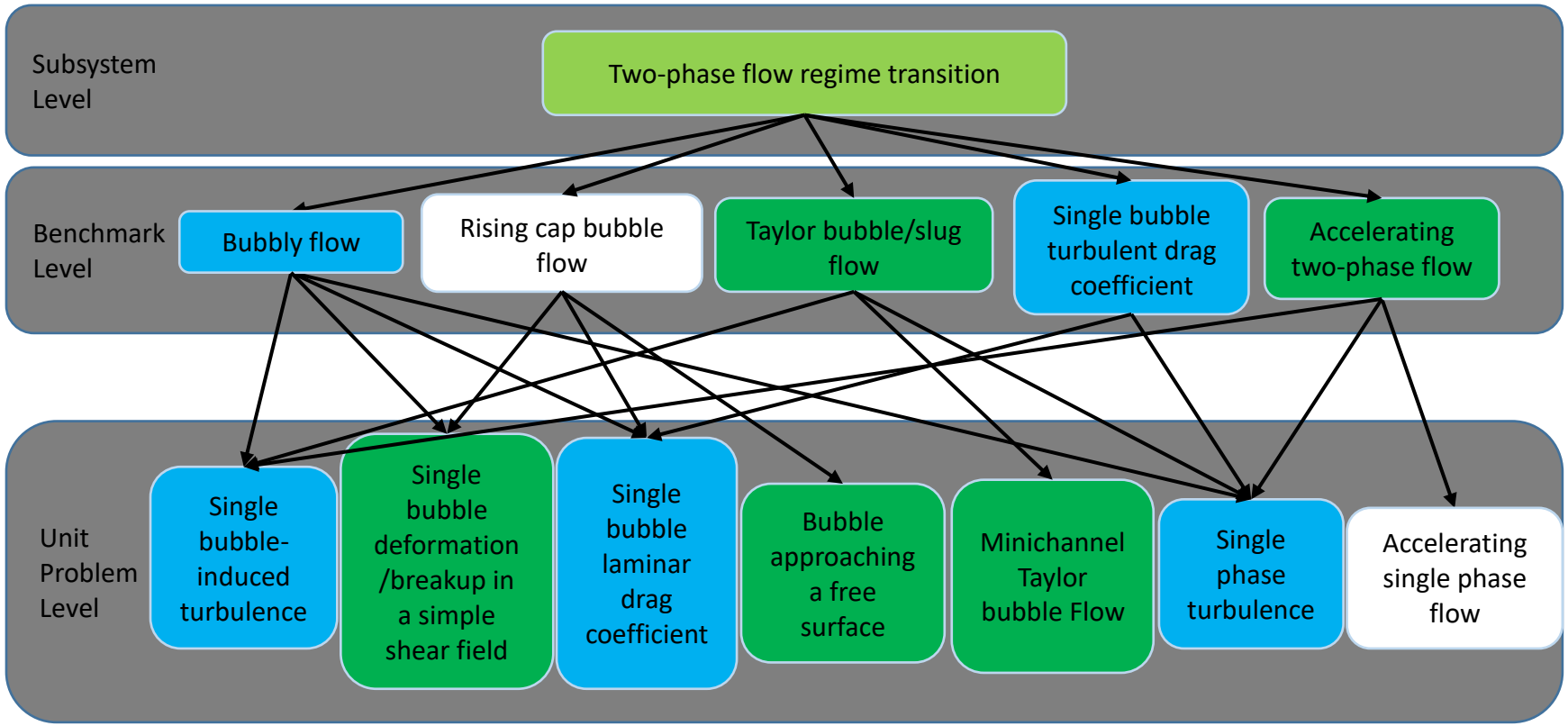

Figure 5.1: Two-phase flow regime transition validation hierarchy. Blue boxes are simulations previously run by other colleagues. Green box simulations were performed in this work. White boxes have not been simulated with PHASTA.

In Figure 5.1 green represents validation cases performed in this work. Blue are simulations that PHASTA has performed, but by colleagues. White means these simulations have not been run in PHASTA but will still be discussed due to their relevance. The following sections will discuss the unit problem and benchmark level simulations that were performed in this work to validate PHASTA for two-phase flow regime transitions. To learn about the simulations in blue, the reader is referred to [11, 63, 3, 38].

5.2 Unit Problem Level

5.2.1 Bubble Approaching a Free Surface

As a bubble approaches a free surface or another bubble, a thin liquid film forms that must drain before coalescence can occur. Due to the dominant viscous forces in the film, the drainage can take a considerable amount of time, and the bubbles sometimes recoil away from each other instead of coalescing. The liquid film is not uniform in thickness and typically takes the shape of a reverse donut, where it is thinnest in a ring surrounding a region of thicker film. The film first forms with a thickness of about 0.1 mm [96] and it will snap in the thin region at only a few micrometers in thickness [96, 52]. However, as two bubbles in a simulation employing the level set method approach one another, their Heaviside function determined property transitions will begin to overlap. As they continue to overlap, the properties between the bubbles become more and more gaseous, making it easier for the bubbles to approach each other. Therefore, the level set method permits coalescence for nearly all situations when one bubble approaches another. To properly simulate two bubbles bouncing off each other, as would be expected in bubbly flows, using the level set method would require a computational mesh fine enough to capture the liquid film between the bubbles. To determine how fine this mesh needs to be, a grid study was designed. This study will analyze increasingly fine meshes for a buoyancy driven bubble rising towards a

free surface. The domain is large enough to allow the bubble to reach its terminal velocity by the time it begins to interact with the surface. In reality, as the bubble reaches the surface, the bubble will bounce off the surface before coalescing. The path and velocity of the bubble will be measured and compared to experiments [97]. Using this data an appropriate mesh size for resolving the liquid film between bubbles will be determined. Table 5.1 shows the total number of elements and the size of the elements that were resolving the liquid film.

Table 5.1: Mesh parameters for the liquid film grid study.

	M0	**M1**	**M2**	**M3**	**M4**
Liquid Film Resolution [μm]	60	30	15	7.50	3.75
Number of Elements [millions]	1.34	1.08	2.76	9.99	34.0

To remain computationally affordable, 30, 15, 7.5, and 3.75 μm sized elements only exist in small cylindrical regions between the bubble and the free surface. The rest of the domain uses recursively coarser element sizes. Figure 5.2 shows an image of the meshing in M3.

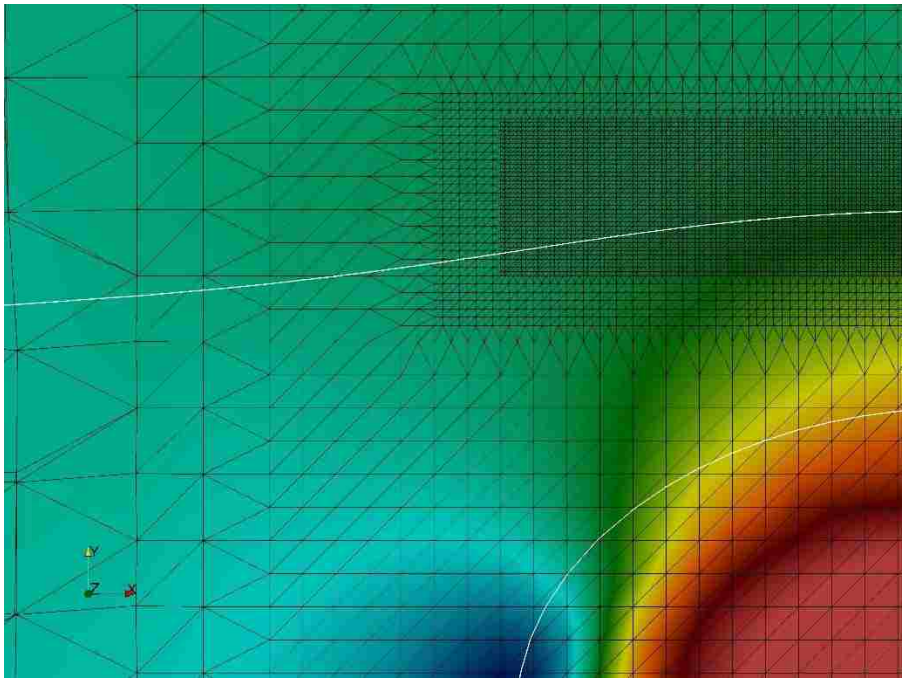

Figure 5.2: An image of the M3 mesh. The color represents vertical (y direction) velocity and the solid white lines show the bubble interface and free surface.

Additionally, the bubble was allowed to rise to the free surface from the bottom of the domain only in the M0 mesh. Future simulations used the solution from a time step from M0 when the bubble was already close to the surface but not close enough to effect whether the bubble bounces off the surface (about 1 bubble diameter away from the surface). This allows the mesh to be coarsened in the path of the bubble that will no longer be important to the bubble-surface interaction. For this reason the first refinement has less elements than the coarsest mesh despite using smaller sized elements. The fluid properties (see Table 5.2) matched the experiments and were based on ethanol and air.

Table 5.2: Fluid properties for bubble rising towards a free surface case

	Ethanol	**Air**
Viscosity [kg/m-s]	0.0012	1.827E-5
Density [kg/m^3]	789.0	1.2
Surface Tension [N/m]	0.0224	
Bubble Diameter [m]	0.00162	

The simulations found the bubble's terminal velocity to be 0.212 m/s, which agrees within 5% to the experimentally measure terminal velocity, 0.223 m/s. Results for the distance from the free surface location normalized by the bubble diameter, and velocity, normalized by terminal velocity, are shown in Figure 5.3 and Figure 5.4, respectively.

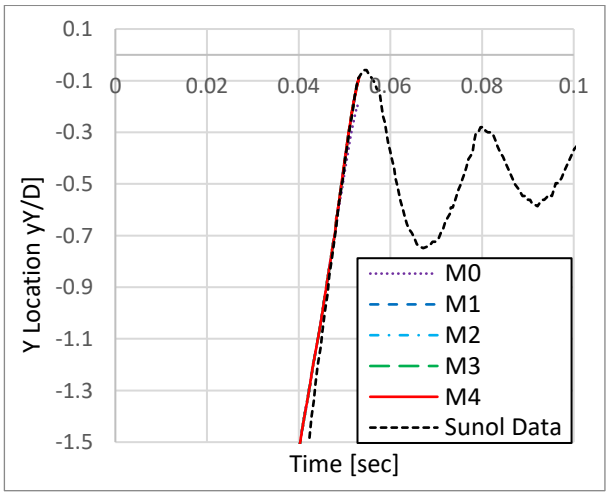

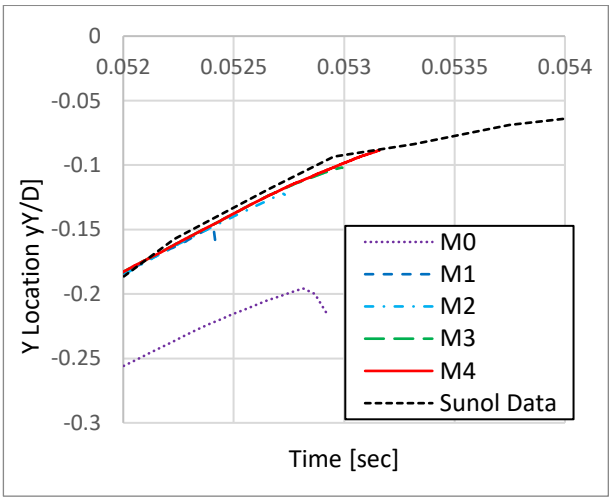

Figure 5.3: Bubble location results. The distance is the distance from the free surface in bubble diameters. Left shows all the data and right zooms in to show more detail.

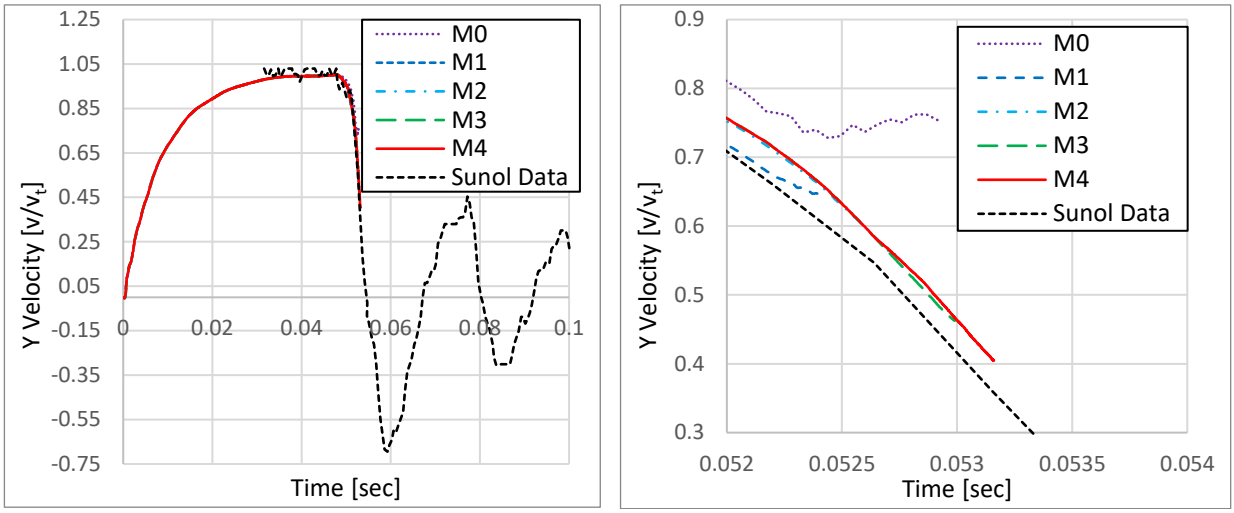

Figure 5.4: Bubble velocity results. The velocity is normalized by the terminal velocity of the bubble. Left shows all the data and right zooms in to show more detail.

As is clear from the final location of the bubble in all the simulations, the bubble did not bounce but rather coalesced with the free surface. All the meshes agreed with the experimental data very well and each new refinements extended the life of the bubble. Even M0 was able to capture the deceleration of the bubble as it approaches the surface. Therefore, the level set method can capture the film drainage process even for meshes that resolve the initial liquid film by only a few computational points. The physics is accurately captured, but once the film thickness approaches the size of the computational elements, the film enters the property transition region of the interface and the bubbles coalesce. Even the finest mesh in this study is about 20 times larger in size than the measured final flim thickness. Further mesh refinements were too expensive for the available computaitonal resources and a fully resolved simulation may even be too expensive for the most powerful computers in the world. Nonetheless, the results are encouraging for the level set method because it implies, first, that given a fine enough mesh and enough computational resources, the simulations would match the experiment, and second, even coarser meshes can capture the film drainage process between two bubbles.

5.2.2 Droplet Deformation in a Simple Shear Field

This study has already been referenced in Section 3.2.1 Interfacial Shear but in the context of what is needed for a simulation to be fully resolved. This section will focus on how the simulations compare to experiments. Accurately predicting how a droplet deforms in a simple shear flow will suggest PHASTA, and the level set method, can accurately predict interfacial shear, which is very important for how the Taylor bubble interacts with the liquid. The simulations contained two parallel plates, moving in equal and opposite directions to form three different shearing rates (see Table 3.2 for details on the flow and mesh properties). The simulations were allowed to run until the droplet was no longer deforming. Experimental work [71, 98] has focused on determining the deformation factor, defined by Eq. (3.3), and the angle of the deformation. Results from the simulations and the experimental measurements are shown in Figure 5.5.

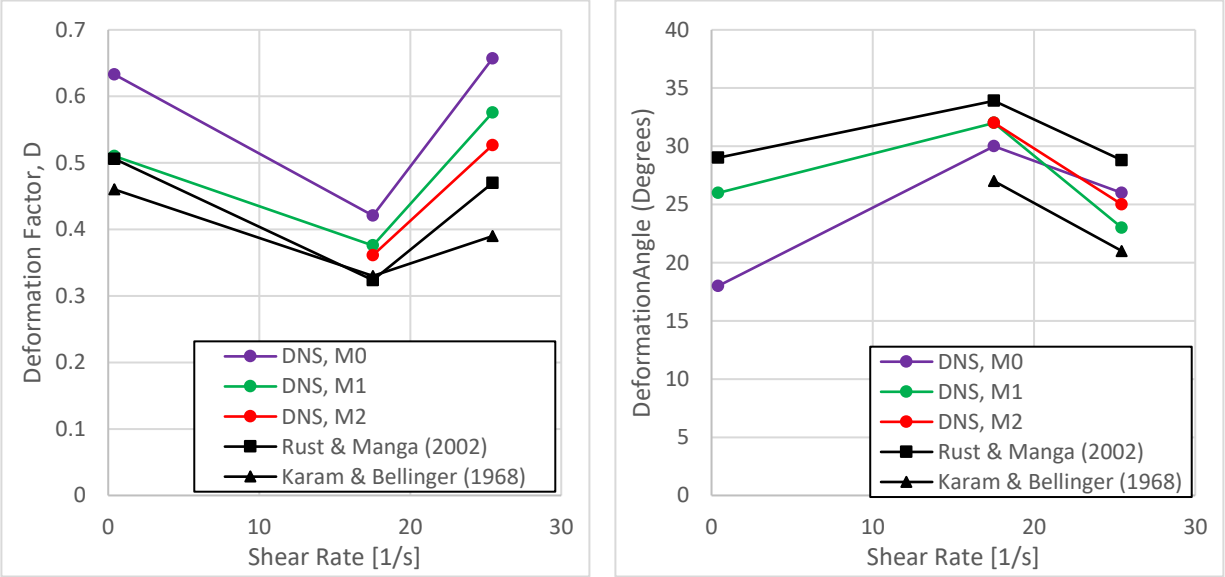

Figure 5.5: Deformation factor, D, (left) and deformation angle (right) results from the droplet shear simulations and experimental work *[71, 98]*.

As Figure 5.5 shows, PHASTA's higher resolution simulations are in better agreement with Rust & Manga than Karam & Bellinger. On average, M2 has a 10% error and M1 has a 12% error compared to Rust & Manga. Compared to Karam and Bellinger M2 and M1 have a 20% average

error. This is likely because Karam & Bellinger had limited precision in their measurement tools and were only able to measure to one significant digit in the deformation of the droplet. The agreement with Rust & Manga is very encouraging however.

5.2.3 Minichannel Taylor Bubble Flow

Taylor bubble flow in small pipes has also been extensively studied [84, 99, 100, 85, 86]. The flows are dominated by viscous and surface tension forces, making the physics relatively simple to understand for two phase flow. Showing PHASTA can accurately simulate these flows is important before turbulent two-phase flows are simulated. The first validation test will examine if PHASTA is consistent with experimental flow regime observations. Figure 5.6 gives a flow regime map for a pipe with the same dimensions as is being used in this study (2.4 mm diameter).

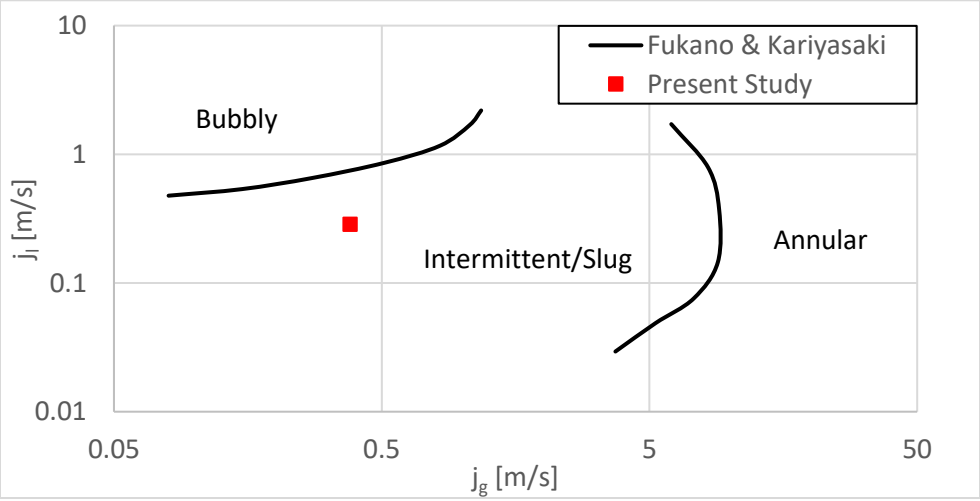

Figure 5.6: Identification of the superficial velocities that PHASTA predicted for the microchannel flow on an experimental flow regime map *[84]*.

PHASTA had predicted slug flow, and this agrees with the map shown in Figure 5.6.

Due to the dominant viscous forces, the flow field is relatively simple and the wake can be described as a toroidal vortex, with the fastest velocity in the center of the pipe. Figure 5.7 (top) shows the flow field found from PIV experiments compared to the flow field found in the simulations.

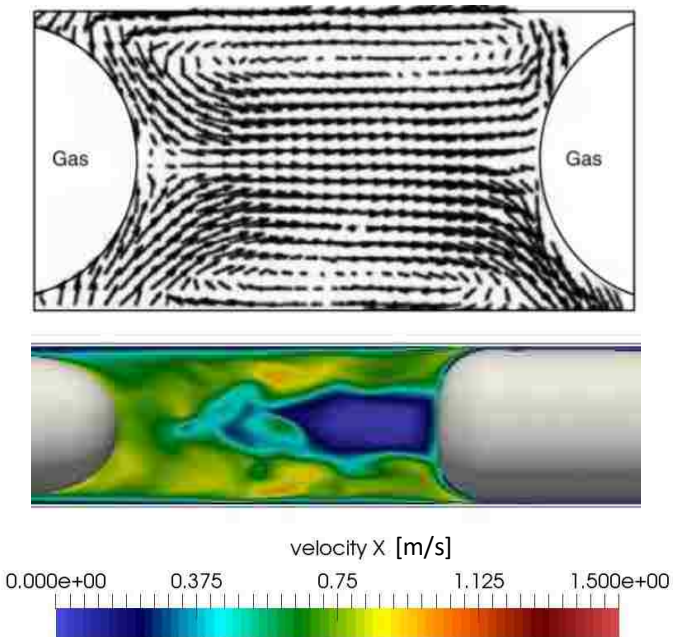

Figure 5.7: Comparison of the flow field from experiment (top) *[86]*, to the flow field from simulation (bottom). In the bottom image x is the streamwise direction.

It is clear that the simulation is not accurately predicting the flow field. There is a negative streamwise velocity region directly behind the Taylor bubble in the center of the pipe. This phenomenon may come from the under resolved mesh on which the flow was initially solved. The low resolution, particularly in the liquid film region, which does not meet the requirements put forth in Section 3.2.2 Liquid Film Resolution, may be inhibiting the downward flow in the liquid film, creating this negative velocity region. When the M1 mesh was created, the solution found with the M0 mesh was used as the initial condition, assuming that after some time, the flow would adjust and reach the expected velocity pattern. This did not occur and the best solution may be to restart with the M1 mesh. However, despite this, the simulation was carried forward in order to observe another phenomenon unique to microchannel slug flow. Fast moving Taylor bubbles in narrow channels develop regular interfacial waves at the tail. Depending on the length of the bubble and size of the channel, the waves move upward along the bubble, decaying in magnitude.

Figure 5.8 (top) shows images of these waves for flow in a 1.1 mm diameter pipe [101]. Figure 5.8 (bottom) shows an image from the simulations on the M1 mesh as the flow is accelerating.

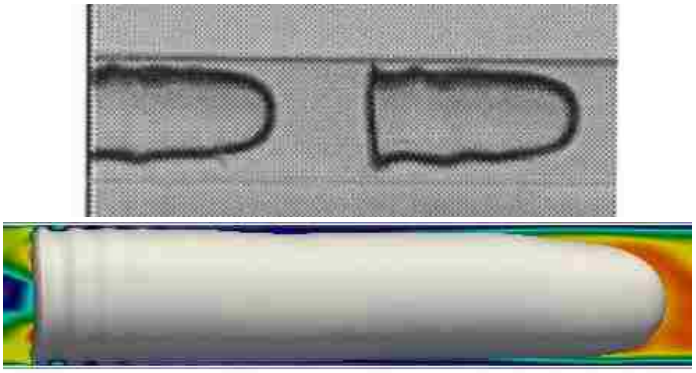

Figure 5.8: Images of the interfacial waves in experiment *[101]* (top) and in simulation (bottom).

As Figure 5.8 (bottom) shows, there are clear interfacial waves in the PHASTA simulations. Capturing these instabilities is important because they will be a driving factor in flow regime transitions in the minichannel. PHASTA's predictions of these waves also show that the level set method can predict this interface behavior without a model to inform the code of this phenomenon.

5.2.4 Accelerating Single Phase Flow

No new simulations were prepared to study accelerating single phase flows. However, the CFD community has acknowledged that the transition from laminar to turbulent single phase regimes requires different meshing requirements than steady laminar or turbulent flows. Therefore, instead of validation, this section will briefly show that the meshes used in these simulations still meet this criterion. The flow regime transition simulations are accelerating flows and are directly relevant to accelerating single phase flows. Wu & Moin [102] and Rai & Moin [103] both designed flow over a flat plate simulations, where, at some point along the plate, the boundary layer transitions from laminar to turbulent. Their results both found that an accurate solution requires a grid refined by a factor of up to two. Wu & Moin used $\Delta x^+ = 5.91$ for the streamwise mesh and $\Delta z^+ = 11.13$ in the spanwise direction. Rai & Moin used $\Delta x^+ = \Delta z^+ = 28.2$ and found the mesh should be

refined by up to a factor of two and likely exceeds typical DNS meshing requirements. Typically, simulations using PHASTA are designed to have 12+ wall units in the streamwise and spanwise direction, meaning this criterion is twice as strict. At the moment of transition from laminar to turbulent flow, M1 maintains a streamwise and spanwise spacing of about 12+ and M2 has about 6+ units. Therefore, M2 is still an accurate simulation despite the strict resolution required. It is worth pointing out again that, as shown in Section 3.1 Single Phase Flow Resolution Requirements, M1's solution is still consistent with M2 up until a certain time for second order statistics despite not meeting meshing requirements.

5.3 Benchmark Level

5.3.1 Accelerating Two-Phase Flows/Flow Regime Maps

In depth analysis and measurement of pressure gradient driven accelerating two-phase flows has not been a focus of much research, making it difficult to directly compare this work. However, flow regime maps represent a two dimensional space that an accelerating two-phase flow can move through. If the flow agrees with the map then the regime should match where the acceleration begins and where it ends. A priority in the validation process was to ensure PHASTA's flow regime predictions match the flow regime maps. To draw conclusions from the simulations about the mechanisms for flow regime transitions, there must be a proven consistency between the simulations and theory/experiments. This study is not meant to prove that PHASTA predicts a transition at the same point the map does. Instead, a matching transition should provide confidence in the mechanisms for the transition. Additionally, since the flow is pressure gradient driven, a drift flux model [29] should be able to approximate the expected acceleration path. Because reverse transitions (decelerating flows) are typically not considered in flow regime transition modeling, only forward transitions are considered here.

Figure 5.9 plots the simulation superficial velocity and drift flux model prediction on the theoretically based Mishima & Ishii [24] and Taitel et al. [27] maps.

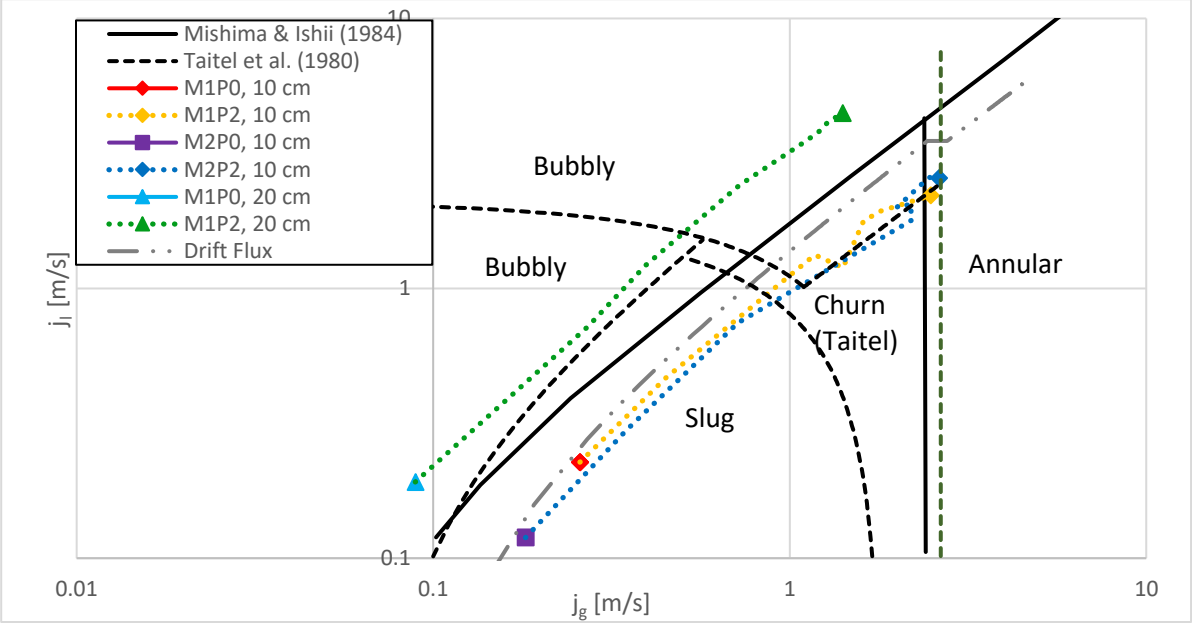

Figure 5.9: Comparison of the simulations to the theoretical Mishima & Ishii *[24]* and Taitel et al. *[27]* flow regime maps. The Drift flux model *[29]* is also included. Mishima & Ishii did not predict churn-turbulent flow at these conditions.

As Figure 5.9 shows, according to the both maps the 10 cm long domain should be starting in the slug flow regime. As the superficial velocities increase, the Taitel et al. maps predict a transition to the churn-turbulent regime and possibly bubbly flow. The Mishima & Ishii maps did not predict any churn-turbulent flow but the flow rates approach the annular regime, and presumably intermittent flow would be breaking down at this condition. PHASTA does predict the initial slug flow and the transition to churn-turbulent. Annular flow was considered to not be reached in the simulations, and the maps show the superficial velocities lie directly on the regime boundary, making a classification difficult. Appendix B shows images of this transition. According to both maps the initial condition in the 20 cm long pipe flow is expected to be bubbly flow. PHASTA did not predict this but this is because slug flow was forced by initializing the entire gas volume in a small region of the pipe, forcing coalescence to one large bubble. As the flow accelerates however,

PHASTA does predict a transition to bubbly flow (see images in Appendix C). Interestingly, this transition only occurs after the superficial velocities are crossing the line in the Taitel et al. map that distinguishes between bubbly flows where turbulent dispersion forces are not and are dominant. When the turbulent dispersion forces become dominant, the Taylor bubble breaks up and becomes bubbly flow, suggesting Taitel et al. are identifying an important flow regime transition criterion. Overall, the flow regime transitions identified in the maps agree with PHASTA's predictions.

Bergles et al. [104] have produced an experimental flow regime map (Figure 5.10) for boiling flow in a 10.3 cm diameter pipe at 6.9 MPa with steam and water. While the presented PHASTA results are at adiabatic conditions, this still provides useful insight into what should be expected at this pressure.

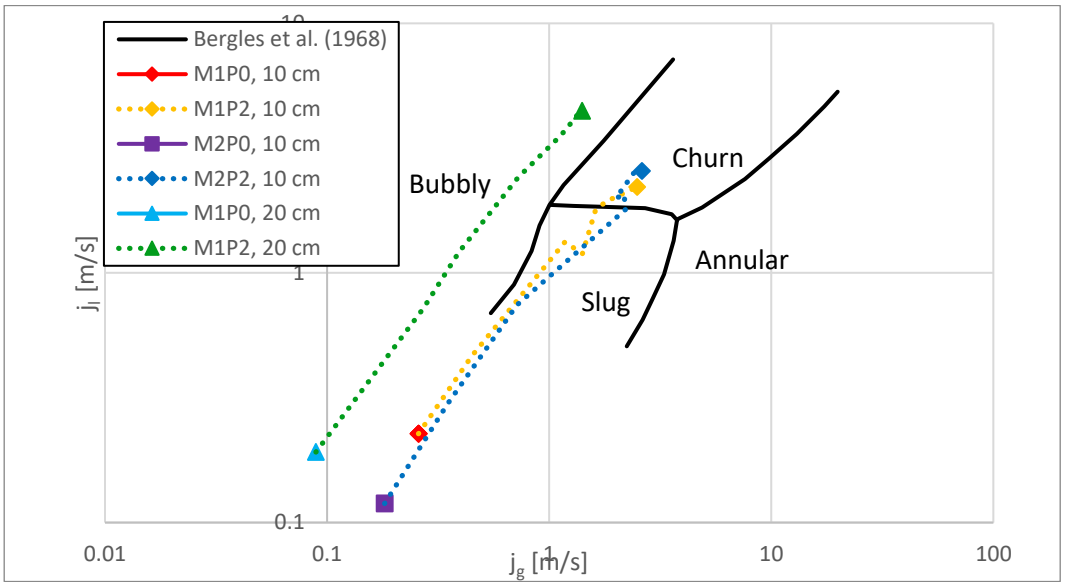

Figure 5.10: Comparison of the Bergles et al. *[104]* experimental flow regime map to the simulations.

This map also agrees with PHASTA's prediction of a transition from slug to churn-turbulent flow in the 10 cm long pipe. This map predicts that the 20 cm long pipe flow remains in the bubbly

regime, but as was mentioned, this is not a concern because the slug flow was a forced initial condition.

5.3.2 Taylor Bubble/Slug Flow

Before accelerating, all the simulations begin with a single Taylor bubble. Therefore, ensuring PHASTA is accurately predicting the behavior of the Taylor bubble is critical to simulating its interaction with the liquid and eventual breakup. The shape of a Taylor bubble has been studied extensively, and for potential flow an exact solution exists [42]. While the simulations were not potential flow, the liquid film thickness should be similar since viscous forces become more significant in the thin film region. To find the film thickness in the simulation, the zero level set locations were collected along eight different slices (see Figure 5.11). These eight profiles were then averaged. The comparison is shown in Figure 5.12.

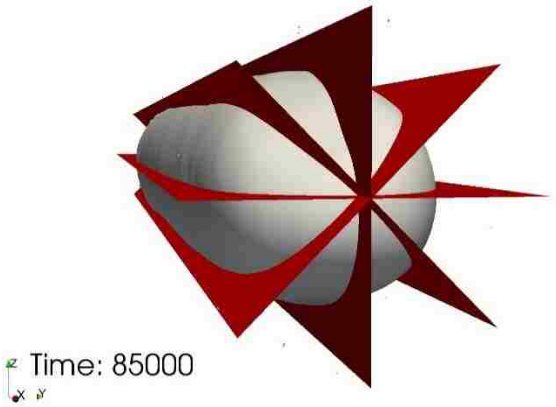

Figure 5.11: The planes (red) used to collect the zero level set locations along the Taylor bubble (grey).

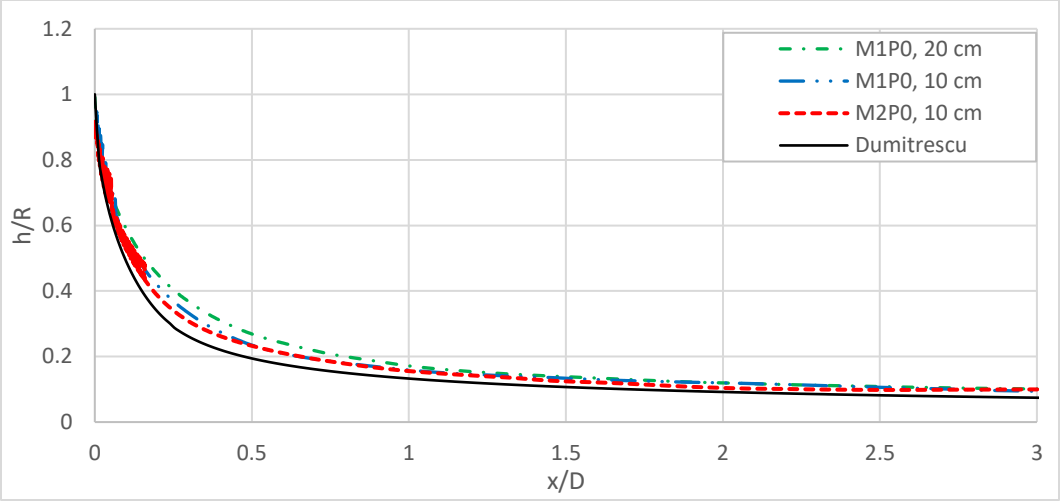

Figure 5.12: The predicted liquid film shape compared to the Dumitrescu *[42]* analytic solution for potential flow.

At three diameters from the nose of the bubble, x/D, all three simulations predict the film thickness is 0.099R, where R is the radius of the pipe. The analytic solution predicts the film is 0.074R. An experiment [77] found that, for similar flow conditions and very long Taylor bubbles, the film thickness stabilizes at 0.086R. These bubbles were long enough to ensure the film thickness was no longer changing. As Figure 5.12 shows, the film thickness is still slowly decreasing. Given a long enough bubble, the simulations would agree even better with the experimental results. Finally, Karapantsios et al. [78] developed an expression for the liquid film thickness of Taylor bubbles rising in stagnant fluid. This expression predicts the film thickness should be 0.094R. Considering the simulations do not have bubbles long enough to achieve a non-changing film thickness, and the variability in literature results, PHASTA is accurately simulating the film thickness associated with slug flow.

The wake structure of the Taylor bubble is complex, fortunately there are studies that provide data for both average and instantaneous velocity information. First, Shemer et al. [83] looked at the mean velocity profiles at different distances behind a Taylor bubble. This experiment used a 14 mm diameter pipe, very close to the 15 mm diameter used in this work. To obtain their statistics

400 bubble p asses, each providing one data point, were collected to make each plot. A simulation in the 20 cm long, 15 mm diameter pipe was created to replicate the Re = 8250 experiment. Figure 5.13 and Figure 5.14 show the comparison between velocity and streamwise velocity fluctuation data from the experiment and simulation, respectively.

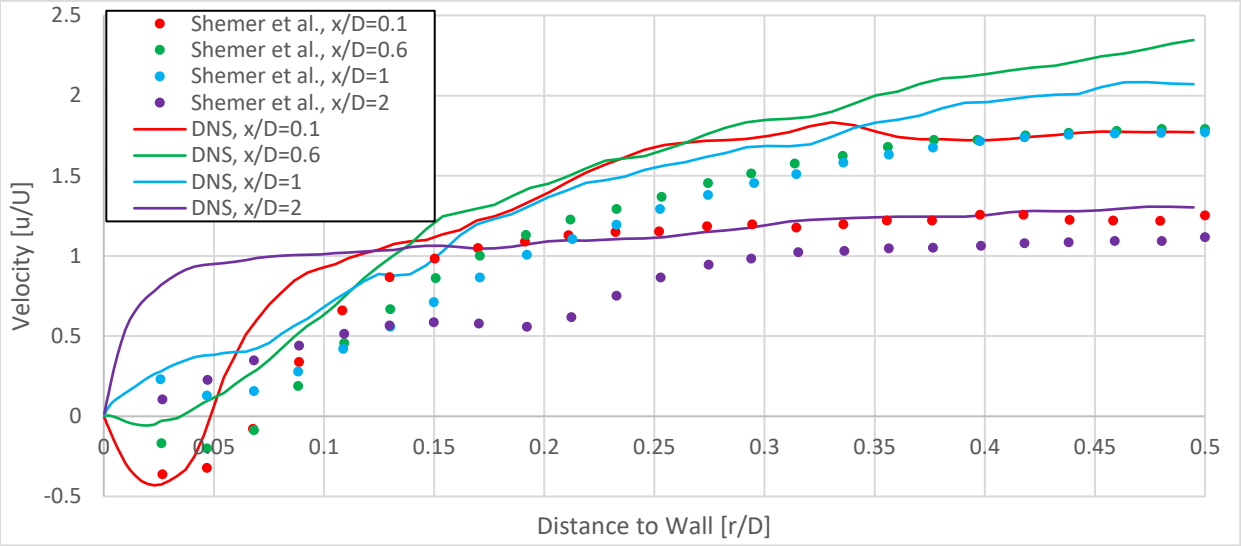

Figure 5.13: Comparison of the Shemer et al. *[83]* streamwise velocity data to the simulation for different locations behind a Taylor bubble.

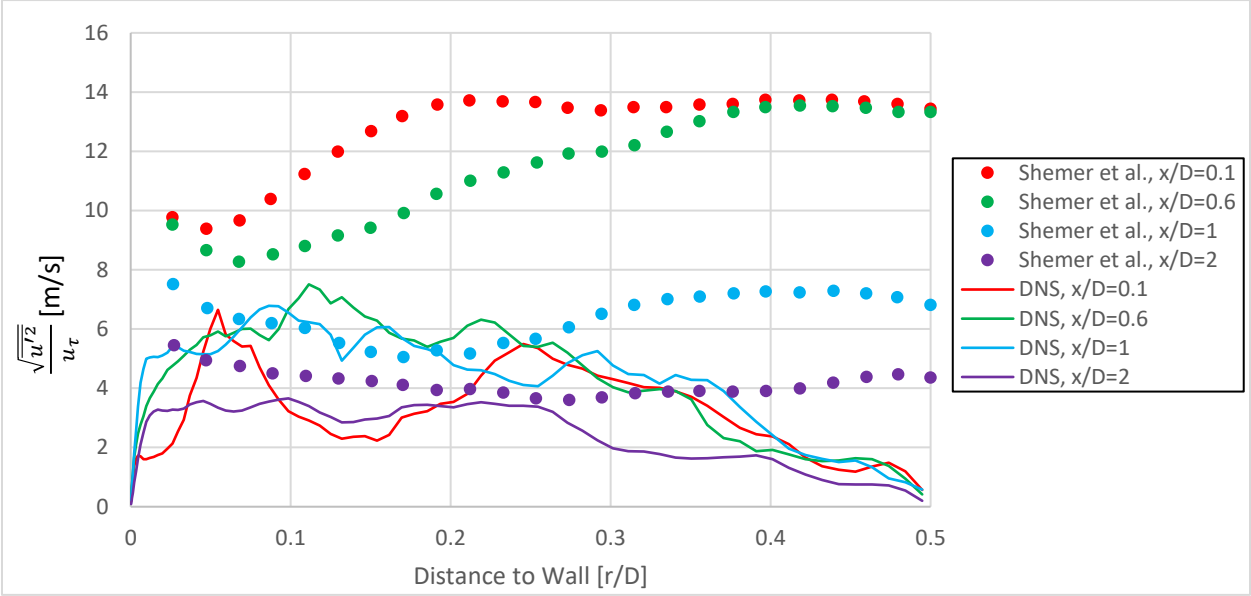

Figure 5.14: Comparison of the Shemer et al. *[83]* streamwise velocity fluctuation data to the simulation for different locations behind a Taylor bubble.

Discrepancy does exist in the data, the most obvious being the velocity is higher in the simulation and the streamwise velocity fluctuations appear to be smaller in the simulation. The difficulty in obtaining a large volume of numerical data may explain some of the discrepancy. As mentioned, the experiments sample from 400 different bubbles, while the numerical data is from one time instance. Therefore, the sampling uncertainty is larger in this particular validation study. A similar discrepancy was observed in [105]. Mikuz et al. noted that their simulations predicted a peak in the streamwise velocity fluctuations directly behind the corner of the Taylor bubble. PHASTA predicts this peak as well, but Shemer did not observe this. The reason why Shemer did not measure this peak is not clear because strong fluctuations are expected in this region, as seen in the data from Shi et al. [106]. The trend in the velocity progression is similar between each dataset. Close behind the bubble, the profile is relatively flat, with a negative region near the wall from the liquid film jets. Further behind the bubble, at $x/D = 0.6$ and 1.0, the velocity in the wake increases and the negative region close to the wall disappears. The $x/D = 2.0$ profiles are the most dissimilar. The simulation predicts the flow returns to a profile close to the typical turbulent log-law profile while the experiment finds a gradual increase in velocity from the wall, eventually reaching an approximately flat profile in the center. Mikuz et al. also found that the return to a more typical turbulent velocity profile was faster in their simulation than Shemer observed. The conclusions drawing from this validation study are unclear. The general trend in the wake velocity agrees with Shemer et al. but the fluctuations display different trends. The DNS data seems to be more consistent with other DNS but could benefit from additional samples to achieve less uncertainty.

Data for the instantaneous velocity field in the wake of a Taylor bubble has been captured by Shi et al. [106]. It is difficult to compare instantaneous velocity due to the variability, but one

phenomenon that has been noticed in the simulations were structures resembling Kelvin-Helmholtz instability arising in the shear layer between the liquid film jet and the wake of the bubble. This phenomenon would not be noticed without the instantaneous velocity information. Figure 5.15 shows these structures circled in black, the color field is the y velocity. For this single vertical plane, the y velocity also corresponds to the radial velocity.

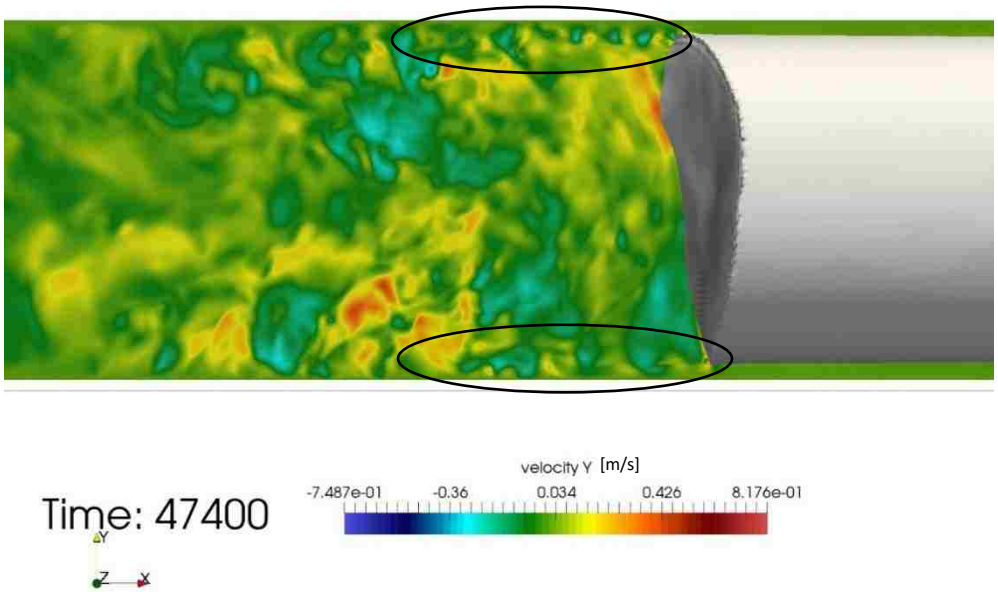

Figure 5.15: An image showing the Kelvin-Helmholtz structures that develop in the shear layer between the liquid film jets and the wake. Colored by y velocity.

At the corner of the bubble the level set field experiences a sharp 90 degree turn which can give rise to undesired level set field stretching that could affect the flow. In order to determine if the velocity is unaffected by the level set field at this corner, autocorrelations are performed on the y velocity in this region of the experimental and numerical flows. The autocorrelation is given by the following:

$$A(d) = \int \frac{v(x)v(x-d)}{v(x)^2} dx \qquad (5.1)$$

where A is the autocorrelation value, v is the y velocity data, and d is the data offset value, or distance behind the Taylor bubble in this case. Autocorrelations measure the periodicity of data. If

the data is regularly oscillating, then the autocorrelation value will oscillate as well. If there is no oscillatory pattern, then the autocorrelation will decay quickly to zero. Two datasets from the experiment and two from the DNS, each named left and right, were used to perform the autocorrelations. The results are shown in Figure 5.16.

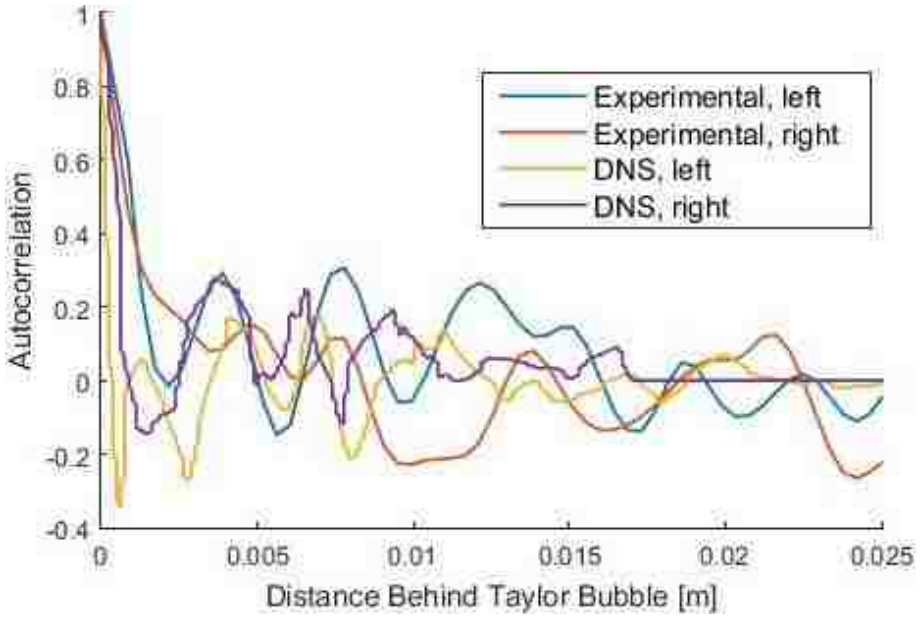

Figure 5.16: The results from the autocorrelations of Shi et al.'s data *[106]* and the DNS data.

As is expected, the DNS autocorrelations show an oscillatory pattern, seen in how the autocorrelation fluctuates around zero. This indicates the transverse velocity is changing sign along the line the data was sampled from. The experimental data displays the same behavior, and with a similar frequency, showing the instabilities do occur in two-phase flows. Averaging the peak-to-peak wavelength of the experimental and computational oscillations shows that the two datasets agree within 7% (about a 3 mm wavelength). This is an encouraging result because it shows the sharp corner in the level set field at the tail of the bubble is not adversely affecting the wake. Additionally, PHASTA is capturing phenomena that are physical and contribute significantly to the turbulence in the wake.

5.3.3 Rising Cap Bubble Flow

As mentioned, the experiment produced by Sun [81] had relatively high flow rates and a Reynolds number that was estimated at just below 100,000. Simulating this flow would be extremely computationally expensive and be on the cutting edge of two-phase DNS. Lower flow rate simulations were also tested but this data was not presented in the text. Recreating this experiment computationally would be extremely valuable in analyzing PHASTA's breakup capability. Due to the liquid momentum driving bubble breakup, one can claim the level set method more accurately captures breakup than coalescence, which is largely dependent on small scale phenomena. Recreating this cap bubble shearing process and observing turbulence as it collides with the bubble would be an excellent test to back up this claim. This simulation would capture both the tail shearing and interfacial instability phenomena and be able to validate these mechanisms for breakup in PHASTA. Even without this simulation recreated perfectly, it appears PHASTA can predict bubbles shearing off of Taylor bubbles that are close in size to what multiple experiments have found. For additional details on this, see the mesh resolution discussion in Sections 3.2.3 Taylor Bubble Breakup Events, 4.3 Mesh Design, and Table 4.5.

5.4 Churn-Turbulent Interface/Void Distribution

This study was not included in the validation hierarchy but is important because showing the interfacial area and void distribution of churn-turbulent flow in PHASTA agrees with experiments would indicate PHASTA can accurately simulate the turbulence of churn-turbulent flow and its interface interactions. Additionally, these measurements pair nicely with Taylor bubble shape measurements due to their similarities. Unfortunately, the best available study uses total interfacial area concentration at different axial positions rather than local/radial measurements [107]. Typically, experimental local interfacial area measurements are only taken in bubbly flow because

interfacial area calculation relies on assumptions of spherical bubble shape. Dejesus & Kawaji [108] developed a correlation for air-water interfacial area concentration from experimental data they produced in a 2.54 cm diameter pipe:

$$A_i''' = 1.535 \frac{dP}{dx}^{0.12} j_l^{-0.14} j_g^{1.2} \alpha_l^{1.6} \quad (5.2)$$

where A_i''' is the total interfacial area concentration of the flow, $\frac{dP}{dx}$ is the pressure gradient, and α_l is the liquid fraction. Using this correlation finds an expected interfacial area concentration of 5.99 cm^2/cm^3. The simulation had an interfacial area concentration of 5.81 cm^2/cm^3, only a 3% difference. This error is similar in agreement to the experiments that were compared to the correlation. This result is important because it demonstrates that even though the level set method will always coalesce two approaching bubbles together (for meshes that do not resolve the micrometer scale liquid film) the interfacial area can still be accurately captured. Experimental radial void and interfacial area concentration distribution data is available in the open literature; however, it is extremely difficult to find cases directly related to the flows performed in this work.

CHAPTER 6. SIMULATING FLOW REGIME TRANSITIONS

Four different classes of simulations are analyzed in this Chapter: forward and reverse transitions in a pipe 10 cm long and 15 mm in diameter with a 40% void fraction, and a 20 cm long pipe 15 mm in diameter with a 20% void fraction. Numerical data from these simulations will be presented first and be followed by a discussion of their associated transition mechanisms. The forward and reverse transitions will be compared and contrasted to determine how the physics differs between accelerating and decelerating flows. Two major transition mechanisms for the forward and reverse transitions were observed, both exhibiting distinctly different flow characteristics. A novel criterion for transition will also be presented in this Chapter. For reference, time is considered to begin (t=0) when the pressure gradient is changed. Unless specified, these simulations were all performed on M2 mesh resolution. Due to lack of available computing resources in some instances, mesh M1 was sometimes used. Numerical data was not collected from the boundary layer mesh in the 40% void fraction flows because the static probe tool cannot collect data from prism elements. The boundary layer mesh in other simulations was tetrahedronized, eliminating this issue.

6.1 40% Void Fraction

In these simulations the forward flow is allowed to develop a single Taylor bubble. The Taylor bubble interface is smooth despite the relatively short liquid slug. The reverse transition's initial condition is taken from a time step when the forward flow is in the churn-turbulent regime. A single static probe plane is placed in the domain for data collection. The forward transition alone represents about 20 million CPU-hours. For a complete set of images of both the forward and reverse simulation see Appendix B and Appendix D.

6.1.1 Accelerating Flows

This simulation is initialized in slug flow and is accelerated to flow rates exceeding 5 m/s where slug flow is no longer observed. Figure 6.1 (a) shows the Taylor bubble prior to acceleration. Behind the Taylor bubble a clear wake exists. This wake consists of a fast turbulent region directly behind the Taylor bubble and a peripheral region where the slower moving liquid film spills out into the wake. The slower moving liquid film jets causes a significant amount of turbulence, as will be discussed, due to the shear created between the fast and slow moving regions. However, the turbulence decays significantly before colliding with the nose. The turbulence decay is sufficient enough that the interface remains completely smooth, as there are no eddies with sufficient energy to collide and cause perturbations. The average liquid velocity is about 0.2 m/s, corresponding to a Reynolds number equal to 2665, nearly completely laminar.

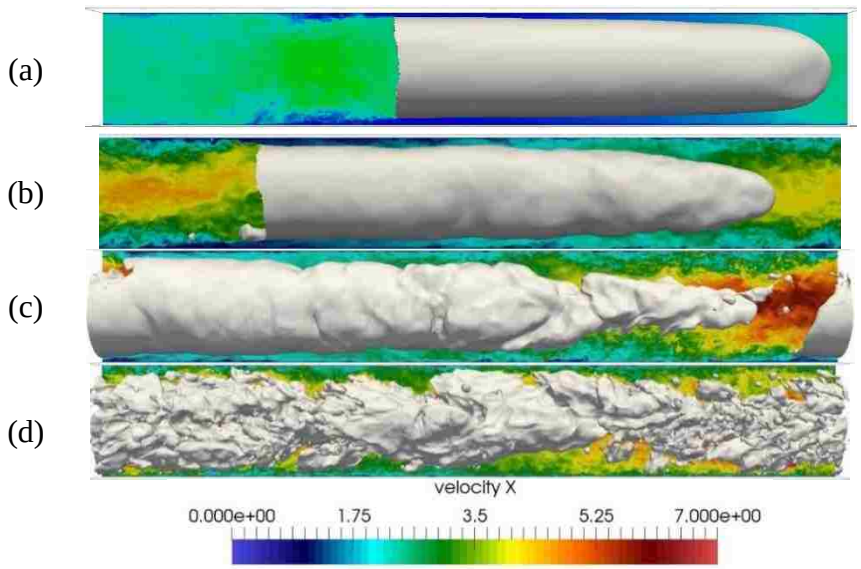

Figure 6.1: Visualization of the flow regime transition of the 40% forward flow regime transition simulation. (a) 0.0 sec, (b) 0.17 sec, (c) 0.219 sec, (d) 0.234 sec.

As the flow accelerates the wake begins to elongate and wall generated turbulence becomes more prevalent. Therefore, eddies are now colliding with the Taylor bubble interface, causing perturbations, as seen in Figure 6.1 (b). Additionally, due to the fast moving wake extending to the

bubble, the bubble's nose accelerates and stretches out the bubble (see Figure 6.1 (b) and (c)). The combination of the large interfacial perturbations and the bubble's extension eventually breaks up the Taylor bubble, creating churn-turbulent flow (Figure 6.1 (d)). Plotting the superficial velocities over time on the Mishima & Ishii [24] and Taitel et al. [27] Maps (Figure 6.2) is consistent with what the flow regime maps predict a slug to churn-turbulent/annular regime.

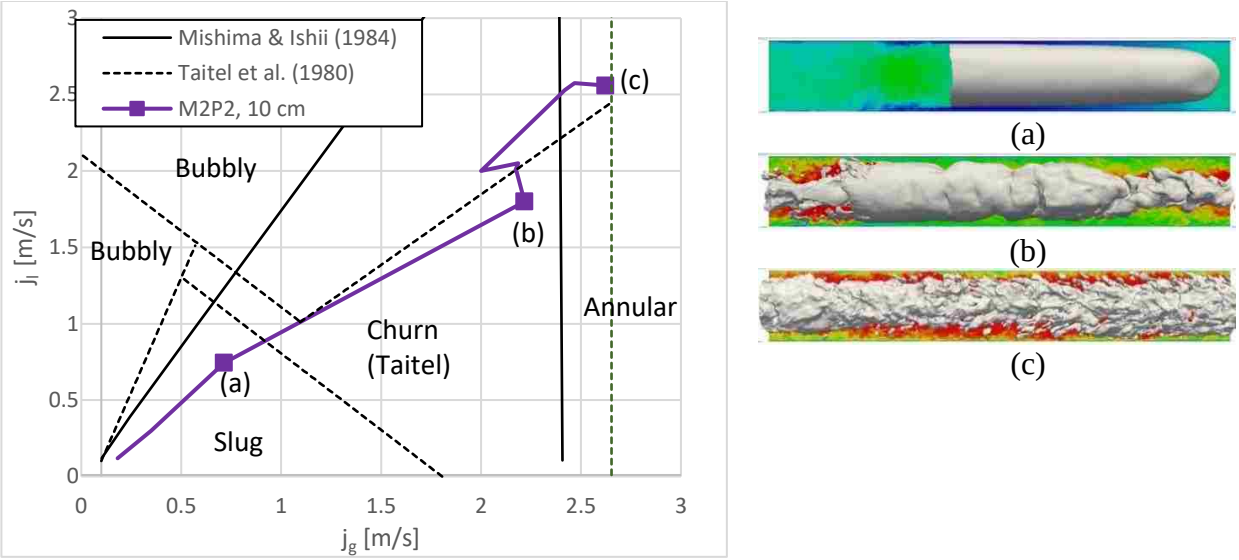

Figure 6.2: Comparison of the computational superficial velocity data form the 40% forward simulation to the Mishima & Ishii *[24]* and Taitel et al. *[27]* flow regime maps. The images show the state of the flow at the three labeled points on the map.

Figure 6.2 shows that the progression of superficial velocity undergoes two different stages. The non-logarithmic axes were chosen to better show the features of the development. First, as the Taylor bubble accelerates, the gas and liquid acceleration both increase together. As the bubble begins to break up, starting at point (b), the gas superficial velocity stagnates, or even seems to slow, as the liquid superficial velocity continues to increase. This lasts for only about 0.025 seconds. Once the bubble is fully broken apart the approximately even acceleration continues, at an elevated liquid flow rate, until the final flow condition is reached. The gas superficial velocity stagnation is likely attributed to the increase in interfacial area that also increases the drag force on the gas phase. The additional drag force on the gas pauses the average velocity of the gas. The

drag would also increase the velocity of the liquid as the gas "pulls" on the liquid more. This is why the churn flow continues at a faster liquid flow rate. This sequence is an excellent demonstration of a flow under transition and illustrates that the flow regime transition process cannot be represented by a hard line. Similar to turbulent transition, there is a time when the flow is neither slug nor churn-turbulent and exhibits different characteristic parameters.

The TKE encountered by the bubble is important to the breakup of the bubble and it drives the formation of interfacial instabilities. Figure 6.3 shows the liquid TKE at three different instances in time; the liquid slug well before the breakup (blue line), the slug as the breakup is initiating (green line), and the churn-turbulent flow (yellow and red lines). A TKE profile based on Moser et al.'s [2] data is included to provide context relative to a typical single phase TKE profile.

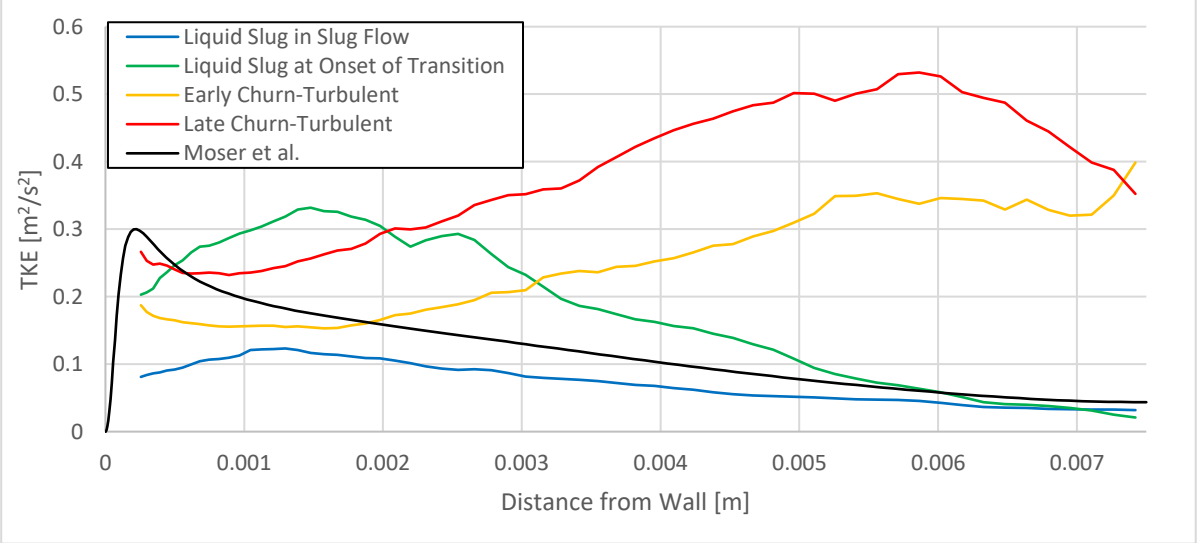

Figure 6.3: TKE plots for three different instances in time in the 10 cm long forward flow as well as single phase computational data from Moser et al. [2].

It is clear that the TKE peak is shifted inward compared to typical turbulent flow. As this shifted TKE profile grows, more eddies, that are also more energetic, begin to collide with the interface. Importantly, due to the shifted TKE peak, the most energetic eddies do not enter the liquid film and instead collide with the nose of the bubble. Eventually, the TKE is strong enough to form

interfacial instabilities that bridge the entire diameter of the pipe, breaking up the bubble. These interfacial instabilities and their growth over time can be seen in Figure 6.4.

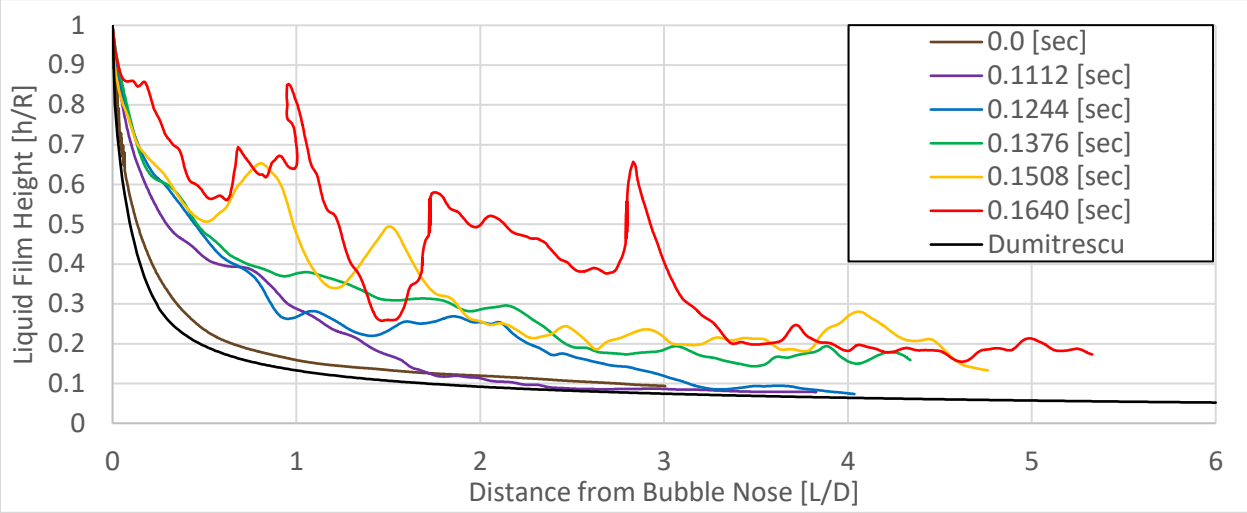

Figure 6.4: Interface profiles for different instances in time of the 10 cm long forward simulation. Dumitrescu's *[42]* profile is also included.

Once churn-turbulent flow is reached, the TKE profile is completely changed. As Figure 6.3 shows, the TKE near the wall decreases by nearly half while the TKE in the center of the pipe increases. As acceleration continues this TKE profile shape is approximately maintained and increases in magnitude. The interfacial area distribution also undergoes a major change after transitioning to churn-turbulent flow. Slug flow exhibits very little interfacial area due to the entire gas volume being contained in one bubble. Most of this interface is located near the wall. Churn-turbulent flow has many more interfaces that are distributed more evenly across the diameter of the pipe. Figure 6.5 shows the mean interfacial area concentration, averaged over the entire domain, of each flow regime.

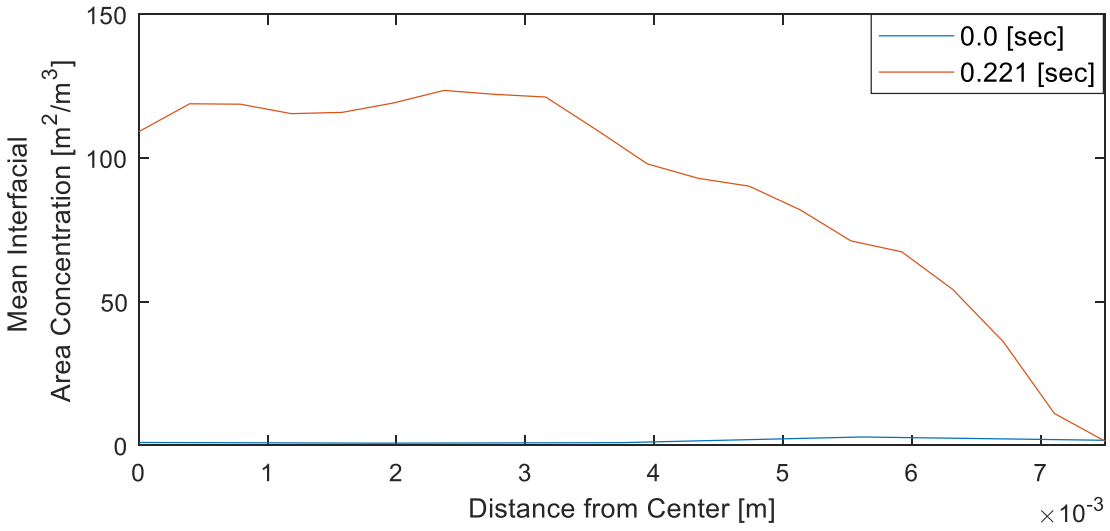

Figure 6.5: Interfacial area concentration for slug flow (blue line) and churn-turbulent flow (red line).

As the bubble breaks down the interfacial area dramatically increases and becomes much more concentrated in the center of the pipe. Even with this sharp increase in interfacial area, large Sauter mean diameters are still calculated in the center of the pipe, as shown in Figure 6.6.

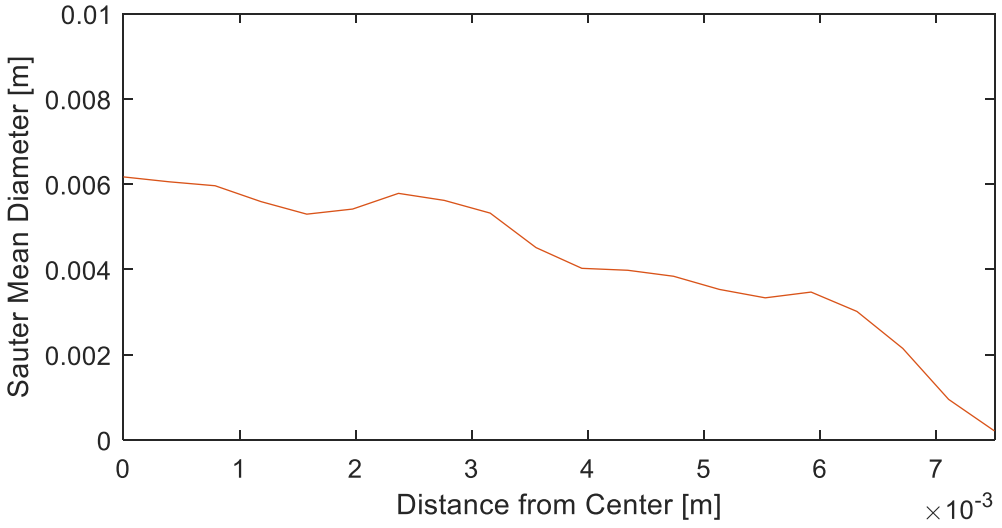

Figure 6.6: Sauter mean diameter calculation for churn-turbulent flow at 0.221 sec.

Close to the wall the Sauter mean diameter is calculated to be only 1.0 mm before reaching effectively zero at 0.5 mm from the wall.

6.1.2 Decelerating Flows

While in the churn-turbulent regime the pressure gradient was stepped back to the P0 value and the flow was allowed to naturally decelerate. Figure 6.7 shows how the interfacial velocities progressed over time and how the progression compares to the Mishima & Ishii [24] and Taitel et al. [27] flow regime maps.

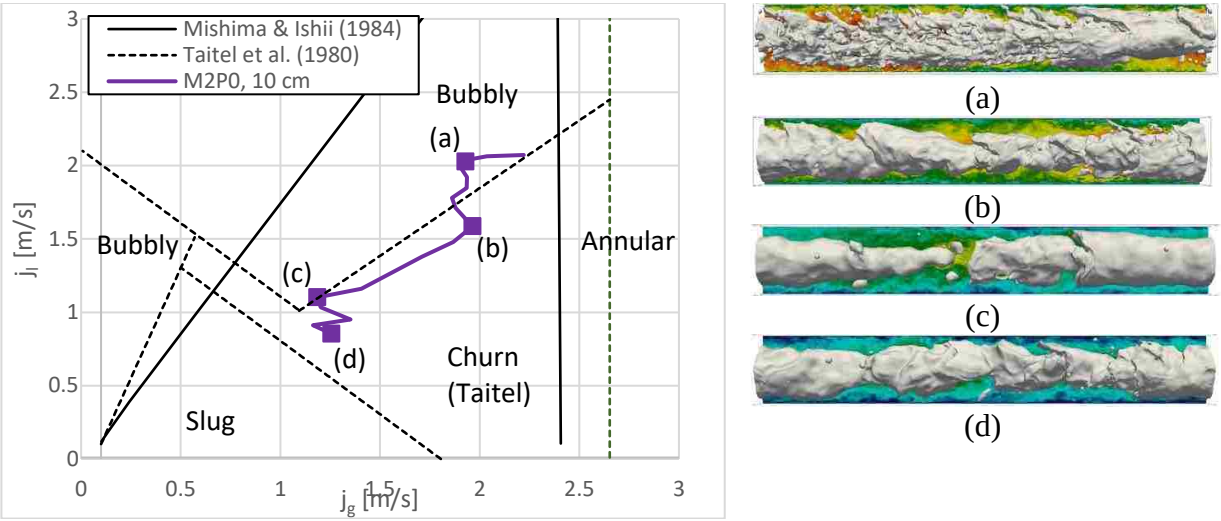

Figure 6.7: Comparison of the computational superficial velocity data form the 40% reverse simulation to the Mishima & Ishii *[24]* and Taitel et al. *[27]* flow regime maps. The images show the state of the flow at the four labeled points on the map.

The flow regime map is on a linear scale to provide more detail to how the superficial velocities develop over time. Similar to the forward transition, the deceleration rate is not constant over time nor is it consistent between phases. The gas phase's deceleration stagnates twice as the liquid continues to slow. This occurs first when the small bubbles in the churn-turbulent flow coalesce with the larger structures to form a wavy gas core and lasts about 0.063 sec. This is seen in Figure 6.7 (a) and (b) and represents the transition out of churn-turbulent flow to annular flow. Coalescence reduces the amount of interfacial shear, meaning the gas is no longer pulling the liquid, therefore slowing it. Additionally, even though the flow is decelerating on average, the migration of gas to the faster moving center of the pipe causes the gas to maintain its velocity. Between (b) and (c) the phases slow down together. The reason for the second gas superficial

velocity stagnation, occurring between points (c) and (d) and lasting about 0.1 sec, is not as clear. However, during this time period the annular flow experiences liquid waves that occupy the entire pipe cross section and temporarily segment the gas core. These bridges form because the TKE in the liquid weakens enough to allow the surface tension to reduce the interfacial area by forming a more spherical interface shape. Since a sphere containing all of the gas cannot be formed, instead the gas column widens, making the liquid film thinner. As the film becomes thinner the gas core can no longer extend along the entire pipe length. When this bridge is formed, a pseudo nose and wake from a Taylor bubble also exists. The fast moving and energetic wake then pulls the nose back into the core. This back-and-forth may maintain the gas's velocity.

Also different from the forward transition, is the TKE development. This difference is caused by the different void distribution. The forward transition allowed the TKE in the slug to increase, but in the reverse simulation there is no slug, only a liquid film. The TKE in the liquid film is what determines if the gas core can continue to be supported or if a Taylor bubble is to be formed. As Figure 6.8 shows, the liquid TKE initially decreases rapidly, but after a little over 0.1 seconds, the TKE only decreases slightly or remains constant.

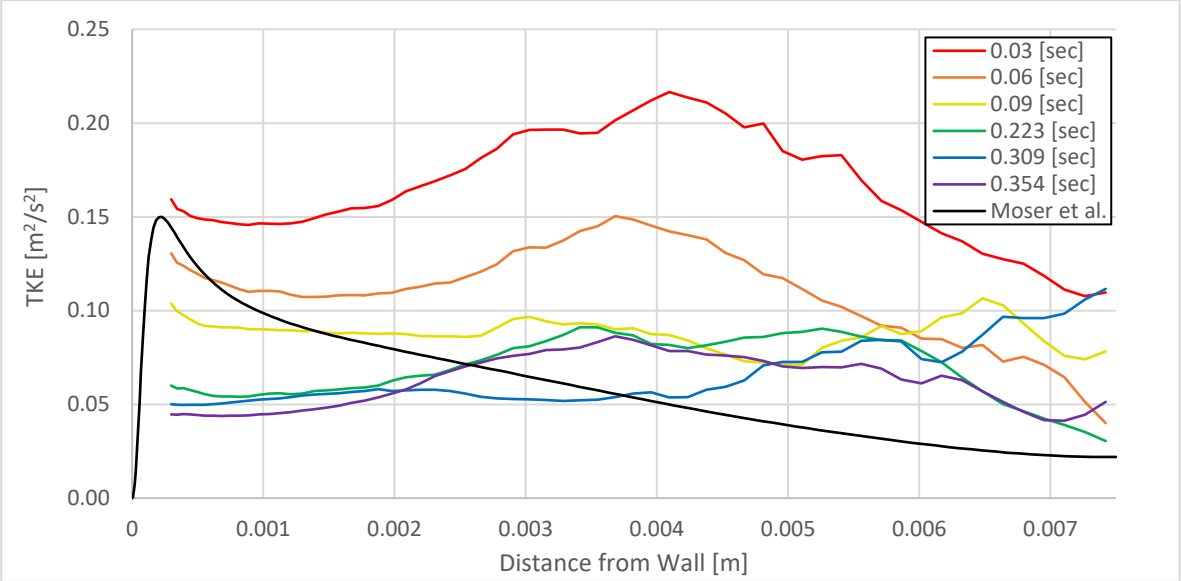

Figure 6.8: TKE plots for different points in time for the 10 cm long reverse flow. Computational Data from Moser et al. *[2]* is included for reference.

This explains why annular flow is maintained for so long, the TKE does not decay evenly in time, and the liquid film TKE is strong enough to still overcome the surface tension force. The second stagnation in gas velocity occurs between the green and purple lines in Figure 6.8, where it is clear the TKE is nearly constant throughout. Here the gas velocity may be maintained by the lower interfacial drag formed by the smoother interface of the gas core. Interestingly, the liquid TKE in the deceleration is never as high near the wall as in the forward simulation. This suggests that the TKE needed to breakup the Taylor bubble is larger than what is required to maintain a single gas column. Therefore, as interfacial structure and TKE change over time, criteria for forming different regimes arise, causing a new flow regime transition. Therefore, the flow regime transitions are dependent on the initial condition and information regarding the time history may not determine how the regimes develop in reverse. This time asymmetry is a novel observation in the field of two-phase flow regime transitions. The theory discussed in Section 1.2.3.2 Theoretically Derived Regime Boundaries only ever considers one criterion for each flow regime boundary. This

suggests that flow regime maps for decelerating flows or condensing flows may vary significantly from their counterparts.

6.2 20% Void Fraction

In these simulations the forward flow is allowed to develop a single Taylor bubble. The Taylor bubble interface is smooth and the liquid slug contains almost no turbulence. The slug is long enough and the flow is slow enough that TKE from the bubble wake decays before reaching the bubble and almost no turbulence is generated at the wall. The reverse transition's initial condition is taken from a time step in the M1 mesh simulation when the forward flow's Taylor bubble is nearly completely broken apart. A single static probe plane is placed in the domain for data collection. The forward transition alone represents about 40 million CPU-hours. For a complete set of images of both the forward and reverse simulation see Appendix C and Appendix E.

6.2.1 Accelerating Flows

This simulation also begins in slug flow, this time with a significantly longer liquid slug due to the longer pipe, 20 cm, and lower void fraction, 20%. As was discussed in Section 6.1.1 Accelerating Flows the turbulence in the wake played a major role in the breakup of the bubble. This simulation was designed to test how the transition differs when the wake is too far away from the bubble to have a major effect on the bubble. Figure 6.9 shows the progression of the superficial velocity for this simulation.

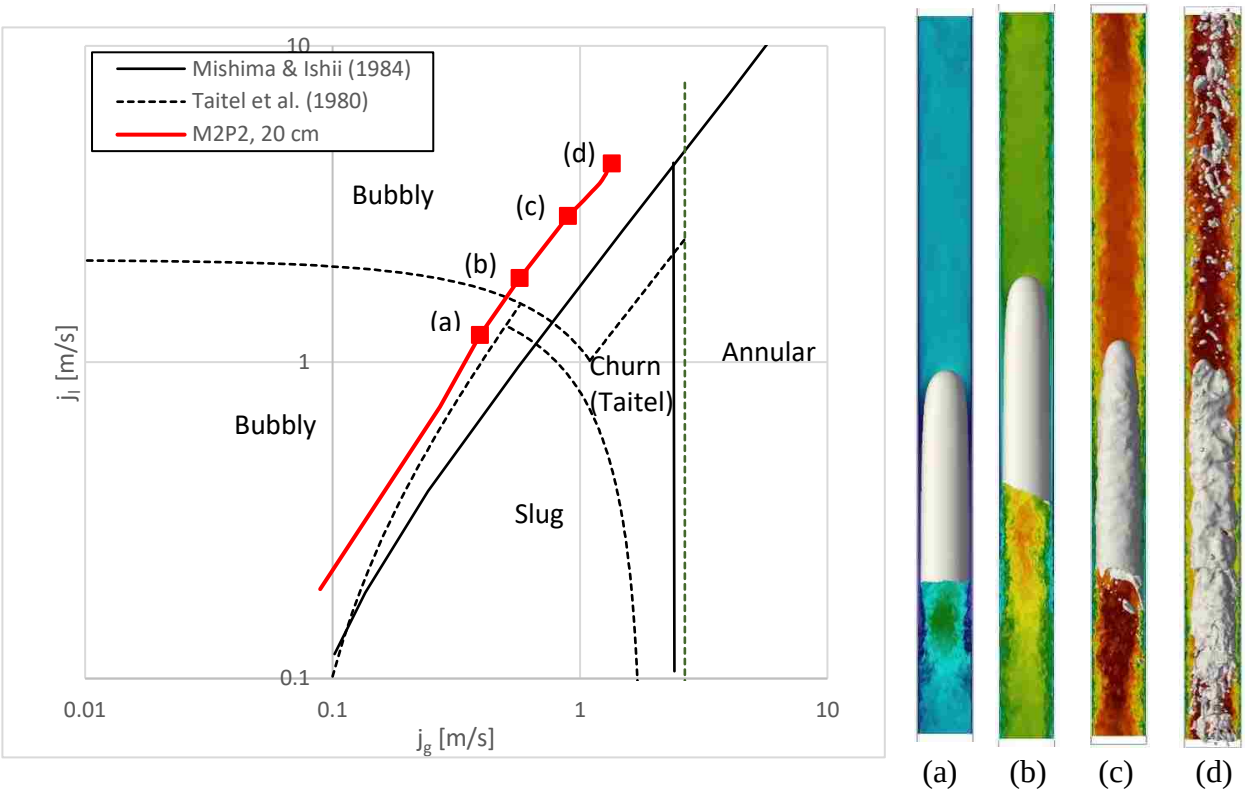

Figure 6.9: Comparison of the computational superficial velocity data from the 20% forward simulation to the Mishima & Ishii *[24]* and Taitel et al. *[27]* flow regime maps. Images from select moments are also shown.

As is immediately clear when comparing the images to the map, the initial regime does not match what was predicted by the map. The flow was predicted to be in the bubbly flow regime. This is because the initial slug flow condition was artificially forced in the simulation by initializing the gas as a single bubble. However, as the flow accelerates, the transition only occurs after the superficial velocities cross into the region where Taitel et al. reason turbulent dispersion forces are dominant in producing bubbly flow by preventing the bubbles from coalescing to form larger structures. Taitel et al.'s hypothesis already suggests that turbulence will play a critical role in the breakup of this bubble. As Figure 6.9 shows, despite the flow accelerating, no bubbles shear off the tail before interfacial perturbations form. The breakup only begins once eddies begin to collide with the interface. However, due to the required development time for the turbulence, the breakup begins well after the superficial velocities have crossed the line defined by Taitel et al.

The turbulence that is colliding with the nose of the bubble is very close to a typical turbulent TKE profile (see Figure 6.10). Therefore, this simulation is successful in isolating the effect of wall generated turbulence on the breakup process.

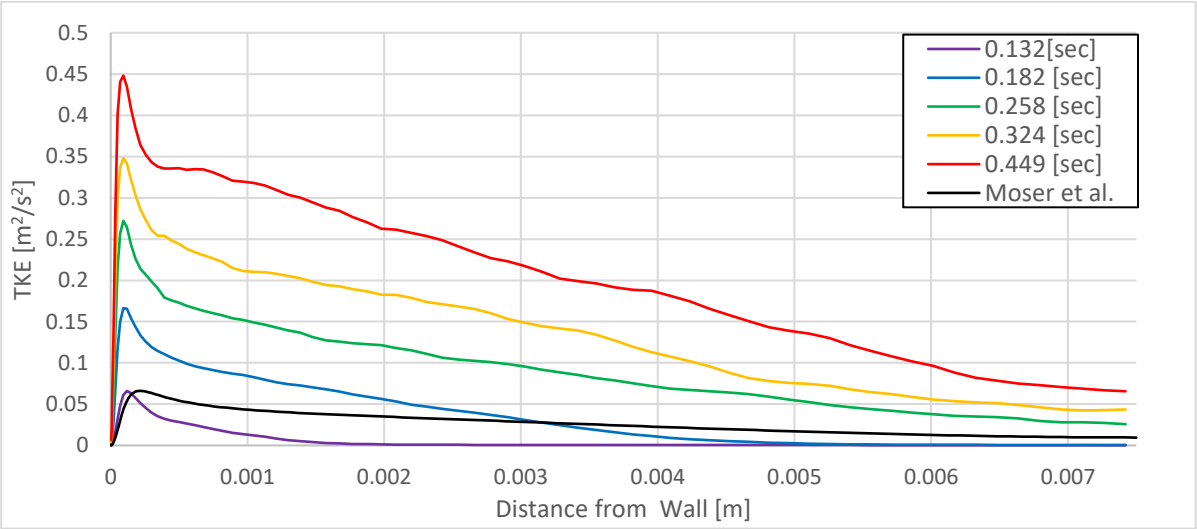

Figure 6.10: The development of the TKE in the 20% forward simulation. Data from Moser *[2]* et al. is included for reference to a typical turbulent TKE profile.

Figure 6.10 shows that Moser et al. found the TKE in the bulk to be larger than what is measured in these simulations. The reason for this is attributed to the transition simulations forming a developing flow, meaning the TKE is continuously diffusing from the wall to the bulk, making this low bulk TKE expected. It is possible to see in the red line of Figure 6.10 that the TKE slightly inward from the peak plateaus before decreasing towards the center. This is likely a bubble-induced contribution to the TKE. At this point in the simulation small bubbles are occupying the liquid slug, at about a 3-4% void fraction. These bubbles are relatively small and will therefore collect near the wall, contributing to the TKE near the wall. As this wall concentrated energetic turbulence collides with the Taylor bubble, interfacial perturbations are formed. Instantaneous bubble interface profiles are shown in Figure 6.11.

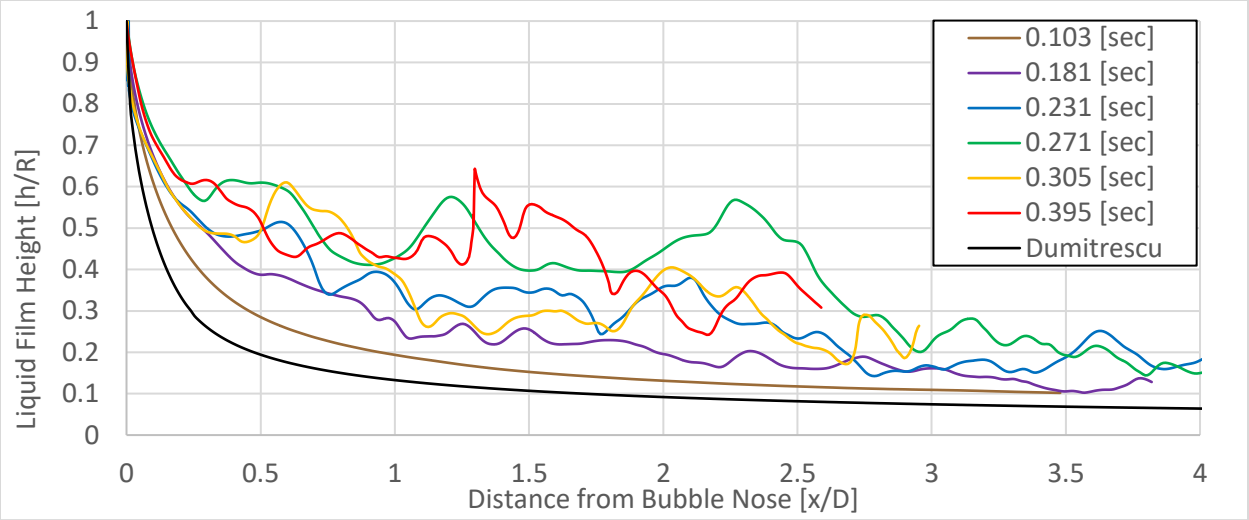

Figure 6.11: Instantaneous interface shapes for the 20% void fraction simulation. Dumitrescu's *[42]* profile is included for reference.

Due to the strongest turbulence being close to the wall, these perturbations are not able to break the bubble up by bridging the full pipe diameter. Instead, the perturbations propagate down the tail of the bubble and cause small bubbles to shear off the tail. The requirement for turbulence to induce the shearing off of bubbles at the tail of a Taylor bubble is consistent with what Delfos et al. [109] observed experimentally. In the work, for Taylor bubbles in laminar flow, no bubbles would shear off the wake until a certain length of Taylor bubble was reached. After this critical length, the liquid film would naturally become turbulent, causing interfacial perturbations.

This tail shearing process is significantly slower in completely breaking up the Taylor bubble and no simulation reached an instance in time when the Taylor bubble's body did not exist. However, the simulation was considered to be approaching bubbly flow, and would likely have reached it given enough computational resources to continue this shearing off process. The interfacial area concentration information, Figure 6.12, shows that interfaces are not most concentrated in the center of the pipe like they were in the churn-turbulent flow.

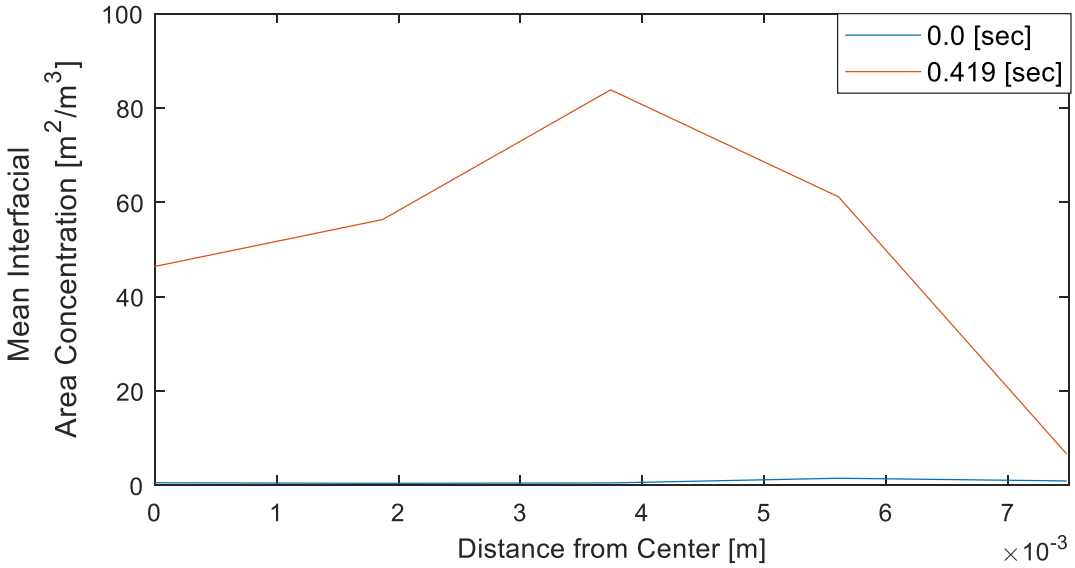

Figure 6.12: Interfacial area concentration information for slug flow (blue line) and highly bubbly slug flow (red line) in the 20% void fraction flow.

This wall shifted interfacial area peak is consistent with bubbly flow behavior. Small bubbles collect near the wall due to the lift force acting on them. In this flow the bubbles are slightly further from the wall than would be expected, but this can be explained by the recirculation of bubbles in the wake of the Taylor bubble as it breaks up. This recirculation flattens the distribution of bubbles and only bubbles that escape the wake and enter the slug will be able to reach the wall. Additionally, a significant amount of interfacial area is still associated with the remaining body of the Taylor bubble, whose interface is located at around 4 or 5 mm from the wall. The Sauter mean diameter, Figure 6.13, also shows that close to the wall, mostly small bubbles exist and in the bulk larger bubbles exist.

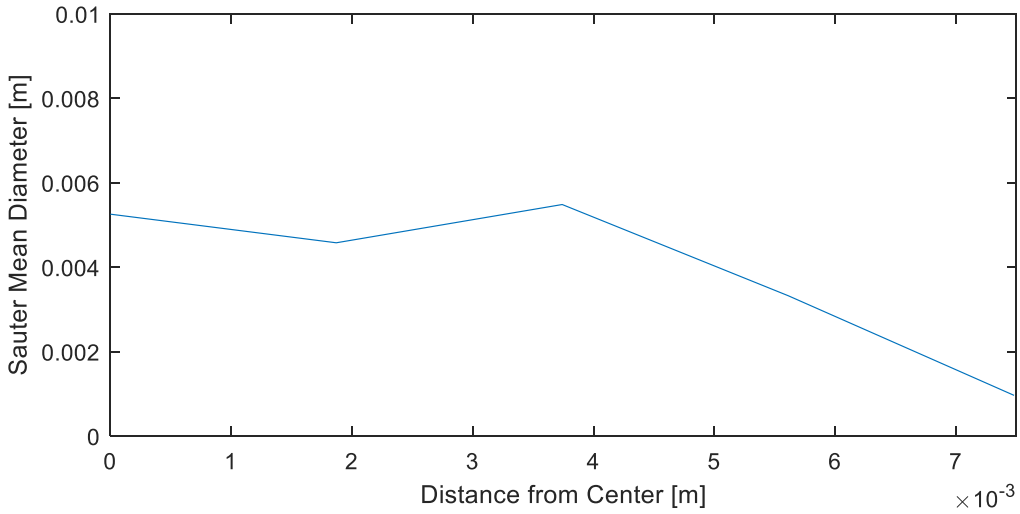

Figure 6.13: Sauter mean diameter information for bubbly slug flow in the 20% void fraction flow (0.419 sec).

The Sauter mean diameter distribution in the liquid slug, Figure 6.14 (left), shows that the bubbles in the slug are smaller than the whole domain distribution. Additionally, the interfacial area concentration in the liquid slug, Figure 6.14 (right), has a prominent peak close to the wall, as would be expected for bubbly flow.

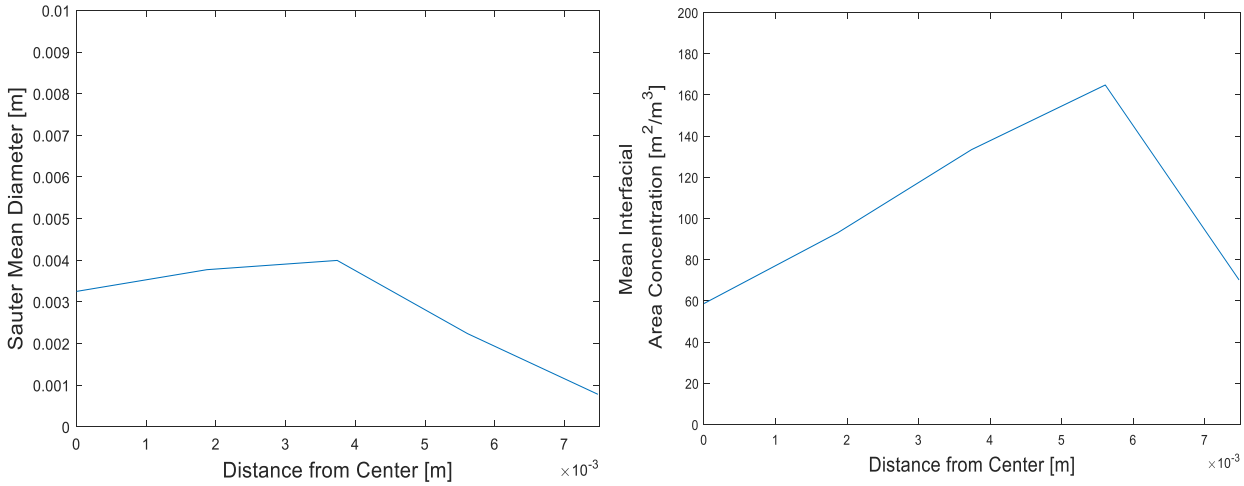

Figure 6.14: Sauter mean diameter (left) and Interfacial area concentration (right) distributions for the liquid slug only in the bubbly slug flow condition at 0.419 sec in the 20% void fraction flow.

Together, these profiles, in addition to visual analysis, suggest that the flow is approaching bubbly flow as breakup continues.

6.2.2 Decelerating Flows

This simulation demonstrates the recombination of the bubbles that sheared off the Taylor bubble to form a single bubble and return to slug flow. The flow was already fully turbulent from time zero and by the end of the simulation almost all turbulence had decayed and smooth slug flow existed. Superficial velocities for this flow are shown in Figure 6.15.

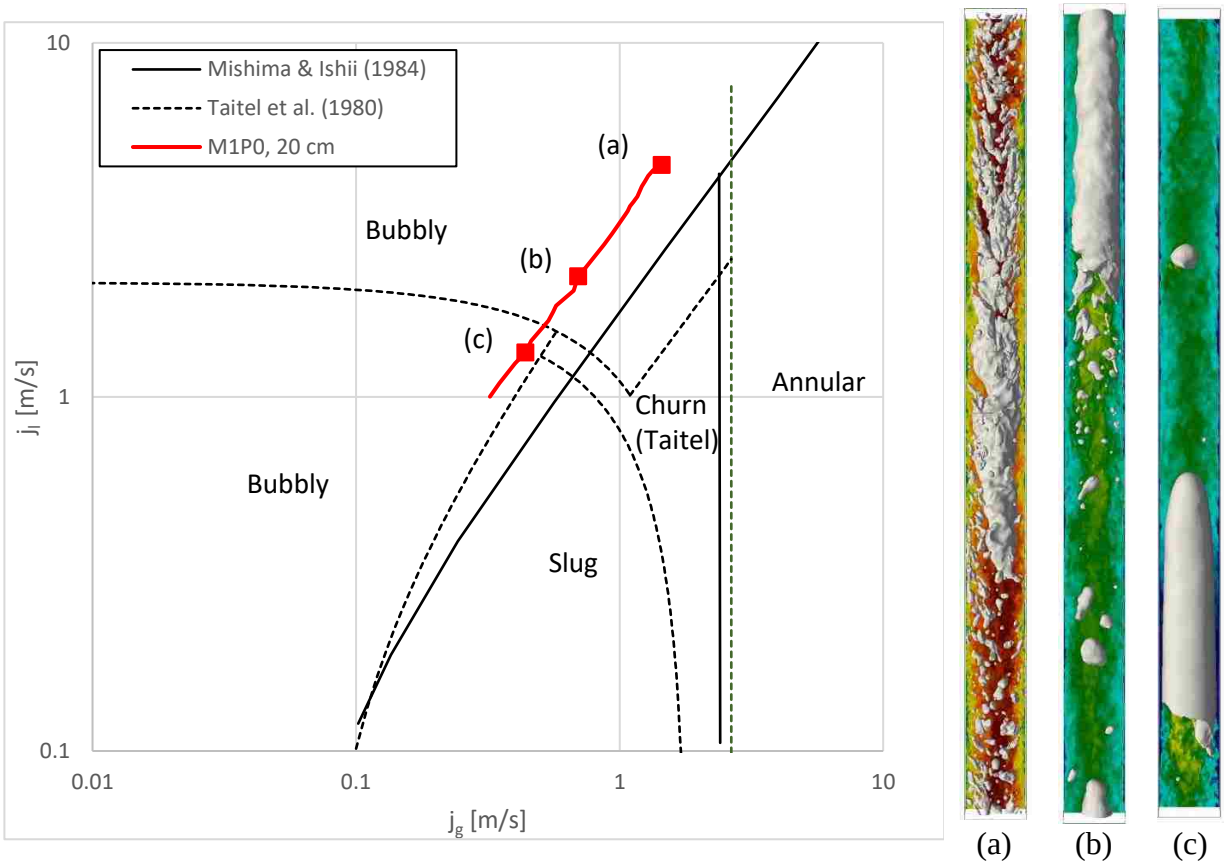

Figure 6.15: Comparison of the computational superficial velocity data from the 20% reverse simulation to the Mishima & Ishii *[24]* and Taitel et al. *[27]* flow regime maps. Images from select moment are also shown

The superficial velocity progression is very similar to the forward transition and follows an approximately consistent rate for both phases. The bubbles slowly recoalesce over a long period of time, tenths of seconds, and the interface of the Taylor bubble becomes smoother as the turbulence decays. The competition between breakup and coalescence still exists, but coalescence becomes dominant because the TKE is decaying. Interestingly, the bubble shearing nearly

completely stops once crossing the Taitel et al. line distinguishing between bubbly flow where turbulent dispersions forces are dominating. This is shown in Figure 6.15 (b) and (c). Since the coalescence process is gradual and continuous, there is no point in time where the gas flow rate diverges from the deceleration like in the 40% flows.

The TKE in this flow, shown in Figure 6.16, is also relatively predictable.

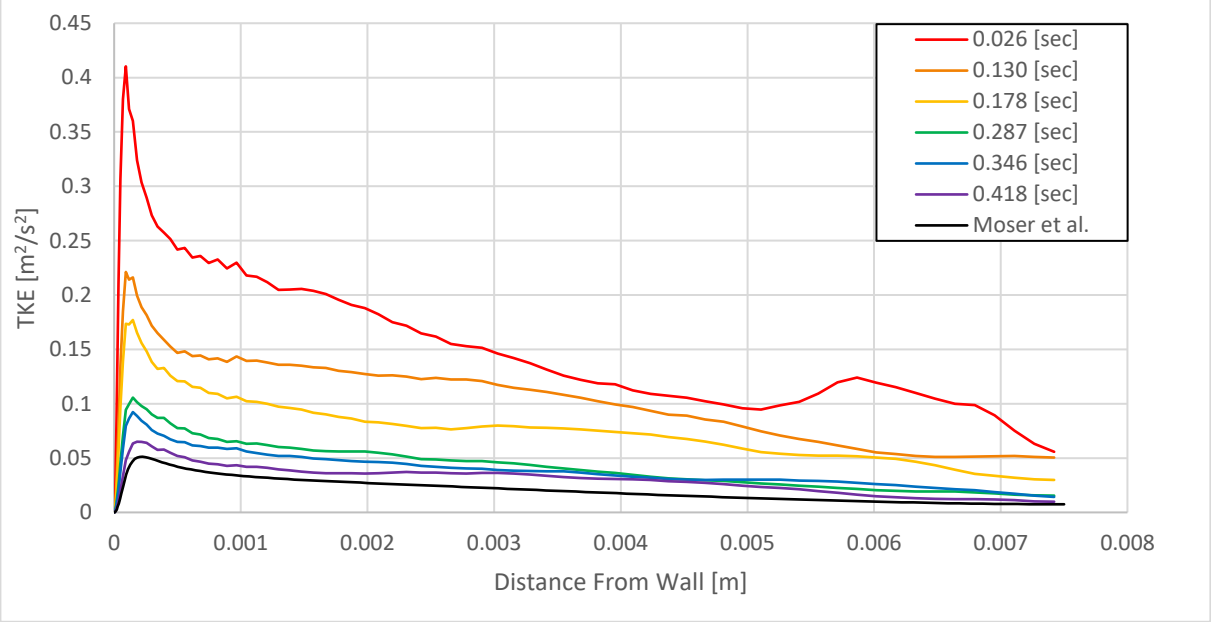

Figure 6.16: TKE plots for different times in the 20% decelerating flow. Data from Moser et al. is also included for reference.

The TKE level decreases over time and maintains its similarity in shape to TKE in a single phase flow. The bubble becomes smooth before the turbulence has fully decayed, showing how the surface tension force is strong enough to completely damp low TKE before any perturbations in the interface reach the tail to cause shearing. When the liquid slug is still turbulent but the TKE is too, no bubble shearing at the tail occurs because the perturbations settle before reaching the tail of the bubble. Instead, the bubble nose slightly elongates as the liquid film becomes thicker from the turbulence entering the film.

6.3 Mechanisms for Transition

This section will describe the mechanisms for the forward and reverse transitions and compare how they are distinct. The key feature of each mechanism is the importance of turbulent kinetic energy. TKE was necessary for the flow regime transition to occur in all forward simulations and its existence in the reverse simulations determined the coalescence rate and interface distribution. Two mechanisms have been identified for the transition out of slug flow:

- In the 10 cm long pipe the flow accelerates and the wake of the Taylor bubble begins to extend until it reaches the nose of the trailing bubble. The turbulence in the liquid slug is dramatically increased by the contribution from the wake. This turbulence collides with the Taylor bubble nose, causing instabilities to form on the interface. If the TKE is high enough, these instabilities grow to bridge the diameter of the pipe, breaking up the Taylor bubble. The void then quickly distributes itself along the length of the pipe until a uniform axial profile is reached and churn-turbulent flow exists. This mechanism requires an inward shifted TKE peak that is very energetic.
- In the 20 cm long pipe, turbulence in the liquid slug collides with the Taylor bubble and forms interfacial instabilities. The perturbations propagate down the bubble until they reach the tail. The perturbations are smaller than the diameter of the pipe and do not bridge the width of the bubble. The shear force of the liquid film on the interface continues to pull the perturbation until it detaches from the bubble entirely, depositing the new daughter bubble in the wake of the Taylor bubble. When sufficient energy is being transferred to the interface, the shearing of bubbles at the tail becomes rapid enough to diminish the volume of the Taylor bubble, causing the void to be evenly distributed along the length of the pipe, forming bubbly flow. This process

is similar to what was discussed by Delfos [110] and Delfos et al. [109]. The TKE profile observed during this mechanism was close to what is expected for single-phase turbulent flow. Both processes rely on turbulence to initiate the transition, and it is clear that the void fraction plays an important role when determining how the interfacial structure develops over time. The distinction is the liquid slug's turbulence in the 10 cm long pipe took on a different distribution due to the wake's significant contribution. In the 20 cm long pipe the liquid slug is long enough to develop a more typical turbulent pipe flow TKE profile.

In contrast, the reverse simulations begin in fully turbulent flows. In order for a reverse transition to occur, this turbulence needed to decay to allow coalescence to become dominant over breakup. Based on a visual analysis of the simulations, a flow regime transition is not always a directly reversible process. As the 20 cm long pipe flow slowed, the coalescence on the bubble closely resembled the breakup process in reverse. However, the 10 cm long pipe's deceleration was distinctly different from the acceleration. These mechanisms for reverse transition are described as follows:

- As the flow in the 10 cm long pipe decelerates, the small bubbles quickly coalesce with the larger structures in the churn-turbulent regime. The turbulence rapidly decays in the center of the pipe. The fast decay of liquid turbulence in the center is mostly due to the lack of liquid in the center due to the collection of gas there. The turbulence that remains on the periphery of the pipe continues to decay but at a slower rate. This is seen by the smooth interface along the gas core that has formed due to the coalescence. The surface tension is not yet able to overcome the turbulence close to the wall and the gas is pushed to the center, forming a column of gas. A transition to annular flow has occurred. Liquid waves and ligaments form and periodically make the gas core discontinuous, forming what seems to be an elongated Taylor bubble.

However, the new nose that was created is quickly pulled back into the gas core by the low pressure zone in front of it, making it continuous again. Eventually, the turbulence on the periphery can no longer continue to push the gas core away from the wall, causing the gas column's radius to grow. Eventually, the liquid bridges the pipe, forming a Taylor bubble and concluding the deceleration in the slug regime. This simulation underwent two transitions, churn-turbulent to annular and then annular to slug. This transition path is not described by flow regime maps. Transitions from churn-turbulent to annular are not known to be caused by a decrease in flow rates. Typically, annular is considered to be a high flow rate regime.

- In the 20 cm long pipe the deceleration closely resembled the forward simulation. As the flow began to slow the breakup rate at the tail from interfacial shearing also slowed. Recoalescence of bubbles at the tail (from gas entrained in the wake colliding with the tail) and in the film (from bubbles in the liquid slug entering the film) began to overcome the breakup and the Taylor bubble grew in size. As the turbulence decayed further, the interfacial perturbations disappeared, ceasing the shearing of bubbles off the tail. The simulation was concluded with a steady slug flow regime.

In both cases, the reverse mechanisms are similar to their forward counterparts in that the time scales for the formation of a new regime. The 40% void fraction flow suddenly forms annular and eventually slug flow once a nose forms. The 20% void fraction flow gradually coalesces the smaller bubbles to form a single Taylor bubble. Additionally, similar to the forward transitions, turbulence was important to the interfacial structures that were formed.

The void fraction played an important role with how the turbulence interacted with the interface. In the 20 cm long pipe the void was dispersed sparsely enough to allow the largest bubble to continue to accumulate volume and grow into one Taylor bubble. As TKE entering the liquid film

weakened, the bubble could grow in radius and shorten in length. Instead of a Taylor bubble forming in the 10 cm long pipe, a gas core was formed because the TKE in the potential film was still too strong for surface tension to overcome. Only when the TKE decayed enough could the bubble widen and form a nose and tail.

Figure 6.17 shows the progression of interfacial area and superficial velocities for each pair of forward and reverse simulations.

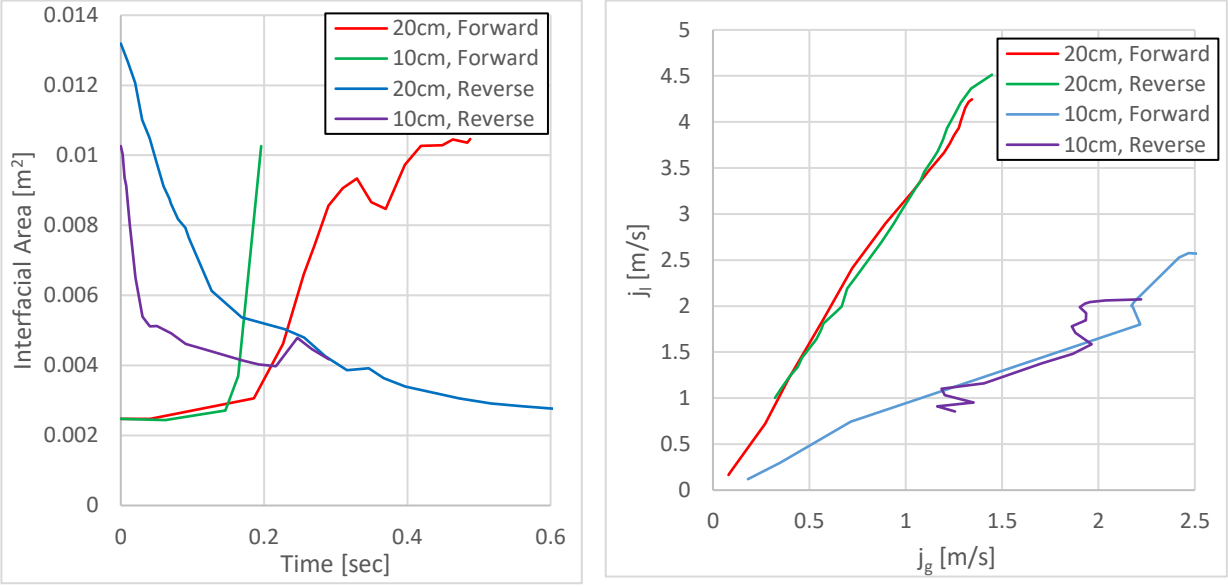

Figure 6.17: Interfacial area and superficial velocity information.

The forward and reverse 20% void fraction simulations appear nearly identical in these plots. Both are characterized by nearly identical superficial velocity paths and the interfacial area each have one dramatic rise/fall whose conclusion matches the interfacial area of the other's beginning. The interfacial shearing mechanism appears to be a reversible process. The bubbles simply coalesce once the turbulence begins to decay. The interfacial area in the 40% void cases are clearly different at the initiation of the acceleration and conclusion of the deceleration. The superficial velocities also do not follow identical paths and diverge in two instances. These differences are indicative of the different flow regime paths taken in each flow and that the interfacial instability mechanism is not reversible. This irreversibility is likely due to the lack of large TKE in the bulk of the flow to

segment the gas core. In the forward transition the TKE from the wake provided this centered TKE peak, but in the reverse the centered gas core and decay of turbulence lead to no large centered TKE peak (see Figure 6.8). Therefore, the gas core remains stable and forms annular flow as the interface smoothens and coalescence occurs.

6.3.1 Interfacial Instability

The interfacial instability mechanism occurs at the nose of the bubble and leads to breakup due to the Taylor bubble being segmented by the large interface waves that are on the scale of the pipe diameter. Due to the center shifted TKE peak, interfacial waves, or instabilities, are allowed to grow until they collapse the bubble. This process is very sudden, taking only 0.03 seconds, because a large amount of energy is being transferred to the main body of the bubble very suddenly (once the wake extends to the bubble). The large energy transfer at the nose implies that the turbulence in this region should be decaying relatively quickly, compared to the rest of the liquid film. Using the Q-criterion to visualize the turbulence would help back up this claim. Q-criterion is a means of visualizing eddies and is defined by the following [111].

$$Q = \frac{1}{2}(|\boldsymbol{\Omega}|^2 - |\boldsymbol{S}|^{\mathbf{2}}) = \frac{1}{2}\left(\left(\frac{\partial u}{\partial y}\frac{\partial v}{\partial x} + \frac{\partial u}{\partial z}\frac{\partial w}{\partial x} + \frac{\partial v}{\partial z}\frac{\partial w}{\partial y}\right) - \left(\left(\frac{\partial u}{\partial x}\right)^2 + \left(\frac{\partial v}{\partial x}\right)^2 + \left(\frac{\partial w}{\partial x}\right)^2\right)\right) \quad (6.1)$$

$\boldsymbol{\Omega}$ is the vorticity tensor and $\boldsymbol{S}$ rate of strain tensor. To support the hypothesis that this mechanism drives breakup from the nose, the Q-criterion should show many eddies at the nose of the bubble, followed by a quick decay into the liquid film. Figure 6.18 (top) shows exactly what is expected.

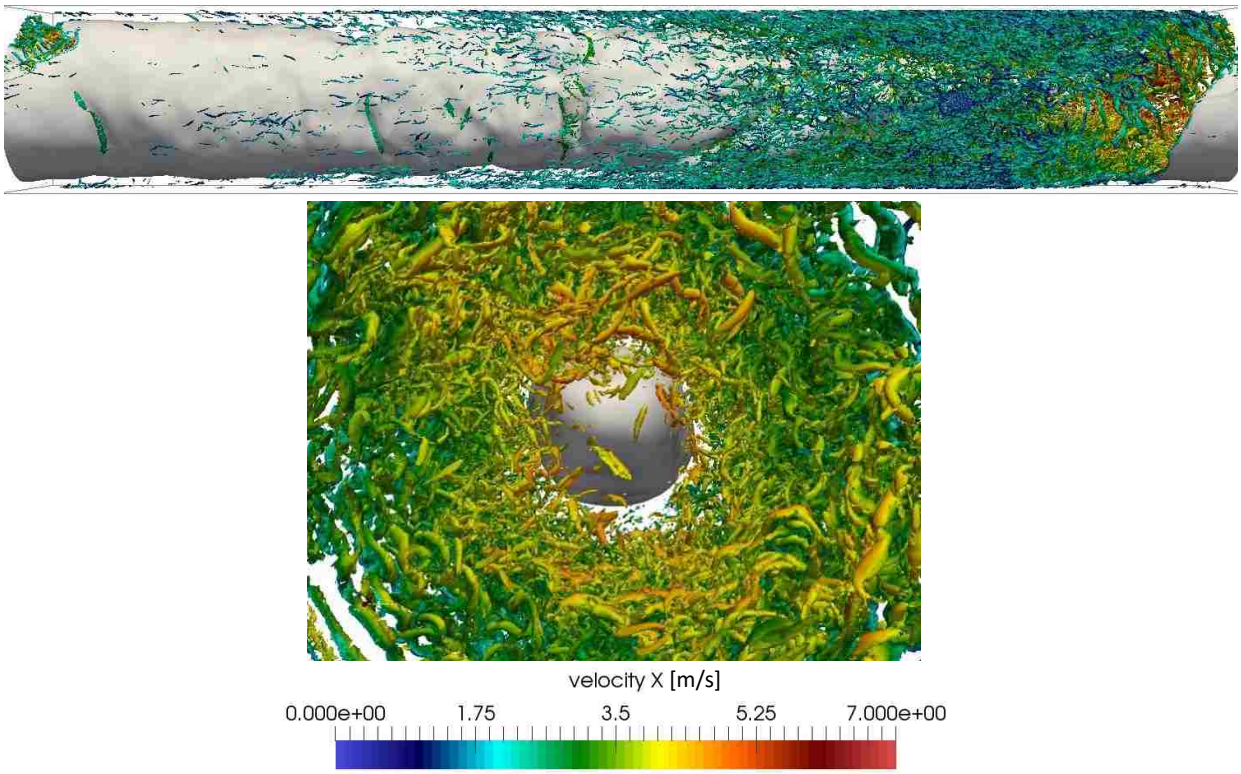

Figure 6.18: Q-criterion iso-contour visualization in the 10 cm long pipe for the same instance in time. The contours are colored by the streamwise velocity.

There is a dramatic decrease in the number of eddies seen in the liquid film compared to those in the wake and near the nose of the bubble. The conclusion is that the nose of the bubble is absorbing the TKE, which provides the energy to cause the interfacial instabilities, decaying the turbulence and breaking up the bubble. Figure 6.18 (bottom) also reinforces the inward shifted TKE peak, visible from the many small (high energy) eddies that exist far from the wall.

It is reasonable to conclude the TKE provides the energy for the breakup of the bubble. However, a vehicle for the transport of energy from the liquid TKE to the interface has not been proposed. Looking at a single small piece of interface, a velocity gradient exists between the liquid and the interface. Very close to the interface the liquid and interface have the same velocity, and the velocity gradient can be broken into interface parallel and interface perpendicular components. The perpendicular components manifests in movement of the interface and the parallel component

is the interfacial shear. As an eddy approaches and then collides with the interface, the rotation and movements of the liquid causes the velocity gradient to change. The change in the velocity gradient knocks the surface tension and velocity gradient induced force out of balance. The surface tension tries to regain balance by deforming the bubble or creating smaller bubbles with higher curvature and therefore larger surface tension forces. This deformation and breakup takes energy, the exact quantity of which is dependent on the surface tension. This energy comes from the eddy, thereby decaying the TKE. Following this logic, the eddy transfers its energy to the interface through the interfacial shear. To help confirm this hypothesis, the interfacial shear information was extracted from the 40% void fraction forward simulation at different time steps. This interfacial shear information is presented in Figure 6.19.

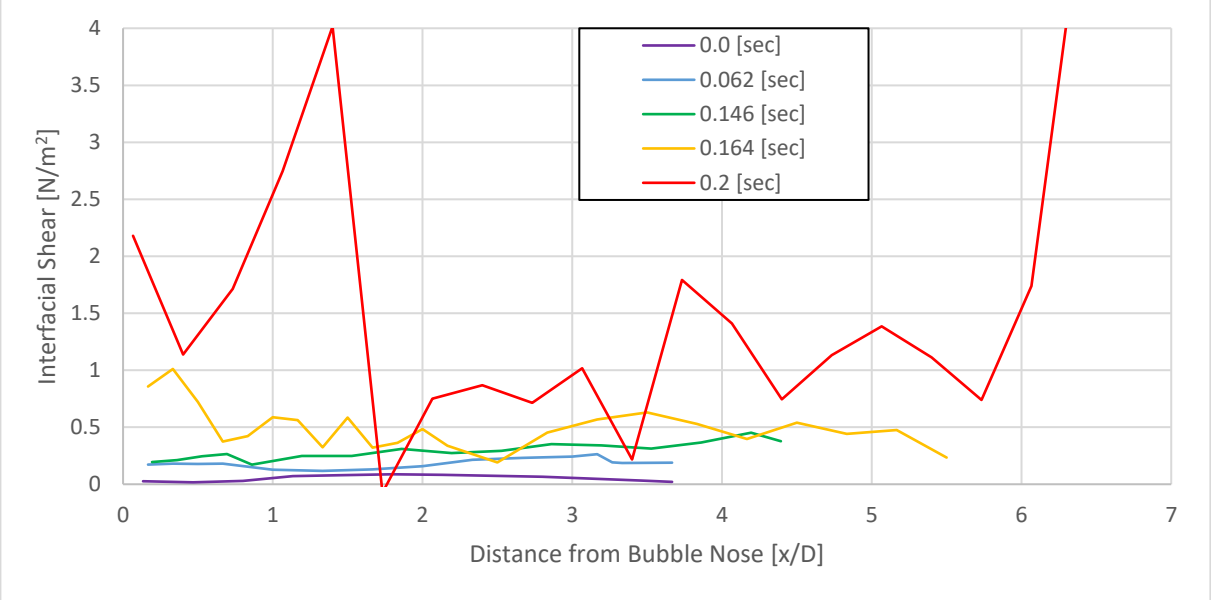

Figure 6.19: Interfacial shear information for the interfacial instability mechanism in forward simulation.

In Figure 6.19 the yellow line corresponds to a time just before the flow transitions and the red line is when the flow is in the churn-turbulent regime. The interfacial shear begins low and smooth across the length of the bubbles. However, the shear quickly increases and magnitude of the shear begins to vary along the length of the bubble. These variations are caused by the turbulence

entering the liquid film, forming different gradients at the interface. To better understand how the interfacial shear is changing relative to the TKE and interfacial area, they are plotted over time in Figure 6.20.

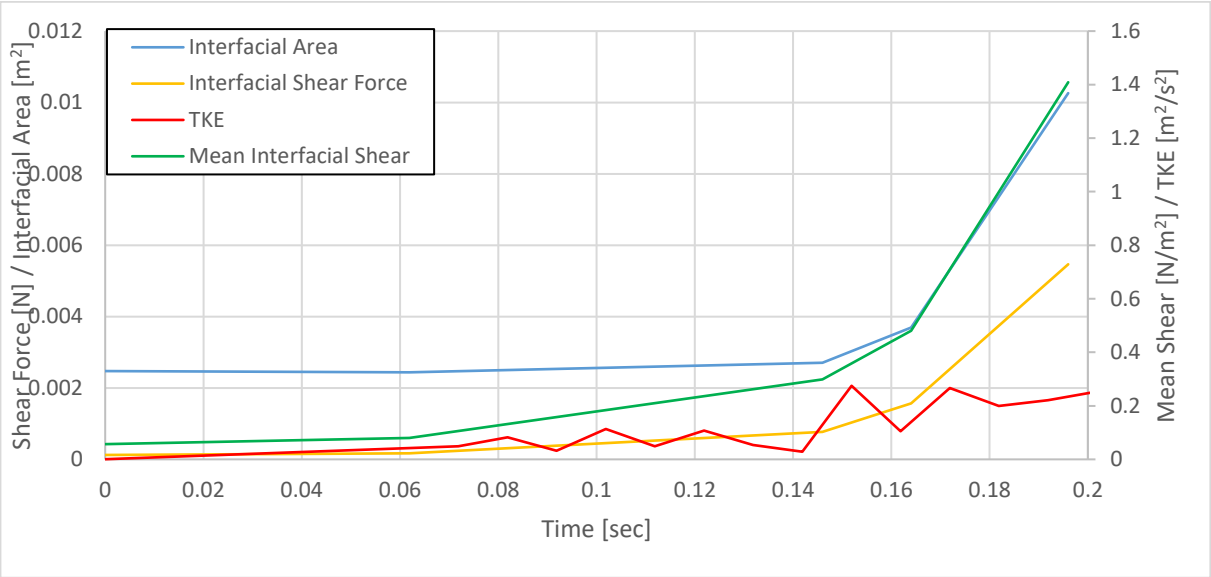

Figure 6.20: Numerical data regarding the interface and TKE for the interfacial instability mechanism in the forward transition.

Note that in Figure 6.20 the interfacial shear is both area averaged and integrated over the Taylor bubble area to calculate a mean interfacial shear and total interfacial shear force (defined below), respectively.

$$F_{\tau_i} = \oint \tau_i dA \qquad (6.2)$$

F_{τ_i} is the interfacial shear force and τ_i is the interfacial shear stress. The interfacial shear and interfacial area follow each other nearly perfectly and the TKE also increases during the transition. The increase in TKE stalls once the interfacial area and shear values begin their sharp increase. Even though the flow continues to accelerate, implying the TKE would also increase, the TKE plateaus. This may be because the TKE is continually donating energy to the interface to cause breakup and form new interfaces, via the interfacial shear. The trends observed in Figure 6.20 back the hypothesis that energy is being transferred from TKE to the interface via the interfacial shear.

The reverse simulation for this mechanism also demonstrates the relationship between the interfacial area and shear. First, Figure 6.21 shows the interfacial shear during the simulation.

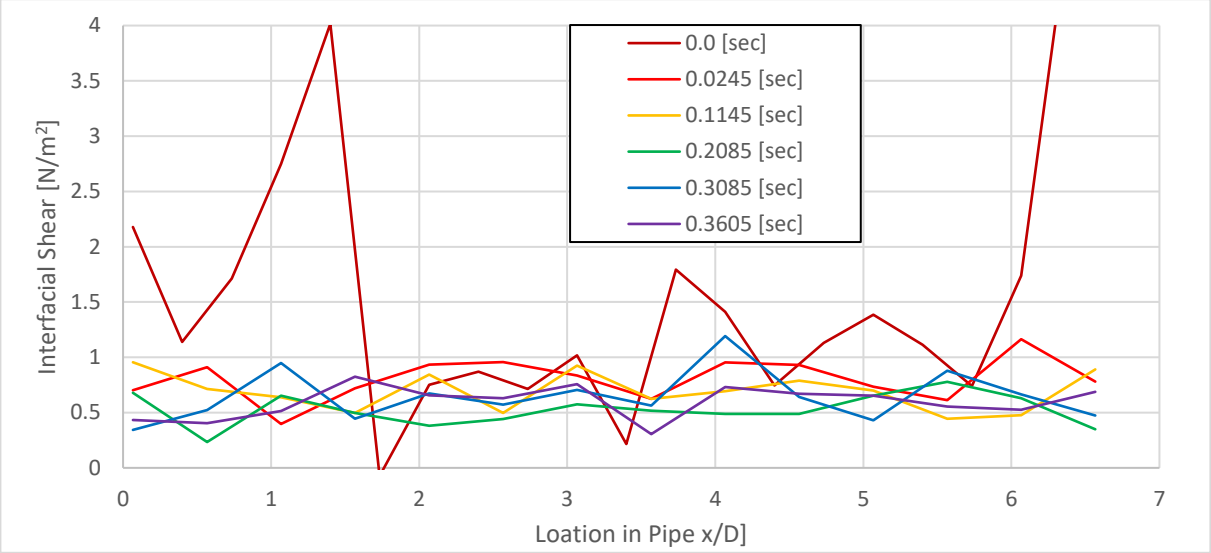

Figure 6.21: Interfacial shear information for the interfacial instability mechanism in reverse simulation.

The interfacial shear quickly decreases but reaches an approximately constant value once annular flow is formed. Figure 6.22 shows that as this plateau in interfacial shear is occurring, a plateau in interfacial area also occurs.

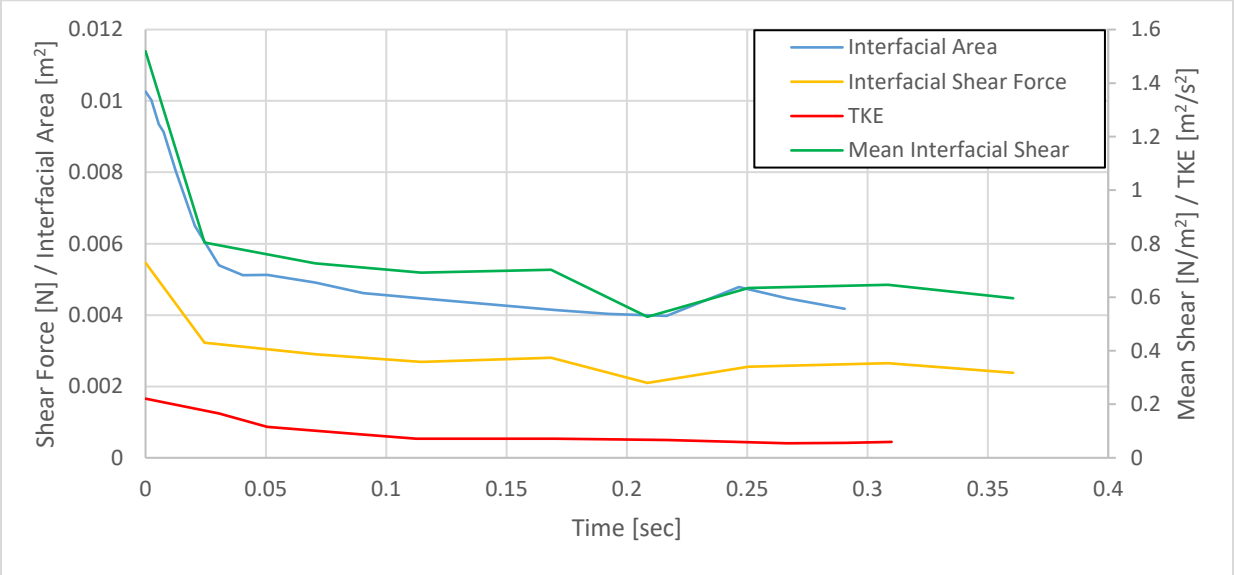

Figure 6.22: Numerical data regarding the interface and TKE for the interfacial instability mechanism in the reverse transition.

Comparing to Figure 6.20 makes it clear that the plateau does not occur at the same interfacial shear, area, or TKE values that the forward transition started at. This suggests a new condition has been reached, showing an asymmetry in time. The reason for this time asymmetry is possibly the source of the turbulence in the flow. In the forward transition the primary source was the wake, but in the reverse there is no wake, making the primary source the wall. The wall generated turbulence is closer to the turbulence observed in the bubble shearing mechanism. However, there is no tail to shear bubbles off so the turbulence promotes a thicker liquid film and extends the gas length of the pipe. The sustained high TKE and interfacial shear also explains why the flow can support a gas core for so long. These forces continue to promote more interfaces and push the interfaces away from the concentration of TKE, which is at the wall.

6.3.2 Bubble Shearing

The bubble shear mechanism occurs at the tail of the bubble, where the shearing is pulling bubbles off the liquid. As discussed, this shearing off of bubbles occurs because turbulence in the liquid film is transferring energy to the interface that manifest as interfacial disturbances, or perturbations. Presumably, the transfer of energy from the turbulence, to the interface does not occur suddenly in liquid film, but rather gradually. By this logic, the visualization of the Q-criterion should show that eddies disappear at approximately an even rate in the film. Since the decay of turbulence in the film is a gradual process whose culmination comes at the tail of the bubble, the Q-criterion should show the eddies evenly diminish along the length of the bubble. Figure 6.23 (top) shows that this expectation is consistent with what is observed in the simulation.

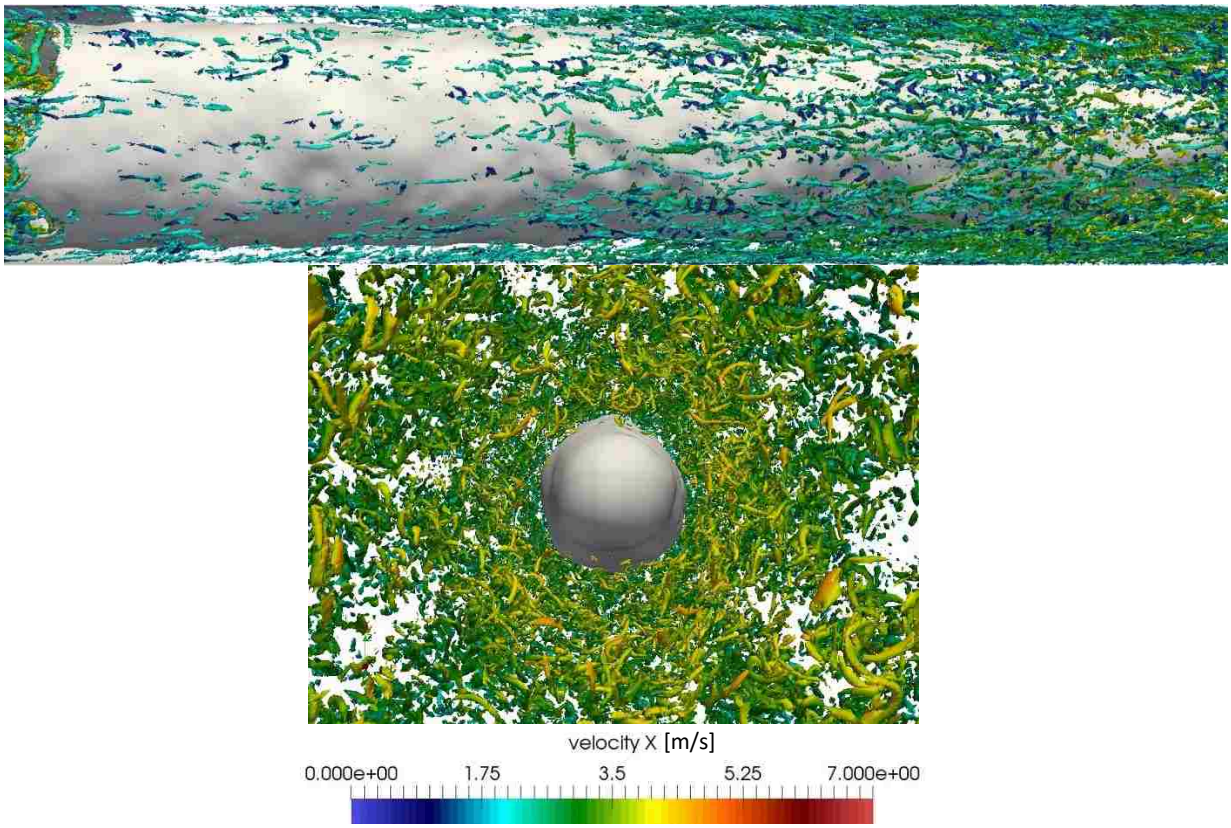

Figure 6.23: Q-criterion iso-contour visualization from a side and front view of the same instance in time. The contours are colored by the streamwise velocity.

Figure 6.23 (bottom) also shows the Q-criterion from a front side view of the bubble to further reinforce the turbulence's distribution, which is peaked close to the wall. The turbulence's small interfacial perturbations force the transition to be bottlenecked by how quickly bubbles can be torn off the tail of the Taylor bubble. Understandably, this mechanism takes significantly longer, upwards of 0.3 seconds.

The next concern is the mechanism(s) that transfer the energy from the turbulence, to the interface. The hypothesis is the interfacial shear drives this energy transfer. For this mechanism, if this hypothesis is correct, the interfacial shear should be approximately equal along the entire

liquid film length at any given instance in time when the shearing is occurring. Figure 6.24 shows that this is true once turbulence does start entering the liquid film.

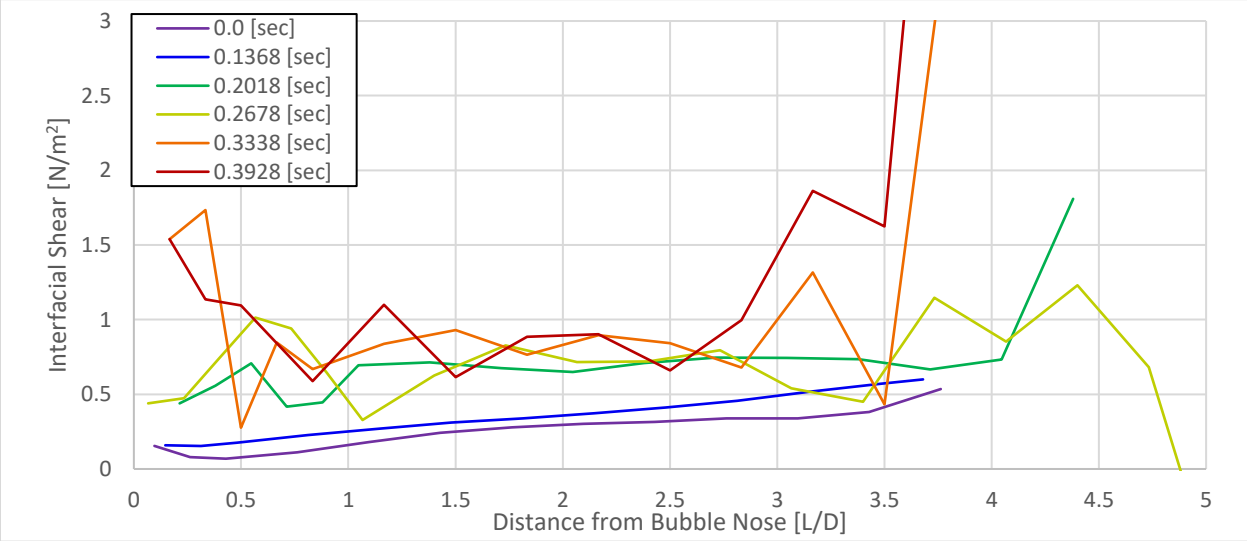

Figure 6.24: Interfacial shear along the bubble in the bubble shearing mechanism.

Random turbulent fluctuations cause instantaneous peaks and valleys, but no obvious sustained local maxima or minima along the length of the bubble. It is difficult to discern due to the fluctuations, but the mean interfacial shear is continuously increasing as the flow accelerates. This is shown in Figure 6.25, which provides the calculated mean interfacial shear, total interfacial shear force, mean TKE, and total interfacial area.

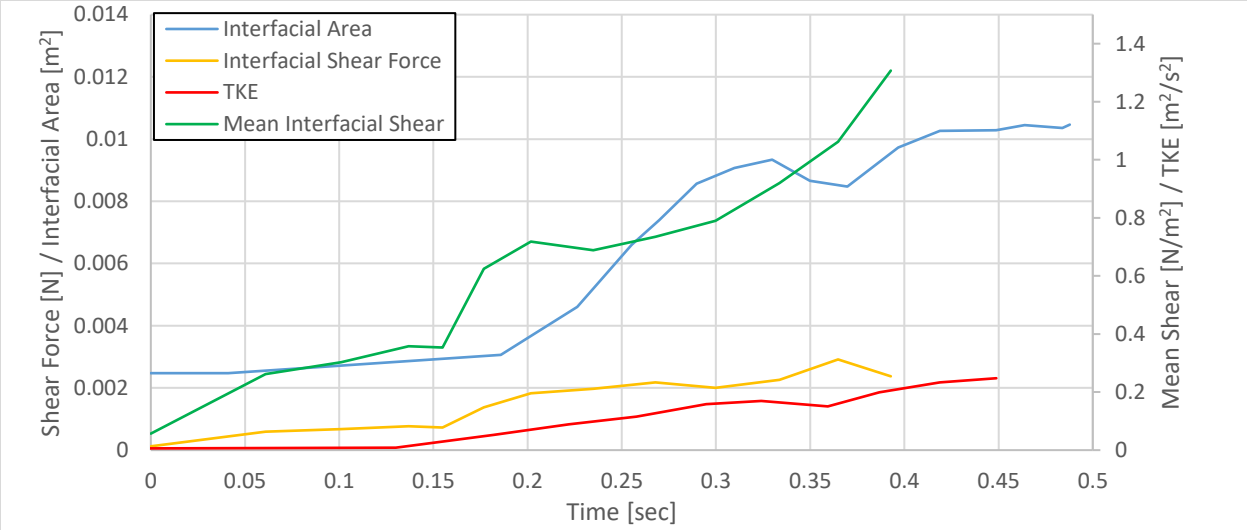

Figure 6.25: Numerical data regarding the interface and TKE for the bubble shearing mechanism in the forward transition.

The constant growth of TKE leads to more energetic eddies colliding with the bubble, prompting larger and larger shearing. However, despite the interfacial shear increasing, the total shear force on the bubble does not continue increasing. This is seen between 0.25 and 0.4 seconds where the shear force remains approximately constant. The breakup of the Taylor bubble means the bubble is getting shorter, providing the interfacial shear with a smaller working area. At a certain point in time, the energy transfer through the shear force becomes approximately constant while the interfacial area and TKE still increases. This suggests that TKE must be committed to not only breaking up the bubble but also preventing recoalescence. If the bubble absorbed all the turbulence then the bubbles would simply coalesce to either form a new Taylor bubble or conserve the already existing one. The turbulent dispersion forces in the liquid slug are critical to dispersing the bubble, and as more bubbles exist in the slug, the stronger these forces must be to continue the flow regime transition. Additionally, during this time period of constant interfacial shear force, the interfacial area generation slows or even plateaus. The plateau suggests that total interfacial shear force is a better predictor for the breakup rate of the Taylor bubble than the shear force. The TKE can only commit so much energy to the Taylor bubble given its shorter length and to preventing the

coalescence of smaller bubbles. Therefore, during this time period the breakup of the Taylor bubble, which has reached a constant rate due to the constant shear force, is matched by the coalescence of smaller bubbles. This balance of breakup and coalescence maintains a constant interfacial area. The interfacial shear and interfacial shear force need to increase further before additional breakup can occur. Finally, when comparing the final conditions for both the forward transitions, the interfacial area and mean interfacial shear are approximately equal despite the flows visually being completely different. This reinforces the interfacial shear's role in breaking apart the bubble.

Unfortunately, the simulation was approaching its final flow rates, meaning the TKE would not increase further. Therefore, a new pressure gradient was chosen to begin a new acceleration time period. Due to the limited computational resources this simulation was run for only 0.0225 seconds. However, during this short time period, because of how fast the flow is, just over one half liquid flow through of the 20 cm long pipe is achieved. However, during this time period the TKE increased to 0.305 m^2/s^2 (23.1% larger) and the interfacial shear decreased to 0.977 N/m^2 (25.3% smaller). The total shear force remained approximately constant at the plateau value observed in Figure 6.25 (0.0018 N). This results in the interfacial area being 0.0121 m^2, a 16.2% increase. This short additional pressure gradient jump provides further evidence to the competition between breakup and coalescence that is determined by the transfer of energy from liquid to gas by the interfacial shear. Additionally, the numbers also bolster the idea that there is a maximum energy transfer rate that is capable across the interface. Even though the TKE significantly increased, the interfacial shear decreased, meaning less energy is being transferred to the interface. Despite this the interfacial area still increased because the shear is still sufficient to breakup the bubble and the additional turbulence can support more new interfaces.

The reverse simulation of the interfacial shearing mechanism follows a very similar pattern to the forward. Initially, the interfacial shear profiles, Figure 6.26, are chaotic due to the turbulence and even energy transfer across the length of the Taylor bubble.

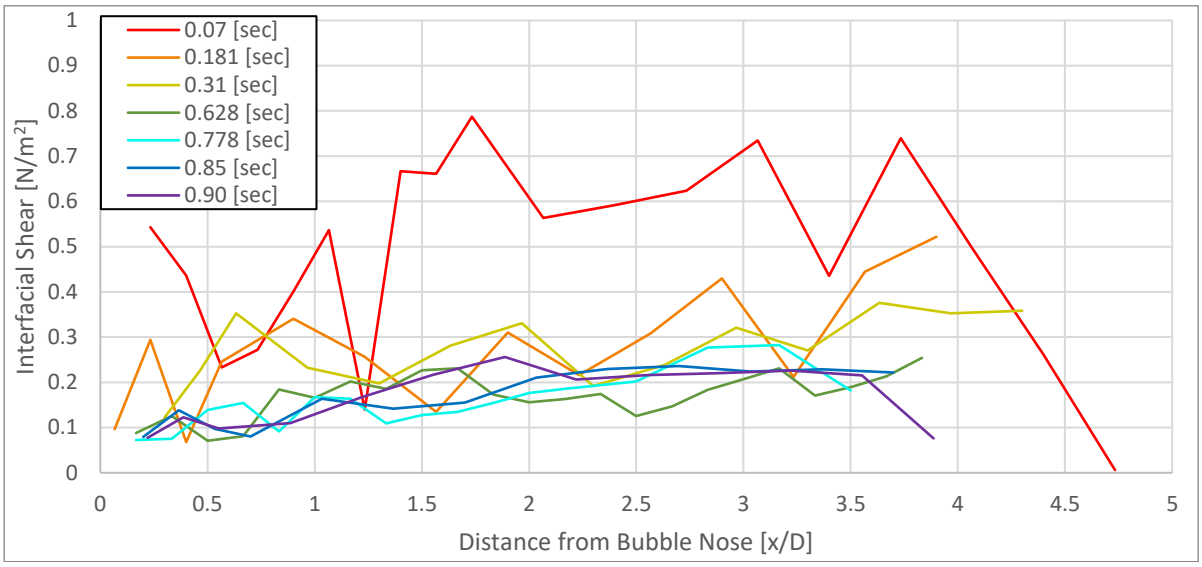

Figure 6.26: Interfacial shear profiles for the reverse of the shearing mechanism.

Over time the shear decreases and eventually becomes constant once the turbulence is nearly completely decayed. The progression of the interfacial area, shear, and shear force, and the TKE are shown in Figure 6.27

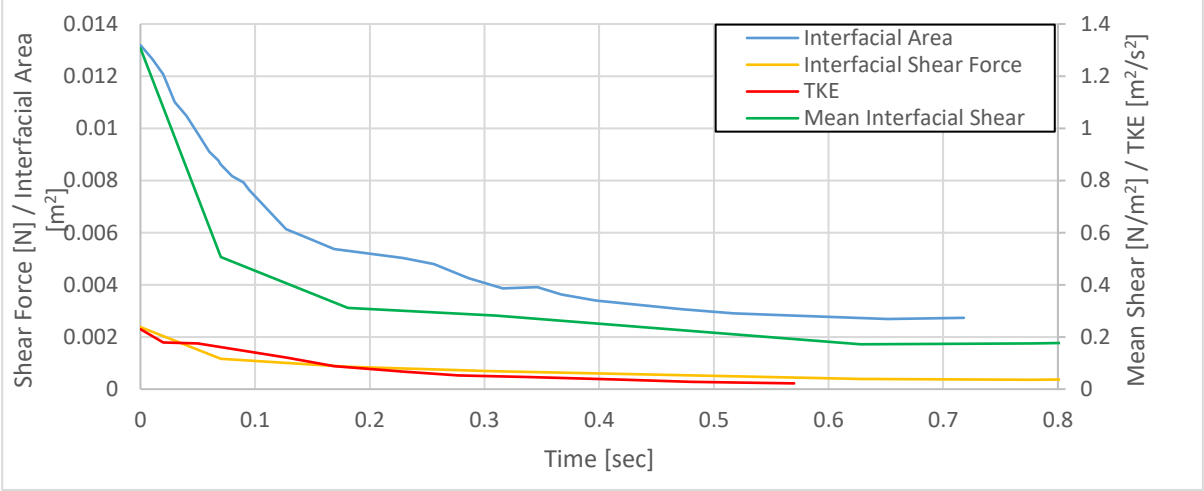

Figure 6.27: Numerical data regarding the interface and TKE for the interfacial shearing mechanism in the reverse transition.

Figure 6.27 only provides further support of the turbulence being the energy supplier, via the interfacial shear. From the start all the parameters are decaying, and the interfacial area seems to respond the slowest. This suggest the interfacial area is responding to the change in TKE and interfacial shear rather than the deceleration. Even after 0.5 seconds, the interfacial area is still decreasing more than the other parameters. This is because the interfacial shear has decreased to the point where no bubble shearing is occurring. The Taylor bubble can then begin to accumulate volume by coalescing with the small bubbles, decreasing the total interfacial area. Important to note is that the parameters are approaching those at the initial state of the forward transition for this flow. This is distinctly different from the instability mechanism and shows how shearing mechanism is reversible.

6.3.3 Summary

Two mechanisms for flow regime transition have been observed, interfacial instability and bubble shearing. These mechanisms drive the transition in both the accelerating and decelerating flows but do not necessarily have a time symmetry, meaning they are not simply the opposite transition in reverse. Both mechanisms are triggered by high TKE colliding with the interface of the bubble and energy being transferred to the interface, causing breakup, through interfacial shearing. What differs between the mechanisms is where the strongest TKE exists relative to the interface and therefore where the TKE deposits its energy on the interface. Despite the different TKE profiles and resulting flow regimes, the relationship between TKE, interfacial shear, and interfacial area was consistent across all the simulations. This reveals the underlying physics for these transitions. The time asymmetry arises because the development of liquid TKE can be different depending on the location of the interfaces at the initiation of the transient. The different TKE development then changes the interfacial shear and interfacial area, producing a new regime.

6.4 Separate Effects Tests

An advantage of DNS is its ability to complete separate effects tests that experiments are not capable of performing. Experiments rely on using real world fluids and are limited to the physical parameters of those fluids. Careful choice of working fluids and proper dimensional analysis can allow experimentalists to quantify the effect a single parameter has on the system, but it is not always a straight forward or possible task, especially for two-phase flows. In DNS, changing one parameter is simply a matter of changing the input value provided by the user. This section will discuss two separate effects tests, the gas viscosity and surface tension.

6.4.1 Gas Viscosity

The viscosity of the gas was hypothesized to be an important contributing factor to the flow regime transition process. As viscosity approaches infinity the Taylor bubble becomes a solid, meaning the interfacial shear would be less effective at shearing off bubbles. Additionally, interfacial shear, as was shown in Section 3.2.1 Interfacial Shear, may affect the gas recirculation flow and interfacial shear strongly enough to change the flow regime transition process. In this study one additional case was run. All other fluid properties were kept the same (0.071 N/m surface tension) but the 20 cm long pipe, with M1, was run with BWR realistic gas viscosity (1.858E-5 [kg/m-s]). This is about 20 times less than previous simulations (2.858E-4 [kg/m-s]). To track this simulation over time, and compare it to the high gas viscosity case, the total interfacial area was recorded at different time steps. The interfacial area is a measurement of how effective the shear/turbulence is at perturbing the Taylor bubble and shearing off smaller bubbles. Figure 6.28 shows the interfacial area information for these two cases.

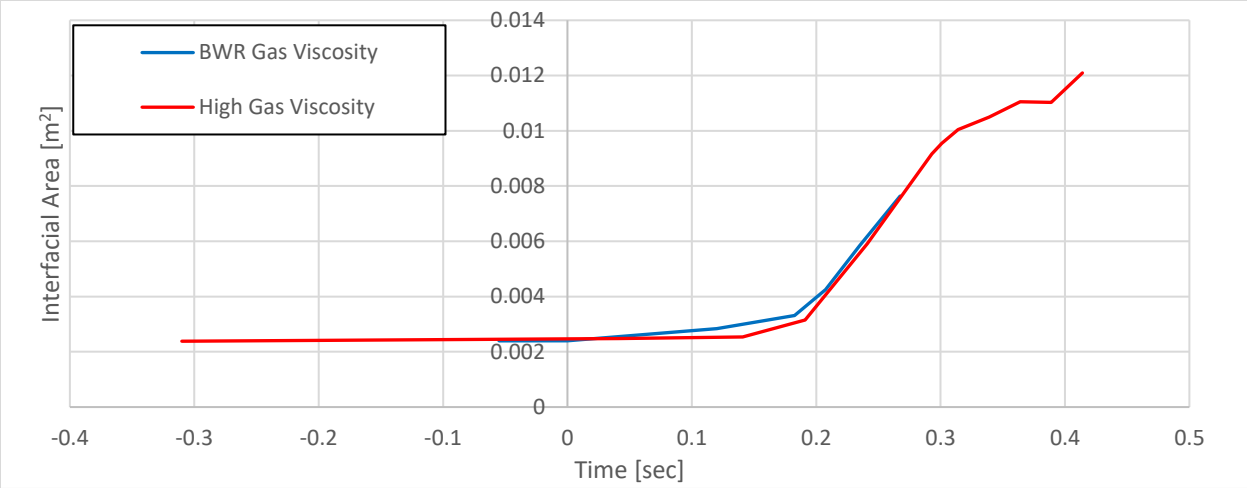

Figure 6.28: Comparison of the total interfacial area of the two gas viscosity cases over time. Time is in reference to when the pressure gradient was increased.

Because the wall generates most of the turbulence encountered by the bubble, as shown earlier, there is no reason to believe the bubble should be encountering significantly different turbulence over time. Therefore, any difference in the interfacial area over time would be because the gas viscosity made the turbulence less/more effective at breaking up the bubble. The BWR gas viscosity case was not run to the same time as the higher viscosity case, but as Figure 6.28 shows, the interfacial area progression is nearly identical. This suggests the liquid momentum makes the gas momentum insignificant. It is expected that for extremely high gas viscosity the interfacial area over time would be different, but these gas viscosities are not relevant to BWRs. Additionally, the liquid side interfacial shear over time was similar (Figure 6.29).

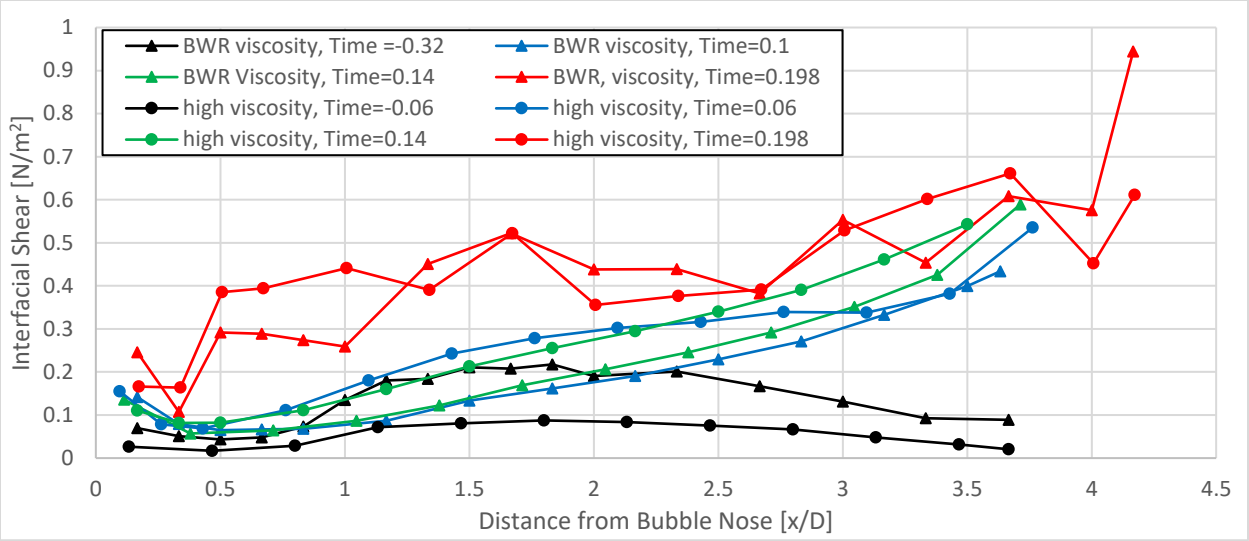

Figure 6.29: The interfacial shear profile over time for the BWR gas viscosity and high gas viscosity simulations. The time refers to time since the pressure gradient was increased.

Figure 6.29 shows there is initially a difference in the magnitude of the shear. The BWR gas viscosity case shows the shear is higher before the acceleration but afterwards this switches and the BWR viscosity case has a lower shear. As the flow accelerates and turbulence begins to collide with the interface, any difference is in the instantaneous fluctuations. Given the large difference in the simulated gas viscosity tests, the effect it has on the flow regime transition was concluded to be minimal. The factor of 20 change in gas viscosity has also not appeared to change the resolution requirements on interfacial shear appreciably either.

6.4.2 Surface Tension

Having proposed where the energy for the flow regime transition comes from and how the energy transfer occurs, the need to determine how much energy is needed for the transition arose. Due to the surface tension being responsible for holding the bubble together, it was theorized that surface tension also dictates how much energy is needed to break up the bubble. Researchers looking at bubble and droplet breakup have made similar claims [112]. Two new simulations, each with different surface tension values, were run. The two surface tension values chosen were 0.023 and 0.014 N/m. The latter is the surface tension at BWR conditions and the former is an

intermediate value between BWR and atmospheric conditions. These simulations used M1 in the 20 cm long pipe. Looking back at Table 4.8, these new surface tension values significantly increase the Weber and Eötvös numbers, making the surface tension even less significant for the Taylor bubble. As was expected, smaller magnitude perturbations were observed in the interfaces and these Taylor bubbles were sheared apart sooner after the acceleration than in the 0.071 N/m surface tension simulation. Images from each simulation are shown in Figure 6.30 (0.014 N/m is left and 0.023 N/m is right).

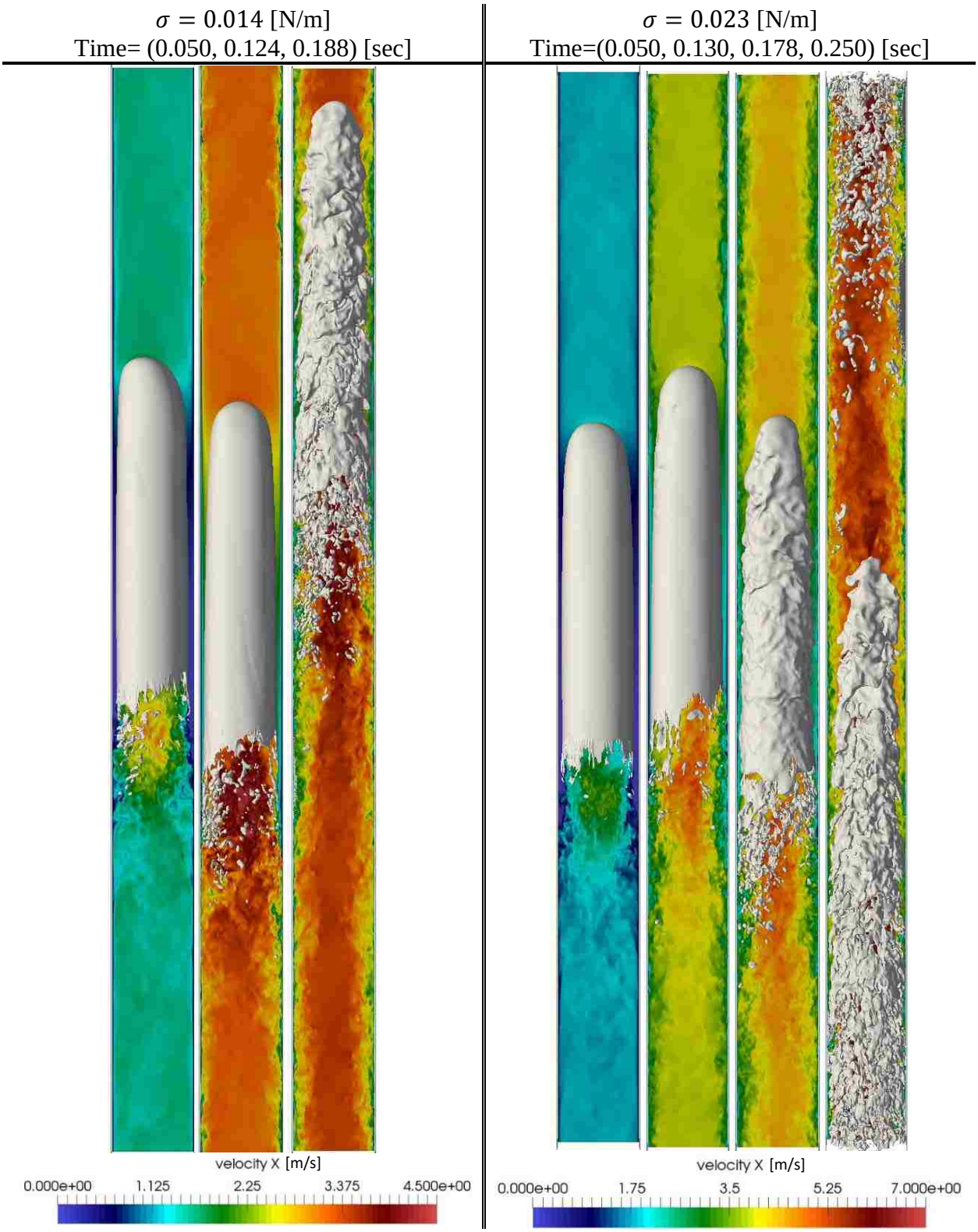

Figure 6.30: Images of the two lower surface tension simulations. Time refers to time since the pressure gradient was increased. Different streamwise velocity scales are used to better show detail in each simulation.

Note that in both simulations the interfaces become so complex that the code had difficulty solving the level set field while maintaining reasonable time step sizes. Therefore, the simulations were stopped soon after the last images shown in Figure 6.30. It was assumed that the bubble would be torn apart, inducing a flow regime transition, if the flow were allowed to continue at these conditions. This is a risky assumption but reasonable considering how weak the surface tension is. As Figure 6.30 shows, both bubbles do not last as long as the atmospheric surface tension case. As was expected, the bubble with the larger surface tension also lasts slightly longer than the BWR surface tension bubble. Comparing the TKE in each of the three simulations just before breakup gives Figure 6.31.

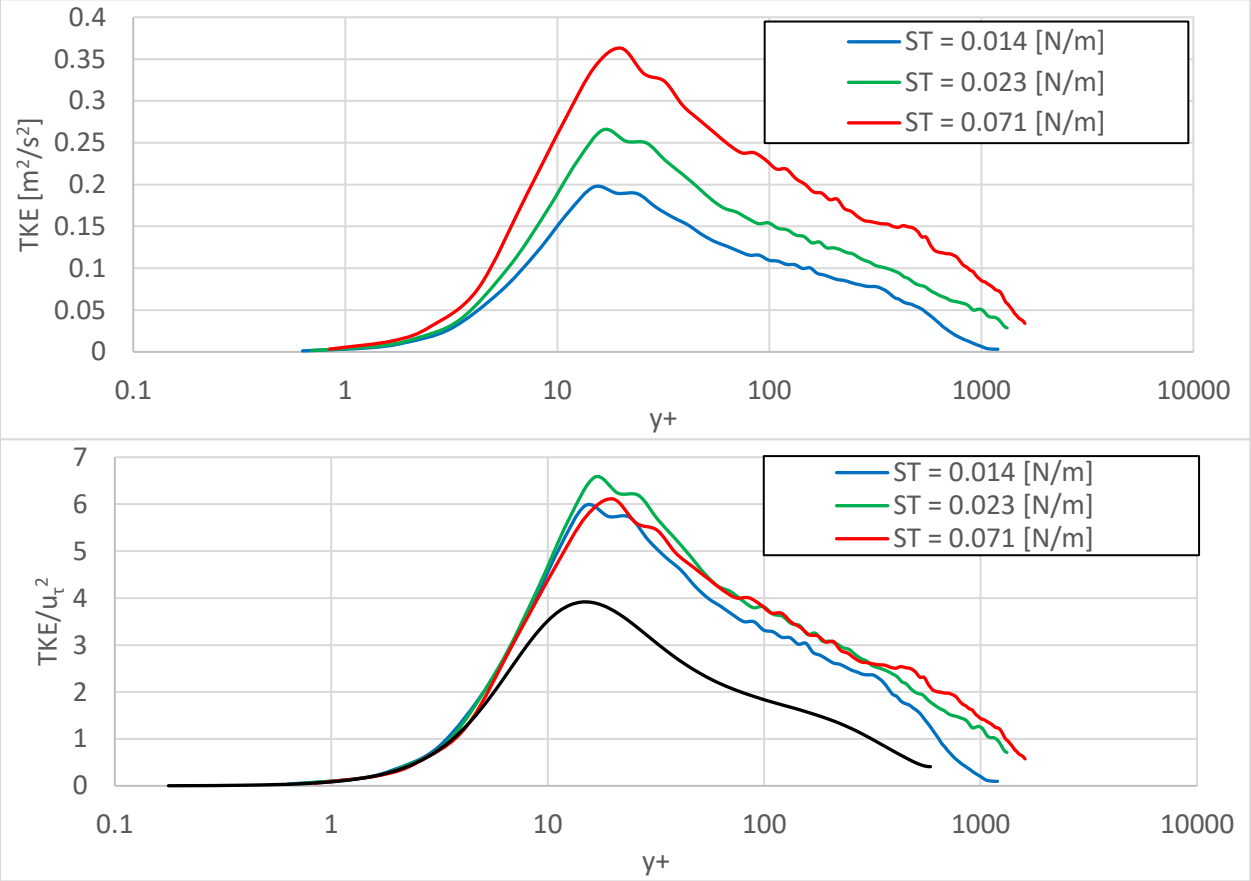

Figure 6.31: TKE profiles for the three different surface tension cases in the 20 cm long pipe. The top image shows the TKE magnitude and the bottom shows the normalized TKE. Data from Moser et al. *[2]* is also included for reference.

It is clear that the necessary TKE magnitude just before the transition correlates with the surface tension. These results support the idea that surface tension determines the critical energy in the liquid and that surface tension can be used to predict how energetic the liquid needs to be. When the TKE profiles are non-dimensionalized by the square of the friction velocity, they collapse to the same shape. This result indicates the different surface tensions were not altering the turbulence in the liquid slug and that each bubble was encountering the same liquid turbulence.

To explore what kind of relationship exists between the surface tension and the mean TKE value, Figure 6.32 plots these two values.

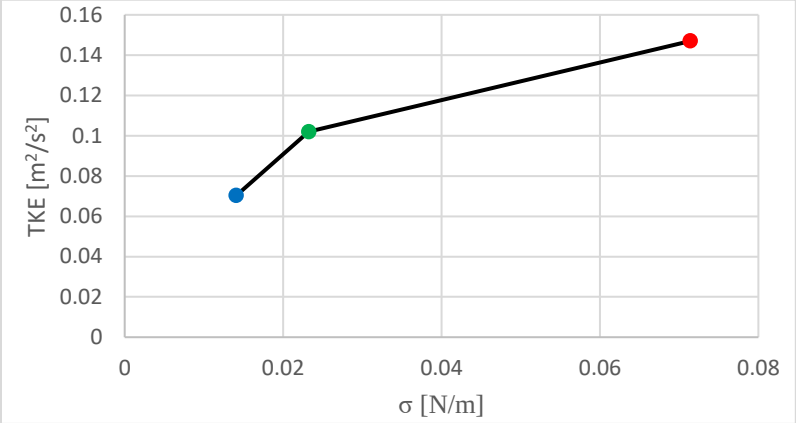

Figure 6.32: A plot showing the relationship between the surface tension and the mean TKE value just before the flow regime transition occurs. The data point colors correspond to the colors in Figure 6.31.

The mean TKE is an area averaged calculation from plots similar to Figure 6.31. From only three data points it is difficult to extract a trend line. However, as surface tension continues to increase, the bubble becomes, essentially, a rigid bullet of gas. At nearly infinite surface tension no level of TKE would be able to break the bubble apart. As the surface tension approaches zero the bubble would fall apart simply due to shear on the interface. The flow could be laminar and the Taylor bubble would break up. This suggests the trend line should hit zero at some non-zero surface tension. Therefore, a linear relationship is not likely. For now, no trend line was created, and more data points are necessary.

When looking at the interfacial shear between these three simulations, the profiles are not significantly different (Figure 6.33).

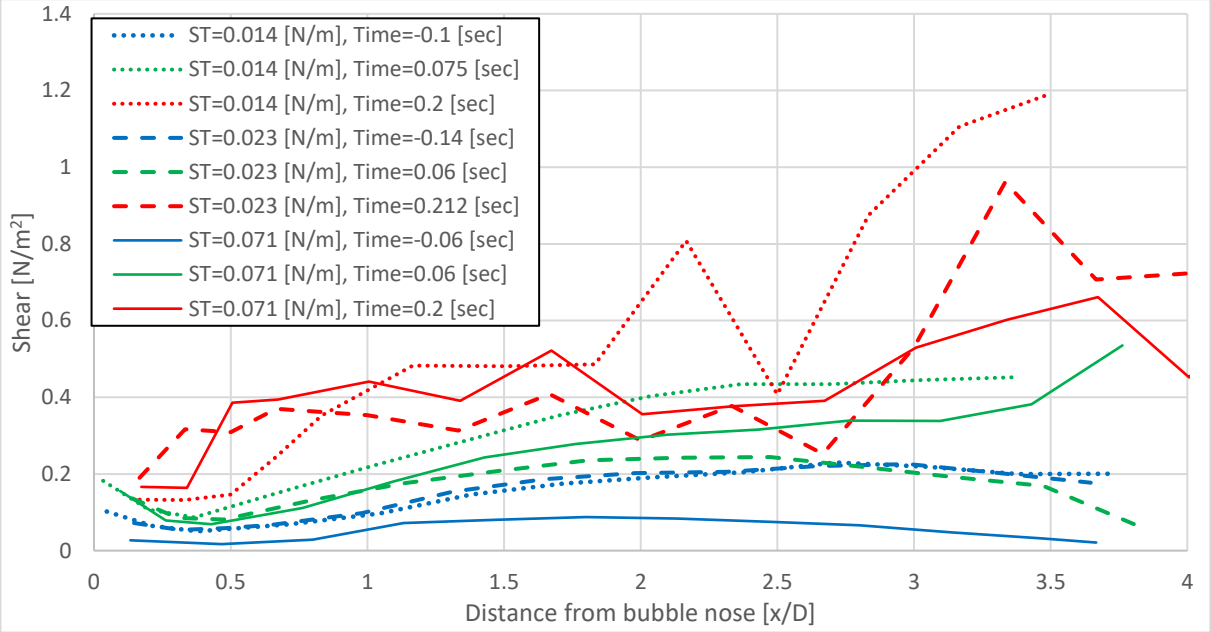

Figure 6.33: A plot showing the interfacial shear profiles for the three simulations with different surface tension values. Time refers to time since the pressure gradient was increased.

There is some variability between each profile but this numerical data is from a single time step, so variation is expected. The important point to note is that bubble shearing begins at different times after the flow is accelerated. This is visible in Figure 6.30 and Appendix C, where the three simulations have different numbers of bubbles being sheared off the tail at the same time in the simulation. Additionally, the largest interfacial shear value is at the tail of the bubble. As discussed earlier, this is a characteristic of the bubble shearing process. Using this knowledge, the method bubble shearing process can be fully described over time. The flow accelerates, increasing the energy in the liquid. The liquid then imparts some of this energy to the Taylor bubble by performing shear work on the interface. This shear work is not strongly dependent on the surface tension, meaning at different points in time each Taylor bubble will begin to be torn apart. As

turbulence begins to form in the liquid, the perturbed interface and even higher interfacial shear enhance the bubble shearing process.

6.5 Flow Regime Transition Criterion

This section dedicates a preliminary effort to developing a flow regime transition criterion that is not dependent on geometry, fluid, temperature, or pressure. Instead, using the knowledge of turbulence being an important factor in overcoming the surface tension of the bubbles, a critical turbulence level for breakup will be discussed and presented. This effort does not claim to be a perfect predictor for two-phase flow regime transitions but rather illustrates the potential for DNS data to provide insight into the phenomenon that experiments have not yet allowed for.

6.5.1 Formulating the Criterion

So far, observations suggest turbulence is necessary for initiating a flow regime transition out of slug flow. Additionally, the turbulence must decay before bubbles in higher flow rate regimes, like churn-turbulent or turbulent bubbly flow, can coalesce to form annular or slug flow. Therefore, the two-phase flow regime transition criteria will be formulated assuming turbulence is necessary. To create a criterion that can be used to determine when a transition out of slug flow is expected, a method to quantify the necessary TKE that accounts for the surface tension is necessary. Historically, a property known as surface energy has been used to determine when a small bubble or droplet will be broken into two daughter bubbles/droplets [112]. Surface energy is defined as:

$$E_{surf} = A_i \sigma \tag{6.3}$$

where A_i is the interfacial area. This definition makes it clear that creating more interfacial area (breakup) requires energy to be added to the interface, and removing interfacial area (coalescence) takes away energy from the interface. Therefore, the bubble will naturally tend to the most stable condition, the least interfacial area, if allowed to. To prevent a system from reaching its most stable

condition, energy must be continuously added to prevent coalescence. For a small bubble, the lowest energy state is a sphere. To break a spherical bubble apart into two smaller spheres of equal diameter would require energy equal to the difference in surface energy between the two conditions:

$$\Delta E_{surf} = 4\pi\left(2\left(\frac{r}{\frac{1}{2^{\frac{1}{3}}}}\right)^2 - r^2\right)\sigma \qquad (6.4)$$

where r is the radius of the initial bubble. A similar concept can be applied to a Taylor bubble. The lowest energy state is the slug flow before the pressure gradient was increased. As the flow accelerates, more energy is created along with more interfacial area. Figure 6.34 plots the interfacial area and area averaged TKE over time, showing how in almost all flows, the change in TKE occurs before the interfacial area changes.

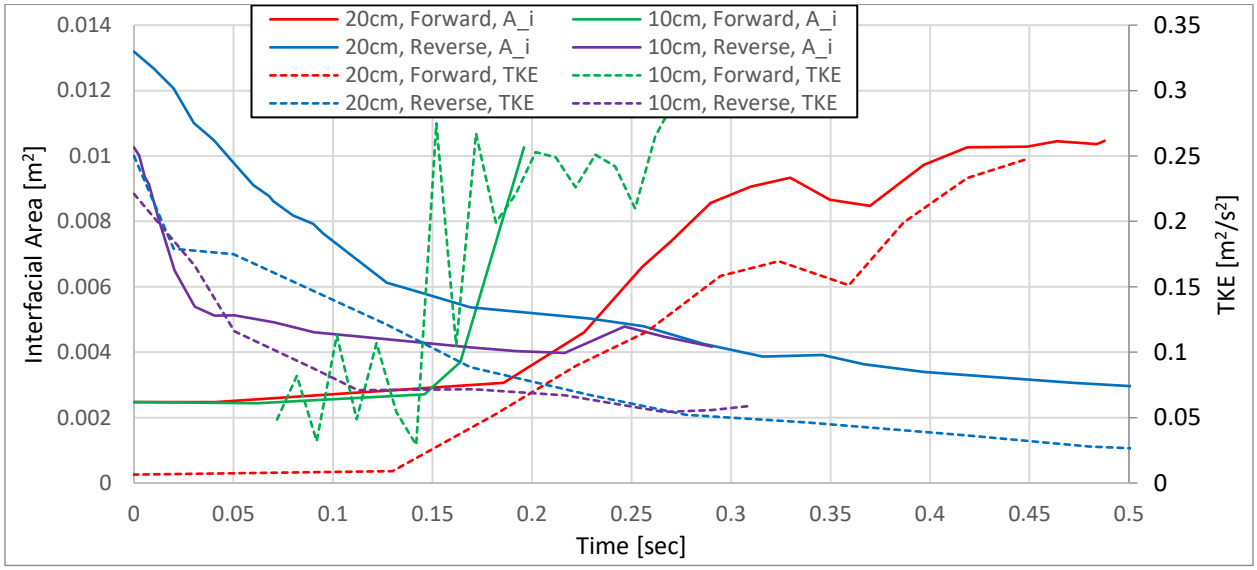

Figure 6.34: Interfacial area and area averaged TKE over time for the STP surface tension simulations.

Even though the interfacial area may still be increasing significantly in Figure 6.34, especially in the forward 10 cm long domain, the transitions have already occurred by the last interfacial area measurement. The numerical data taken from the two additional surface tension simulations shows the same trend, but the interfacial area changes faster due to the weak surface tension requiring

less energy to add new interfaces. Figure 6.35 shows how there appears to be a linear relationship, with a slope approximately equal to one, between the interfacial area and the TKE when it is converted to joules.

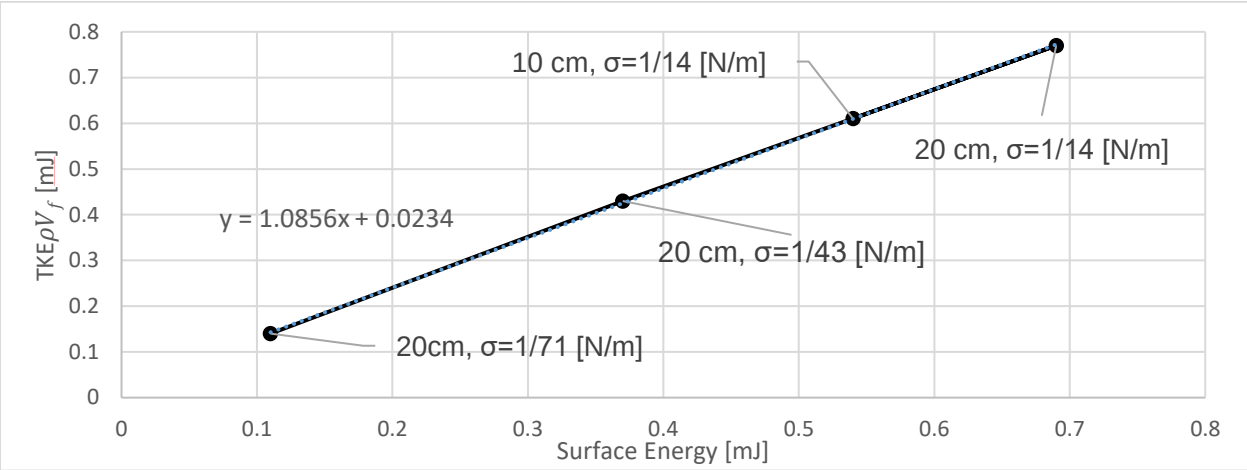

Figure 6.35: Depiction of the relationship between the surface energy and TKE when the flows are transitioning in the forward simulations. Trend line equation is shown.

TKE's units are m^2/s^2, meaning it must be translated to Joules by multiplying by mass of the liquid. To do so the volume of the liquid film was integrated and multiplied by the density. The liquid film's volume was chosen, rather than the entire volume of the liquid, because the liquid film is where the energy transfer between the liquid and interface occurs. The liquid in the slug only interacts with the interface once it enters the liquid film. Additionally, the TKE is integrated across the entire diameter of the pipe because using a single value, the peak TKE for example, would not be representative. Using this information, the energy needed to create these interfaces, ΔE_{FRT}, and therefore cause a two-phase flow regime transition, can be calculated from:

$$\Delta E_{FRT} = (A_{FRT} - A_{slug})\sigma \qquad (6.5)$$

where A_{FRT} is the interfacial area after the flow regime transition and A_{slug} is the interfacial area of the slug flow. Using the four flow regime transition simulations, a mean $\Delta E_{FRT} = 3.66(A_{slug}\sigma)$ can be calculated. Turbulence, surface tension, and interfacial area are the key components of the

mechanisms for flow regime transition and Eq. (6.5) only takes these into account, making it universal and also more fundamental than flow regime maps. If this criteria is accurate, the TKE during the flow regime transition should be equal to, or larger than, this value. Table 6.1 compares the predicted ΔE_{FRT} and TKE values for each simulation.

Table 6.1: Calculated critical energy for a flow regime transition compared to the TKE during the transition.

	ΔE_{FRT} [mJ]	TKE [mJ]
σ = 0.071 [N/m], L = 10.0 [cm]	0.627	0.849
σ = 0.071 [N/m], L = 20.0 [cm]	0.627	0.709
σ = 0.023 [N/m], L = 20.0 [cm]	0.204	0.295
σ = 0.014 [N/m], L = 20.0 [cm]	0.124	0.203

The ΔE_{FRT} from Eq. (6.5) is close to the TKE in all simulations. This is particularly interesting because the 10 cm long pipe underwent a transition different from that in the 20 cm long pipe, demonstrating its universal applicability.

It is not expected that this criterion will be perfect as it is based on a limited number of virtual experiments. However, it does represent a preliminary effort to describe flow regime transitions using physical phenomena and without flow regime maps, correlations, or condition dependent properties. The relationship between TKE and interfacial area described by this section also allows researchers to better describe the gradual transition from one regime to another as more interfaces are created. This development of interfacial area is more accurate to the transition from one regime to another compared to the hard lines put forth by flow regime maps.

6.5.2 Testing the Criterion

To test the validity of this criterion two simulations were designed such that the expected TKE was below the critical value, meaning no transition is expected. The two TKE levels used a multiplication coefficient of $\frac{2.5\sigma A_{i,slug}}{\rho_l V_f}$ and $\frac{3.2\sigma A_{i,slug}}{\rho_l V_f}$, compared to the $\frac{3.66\sigma A_{i,slug}}{\rho_l V_f}$ presented

previously. To maintain computational affordability these simulations used M1. The Δy_w^+ values, extracted after completing the simulations, were about 2.6 and 3.1, meaning, by traditional standards, they are under resolved. However, the purpose of this test was not to produce accurate turbulence levels but to test if the flow will undergo transition for a desired TKE level. With this in mind the test was performed. The flows were extracted at points in time during the acceleration where the TKE approximately equaled the desired levels. A pressure gradient that would produce the desired turbulence level was calculated and the flow was allowed to develop over the course of at least three flow throughs, or 40 pipe diameter lengths. Figure 6.36 shows the TKE profiles in both simulations for their last two flow throughs.

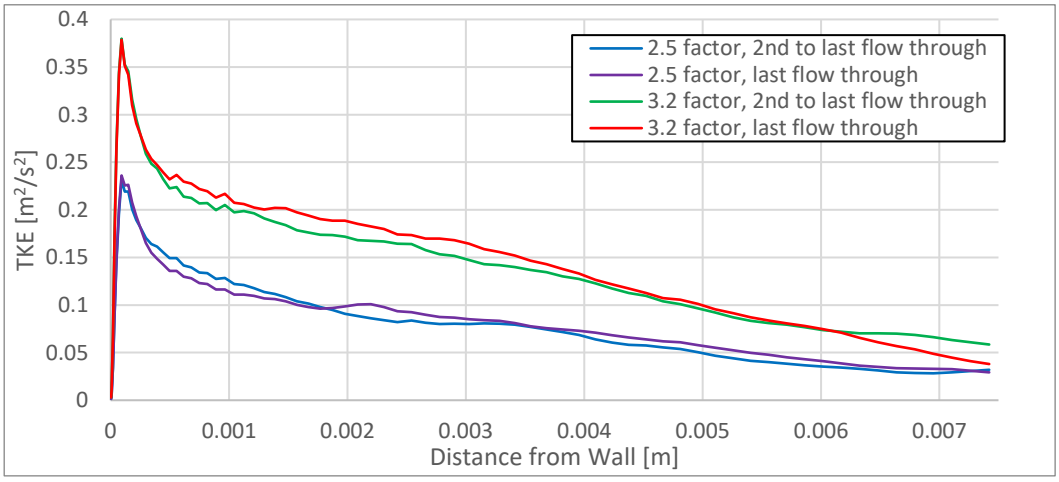

Figure 6.36: TKE plots for the last two flow throughs in the criterion testing simulations.

As can be seen, the TKE is no longer appreciably changing between flow throughs, and the differences can be attributed to sampling uncertainty. Therefore, the flow was considered to be at a statistically steady state. Calculating the actual multiplication factors, 2.8 and 3.5, reveals the TKE levels in both simulations were both slightly higher than expected but still under the critical value. As seen in Figure 6.37 both simulations remain in slug flow in the last time step.

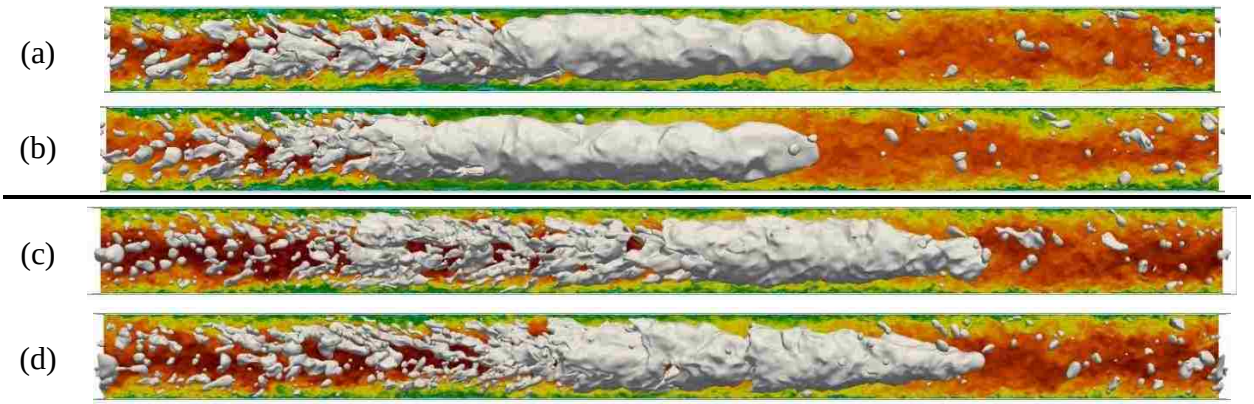

Figure 6.37: Images of the last two flow throughs of the simulations testing the flow regime transition simulation. (a) and (b) are the 2.5 factor simulation and (c) and (d) are the 3.2 factor simulation.

There is a significant amount of gas that has broken off the Taylor bubble and been redistributed in the wake and liquid slug, especially in the faster flow simulation (Figure 6.37 (c) and (d)). However, even this with void redistribution slug flow persists, indicating the transition criterion is still valid. Additional testing is needed to refine the criterion and analyze its application in different geometries, fluids, etc.

CHAPTER 7. CONCLUSIONS

The foundation for simulating two-phase flow regime transitions using interface capturing methods has been laid out. The studies performed in this work developed an understanding of what phenomena must be properly resolved in order to capture the physics of two-phase flow regime transitions. The two fluids are coupled together by their interaction with the interface, making the interfacial shear a new consideration for computational resolution. It was shown that fully resolving two-phase flow can require a vastly finer computational mesh due to the importance of obtaining accurate interfacial shear calculation. A meshing requirement was proposed for designing flow regime transition simulations. This requirement is determined from the most limiting condition of three different factors:

- Resolving the smallest expected bubbles by at least 11 computational points across the shortest dimension.
- Fully resolving the bubble-induced turbulence using interfacial shear to calculate Δy^+ units from both sides of the interface. The standard DNS condition of $\Delta y^+ = 12$ is thereby applied to the bulk mesh using the more stringent of the calculations.
- Maintaining at least 6 computational points across the liquid film of a Taylor bubble.
- PHASTA can accurately capture the thin liquid film drainage phenomenon even without mesh sizes on the fractions of micrometer scale.

Although this resolution requirement was developed with flow regime transition simulations in mind, it is broadly applicable to any interface resolved two-phase flow simulation.

A validation hierarchy for two-phase flow regime transitions was proposed. This hierarchy fully describes the major components of flow regime transitions and what capabilities are necessary to validate a code for two-phase flow regime transitions. Five new components of the hierarchy were

tackled, and the results continue to support PHASTA as a useful tool for this application. For the first time PHASTA was shown to be able to capture multiple two-phase phenomena:

- The thin film, and its donut shape, that forms between a buoyancy driven bubble and a free surface. A computational mesh matching the experimentally measured fraction of micrometer thickness of the film was not necessary.
- Bubble deformation in a simple shear field
- Taylor bubble induced wake structure
- Churn-turbulent interfacial area concentration despite the level set method's automatic coalescence property

Additional work needs to be done in order to complete the hierarchy but preliminary results do not raise concern.

First of their kind simulations were designed and run. These simulations represent a first effort in using "virtual experiments" to analyze the complex two-phase flow regime transition phenomena. In these flows the fluids were both accelerated and decelerated to observe the development and analyze their mechanisms for transition. Two mechanisms for transition were identified, interfacial instability and bubble shearing. The flows showed that these mechanisms are not necessarily reversible, as the interfacial instability mechanism transitioned from slug to churn-turbulent flow in the acceleration and churn-turbulent to annular and eventually to slug in the deceleration. This observation has never been made either computationally or experimentally. The relationship between TKE and the breakup of the Taylor bubble was demonstrated and the interfacial shear was proposed as the vehicle for the transfer of energy from TKE to the interface. Using this knowledge a flow regime transition criterion was proposed and supported through two tests.

CHAPTER 8. FUTURE WORK

This work has provided the foundation for future computational flow regime transition research by defining the important considerations that must be taken into account before the large-scale simulations are performed. The analysis in this work also highlighted significant physical phenomena relating to the transitions. This novel research has opened the door to future research involving "virtual experiments" that can provide scientists with opportunities for new insights into the flow regime transitions. To address the path forward in this field and improve on the current research, this section will discuss where future efforts can be placed in order to benefit the field. Figure 8.1 lays out the already completed and ongoing work as well as the future work discussed here.

Figure 8.1: A map of the completed, ongoing, and proposed work.

8.1 Simulating other Two-Phase Flow Regime Transitions

The simulations performed in this work tackled only a portion of the total flow regime transition field. The simulations began in the slug regime, skipping the bubbly regime, which is typically observed at lower superficial gas velocities/void fractions, and briefly discussed the annular regime. Similar to experiments, research that extends this work to cover all regimes is crucial to understand the transition phenomena. There are certainly mechanisms for bubbly to slug transition that are much more prevalent than in the slug to churn-turbulent transition. Covering all regimes allows for analysis and modeling that will be discussed in the following sections. Having the full picture is important for full comprehension.

Unlike experiments, simulation allows for the evaluation of phenomena that experiments cannot achieve. This is done through advanced analysis techniques and simulation design. This capability is not one that should be ignored when studying such a complex phenomenon because full analysis of the individual components of a full flow regime transition simulation may be extremely difficult. Similar to the validation hierarchy created in this dissertation, flow regime transitions have a web of underlying pieces that each contribute to the process as a whole. Understanding this web leads to designing simulations that elucidate each of these pieces. This method of studying flow regimes may be a more effective way of learning about their transitions from a computational standpoint. The data analysis process is simplified due to the single phenomena of interest, and isolating the effect of that phenomena on the flow is more feasible. Examples of such simulations have already been performed in this work. The bubble rising towards a free surface, discussed in Section 5.2.1 Bubble Approaching a Free Surface, is an examination of the coalescence process, which is very important for any two-phase flow. On its own this simulation could easily become very expensive due to the small scale of the liquid film, but due to

the event of interest only occurring in a small volume the numerical data would be more manageable. Additionally, learning how the film drains is difficult to study experimentally, making a DNS potentially very informative of the liquid film velocity, bubble residence time, etc. The simple bubble shear simulations discussed in Section 5.2.2 Droplet Deformation in a Simple Shear Field are also valuable to understand the breakup process. Increasing the shear rate beyond what was examined here would eventually lead to breakup, a mechanism also very important in flow regime transitions. Combining what is learned from the DNS of coalescence and breakup may be able to reveal a better understanding of the flow regime transition from any regime to any other.

The interaction of turbulent eddies with the interface is also an event of interest for this research. Examining how the eddy changes and transfers energy to the interface would be a valuable process to understand. How efficient is the energy transfer, how does surface tension and deformability play a role in transferring energy, and how does the eddy shape/velocity change after the collision are all questions that could be explained by a simple simulation that directs eddies at an interface. This sort of simulation is a logical next step in two-phase DNS. Single phase DNS researchers have already characterized the shape of eddies being generated at the wall [5] and how the structure can change in the bulk of the flow [113]. Extending this practice to two-phase flow would be valuable, not only to this study, but to the community as a whole.

With this more complete understanding of the behavior of interfaces in turbulent flow the hope would be to eliminate the need for the flow regime classification system altogether. It would be replaced with an understanding of how the liquid is going to distribute the void and what the consequences, for example on pressure drop and heat transfer, would be.

8.2 CFD Modeling

A popular focus of two-phase flow research is using high-fidelity data to inform models. The two-phase flow regime transition phenomenon is rich with large volumes of numerical data and opportunities for advanced analysis. As was discussed, interfacial area concentration is a common way to model regimes and extract heat transfer and pressure drop. The interfacial area code generated for this work produces data directly relevant to the interfacial area transport equations. Figure 8.2 shows an example of the local interfacial area concentration for a single time step.

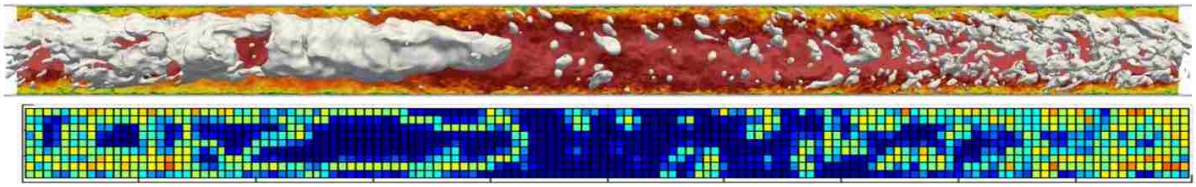

Figure 8.2: The interfacial area concentration information for a middle slice (top) and an image of its associated time step (bottom).

Coupling the knowledge of the flow, like turbulence level, pressure drop, and interfacial area concentration that DNS allows can lead to more high-fidelity models for flow regimes in CFD codes.

This work has already developed a transition mechanism that is independent of the fluid or geometry. Continuing on this path would be valuable to other codes that rely on accurate model for important real world systems. A new flow regime map could be produced to completely describe the flow across any flow rate or void fraction.

Mechanistic modeling can even be performed using the smaller scale simulations mentioned in the previous section. If the individual mechanisms for a flow regime transition can be fully understood then a mechanistic model for a CFD code is possible.

8.3 Machine Learning Application

Machine learning is an exciting field whose application can inform humans more efficiently and effectively than manual techniques. As mentioned, these flow regime transition simulations create tens of terabytes of numerical data. This immense amount of data makes it difficult for humans to analyze. Even when humans analyze this data it is nearly impossible to use every data point to its maximum potential. Machine learning algorithms help optimize the analysis process and better take advantage of a larger percentage of numerical data. A properly formulated neural network may be able to decipher flow regime transitions and produce data-driven mechanistic models for the transitions, essentially tackling the research described in the previous two sections. More advanced modeling may be able to eliminate the need for flow regimes all together. By fully understanding the physics involved with the transitions it may not be necessary to define the flow as a regime. Instead, the machine-produced model may be able to calculate an interfacial structure from which it can determine expected properties like pressure drop and heat transfer.

REFERENCES

[1] M. Lee and R. D. Moser, "Direct numerical simulation of turbulent channel flow up to Re_tau = 5200," *Journal of Fluid Mechanics,* vol. 774, pp. 395-415, 2015.

[2] R. D. Moser, J. Kim and N. N. Mansour, "Direct numerical simulation of turbulent channel flow up to Re_tau=590," *Physics of Fluids,* vol. 11, no. 4, pp. 943-945, 1999.

[3] A. V. Trofimova, A. E. Tejada-Martinez, K. E. Jansen and R. T. Lahey Jr., "Direct numerical simulation of turbulent channel flows using stabilized finite element method," *Computers and Fluids,* vol. 38, pp. 924-938, 2009.

[4] "ABWR Design Control Document Rev. 4," ML11126A100, 1997.

[5] P. Moin, M. M. Rogers and R. D. Moser, "Structure of turbulence in the presence of uniform shear," in *Symposium on Turbulent Shear Flows*, Ithaca, NY, 1985.

[6] J. Fang, C. S. Brown, J. Feng, M. Li and I. A. Bolotnov, "DNS of two-phase flow and growing HPC performance: review of capabilities and future outlook," in *Japan-US seminar on Two-Phase flow Dynamics*, Sapporo, Hokkaido, Japan, 2017.

[7] F. Behafarid, K. E. Jensen and M. Z. Podowski, "A study on large bubble motion and liquid film in vertical pipes and inclined narrow channels," *International Journal of Multiphase Flow,* vol. 775, pp. 288-299, 2015.

[8] J. Fang and I. A. Bolotnov, "Bubble tracking analysis of PWR two-phase flow simulations based on the level set method," *Nuclear Engineering and Design,* vol. 323, pp. 68-77, 2017.

[9] J. Lu and G. Tryggvason, "Effect of bubble deformability in turbulent bubbly upflow in a vertical channel," *Physics of Fluids,* vol. 20, pp. 040701-1-6, 2008.

[10] J. Lu and g. Tryggvason, "Direct numerical simulation of multifluid flows in a vertical channel undergoing topology changes," *Physical Review Fluids,* vol. 3, p. 084401, 2018.

[11] J. Feng and I. A. Bolotnov, "Evaluation of bubble-induced turbulence using direct numerical simulation," *International Journal of Multiphase Flow,* vol. 93, pp. 92-107, 2017.

[12] N. K. Tutu, "Pressure fluctuations and flow pattern recognition in vertical two phase gas-liquid flows," *International Journal of Multiphase Flow,* vol. 8, no. 4, pp. 443-447, 1982.

[13] H. Shaban and S. Tavoularis, "Identification of flow regime in vertical upward air-water pipe flow using differential pressure signals and elastic maps," *International Journal of Multiphase Flow,* vol. 61, pp. 62-72, 2014.

[14] Y. Taitel and D. Barnea, "Two-phase slug flow," *Advances in Heat Transfer,* vol. 20, pp. 83-132, 1990.

[15] G. F. Hewitt and N. S. Taylor, Annular Two-Phase Flow, Oxford: Pergamon Press Ltd., 1970.

[16] K. Mishima and T. Hibiki, "Some characteristics of air-water two-phase flow in small diameter vertical tubes," *International Journal of Multiphase Flow,* vol. 22, pp. 703-712, 1996.

[17] J. E. Julia, Y. Liu and M. I. Sidharth Paranjape, "Upward vertical two-phase flow local flow regime identification using neural network techniques," *Nuclear Engineering and Design,* vol. 238, pp. 156-169, 2008.

[18] J. E. Julia, Y. Liu, T. Hibiki and M. Ishii, "Local flow regime analysis in vertical co-current downward two-phase flow," *Experimental Thermal and FLuid Science,* vol. 44, pp. 345-355, 2013.

[19] L. Hernandez, J. E. Julia, S. Chiva, S. Paranjape and M. Ishii, "Fast Classification of two-phase flow regimes based on conductivity signals and artificial neural networks," *Measurement Science and Technology,* vol. 17, no. 6, pp. 1511-1521, 2006.

[20] P. L. Spedding and V. T. Nguyen, "Regime maps for air water two phase flow," *Chemical Engineering Science,* vol. 35, no. 4, pp. 779-793, 1980.

[21] Q.-y. Ren, W.-x. Zhou, S.-j. Du, Z.-c. Li and L.-m. Pan, "Sub-channel flow regime maps in vertical rod bundles with spacer grids," *International Journal of Heat and Mass Transfer,* vol. 122, pp. 1138-1152, 2018.

[22] Y. Zhou, Y. Hou, H. Li, B. Sun and D. Yang, "Flow pattern map and multi-scale entropy analysis in 3x3 rod bundle channel," *Annals of Nuclear Energy,* vol. 80, pp. 144-150, 2015.

[23] C. L. Williams and A. C. Peterson Jr, "Two-phase flow patterns with high-pressure water in a heated four-rod bundle," *Nuclear Science and Engineering,* vol. 68, pp. 155-169, 1978.

[24] K. Mishima and M. Ishii, "Flow regime transition critieria for upward two-phase flow in vertical tubes," *International Journal of Heat and Mass Transfer,* vol. 27, pp. 723-737, 1984.

[25] S. Paranjape, S. W. Chen, T. Hibiki and M. Ishii, "Flow regime identification under adiabatic upward two-phase flow in a vertical rod bundle," *Journal of Fluids Engineering,* vol. 133, no. 9, 2011.

[26] H. Liu and T. Hibiki, "Flow regime transition criteria for upward two-phase flow in vertical rod bundles," *International Journal of Heat and Mass Transfer,* vol. 108, pp. 423-433, 2017.

[27] Y. Taitel, D. Bornea and A. E. Dukler, "Modelling flow pattern transitions for steady upward gas-liquid flow in vertical tubes," *American Institute of the American Institute of Chemical Engineers Journal,* vol. 26, no. 3, pp. 345-354, 1980.

[28] D. Barnea, "A unified model for predicting flow-pattern transitions for the whole range of pipe inclinations," *International Journal of Multiphase Flows,* vol. 13, no. 1, pp. 1-12, 1987.

[29] M. Ishii, "One-dimensional drift-flux model and constituitive equations for relative motion between phases in various two-phase flow regimes," Argonne National Laboratory, Argonne, IL, 1977, ANL-77-47.

[30] R. K. Salko and M. N. Avramova, "COBRA-TF Subchannel Thermal-Hydraulics Code (CTF) Theory Manual: Revision 0," 2015.

[31] D. Bestion, "The difficult challenge of a two-phase CFD modelling for all flow regimes.," *Nuclear Engineering and Design,* vol. 279, pp. 116-125, 2014.

[32] G. Kocamustafaogullari and M. Ishii, "Foundation of the interfacial area transport equation and its closure relations," *International Journal of Mass and Heat Transfer,* vol. 38, no. 3, pp. 481-493, 1995.

[33] M. Ishii and T. Hibiki, Thermo-Fluid Dynamics of Two-Phase Flow, New York, USA: Springer, 2010.

[34] X. Sun, S. Kim, M. Ishii and S. G. Beus, "Model evaluation of two-group interfacial area transport equation for confined upward flow," *Nuclear Engineering and Design,* vol. 230, pp. 27-47, 2004.

[35] M. Ishii, S. Kim and J. Uhle, "Interfacial area transport equation: model development and benchmark experiments," *International Journal of Heat and Mass Transfer,* vol. 45, pp. 3111-3123, 2002.

[36] A. Esmaeeli and G. Tryggason, "Direct numerical simulation of bubbly flows. Part 1. Low Reynolds number arrays," *Journal of Fluid Mechanics,* vol. 377, no. 25, pp. 313-345, 1998.

[37] A. Esmaeeli and G. Tryggvason, "Direct numerical simulation of bubbly flows Part 2. Moderate Reynolds number arrays," *Journal of Fluid Mechanics,* vol. 385, no. 25, pp. 325-358, 1999.

[38] I. A. Bolotnov, "Influence of bubbles on the turbulence anisotropy," *Journal of Fluids Engineering,* vol. 135, pp. 051301:1-9, 2013.

[39] S. Elghobashi, "Direct numerical simulation of turbulent flows laden with droplets and bubbles," *Annual Review of Fluid Mechanics,* vol. 51, pp. 217-244, 2019.

[40] W. Dijkhuizen, I. Roghair, M. V. S. Annaland and J. Kuipers, "DNS of gas bubbles behavior using an improved 3d front tracking model-drag force on isolated bubbles and comparison with experiments," *Chemical Engineering Science,* vol. 65, no. 4, pp. 1415-1426, 2010.

[41] J. Fang, J. J. Cambareri, M. Rasquin, A. Gouws, R. Balakishnan, K. E. Jansen and I. A. Bolotnov, "Interface Tracking Investigation of Geometric Effects on the Bubbly Flow in PWR Subchannels," *Nuclear Science and Engineering,* vol. 193, pp. 46-62, 2019.

[42] D. T. Dumitrescu, "Strömung an einer Luftblase im Senkrechten Rohr," *Zeitschrift fur Angewandte Mathematik und Mechanik,* vol. 23, pp. 139-149, 1943.

[43] J. M. Rodriguez, "Numerical simulation of two-phase annular flow," *Ph.D. dissertation, Rensselaer Polytechnic Institute, Troy, NY,* 2009.

[44] J. Lu and G. Tryggvason, "Multifluid flows in a vertical channel undergoing topology changes: Effect of void fraction," *Physical Review Fluids,* vol. 4, 2019.

[45] J. Lu and G. Tryggvason, "Simulating high void fraction flows undergoing massive topology changes in vertical channels," in *72nd Annual Meeting of the APS Division of Fluid Dynamics,* Seattle, Weashington, 2019.

[46] J. Lu and G. Tryggvason, "Direct numerical simulations and characterizations of multiphase flows with complex topolgy changes in a turbulent channel," in *71st Annual Meeting of the APS Division of Fluid Dynamics,* Atlanta, Georgia, 2018.

[47] M. Mohammadi, S. Shahhosseini and M. Bayat, "Direct numerical simulation of water droplet coalescence in the oil," *International Journal of Heat and Fluid Flow,* vol. 36, pp. 58-71, 2012.

[48] F. Xie, X. Zheng, M. S. Triantafyllou, Y. Constantinides, Y. Zheng and G. E. Karniadakis, "Direct numerical simulations of two-phase flow in an inclined pipe," *Journal of Fluid Mechanics,* vol. 825, pp. 189-207, 2017.

[49] J. M. Wallace and J. F. Foss, "The measurement of vorticity in turbulent flows," *Annual Review of Fluid Mehcanics,* vol. 27, pp. 469-514, 1995.

[50] S. K. Robinson, "Coherent motions in the turbulent boundary layer," *Annual Review of Fluid Mechanics,* vol. 23, pp. 601-639, 1991.

[51] P. Moin and K. Mahesh, "Direct numerical simulation: A tool in turbulence research," *Annual Review of Fluid Mechanics,* vol. 30, pp. 539-578, 1998.

[52] T. Morokuma and Y. Utaka, "Variation of the liquid film thickness distribution between contacting twin air bubbles during the coalescence process in water and ethanol pools," *International Journal of Heat and Mass Transfer,* vol. 98, pp. 96-107, 2016.

[53] B. Lewandowski, M. Fertig, G. Krekel and M. Ulbricht, "Analysis of wake structures in bubbly flows using Particle Image Velocimetry (PIV)," in *7th European Young Engineers Conference*, Warsaw, Poland, 2018.

[54] Z. Liu, Y. Zheng, L. Jia and Q. Zhang, "Study of bubble induced flow structure using PIV," *Chemical Enginering Science,* vol. 60, pp. 3537-3552, 2005.

[55] W. Abassi, S. Besbes, M. Elhajem, H. B. Aissia and J. Y. Champagne, "Numerical simulation of free ascension and coaxial coalescence of air bubbles using the volume of fluid method (VOF)," *Computers and Fluids,* vol. 161, pp. 47-59, 2018.

[56] R. T. Lahey Jr., "On the direct numerical simulation of two-phase flows," *Nuclear Engineering and Design,* vol. 239, pp. 867-879, 2009.

[57] W. L. Oberkampf and C. J. Roy, Verification and Validation in Scientific Computing, Cambridge University Press, 2010.

[58] W. L. Oberkampf and T. G. Trucano, "Validation methodology in computational fluid dynamics," *AIAA,* pp. 2000-2549, 2000.

[59] W. L. Oberkampf and T. G. Trucano, "Verification and validation in computational fluid dynamics," *Progress in Aerospace Sciences,* vol. 38, pp. 209-272, 2002.

[60] C. H. Whiting, "Stabilized finite element methods for fluid dynamics using a hierarchical basis," *Ph.D. dissertation, Rensselaer Polytechnic Institute, Troy, NY,* 1999.

[61] S. Nagrath, "Adapative stabilized finite element analysis of multi-phase flows using a level set approach," *Ph.D. disserations, Mechanical Engineering Department, Rensselaer Polytechnic Institute, Troy, NY,* 2004.

[62] S. Nagrath, K. E. Jansen and R. T. Lahey, "Computation of incompressible bubble dynamics with a stabilized finite element level set method," *Computational Methods in Applied Mechanics and Engineering,* vol. 194, no. 42-44, pp. 4565-4587, 2005.

[63] K. E. Jansen, "A stabilized finite element method for computing turbulence," *Computational Methods in Applied Mechanics and Engineering,* vol. 174, pp. 299-317, 1999.

[64] C. H. Whiting and K. E. Jansen, "A stabilized finite element method for the incompressible Navier-Stokes equations using a hierarchical basis," *International Journal of Numerical Methods in Fluids,* vol. 35, pp. 93-116, 2001.

[65] J. A. Sethian, "Level set methods and fast marching methods: Evolving interfaces in computational geometry, fluid mechanics, computer vision, and materials science," *Cambridge university press,* 1999.

[66] M. Sussman and E. Fatemi, "An efficient, interface-preserving level set redistancing algorithm and its application to interfacial incompressible fluid flow," *SIAM Journal on Scientific Computing,* vol. 20, pp. 1165-1191, 1999.

[67] M. Sussman, A. S. Almrgen, J. B. Bell, P. Colella, L. H. Howell and M. L. Welcome, "An adaptive level set approach for incompressible two-phase flows," *Journal of Computational Physics,* vol. 148, pp. 81-124, 1999.

[68] A. M. Thomas, J. Fang and I. A. Bolotnov, "Estimation of shear-induced life force in laminar and turbulent flows," *Nuclear Technology,* vol. 190, pp. 274-291, 2015.

[69] A. Tomiyama, I. Kataoka, I. Zun and T. Sakaguchi, "Drag coefficients of single bubbles under normal and micro gravity conditions," *JSME International Journal of Fluids and Thermal Engineering Series B,* vol. 41, no. 2, pp. 472-479, 1998.

[70] I. A. Bolotnov, K. E. Jansen, D. A. Drew, A. A. Oberai and R. T. Lahey, "Detached direct numerical simulations of turbulent two-phase bubble channel flow," *International Journal of Multiphase Flow,* vol. 37, pp. 647-699, 2011.

[71] H. J. Karam and J. C. Bellinger, "Deformation and breakup of liquid droplets in a simple shear field," *Industrial and Engineering Chemical Fundamentals,* vol. 7, no. 4, pp. 576-581, 1968.

[72] U. Ayachit, The Paraview Guide, Kitware Inc, 2019.

[73] I. B. Celik, U. Ghia, P. J. Roache, C. J. Freitas, H. Coleman and P. E. Raad, "Procedure for estimation and reporting of uncertainty due to discretization in CFD application," *Journal of Fluids Engineering,* vol. 130, 2008.

[74] N. Muller-Fischer, P. Tobler, M. Dressler, P. Fischer and E. J. Windhab, "Single bubble deformation and breakup in simple shear flow," *Experiments in Fluids,* vol. 45, pp. 917-926, 2008.

[75] S. Nogueira, M. L. Riethmuler, J. B. L. M. Campos and A. M. F. R. Pinto, "Flow in the nose region and annular film around a Taylor bubble rising through vertical columns of stagnant and flowing Newtonian Fluids," *Chemical Engineering Science,* vol. 61, pp. 845-857, 2006.

[76] S. Nogueira, M. L. Reithmuller, J. B. L. M. Campos and A. M. F. R. Pinto, "Flow patterns in the wake of a Taylor bubble rising though vertical columns of stagnant and flowing Newtonian liquids: An experimental study," *Chemical Engineering Science,* vol. 61, pp. 7199-7212, 2006.

[77] E. W. Llewellin, E. D. Bello, J. Taddeucci and P. Scarlato, "The thickness of the falling film of liquid around a Taylor bubble," *Proceedings of the Royal Society A: Mathematical, Physical and Engineering Sciences,* vol. 468, no. 2140, pp. 1041-1064, 2012.

[78] T. D. Karapantsios, S. V. Paras and A. J. Karabelas, "Statistical characteristics of free falling films at high Reynolds numbers," *International Journal of Multiphase Flow,* vol. 15, pp. 1-21, 1989.

[79] G. M. Evans, P. M. Machniewski and A. K. Bin, "Bubble size distribution and void fraction in the wake region below a ventilated gas cavity in downward pipe flow," *Chemical Engineering Research and Design,* vol. 82, no. A9, pp. 1095-1104, 2004.

[80] F. Lehr, M. Millies and D. Mewes, "Bubble-size distribution and flow fields in bubbles columns," *Fluid Mechanics and Transport Phenomena,* vol. 48, no. 11, pp. 2426-2443, 2002.

[81] X. Sun, "Two-group interfacial area transport equation for a confined test section," *Ph.D. Dissertation, Purdue University, West Lafayette, Indiana,* 2001.

[82] B. Ozar, A. Dixit, S. W. Chen, T. Hibiki and M. Ishii, "Interfacial area concentration in gas-liquid bubbly to churn-turbulent flow regime," *International Journal of heat anf fluid flow,* vol. 38, pp. 168-179, 2012.

[83] L. Shemer, A. Gulitski and D. Barnea, "On the turbulent structure in the wake of Taylor bubbles rising in vertical pipes," *Physics of Fluids,* vol. 19, 2007.

[84] T. Fukano and A. Kariyasaki, "Characteristics of gas-liquid two-phase flow in a capillary tube," *Nuclear Engineering and Design,* vol. 141, pp. 59-68, 1993.

[85] R. Gupta, D. F. Fletcher and B. S. Hayes, "Taylor flow in microchannels: A review of experimental and computational work," *The Journal of Computational Multiphase Flows,* vol. 2, no. 1, pp. 1-31, 2010.

[86] A. Gunther, M. Jhunjhunwala, M. Thalmann, M. A. Schmidt and K. F. Jensen, "Micromixing of miscible liquids in segmented gas-liquid flow," *Langmuir,* vol. 21, pp. 1547-1555, 2005.

[87] R. v. Hout and L. S. D. Barnea, "Evolution of statistical parameters of gas-liquid slug flow along vertical pipes," *International Journal of Multiphase Flow,* vol. 27, pp. 1579-1602, 2001.

[88] Y. Wang, C. Yan, D. Xing, G. Jin, L. Sun and G. Yang, "Slug flow in a vertical narrow rectangular channel - Laminar and turbulent regimes in the main flow and turbulent regime in the wake region of the Taylor bubble," *Progress in Nuclear Energy,* vol. 85, pp. 164-177, 2015.

[89] R. Moissis and P. Griffith, "Entrance effects in a two-phase slug flow," *Journal of Heat Transfer,* vol. 84, no. 1, pp. 29-38, 1962.

[90] A. M. F. Pinto, M. N. C. Pinheiro and J. B. L. Campos, "On the interaction of Taylor bubbles rising in two-phase co-current slug flow in vertical columns: turbulent wakes," *Experiments in Fluids,* vol. 31, pp. 643-652, 2001.

[91] J. Fang, Development of advance analysis toolkit for turbulent bubbly flow simulation, PhD Dissertation, 2016.

[92] M. Li and I. A. Bolotnov, "Interface tracking simulation of phase-change phenomena: an evaporation and condensation model," *International Journal of Heat and Mass Transfer,* under review.

[93] L. Fernanadez-Moguel, A. Rydl and T. Lind, "Updated analysis of Fukushima unit 3 with MELCOR 2.1. Part 2: Fission product release and transport analysis," *Annals of Nuclear Energy,* vol. 130, pp. 93-106, 2019.

[94] L. Fernandez-Moguel, A. Rydl and T. Lind, "Updated analysis of Fukushima unit 3 with MELCOR 2.1. Part 1: Thermal-hydraulic analysis," *Annals of Nuclear Energy,* vol. 123, pp. 59-77, 2019.

[95] D. L. Luxat, J. R. Gabor, R. M. Wachowiak and R. L. Yang, "EPRI MAAP5 Fukushima Daiichi Analysis," *Nuclear Technology,* vol. 196, no. 3, pp. 698-711, 2016.

[96] R. D. Kirkpatrick and M. J. Lockett, "The influence of approach velocity on bubble coalescence," *Chemical Engineering Science,* vol. 29, pp. 2263-2373, 1974.

[97] F. Sunol and R. Gonzalez-Cinca, "Rise, bouncing and coalescence of bubbles impacting at a free surface," *Colloids and Surfaces A; Physiochemical and Engineering Aspects,* vol. 365, pp. 36-42, 2010.

[98] A. C. Rust and M. Manga, "Bubble shapes and orientations in low Re simple shear flow," *Journal of Colloid and Interface Science,* vol. 249, pp. 476-480, 2002.

[99] S. Irandoust and B. Andersson, "Liquid film in a Taylor flow through a capillary," *Industrial and Chemical Research,* vol. 28, pp. 1684-1688, 1989.

[100] L. A. M. Rocha, J. M. Miranda and J. B. L. M. Campos, "Wide range simulation study of Taylor bubbles in circular milli and microchannels," *Micromachines,* vol. 8, 2017.

[101] K. A. Triplett, S. M. Ghiaasiaan, S. I. Abdel-Khalik and D. L. Sadowski, "Gas-liquid two-phase flow in microchannels Part I: two-phase flow patterns," *International Journal of Multiphase Flow,* vol. 25, pp. 377-394, 1999.

[102] X. Wu and P. Moin, "Direct numerical simulation of turbulence in a nominally zero-pressure-gradient flat plate boundary layer," *Journal of Fluid Mechanics,* vol. 630, pp. 5-41, 2009.

[103] M. M. Rai and P. Moin, "Direct numerical simulation of transition and turbulence in a spatially evolving boundary layer," *Journal of Computational Physics,* vol. 109, pp. 169-192, 1993.

[104] A. E. Bergles, J. P. Roos and J. G. Bourne, "Investigation of boiling flow regimes and critical heat flux," *NYO-3304-13,* 1968.

[105] B. Mikuz, E. M. A. Frederix, I. Tiselj and E. M. J. Komen, "High-fidelity simulation of a Taylor bubble in co-current turbulent flow," in *18th International Topical Meeting on Nuclear Reactor Thermal Hydraulics,* Portland, Oregon, 2019.

[106] S. Shi, L. Wang, J. Yin and X. Sun, "Measurement of liquid-phase velocity field around Taylor bubbles in slug flows," in *2017 Japan-US Seminar on Two-Phase Flow Dynamics,* Sapporo, Hokkaido, Japan, 2017.

[107] T. Hibiki and M. Ishii, "Interfacial area transport equations for gas-liquid flows," *Journal of Computational Multiphase Flows,* vol. 1, no. 1, pp. 1-22, 2009.

[108] J. M. Dejesus and M. Kawaji, "Investigation of interfacial area and void fraction in upward cocurrent gas-liquid flow," *The Canadian Journal of Chemical Engineering,* vol. 68, pp. 904-912, 1990.

[109] R. Delfos, C. J. Wisse and R. V. A. Oliemans, "Measurement of air-entrainment from a stationary Taylor bubble in a vertical tube," *International Journal of Multiphase Flow,* vol. 27, pp. 1769-1787, 2001.

[110] R. Delfos, Experiments on air entrainment from a stationary slug bubble in a vertical tube, Delft University of Technology: Ph.D. Thesis, 1996.

[111] G. Haller, "An objective definition of a vortex," *Journal of Fluid Mechanics,* vol. 525, pp. 1-26, 2005.

[112] Y. Liao and D. Lucas, "A literature review of theoretical models for drop and bubble breakup in turbulent dispersions," *Chemical Engineering Science,* vol. 64, pp. 3389-3406, 2009.

[113] J. L. Lumley and G. R. Newman, "The return to isotropy of homogeneous turbulence," *Journal of Fluid Mechanics*, vol. 82, no. 1, pp. 161-178, 1977.

APPENDICES

Appendix A.1

Interfacial area calculation code

```
  c..********************************************************
  c....this routine calculates the interfacial area
  c********************************************************
          subroutine get_int_area(yl, shape, WdetJ, xl, A_ill, A_il)
  c
  c--------------------------------------------------------------------
  c This routine calculates interfacial surface area, Matt Z
  c
  c input:
  c  yl(npro,nshl,ndof)           : solution
  c  shape  (npro, nshl)          : element shape-functions
  c  WdetJ  (npro)                : Jacobian
  c output:
  c  A_i                          : Interfacial Surface Area
  c  A_ili                        : Partition local interfacial area grid
  c--------------------------------------------------------------------
  c
        use spat_var_eps   ! use spatially-varying epl_ls
        include "common.h"
        include "mpif.h"
        include "auxmpi.h"
  c....Passed arrays
        dimension shape(npro,nshl),
       &          yl(npro,nshl,ndof), WdetJ(npro)
  c
  c local arrays
  c
        integer iel, n, A_i_flag(nshl)!, vol_flag(nshl)
        integer i, nx, ny, nz, nn, ix, iy, iz, intp
        real*8 A_il(nx_Ai,ny_Ai,nz_Ai,2), A_ill(nx_Ai*ny_Ai*nz_Ai*2)
        real*8 Sclr_i(nshl), Sclr(npro), epsilon_ls_tmp
        real*8 xl(npro,nenl,nsd), xd, yd, zd
  c
  c compute level set at gauss point
  c
  ! Define the x,y,z dimensions of the A_i mesh
        isc=abs(iRANS)+6
  !      A_i = zero
  ! Determine the number of meshes in each direction
        xd = (DomainSize(2)-DomainSize(1))/nx_Ai
        yd = (DomainSize(4)-DomainSize(3))/ny_Ai
        zd = (DomainSize(6)-DomainSize(5))/nz_Ai
      nn_Ai = nx_Ai*ny_Ai*nz_Ai
      Sclr = zero
      do n = 1,nshl
        Sclr = Sclr + shape(:,n)*yl(:,n,isc)
      enddo
! Initialize
      do iel = 1,npro
        epsilon_ls_tmp = epsilon_ls *
     &  elem_local_size(lcblk(1,iblk)+iel-1)
        A_i_flag = zero
```

```
!        vol_flag = zero
         Sclr_i = 1.0E11
! Start finding cell volumes
         ix = int((xl(iel,1,1) - DomainSize(1))/xd) + 1.0
         iy = int((xl(iel,1,2) - DomainSize(3))/yd) + 1.0
         iz = int((xl(iel,1,3) - DomainSize(5))/zd) + 1.0
         do n = 1, nshl
           Sclr_i(n) = shape(iel,n)*yl(iel,n,isc)
           if (abs(Sclr_i(n)).le.epsilon_ls_tmp) A_i_flag(n) = 1 !A_i_flag + 1
!           if (Sclr_i(n).le.zero) vol_flag(n) = 1
!         enddo
! Find A_i mesh ID's for each point in domain and assign them their A_i
! values
!          if (A_i_flag(n).ge.1) then
           if (abs(Sclr_i(n)).le.epsilon_ls_tmp) then !if (A_i_flag(n).eq.1)
then !collect interfacial area info
              A_il(ix,iy,iz,1) = A_il(ix,iy,iz,1) +
     &                abs(shape(iel,n)*WdetJ(iel))/(2.0*epsilon_ls_tmp)
              A_i = A_i +
     &                abs(shape(iel,n)*WdetJ(iel))/(2.0*epsilon_ls_tmp)
           endif
           do intp = 1, ngauss
           if (Sclr(iel).le.zero) then !collect volume info
               A_il(ix,iy,iz,2) = A_il(ix,iy,iz,2) +
     &                abs(shape(iel,n)*WdetJ(iel))
           endif
           enddo
         enddo
       enddo

       do i = 1, 2
         do ix = 1, nx_Ai
           do iy = 1, ny_Ai
             do iz = 1, nz_Ai
         A_ill(iz+nz_Ai*(iy-1.0+ny_Ai*(ix-1.0))+(i-1)*nx_Ai*ny_Ai*nz_Ai)
     &           =  A_il(ix,iy,iz,i)
           enddo
         enddo
       enddo
       enddo

       return
       end
```

Appendix A.2

Interfacial area analysis code, in Matlab

```
format LONG
ix(1) = 135;
iy(1) = 10;
iz(1) = 10;
%Inputs
Ai=Ai41800;
voli=voli41800;
Ai_M2=AiM2199200; %Ai10cmM2109800; %
voli_M2=voliM2199200; %voli10cmM2109800; %
ix(2) = 135;
iy(2) = 10;
iz(2) = 10;
div(1,1:3) = 1;
div(2,1) = 1;
div(2,2:3) = 1;
L=0.2;
D=0.015;
%[y,z]=meshgrid(0.0001875:D/40:D,0.0001875:D/40:D);
pf = 2; %plotting factor, decides which dataset to plot, also need to change
figure inputs at bottom of script
[xp,z]=meshgrid(L/(ix(pf)/div(pf,1)*2):L/(ix(pf)/div(pf,1)):L,D/(iy(pf)/div(p
f,2)*2):D/(iy(pf)/div(pf,2)):D);
steps(1) = 8; %size(Ai,1)
steps(2) = size(Ai_M2,1);
Ai=table2array(Ai);
voli=table2array(voli);
Ai_M2=table2array(Ai_M2);
voli_M2=table2array(voli_M2);
A_i(1:ix(1),1:iy(1),1:iz(1),1:2,1:steps(1)) = 0.0;
A_i_M2(1:ix(2),1:iy(2),1:iz(2),1:2,1:steps(2)) = 0.0;
A_xtot(1:ix(1)/div(1,1),1:2,1:steps(1)) = 0.0;
A_xtot_M2(1:ix(2)/div(2,1),1:2,1:steps(2)) = 0.0;
D_s(1:ix(1)/div(1,1),1:steps(1)) = 0.0;
D_s_M2(1:ix(2)/div(2,1),1:steps(2)) = 0.0;
D_s_temp(1:ix(1)/div(1,1),1:steps(1)) = 0.0;
D_s_M2_temp(1:ix(2)/div(2,1),1:steps(2)) = 0.0;
x(1:ix(1)/div(1,1),1:steps(2)) = 0.0;
x_M2(1:ix(2)/div(2,1),1:steps(2)) = 0.0;
x_temp(1:ix(1)/div(1,1),1:steps(2)) = 0.0;
x_M2_temp(1:ix(2)/div(2,1),1:steps(2)) = 0.0;
time(1:steps(1)) = 0.0;
time_M2(1:steps(2)) = 0.0;
x_max(1:2,1:steps(1)) = 1000000.0;
x_max(1:2,1:steps(2)) = 1000000.0;
error(1:ix(1)/div(1,1),1:iy(1)/div(1,2),1:iz(1)/div(1,3)) = 0.0;
var_l(1:ix(1)/div(1,1),1:iy(1)/div(1,2),1:iz(1)/div(1,3),1:steps(1)) = 0.0;
var_l_M2(1:ix(2)/div(2,1),1:iy(2)/div(2,2),1:iz(2)/div(2,3),1:steps(2)) =
0.0;
reg_l(1:ix(1)/div(1,1),1:iy(1)/div(1,2),1:iz(1)/div(1,3),1:steps(1)) = 0.0;
reg_g(1:ix(1)/div(1,1),1:iy(1)/div(1,2),1:iz(1)/div(1,3),1:steps(1)) = 0.0;
reg_l_M2(1:ix(2)/div(2,1),1:iy(2)/div(2,2),1:iz(2)/div(2,3),1:steps(2)) =
0.0;
```

```
reg_g_M2(1:ix(2)/div(2,1),1:iy(2)/div(2,2),1:iz(2)/div(2,3),1:steps(2)) =
0.0;
combo(1:ix(2)/div(2,1),1:iy(2)/div(2,2),1:iz(2)/div(2,3),1:steps(2)) = 0.0;

for m = 1:2
    for t = 1:steps(m)
       for n = 1:2
            for i = 1:ix(m)
                for j = 1:iy(m)
                    for k = 1:iz(m)
                        if n==1
                            if m==1
                                A_i(i,j,k,n,t) = Ai(1,(t-
1)*(ix(m)*iy(m)*iz(m))+(i+ix(1)*(j-1+iy(1)*(k-1))));
                            elseif m==2
                                A_i_M2(i,j,k,n,t) = Ai_M2(t,i+ix(2)*(j-
1+iy(2)*(k-1)));
                            end
                        elseif n==2
                            if m==1
                                A_i(i,j,k,n,t) = voli(1,(t-
1)*(ix(m)*iy(m)*iz(m))+(i+ix(1)*(j-1+iy(1)*(k-1))));
                            elseif m==2
                                A_i_M2(i,j,k,n,t) = voli_M2(t,i+ix(2)*(j-
1+iy(2)*(k-1)));
                            end
                        end
                    end
                end
            end
        end
    end
end

for m = 1:2
    for t = 1:steps(m)
        for n = 1:2
            for i = 1:ix(m)/div(m,1)
                for j = 1:iy(m)/div(m,2)
                    for k = 1:iz(m)/div(m,2)
                        A_i_temp = 0.0;
                        for e = 1:div(m,1)
                            for f = 1:div(m,2)
                                for g = 1:div(m,3)
                                    if m==1
                                        A_i_temp = A_i_temp + A_i((i-
1)*div(m,1)+e,(j-1)*div(m,2)+f,(k-1)*div(m,3)+g,n,t);
                                    elseif m==2
                                        A_i_temp = A_i_temp + A_i_M2((i-
1)*div(m,1)+e,(j-1)*div(m,2)+f,(k-1)*div(m,3)+g,n,t);
                                    end
                                end
                            end
                        end
                        if m==1
                            A_i(i,j,k,n,t) = A_i_temp;
```

```
                        elseif m==2
                            A_i_M2(i,j,k,n,t) = A_i_temp;
                        end
                    end
                end
            end
        end
    end

for m = 1:2 %meshes
    for t = 1:steps(m) %time steps
        for n = 1:2 %1 - interfacial area, 2 - gas volume
            for i = 1:ix(m)/div(m,1)
                for j = 1:iy(m)
                    for k = 1:iz(m)
                        for e = 1:div(m,1) %if you are further coarsening the
boxes
                            if m==1
                               A_xtot(i,n,t) = A_xtot(i,n,t) + A_i((i-
1)*div(m,1)+e,j,k,n,t);
                            else
                               A_xtot_M2(i,n,t) = A_xtot_M2(i,n,t) +
A_i_M2((i-1)*div(m,1)+e,j,k,n,t);
                            end
                        end
                    end
                end
            end
        end
    end
end

for m = 1:2
    for t = 1:steps(m)
        for i = 1:ix(m)/div(m,1)
                if m==1
                    if (A_xtot(i,1,t)>0.0)
                        D_s(i,t) = 6*A_xtot(i,2,t)/A_xtot(i,1,t);
                    end
                else
                    if (A_xtot_M2(i,1,t)>0.0)
                        D_s_M2(i,t) = 6*A_xtot_M2(i,2,t)/A_xtot_M2(i,1,t);
                    end
                end
            if m==1
                x(i,t) = L/ix(m)*i*div(m,1);
            else
                x_M2(i,t) = L/ix(m)*i*div(m,1);
            end
        end
        if m==1
            time(t) = 1E-5*t;
        else
            time_M2(t) = 1E-5*t;
        end
```

```
    end
end
for m = 1:2
    for t = 1:steps(m)
        for i = ix(m)/div(m,1):-1:1
           if (m==1) && (D_s(i,t)<=1E-3) && (i<x_max(m,t)) && (x(i,t)>=0.05)
               x_max(m,t) = i;%x(i-1);
           elseif (m==2) && (D_s_M2(i,t)<=3E-3) && (i<x_max(m,t)) &&
(x_M2(i,t)>=0.05)
               x_max(m,t) = i;%x_M2(i-1);
           end
        end
    end
end
for m = 1:2
    for t = 1:steps(m)
        for i = 1:ix(m)/div(m,1)
            if m==1
                if i<=x_max(m,t) %x(i,t)<=x_max(m,t)
                    x_temp(x_max(m,t)-i+1,t) = (x(x_max(m,t),t) - x(i,t))/D;
                    D_s_temp(i,t) = D_s(x_max(m,t)-i+1,t);
                else
                    x_temp(ix(m)/div(m,1)-i+x_max(m,t)+1,t) = (L +
x(x_max(m,t),t) - x(i,t))/D;
                    D_s_temp(i,t) = D_s(ix(m)/div(m,1)-i+x_max(m,t)+1,t);
                end
            else
                if i<=x_max(m,t)
                    x_M2_temp(x_max(m,t)-i+1,t) = (x_M2(x_max(m,t),t) -
x_M2(i,t))/D;
                    D_s_M2_temp(i,t) = D_s_M2(x_max(m,t)-i+1,t);
                else
                    x_M2_temp(ix(m)/div(m,1)-i+x_max(m,t)+1,t) = (L +
x_M2(x_max(m,t),t) - x_M2(i,t))/D;
                    D_s_M2_temp(i,t) = D_s_M2(ix(m)/div(m,1)-
i+x_max(m,t)+1,t);
                end
            end
        end
    end
end
x = x_temp;
x_M2 = x_M2_temp;
D_s = D_s_temp;
D_s_M2 = D_s_M2_temp;
st_dev = 0.0;
error_mean = 0.0;
error = 0.0
error_ds= 0.0
if ix(1)/div(1,1)==ix(2)/div(2,1)
    for i = 1:ix(1)/div(1,1)
        for j = 1:iy(1)/div(1,2)
            for k = 1:iz(1)/div(1,3)
                if i>1
                    error(i,j,k) = abs(A_i_M2(i-1,j,k,1,1) -
A_i(i,j,k,1,1))/(D/iy(1))^2*100; %(D_s(i,1) - D_s_M2(i,1))/D;
                elseif i<=1
```

```
                    error(i,j,k) = abs(A_i_M2(ix(1)/div(1,1)-1+i,j,k,1,1) -
A_i(i,j,k,1,1))/(D/iy(1))^2*100;
                end
                st_dev = st_dev + (error(i,j,k))^2;
                error_mean = error_mean + error(i,j,k)/(ix(1)*iy(1)*iz(1));
%abs(D_s(i,1) - D_s_M2(i,1))/(D*ix(1)*iy(1)*iz(1));
            end
        end
        error_ds(i) = (D_s(i,1) - D_s_M2(i,1))/D;
    end
end
st_dev = (st_dev/(ix(1)*iy(1)*iz(1)))^0.5;
Ai_sum = 0.0;
for i = 1:ix(2)/div(2,1)
        for j = 1:iy(2)/div(2,2)
            for k = 1:iz(2)/div(2,3)
                Ai_sum = Ai_sum + A_i_M2(i,j,k,1,1);
            end
        end
end
Ai_sum
st_dev = (st_dev/ix(1))
error_mean=error_mean
%calculating a local variance, helps categorize the current regime, tallies
%local gradients in interfacial area but also how many regions of no
%interfaces there are. This is an attempt to classify regimes. IE if there
%are a lot of areas with no interfaces where no volume is present, probably
%bubbly, but the same with volume is probably slug. reg is a measure of if
%there are nearby interfaces and var is a measure of the gradient of the
%nearby interfaces
for m = 1:2 %meshes
    for t = 1:steps(m) %time steps
        for i = 1:ix(m)/div(m,1) %x
            for j = 1:iy(m)/div(m,2) %y
                for k = 1:iz(m)/div(m,3) %z
                    if m==1
                        if i==1
                            var_l(i,j,k,t) = var_l(i,j,k,t) +
abs(A_i(i+1,j,k,1,t) - A_i(i,j,k,1,t))/(L/ix(m)*div(m,1));
                        elseif i==ix(1)/div(m,1)
                            var_l(i,j,k,t) = var_l(i,j,k,t) +
abs(A_i(i,j,k,1,t) - A_i(i-1,j,k,1,t))/(L/ix(m)*div(m,1));
                        else
                            var_l(i,j,k,t) = var_l(i,j,k,t) +
(abs(A_i(i+1,j,k,1,t) - A_i(i,j,k,1,t)) + abs(A_i(i,j,k,1,t) - A_i(i-
1,j,k,1,t)))/(L/ix(m)*div(m,1));
                        end
                        if j==1
                            var_l(i,j,k,t) = var_l(i,j,k,t) +
abs(A_i(i,j+1,k,1,t) - A_i(i,j,k,1,t))/(D/iy(m)*div(m,2));
                        elseif j==iy(1)/div(m,2)
                            var_l(i,j,k,t) = var_l(i,j,k,t) +
abs(A_i(i,j,k,1,t) - A_i(i,j-1,k,1,t))/(D/iy(m)*div(m,2));
                        else
                            var_l(i,j,k,t) = var_l(i,j,k,t) +
(abs(A_i(i,j+1,k,1,t) - A_i(i,j,k,1,t)) + abs(A_i(i,j,k,1,t) - A_i(i,j-
1,k,1,t)))/(D/iy(m)*div(m,2));
```

```
                        end
                        if k==1
                            var_l(i,j,k,t) = var_l(i,j,k,t) +
abs(A_i(i,j,k+1,1,t) - A_i(i,j,k,1,t))/(D/iz(m)*div(m,3));
                        elseif k==iz(1)/div(m,3)
                            var_l(i,j,k,t) = var_l(i,j,k,t) +
abs(A_i(i,j,k,1,t) - A_i(i,j,k-1,1,t))/(D/iz(m)*div(m,3));
                        else
                            var_l(i,j,k,t) = var_l(i,j,k,t) +
(abs(A_i(i,j,k+1,1,t) - A_i(i,j,k,1,t)) + abs(A_i(i,j,k,1,t) - A_i(i,j,k-
1,1,t)))/(D/iz(m)*div(m,3));
                        end
 %                       var_l(i,j,k,t) = (abs(A_i(i+1,j,k,1,t) -
A_i(i,j,k,1,t)) + abs(A_i(i,j,k,1,t) - A_i(i-1,j,k,1,t)) +
abs(A_i(i,j,k+1,1,t) - A_i(i,j,k,1,t)) + abs(A_i(i,j,k,1,t) - A_i(i,j,k-
1,1,t)) + abs(A_i(i,j,k+1,1,t) - A_i(i,j,k,1,t)) + abs(A_i(i,j,k,1,t) -
A_i(i,j,k-1,1,t)))/(D/iz(1));
                        if  i>1 && j<iy(1)/div(m,2) && k>1 && A_i(i-1,j+1,k-
1,1,t)>0.0
                            reg_l(i,j,k,t) = reg_l(i,j,k,t) + 1;% - A_i(i-
1,j+1,k-1,1,t)/((D/(iz(1)/div(1)))^2*L/(ix(1)/div(1)));
                            reg_g(i,j,k,t) = reg_g(i,j,k,t) + 1;%A_i(i-
1,j+1,k-1,1,t)/((D/(iz(1)/div(1)))^2*L/(ix(1)/div(1)));
                        end
                        if i>1 && j<iy(1)/div(m,2) && A_i(i-1,j+1,k,1,t)>0.0
                            reg_l(i,j,k,t) = reg_l(i,j,k,t) + 1 - A_i(i-
1,j+1,k,1,t)/((D/(iz(1)/div(1)))^2*L/(ix(1)/div(1)));
                            reg_g(i,j,k,t) = reg_g(i,j,k,t) + 1;%A_i(i-
1,j+1,k,1,t)/((D/(iz(1)/div(1)))^2*L/(ix(1)/div(1)));
                        end
                        if i>1 && j<iy(1)/div(m,2) && k<iz(1)/div(m,3) &&
A_i(i-1,j+1,k+1,1,t)>0.0
                            reg_l(i,j,k,t) = reg_l(i,j,k,t) + 1 - A_i(i-
1,j+1,k+1,1,t)/((D/(iz(1)/div(1)))^2*L/(ix(1)/div(1)));
                            reg_g(i,j,k,t) = reg_g(i,j,k,t) + 1;%A_i(i-
1,j+1,k+1,1,t)/((D/(iz(1)/div(1)))^2*L/(ix(1)/div(1)));
                        end
                        if j<iy(1)/div(m,2) && k>1 && A_i(i,j+1,k-1,1,t)>0.0
                            reg_l(i,j,k,t) = reg_l(i,j,k,t) + 1 -
A_i(i,j+1,k-1,1,t)/((D/(iz(1)/div(1)))^2*L/(ix(1)/div(1)));
                            reg_g(i,j,k,t) = reg_g(i,j,k,t) + 1;%A_i(i,j+1,k-
1,1,t)/((D/(iz(1)/div(1)))^2*L/(ix(1)/div(1)));
                        end
                        if j<iy(1)/div(m,2) && A_i(i,j+1,k,1,t)>0.0
                            reg_l(i,j,k,t) = reg_l(i,j,k,t) + 1 -
A_i(i,j+1,k,1,t)/((D/(iz(1)/div(1)))^2*L/(ix(1)/div(1)));
                            reg_g(i,j,k,t) = reg_g(i,j,k,t) +
1;%A_i(i,j+1,k,1,t)/((D/(iz(1)/div(1)))^2*L/(ix(1)/div(1)));
                        end
                        if j<iy(1)/div(m,2) && k<iz(1)/div(m,3) &&
A_i(i,j+1,k+1,1,t)>0.0
                            reg_l(i,j,k,t) = reg_l(i,j,k,t) + 1 -
A_i(i,j+1,k+1,1,t)/((D/(iz(1)/div(1)))^2*L/(ix(1)/div(1)));
                            reg_g(i,j,k,t) = reg_g(i,j,k,t) +
1;%A_i(i,j+1,k+1,1,t)/((D/(iz(1)/div(1)))^2*L/(ix(1)/div(1)));
                        end
```

```
                        if i<ix(1)/div(m,1) && j<iy(1)/div(m,2) && k>1 &&
A_i(i+1,j+1,k-1,1,t)>0.0
                            reg_l(i,j,k,t) = reg_l(i,j,k,t) + 1 -
A_i(i+1,j+1,k-1,1,t)/((D/(iz(1)/div(1)))^2*L/(ix(1)/div(1)));
                            reg_g(i,j,k,t) = reg_g(i,j,k,t) +
1;%A_i(i+1,j+1,k-1,1,t)/((D/(iz(1)/div(1)))^2*L/(ix(1)/div(1)));
                        end
                        if i<ix(1)/div(m,1) && j<iy(1)/div(m,2) &&
A_i(i+1,j+1,k,1,t)>0.0
                            reg_l(i,j,k,t) = reg_l(i,j,k,t) + 1 -
A_i(i+1,j+1,k,1,t)/((D/(iz(1)/div(1)))^2*L/(ix(1)/div(1)));
                            reg_g(i,j,k,t) = reg_g(i,j,k,t) +
1;%A_i(i+1,j+1,k,1,t)/((D/(iz(1)/div(1)))^2*L/(ix(1)/div(1)));
                        end
                        if i<ix(1)/div(m,1) && j<iy(1)/div(m,2) &&
k<iz(1)/div(m,3) && A_i(i+1,j+1,k+1,1,t)>0.0
                            reg_l(i,j,k,t) = reg_l(i,j,k,t) + 1 -
A_i(i+1,j+1,k+1,1,t)/((D/(iz(1)/div(1)))^2*L/(ix(1)/div(1)));
                            reg_g(i,j,k,t) = reg_g(i,j,k,t) +
1;%A_i(i+1,j+1,k+1,1,t)/((D/(iz(1)/div(1)))^2*L/(ix(1)/div(1)));
                        end
                        if i>1 && k>1 && A_i(i-1,j,k-1,1,t)>0.0
                            reg_l(i,j,k,t) = reg_l(i,j,k,t) + 1 - A_i(i-
1,j,k-1,1,t)/((D/(iz(1)/div(1)))^2*L/(ix(1)/div(1)));
                            reg_g(i,j,k,t) = reg_g(i,j,k,t) + 1;%A_i(i-1,j,k-
1,1,t)/((D/(iz(1)/div(1)))^2*L/(ix(1)/div(1)));
                        end
                        if i>1 && A_i(i-1,j,k,1,t)>0.0
                            reg_l(i,j,k,t) = reg_l(i,j,k,t) + 1 - A_i(i-
1,j,k,1,t)/((D/(iz(1)/div(1)))^2*L/(ix(1)/div(1)));
                            reg_g(i,j,k,t) = reg_g(i,j,k,t) + 1;%A_i(i-
1,j,k,1,t)/((D/(iz(1)/div(1)))^2*L/(ix(1)/div(1)));
                        end
                        if i>1 && k<iz(1)/div(m,3) && A_i(i-1,j,k+1,1,t)>0.0
                            reg_l(i,j,k,t) = reg_l(i,j,k,t) + 1 - A_i(i-
1,j,k+1,1,t)/((D/(iz(1)/div(1)))^2*L/(ix(1)/div(1)));
                            reg_g(i,j,k,t) = reg_g(i,j,k,t) + 1;%A_i(i-
1,j,k+1,1,t)/((D/(iz(1)/div(1)))^2*L/(ix(1)/div(1)));
                        end
                        if k>1 && A_i(i,j,k-1,1,t)>0.0
                            reg_l(i,j,k,t) = reg_l(i,j,k,t) + 1 - A_i(i,j,k-
1,1,t)/((D/(iz(1)/div(1)))^2*L/(ix(1)/div(1)));
                            reg_g(i,j,k,t) = reg_g(i,j,k,t) + 1;%A_i(i,j,k-
1,1,t)/((D/(iz(1)/div(1)))^2*L/(ix(1)/div(1)));
                        end
                        if A_i(i,j,k,1,t)>0.0
                            reg_l(i,j,k,t) = reg_l(i,j,k,t) + 1 -
A_i(i,j,k,1,t)/((D/(iz(1)/div(1)))^2*L/(ix(1)/div(1)));
                            reg_g(i,j,k,t) = reg_g(i,j,k,t) +
1;%A_i(i,j,k,1,t)/((D/(iz(1)/div(1)))^2*L/(ix(1)/div(1)));
                        end
                        if  k<iz(1)/div(m,3) && A_i(i,j,k+1,1,t)>0.0
                            reg_l(i,j,k,t) = reg_l(i,j,k,t) + 1 -
A_i(i,j,k+1,1,t)/((D/(iz(1)/div(1)))^2*L/(ix(1)/div(1)));
                            reg_g(i,j,k,t) = reg_g(i,j,k,t) +
1;%A_i(i,j,k+1,1,t)/((D/(iz(1)/div(1)))^2*L/(ix(1)/div(1)));
                        end
```

```
                        if i<ix(1)/div(m,1) && k>1 && A_i(i+1,j,k-1,1,t)>0.0
                            reg_l(i,j,k,t) = reg_l(i,j,k,t) + 1 -
A_i(i+1,j,k-1,1,t)/((D/(iz(1)/div(1)))^2*L/(ix(1)/div(1)));
                            reg_g(i,j,k,t) = reg_g(i,j,k,t) + 1;%A_i(i+1,j,k-
1,1,t)/((D/(iz(1)/div(1)))^2*L/(ix(1)/div(1)));
                        end
                        if i<ix(1)/div(m,1) && A_i(i+1,j,k,1,t)>0.0
                            reg_l(i,j,k,t) = reg_l(i,j,k,t) + 1 -
A_i(i+1,j,k,1,t)/((D/(iz(1)/div(1)))^2*L/(ix(1)/div(1)));
                            reg_g(i,j,k,t) = reg_g(i,j,k,t) +
1;%A_i(i+1,j,k,1,t)/((D/(iz(1)/div(1)))^2*L/(ix(1)/div(1)));
                        end
                        if i<ix(1)/div(m,1) && k<iz(1)/div(m,3) &&
A_i(i+1,j,k+1,1,t)>0.0
                            reg_l(i,j,k,t) = reg_l(i,j,k,t) + 1 -
A_i(i+1,j,k+1,1,t)/((D/(iz(1)/div(1)))^2*L/(ix(1)/div(1)));
                            reg_g(i,j,k,t) = reg_g(i,j,k,t) +
1;%A_i(i+1,j,k+1,1,t)/((D/(iz(1)/div(1)))^2*L/(ix(1)/div(1)));
                        end
                        if i>1 && j>1 && k>1 && A_i(i-1,j-1,k-1,1,t)>0.0
                            reg_l(i,j,k,t) = reg_l(i,j,k,t) + 1 - A_i(i-1,j-
1,k-1,1,t)/((D/(iz(1)/div(1)))^2*L/(ix(1)/div(1)));
                            reg_g(i,j,k,t) = reg_g(i,j,k,t) + 1;%A_i(i-1,j-
1,k-1,1,t)/((D/(iz(1)/div(1)))^2*L/(ix(1)/div(1)));
                        end
                        if i>1 && j>1 && A_i(i-1,j-1,k,1,t)>0.0
                            reg_l(i,j,k,t) = reg_l(i,j,k,t) + 1 - A_i(i-1,j-
1,k,1,t)/((D/(iz(1)/div(1)))^2*L/(ix(1)/div(1)));
                            reg_g(i,j,k,t) = reg_g(i,j,k,t) + 1;%A_i(i-1,j-
1,k,1,t)/((D/(iz(1)/div(1)))^2*L/(ix(1)/div(1)));
                        end
                        if i>1 && j>1 && k<iz(1)/div(m,3) && A_i(i-1,j-
1,k+1,1,t)>0.0
                            reg_l(i,j,k,t) = reg_l(i,j,k,t) + 1 - A_i(i-1,j-
1,k+1,1,t)/((D/(iz(1)/div(1)))^2*L/(ix(1)/div(1)));
                            reg_g(i,j,k,t) = reg_g(i,j,k,t) + 1;%A_i(i-1,j-
1,k+1,1,t)/((D/(iz(1)/div(1)))^2*L/(ix(1)/div(1)));
                        end
                        if j>1 && k>1 && A_i(i,j-1,k-1,1,t)>0.0
                            reg_l(i,j,k,t) = reg_l(i,j,k,t) + 1 - A_i(i,j-
1,k-1,1,t)/((D/(iz(1)/div(1)))^2*L/(ix(1)/div(1)));
                            reg_g(i,j,k,t) = reg_g(i,j,k,t) + 1;%A_i(i,j-1,k-
1,1,t)/((D/(iz(1)/div(1)))^2*L/(ix(1)/div(1)));
                        end
                        if j>1 && A_i(i,j-1,k,1,t)>0.0
                            reg_l(i,j,k,t) = reg_l(i,j,k,t) + 1 - A_i(i,j-
1,k,1,t)/((D/(iz(1)/div(1)))^2*L/(ix(1)/div(1)));
                            reg_g(i,j,k,t) = reg_g(i,j,k,t) + 1;%A_i(i,j-
1,k,1,t)/((D/(iz(1)/div(1)))^2*L/(ix(1)/div(1)));
                        end
                        if j>1 && k<iz(1)/div(m,3) && A_i(i,j-1,k+1,1,t)>0.0
                            reg_l(i,j,k,t) = reg_l(i,j,k,t) + 1 - A_i(i,j-
1,k+1,1,t)/((D/(iz(1)/div(1)))^2*L/(ix(1)/div(1)));
                            reg_g(i,j,k,t) = reg_g(i,j,k,t) + 1;%A_i(i,j-
1,k+1,1,t)/((D/(iz(1)/div(1)))^2*L/(ix(1)/div(1)));
                        end
```

```
                        if i<ix(1)/div(m,1) && j>1 && k>1 && A_i(i+1,j-1,k-
1,1,t)>0.0
                            reg_l(i,j,k,t) = reg_l(i,j,k,t) + 1 - A_i(i+1,j-
1,k-1,1,t)/((D/(iz(1)/div(1)))^2*L/(ix(1)/div(1)));
                            reg_g(i,j,k,t) = reg_g(i,j,k,t) + 1;%A_i(i+1,j-
1,k-1,1,t)/((D/(iz(1)/div(1)))^2*L/(ix(1)/div(1)));
                        end
                        if i<ix(1)/div(m,1) && j>1 && A_i(i+1,j-1,k,1,t)>0.0
                            reg_l(i,j,k,t) = reg_l(i,j,k,t) + 1 - A_i(i+1,j-
1,k,1,t)/((D/(iz(1)/div(1)))^2*L/(ix(1)/div(1)));
                            reg_g(i,j,k,t) = reg_g(i,j,k,t) + 1;%A_i(i+1,j-
1,k,1,t)/((D/(iz(1)/div(1)))^2*L/(ix(1)/div(1)));
                        end
                        if i<ix(1)/div(m,1) && j>1 && k<iz(1)/div(m,3) &&
A_i(i+1,j-1,k+1,1,t)>0.0
                            reg_l(i,j,k,t) = reg_l(i,j,k,t) + 1 - A_i(i+1,j-
1,k+1,1,t)/((D/(iz(1)/div(1)))^2*L/(ix(1)/div(1)));
                            reg_g(i,j,k,t) = reg_g(i,j,k,t) + 1;%A_i(i+1,j-
1,k+1,1,t)/((D/(iz(1)/div(1)))^2*L/(ix(1)/div(1)));
                        end
                        if i==1 && j==1 && k==1 || i==ix(m)/div(m,1) &&
j==iy(m)/div(m,2) && k==iz(m)/div(m,3) || i==ix(m)/div(m,1) &&
j==iy(m)/div(m,2) && k==1 || i==ix(m)/div(m,1) && j==1 && k==iz(m)/div(m,3)
||  i==1 && j==iy(m)/div(m,2) && k==iz(m)/div(m,3) ||  i==1 && j==1 &&
k==iz(m)/div(m,3) ||  i==1 && j==iy(m)/div(m,2) && k==1 ||  i==ix(m)/div(m,1)
&& j==1 && k==1
                            reg_g(i,j,k) = reg_g(i,j,k)/8;
                        elseif i==1 && j==1 || i==ix(m)/div(m,1) &&
j==iy(m)/div(m,2) || i==1 && j==iy(m)/div(m,3) || i==ix(m)/div(m,1) && j==1
|| i==1 && k==1 || i==ix(m)/div(m,1) && k==iz(m)/div(m,3) || i==1 &&
k==iz(m)/div(m,3) || i==ix(m)/div(m,1) && k==1 || j==1 && k==1 ||
j==iy(m)/div(m,2) && k==iz(m)/div(m,3) || j==1 && k==iz(m)/div(m,3) ||
j==iy(m)/div(m,2) && k==1
                            reg_g(i,j,k,t) = reg_g(i,j,k,t)/12;
                        elseif i==1 || i==ix(m)/div(m,1) || j==1 ||
j==iy(m)/div(m,2) || k==1 || k==iz(m)/div(m,3)
                            reg_g(i,j,k,t) = reg_g(i,j,k,t)/18;
                        else
                            reg_g(i,j,k,t) = reg_g(i,j,k,t)/27;
                        end
                    elseif m==2
                        if i==1
                            var_l_M2(i,j,k,t) = var_l_M2(i,j,k,t) +
abs(A_i_M2(i+1,j,k,1,t) - A_i_M2(i,j,k,1,t))/(L/ix(m)*div(m,1));
                        elseif i==ix(2)/div(m,1)
                            var_l_M2(i,j,k,t) = var_l_M2(i,j,k,t) +
abs(A_i_M2(i,j,k,1,t) - A_i_M2(i-1,j,k,1,t))/(L/ix(m)*div(m,1));
                        else
                            var_l_M2(i,j,k,t) = var_l_M2(i,j,k,t) +
(abs(A_i_M2(i+1,j,k,1,t) - A_i_M2(i,j,k,1,t)) + abs(A_i_M2(i,j,k,1,t) -
A_i_M2(i-1,j,k,1,t)))/(L/ix(m)*div(m,1));
                        end
                        if j==1
                            var_l_M2(i,j,k,t) = var_l_M2(i,j,k,t) +
abs(A_i_M2(i,j+1,k,1,t) - A_i_M2(i,j,k,1,t))/(D/iy(m)*div(m,2));
                        elseif j==iy(2)/div(m,2)
```

```
                            var_l_M2(i,j,k,t) = var_l_M2(i,j,k,t) +
abs(A_i_M2(i,j,k,1,t) - A_i_M2(i,j-1,k,1,t))/(D/iy(m)*div(m,2));
                        else
                            var_l_M2(i,j,k,t) = var_l_M2(i,j,k,t) +
(abs(A_i_M2(i,j+1,k,1,t) - A_i_M2(i,j,k,1,t)) + abs(A_i_M2(i,j,k,1,t) -
A_i_M2(i,j-1,k,1,t)))/(D/iy(m)*div(m,2));
                        end
                        if k==1
                            var_l_M2(i,j,k,t) = var_l_M2(i,j,k,t) +
abs(A_i_M2(i,j,k+1,1,t) - A_i_M2(i,j,k,1,t))/(D/iz(m)*div(m,3));
                        elseif k==iz(2)/div(m,3)
                            var_l_M2(i,j,k,t) = var_l_M2(i,j,k,t) +
abs(A_i_M2(i,j,k,1,t) - A_i_M2(i,j,k-1,1,t))/(D/iz(m)*div(m,3));
                        else
                            var_l_M2(i,j,k,t) = var_l_M2(i,j,k,t) +
(abs(A_i_M2(i,j,k+1,1,t) - A_i_M2(i,j,k,1,t)) + abs(A_i_M2(i,j,k,1,t) -
A_i_M2(i,j,k-1,1,t)))/(D/iz(m)*div(m,3));
                        end
                        %                           var_l_M2(i,j,k,t) =
(abs(A_i_M2(i+1,j,k,1,t) - A_i_M2(i,j,k,1,t)) + abs(A_i_M2(i,j,k,1,t) -
A_i_M2(i-1,j,k,1,t)) + abs(A_i_M2(i,j,k+1,1,t) - A_i_M2(i,j,k,1,t)) +
abs(A_i_M2(i,j,k,1,t) - A_i_M2(i,j,k-1,1,t)) + abs(A_i_M2(i,j,k+1,1,t) -
A_i_M2(i,j,k,1,t)) + abs(A_i_M2(i,j,k,1,t) - A_i_M2(i,j,k-1,1,t)))/(D/iz(2));
                        if i>1 && j<iy(m)/div(m,2) && k>1 && A_i_M2(i-
1,j+1,k-1,1,t)>0.0
                            reg_l_M2(i,j,k,t) = reg_l_M2(i,j,k,t) + 1 -
A_i_M2(i-1,j+1,k-1,1,t)/((D/(iz(1)/div(1)))^2*L/(ix(1)/div(1)));
                            reg_g_M2(i,j,k,t) = reg_g_M2(i,j,k,t) + 1;%A_i(i-
1,j+1,k-1,1,t)/((D/(iz(1)/div(1)))^2*L/(ix(1)/div(1)));
                        end
                        if i>1 && j<iy(m)/div(m,2) && A_i_M2(i-
1,j+1,k,1,t)>0.0
                            reg_l_M2(i,j,k,t) = reg_l_M2(i,j,k,t) + 1 -
A_i_M2(i-1,j+1,k,1,t)/((D/(iz(1)/div(1)))^2*L/(ix(1)/div(1)));
                            reg_g_M2(i,j,k,t) = reg_g_M2(i,j,k,t) + 1;%A_i(i-
1,j+1,k,1,t)/((D/(iz(1)/div(1)))^2*L/(ix(1)/div(1)));
                        end
                        if i>1 && j<iy(m)/div(m,2) && k<iz(2)/div(m,3) &&
A_i_M2(i-1,j+1,k+1,1,t)>0.0
                            reg_l_M2(i,j,k,t) = reg_l_M2(i,j,k,t) + 1 -
A_i_M2(i-1,j+1,k+1,1,t)/((D/(iz(1)/div(1)))^2*L/(ix(1)/div(1)));
                            reg_g_M2(i,j,k,t) = reg_g_M2(i,j,k,t) + 1;%A_i(i-
1,j+1,k+1,1,t)/((D/(iz(1)/div(1)))^2*L/(ix(1)/div(1)));
                        end
                        if j<iy(m)/div(m,2) && k>1 && A_i_M2(i,j+1,k-
1,1,t)>0.0
                            reg_l_M2(i,j,k,t) = reg_l_M2(i,j,k,t) + 1 -
A_i_M2(i,j+1,k-1,1,t)/((D/(iz(1)/div(1)))^2*L/(ix(1)/div(1)));
                            reg_g_M2(i,j,k,t) = reg_g_M2(i,j,k,t) +
1;%A_i(i,j+1,k-1,1,t)/((D/(iz(1)/div(1)))^2*L/(ix(1)/div(1)));
                        end
                        if j<iy(m)/div(m,2) && A_i_M2(i,j+1,k,1,t)>0.0
                            reg_l_M2(i,j,k,t) = reg_l_M2(i,j,k,t) + 1 -
A_i_M2(i,j+1,k,1,t)/((D/(iz(1)/div(1)))^2*L/(ix(1)/div(1)));
                            reg_g_M2(i,j,k,t) = reg_g_M2(i,j,k,t) +
1;%A_i(i,j+1,k,1,t)/((D/(iz(1)/div(1)))^2*L/(ix(1)/div(1)));
                        end
```

```
                        if i>1 && j<iy(m)/div(m,2) && k<iz(2)/div(m,3) &&
A_i_M2(i,j+1,k+1,1,t)>0.0
                            reg_l_M2(i,j,k,t) = reg_l_M2(i,j,k,t) + 1 -
A_i_M2(i,j+1,k+1,1,t)/((D/(iz(1)/div(1)))^2*L/(ix(1)/div(1)));
                            reg_g_M2(i,j,k,t) = reg_g_M2(i,j,k,t) +
1;%A_i(i,j+1,k+1,1,t)/((D/(iz(1)/div(1)))^2*L/(ix(1)/div(1)));
                        end
                        if i<ix(m)/div(m,1) && j<iy(m)/div(m,2) && k>1 &&
A_i_M2(i+1,j+1,k-1,1,t)>0.0
                            reg_l_M2(i,j,k,t) = reg_l_M2(i,j,k,t) + 1 -
A_i_M2(i+1,j+1,k-1,1,t)/((D/(iz(1)/div(1)))^2*L/(ix(1)/div(1)));
                            reg_g_M2(i,j,k,t) = reg_g_M2(i,j,k,t) +
1;%A_i(i+1,j+1,k-1,1,t)/((D/(iz(1)/div(1)))^2*L/(ix(1)/div(1)));
                        end
                        if i<ix(m)/div(m,1) && j<iy(m)/div(m,2) &&
A_i_M2(i+1,j+1,k,1,t)>0.0
                            reg_l_M2(i,j,k,t) = reg_l_M2(i,j,k,t) + 1 -
A_i_M2(i+1,j+1,k,1,t)/((D/(iz(1)/div(1)))^2*L/(ix(1)/div(1)));
                            reg_g_M2(i,j,k,t) = reg_g_M2(i,j,k,t) +
1;%A_i(i+1,j+1,k,1,t)/((D/(iz(1)/div(1)))^2*L/(ix(1)/div(1)));
                        end
                        if i<ix(m)/div(m,1) && j<iy(m)/div(m,2) &&
k<iz(m)/div(m,3) && A_i_M2(i+1,j+1,k+1,1,t)>0.0
                            reg_l_M2(i,j,k,t) = reg_l_M2(i,j,k,t) + 1 -
A_i_M2(i+1,j+1,k+1,1,t)/((D/(iz(1)/div(1)))^2*L/(ix(1)/div(1)));
                            reg_g_M2(i,j,k,t) = reg_g_M2(i,j,k,t) +
1;%A_i(i+1,j+1,k+1,1,t)/((D/(iz(1)/div(1)))^2*L/(ix(1)/div(1)));
                        end
                        if i>1 && k>1 && A_i_M2(i-1,j,k-1,1,t)>0.0
                            reg_l_M2(i,j,k,t) = reg_l_M2(i,j,k,t) + 1 -
A_i_M2(i-1,j,k-1,1,t)/((D/(iz(1)/div(1)))^2*L/(ix(1)/div(1)));
                            reg_g_M2(i,j,k,t) = reg_g_M2(i,j,k,t) + 1;%A_i(i-
1,j,k-1,1,t)/((D/(iz(1)/div(1)))^2*L/(ix(1)/div(1)));
                        end
                        if i>1 && A_i_M2(i-1,j,k,1,t)>0.0
                            reg_l_M2(i,j,k,t) = reg_l_M2(i,j,k,t) + 1 -
A_i_M2(i-1,j,k,1,t)/((D/(iz(1)/div(1)))^2*L/(ix(1)/div(1)));
                            reg_g_M2(i,j,k,t) = reg_g_M2(i,j,k,t) + 1;%A_i(i-
1,j,k,1,t)/((D/(iz(1)/div(1)))^2*L/(ix(1)/div(1)));
                        end
                        if i>1 && k<iz(m)/div(m,3) && A_i_M2(i-
1,j,k+1,1,t)>0.0
                            reg_l_M2(i,j,k,t) = reg_l_M2(i,j,k,t) + 1 -
A_i_M2(i-1,j,k+1,1,t)/((D/(iz(1)/div(1)))^2*L/(ix(1)/div(1)));
                            reg_g_M2(i,j,k,t) = reg_g_M2(i,j,k,t) + 1;%A_i(i-
1,j,k+1,1,t)/((D/(iz(1)/div(1)))^2*L/(ix(1)/div(1)));
                        end
                        if k>1 && A_i_M2(i,j,k-1,1,t)>0.0
                            reg_l_M2(i,j,k,t) = reg_l_M2(i,j,k,t) + 1 -
A_i_M2(i,j,k-1,1,t)/((D/(iz(1)/div(1)))^2*L/(ix(1)/div(1)));
                            reg_g_M2(i,j,k,t) = reg_g_M2(i,j,k,t) +
1;%A_i(i,j,k-1,1,t)/((D/(iz(1)/div(1)))^2*L/(ix(1)/div(1)));
                        end
                        if A_i_M2(i,j,k,1,t)>0.0
                            reg_l_M2(i,j,k,t) = reg_l_M2(i,j,k,t) + 1 -
A_i_M2(i,j,k,1,t)/((D/(iz(1)/div(1)))^2*L/(ix(1)/div(1)));
```

```
                            reg_g_M2(i,j,k,t) = reg_g_M2(i,j,k,t) +
1;%A_i(i,j,k,1,t)/((D/(iz(1)/div(1)))^2*L/(ix(1)/div(1)));
                        end
                        if k<iz(m)/div(m,3) && A_i_M2(i,j,k+1,1,t)>0.0
                            reg_l_M2(i,j,k,t) = reg_l_M2(i,j,k,t) + 1 -
A_i_M2(i,j,k+1,1,t)/((D/(iz(1)/div(1)))^2*L/(ix(1)/div(1)));
                            reg_g_M2(i,j,k,t) = reg_g_M2(i,j,k,t) +
1;%A_i(i,j,k+1,1,t)/((D/(iz(1)/div(1)))^2*L/(ix(1)/div(1)));
                        end
                        if i<ix(m)/div(m,1) && k>1 && A_i_M2(i+1,j,k-
1,1,t)>0.0
                            reg_l_M2(i,j,k,t) = reg_l_M2(i,j,k,t) + 1 -
A_i_M2(i+1,j,k-1,1,t)/((D/(iz(1)/div(1)))^2*L/(ix(1)/div(1)));
                            reg_g_M2(i,j,k,t) = reg_g_M2(i,j,k,t) +
1;%A_i(i+1,j,k-1,1,t)/((D/(iz(1)/div(1)))^2*L/(ix(1)/div(1)));
                        end
                        if i<ix(m)/div(m,1) && A_i_M2(i+1,j,k,1,t)>0.0
                            reg_l_M2(i,j,k,t) = reg_l_M2(i,j,k,t) + 1 -
A_i_M2(i+1,j,k,1,t)/((D/(iz(1)/div(1)))^2*L/(ix(1)/div(1)));
                            reg_g_M2(i,j,k,t) = reg_g_M2(i,j,k,t) +
1;%A_i(i+1,j,k,1,t)/((D/(iz(1)/div(1)))^2*L/(ix(1)/div(1)));
                        end
                        if i<ix(m)/div(m,1) && k<iz(m)/div(m,3) &&
A_i_M2(i+1,j,k+1,1,t)>0.0
                            reg_l_M2(i,j,k,t) = reg_l_M2(i,j,k,t) + 1 -
A_i_M2(i+1,j,k+1,1,t)/((D/(iz(1)/div(1)))^2*L/(ix(1)/div(1)));
                            reg_g_M2(i,j,k,t) = reg_g_M2(i,j,k,t) +
1;%A_i(i+1,j,k+1,1,t)/((D/(iz(1)/div(1)))^2*L/(ix(1)/div(1)));
                        end
                        if i>1 && j>1 && k>1 && A_i_M2(i-1,j-1,k-1,1,t)>0.0
                            reg_l_M2(i,j,k,t) = reg_l_M2(i,j,k,t) + 1 -
A_i_M2(i-1,j-1,k-1,1,t)/((D/(iz(1)/div(1)))^2*L/(ix(1)/div(1)));
                            reg_g_M2(i,j,k,t) = reg_g_M2(i,j,k,t) + 1;%A_i(i-
1,j-1,k-1,1,t)/((D/(iz(1)/div(1)))^2*L/(ix(1)/div(1)));
                        end
                        if i>1 && j>1 && A_i_M2(i-1,j-1,k,1,t)>0.0
                            reg_l_M2(i,j,k,t) = reg_l_M2(i,j,k,t) + 1 -
A_i_M2(i-1,j-1,k,1,t)/((D/(iz(1)/div(1)))^2*L/(ix(1)/div(1)));
                            reg_g_M2(i,j,k,t) = reg_g_M2(i,j,k,t) + 1;%A_i(i-
1,j-1,k,1,t)/((D/(iz(1)/div(1)))^2*L/(ix(1)/div(1)));
                        end
                        if i>1 && j>1 && k<iz(m)/div(m,3) && A_i_M2(i-1,j-
1,k+1,1,t)>0.0
                            reg_l_M2(i,j,k,t) = reg_l_M2(i,j,k,t) + 1 -
A_i_M2(i-1,j-1,k+1,1,t)/((D/(iz(1)/div(1)))^2*L/(ix(1)/div(1)));
                            reg_g_M2(i,j,k,t) = reg_g_M2(i,j,k,t) + 1;%A_i(i-
1,j-1,k+1,1,t)/((D/(iz(1)/div(1)))^2*L/(ix(1)/div(1)));
                        end
                        if j>1 && k>1 && A_i_M2(i,j-1,k-1,1,t)>0.0
                            reg_l_M2(i,j,k,t) = reg_l_M2(i,j,k,t) + 1 -
A_i_M2(i,j-1,k-1,1,t)/((D/(iz(1)/div(1)))^2*L/(ix(1)/div(1)));
                            reg_g_M2(i,j,k,t) = reg_g_M2(i,j,k,t) +
1;%A_i(i,j-1,k-1,1,t)/((D/(iz(1)/div(1)))^2*L/(ix(1)/div(1)));
                        end
                        if j>1 && A_i_M2(i,j-1,k,1,t)>0.0
                            reg_l_M2(i,j,k,t) = reg_l_M2(i,j,k,t) + 1 -
A_i_M2(i,j-1,k,1,t)/((D/(iz(1)/div(1)))^2*L/(ix(1)/div(1)));
```

```
                                reg_g_M2(i,j,k,t) = reg_g_M2(i,j,k,t) +
1;%A_i(i,j-1,k,1,t)/((D/(iz(1)/div(1)))^2*L/(ix(1)/div(1)));
                            end
                            if j>1 && k<iz(m)/div(m,3) && A_i_M2(i,j-
1,k+1,1,t)>0.0
                                reg_l_M2(i,j,k,t) = reg_l_M2(i,j,k,t) + 1 -
A_i_M2(i,j-1,k+1,1,t)/((D/(iz(1)/div(1)))^2*L/(ix(1)/div(1)));
                                reg_g_M2(i,j,k,t) = reg_g_M2(i,j,k,t) +
1;%A_i(i,j-1,k+1,1,t)/((D/(iz(1)/div(1)))^2*L/(ix(1)/div(1)));
                            end
                            if i<ix(m)/div(m,1) && j>1 && k>1 && A_i_M2(i+1,j-
1,k-1,1,t)>0.0
                                reg_l_M2(i,j,k,t) = reg_l_M2(i,j,k,t) + 1 -
A_i_M2(i+1,j-1,k-1,1,t)/((D/(iz(1)/div(1)))^2*L/(ix(1)/div(1)));
                                reg_g_M2(i,j,k,t) = reg_g_M2(i,j,k,t) +
1;%A_i(i+1,j-1,k-1,1,t)/((D/(iz(1)/div(1)))^2*L/(ix(1)/div(1)));
                            end
                            if i<ix(m)/div(m,1) && j>1 && A_i_M2(i+1,j-
1,k,1,t)>0.0
                                reg_l_M2(i,j,k,t) = reg_l_M2(i,j,k,t) + 1 -
A_i_M2(i+1,j-1,k,1,t)/((D/(iz(1)/div(1)))^2*L/(ix(1)/div(1)));
                                reg_g_M2(i,j,k,t) = reg_g_M2(i,j,k,t) +
1;%A_i(i+1,j-1,k,1,t)/((D/(iz(1)/div(1)))^2*L/(ix(1)/div(1)));
                            end
                            if i<ix(m)/div(m,1) && j>1 && k<iz(m)/div(m,3) &&
A_i_M2(i+1,j-1,k+1,1,t)>0.0
                                reg_l_M2(i,j,k,t) = reg_l_M2(i,j,k,t) + 1 -
A_i_M2(i+1,j-1,k+1,1,t)/((D/(iz(1)/div(1)))^2*L/(ix(1)/div(1)));
                                reg_g_M2(i,j,k,t) = reg_g_M2(i,j,k,t) +
1;%A_i(i+1,j-1,k+1,1,t)/((D/(iz(1)/div(1)))^2*L/(ix(1)/div(1)));
                            end
                            if i==1 && j==1 && k==1 || i==ix(m)/div(m,1) &&
j==iy(m)/div(m,2) && k==iz(m)/div(m,3) || i==ix(m)/div(m,1) &&
j==iy(m)/div(m,2) && k==1 || i==ix(m)/div(m,1) && j==1 && k==iz(m)/div(m,3)
||  i==1 && j==iy(m)/div(m,2) && k==iz(m)/div(m,3) ||  i==1 && j==1 &&
k==iz(m)/div(m,3) ||  i==1 && j==iy(m)/div(m,2) && k==1 ||  i==ix(m)/div(m,1)
&& j==1 && k==1
                                reg_g_M2(i,j,k) = reg_g_M2(i,j,k)/8;
                            elseif i==1 && j==1 || i==ix(m)/div(m,1) &&
j==iy(m)/div(m,2) || i==1 && j==iy(m)/div(m,3) || i==ix(m)/div(m,1) && j==1
|| i==1 && k==1 || i==ix(m)/div(m,1) && k==iz(m)/div(m,3) || i==1 &&
k==iz(m)/div(m,3) || i==ix(m)/div(m,1) && k==1 || j==1 && k==1 ||
j==iy(m)/div(m,2) && k==iz(m)/div(m,3) || j==1 && k==iz(m)/div(m,3) ||
j==iy(m)/div(m,2) && k==1
                                reg_g_M2(i,j,k,t) = reg_g_M2(i,j,k,t)/12;
                            elseif i==1 || i==ix(m)/div(m,1) || j==1 ||
j==iy(m)/div(m,2) || k==1 || k==iz(m)/div(m,3)
                                reg_g_M2(i,j,k,t) = reg_g_M2(i,j,k,t)/18;
                            else
                                reg_g_M2(i,j,k,t) = reg_g_M2(i,j,k,t)/27;
                            end
                        end
                    end
                end
            end
        end
    end
end
```

```
combo(:,:,:,:) = var_l_M2(:,:,:,:).*reg_g_M2(:,:,:,:);
opengl software
figure;
plot(x(:,1),D_s(:,1));
ylabel('Sauter Mean Diameter [m]');
xlabel('Distance from Nose [x/D]');
hold on
plot(x_M2(:,1),D_s_M2(:,1),'r');
ylabel('Sauter Mean Diameter [m]');
xlabel('Distance from Nose [x/D]');
figure;
plot(x(:,1),error_ds)
ylabel('(Difference in Sauter Mean Diameter)/(Pipe Diameter)');
xlabel('Distance from Nose [x/D]');

if ix(1)/div(1,1)==ix(2)/div(2,1) & iy(1)/div(1,2)==iy(2)/div(2,2)
    for i = 1:ix(1)/div(1,1)
        for k = 1:iz(pf)/div(pf,3)
            error_plot(k,i) = error(i,5,k);
        end
    end
figure;
surf(xp,z,error_plot)%,A_iplane);
axis([0.0 L 0.0 D 0.0 1500.0]);
ylabel('y [m]');
xlabel('x [m]');
%zlabel('Volume Fraction');
%plot(x(:,1),error(:,5,5));
zlabel('Interfacial Area Difference [%]');
end

for i = 1:ix(pf)/div(pf,1)
    for k = 1:iz(pf)/div(pf,3)
        vol_iplane(k,i) =
A_i_M2(i,5,k,2,1)/((D/(iz(pf)/div(pf,3)))^2*L/(ix(pf)/div(pf,1)));
        A_iplane(k,i) = A_i_M2(i,5,k,1,1);
    end
end

for i = 1:ix(pf)/div(pf,1)
    for k = 1:iz(pf)/div(pf,3)
        var_g_iplane(k,i) = combo(i,5,k,1);%var_l_M2(i,5,k,1);
%reg_g(i,5,k,1);
        reg_g_iplane(k,i) = reg_g_M2(i,5,k,1);
    end
end

alp=0;
for i=1:ix(1)
    for j=1:iy(1)
        for k=1:iz(1)
            alp=alp+A_i(i,j,k,2,1);
        end
    end
end
```

```
%calculating radial profiles
A_i_axial(1:iy(1),1:iz(1),1:2,1) = 0.0;
A_i_axial(1:iy(2),1:iz(2),1:2,2) = 0.0;
for m=1:2
    for n=1:2
        for i=63:ix(m)
            for j=1:iy(m)
                for k=1:iz(m)
                    if ((D/iy(m)/2+D/iy(m)*(j-1))^2 + (D/iz(m)/2+D/iz(m)*(k-
1))^2)^0.5 <= 0.075;
                    end
                    if m==1 & A_i(i,j,k,1,1)>0.0;
                        A_i_axial(j,k,n,1) = A_i_axial(j,k,n,1) +
A_i(i,j,k,n,4);%/((D/iz(m))^2*L/ix(m));
%6*A_i(i,j,k,2,1)/A_i(i,j,k,1,1)/ix(1); %
                    elseif m==2 & A_i_M2(i,j,k,1,1)>0.0;
                        A_i_axial(j,k,n,2) = A_i_axial(j,k,n,2) +
A_i_M2(i,j,k,n,1);%/((D/iz(m))^2*L/ix(m));
%6*A_i_M2(i,j,k,2,1)/A_i_M2(i,j,k,1,1)/ix(2); %
                    end
                end
            end
        end
    end
end
A_i_axial_mean(1:iy(2)/2,1:2) = 0.0;
for m=1:2
    for n=1:2
        for j=1:iy(m)/2
            if m==1
                A_i_axial_mean(iy(m)/2+1-j,n,m) = (A_i_axial(j,iy(m)/2,n,m) +
A_i_axial(iy(m)+1-j,iy(m)/2,n,m)+A_i_axial(iy(m)/2,j,n,m) +
A_i_axial(iy(m)/2,iy(m)+1-j,n,m))/4;
            elseif m==2
                A_i_axial_mean(iy(m)/2+1-j,n,m) = (A_i_axial(j,iy(m)/2,n,m) +
A_i_axial(iy(m)+1-j,iy(m)/2,n,m)+A_i_axial(iy(m)/2,j,n,m) +
A_i_axial(iy(m)/2,iy(m)+1-j,n,m))/4;
            end
        end
    end
end
%Sauter mean diameter calculation
for m=1:2
    for j=1:iy(m)/2
        A_i_axial_mean(j,1,m) =
A_i_axial_mean(j,1,m)/((D/iz(m))^2*L/ix(m)*ix(m));%6*A_i_axial_mean(j,2,m)/A_
i_axial_mean(j,1,m);
    end
end
alp
figure;
%plot(0.0:0.00187:.0356,2*A_i_axial_mean(:,1,1))
%hold on
plot(0.0:0.00187:D/2,A_i_axial_mean(:,1,2))
axis([0.0 D/2 0 150]);
xlabel('Distance from Center [m]');
```

```
ylabel('Sauter Mean Diameter [m]'); %Mean Interfacial Area Concentration
[m^2/m^3]');

figure;
surf(xp,z,A_iplane)%,A_iplane);
axis([0.0 L 0.0 D 0.0 1.0]);
ylabel('y [m]');
xlabel('x [m]');
zlabel('Volume Fraction');

figure;
surf(xp,z,var_g_iplane)%,A_iplane);
axis([0.0 L 0.0 D 0.0 0.02]);
ylabel('y [m]');
xlabel('x [m]');
zlabel('Local Interface Gradient');

figure;
surf(xp,z,reg_g_iplane)%,A_iplane);
axis([0.0 L 0.0 D 0.0 1.0]);
ylabel('y [m]');
xlabel('x [m]');
zlabel('Local Interface Density');

% P(1) = getframe(gcf);
% for i = ix(2):-1:2
%     Zdata(:,:) = A_i_M2(i,:,:,2,1)/((D/iz(2))^3)*4;
%     Cdata(:,:) = A_i_M2(i,:,:,1,1);
%     s.ZData = Zdata;
%     s.CData = Cdata;
%     pause(0.05);
%     P(i) = getframe(gcf);
%     axis([0.0 0.015 0.0 0.015 0.0 1.0 ]);
%     ylabel('y [m]');
%     xlabel('z [m]');
%     zlabel('Volume Fraction');
% end
% v = VideoWriter('surfanim')
% open(v);
% writeVideo(v,P(:));
% close(v);
```

Appendix B

Time steps from the 10 cm long M2 forward simulation. Surface tension is 0.0714 N/m.

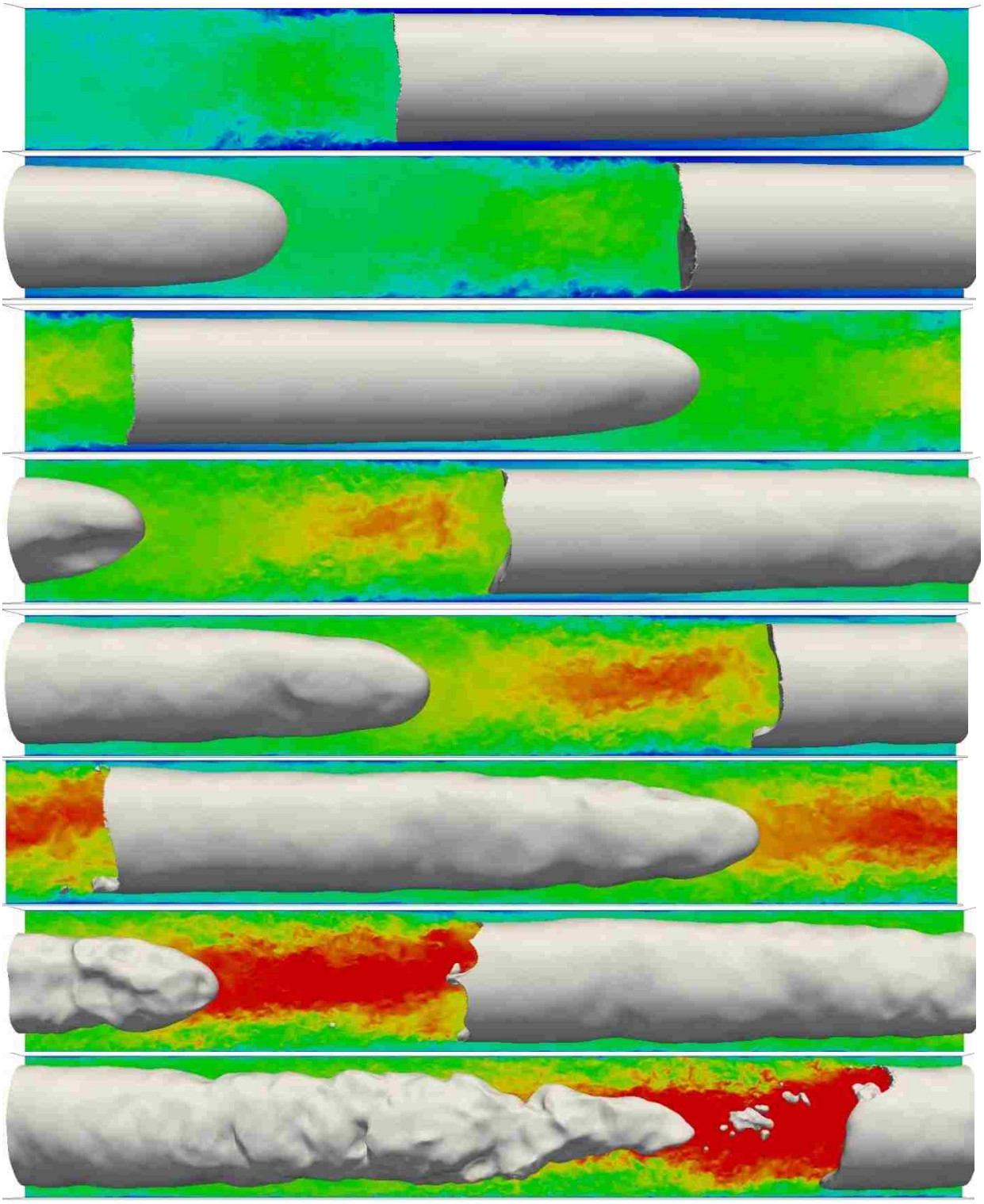

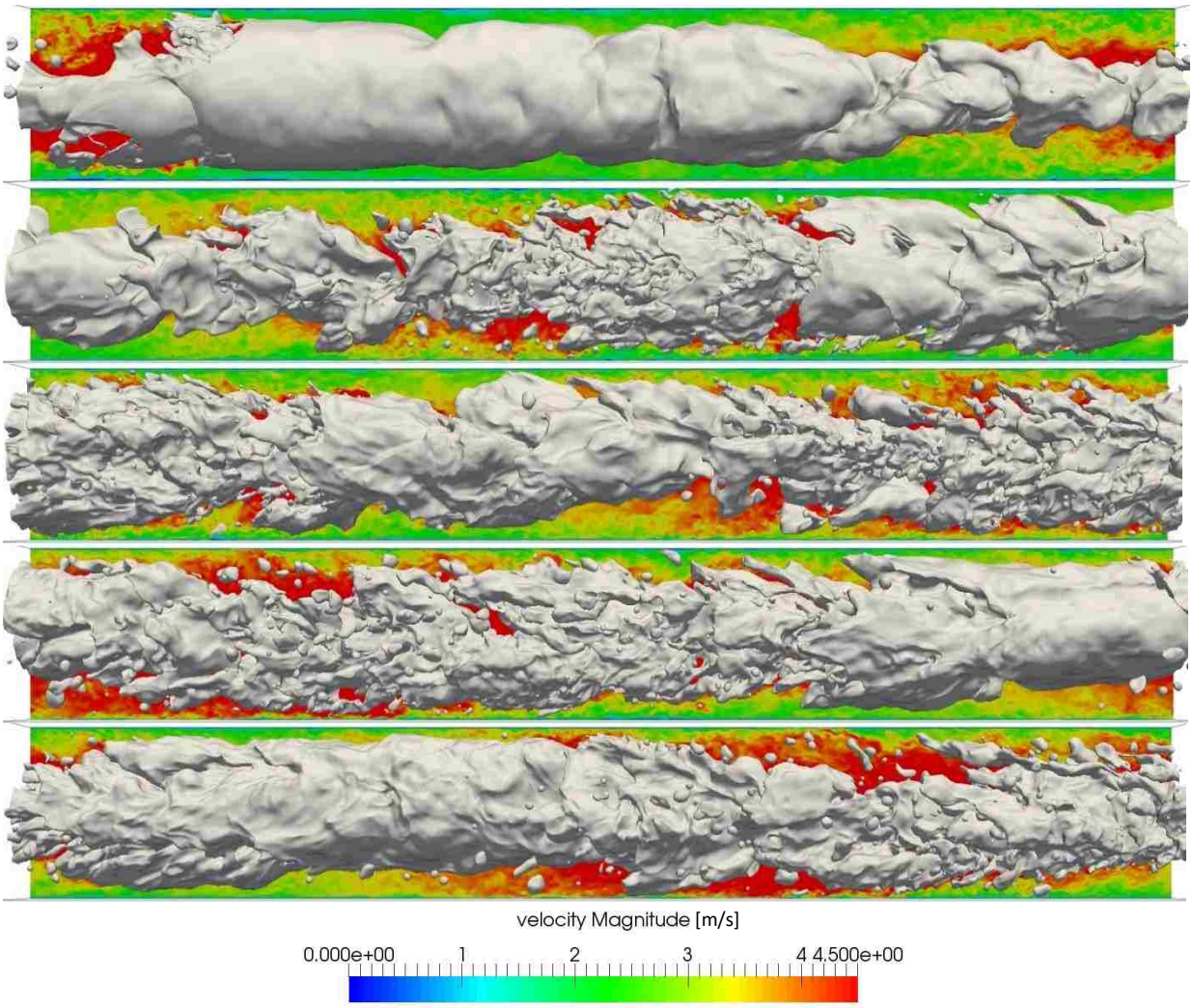
velocity Magnitude [m/s]
0.000e+00
1
2
3
4
4.500e+00

Appendix C

Time steps from the 20 cm long, M2 and M1 forward simulation. Surface tension equals 0.0714 N/m. Due to limited computational availability the M2 case has not been run as far as the M1. When M2 reaches its last point M1 images are shown afterwards.

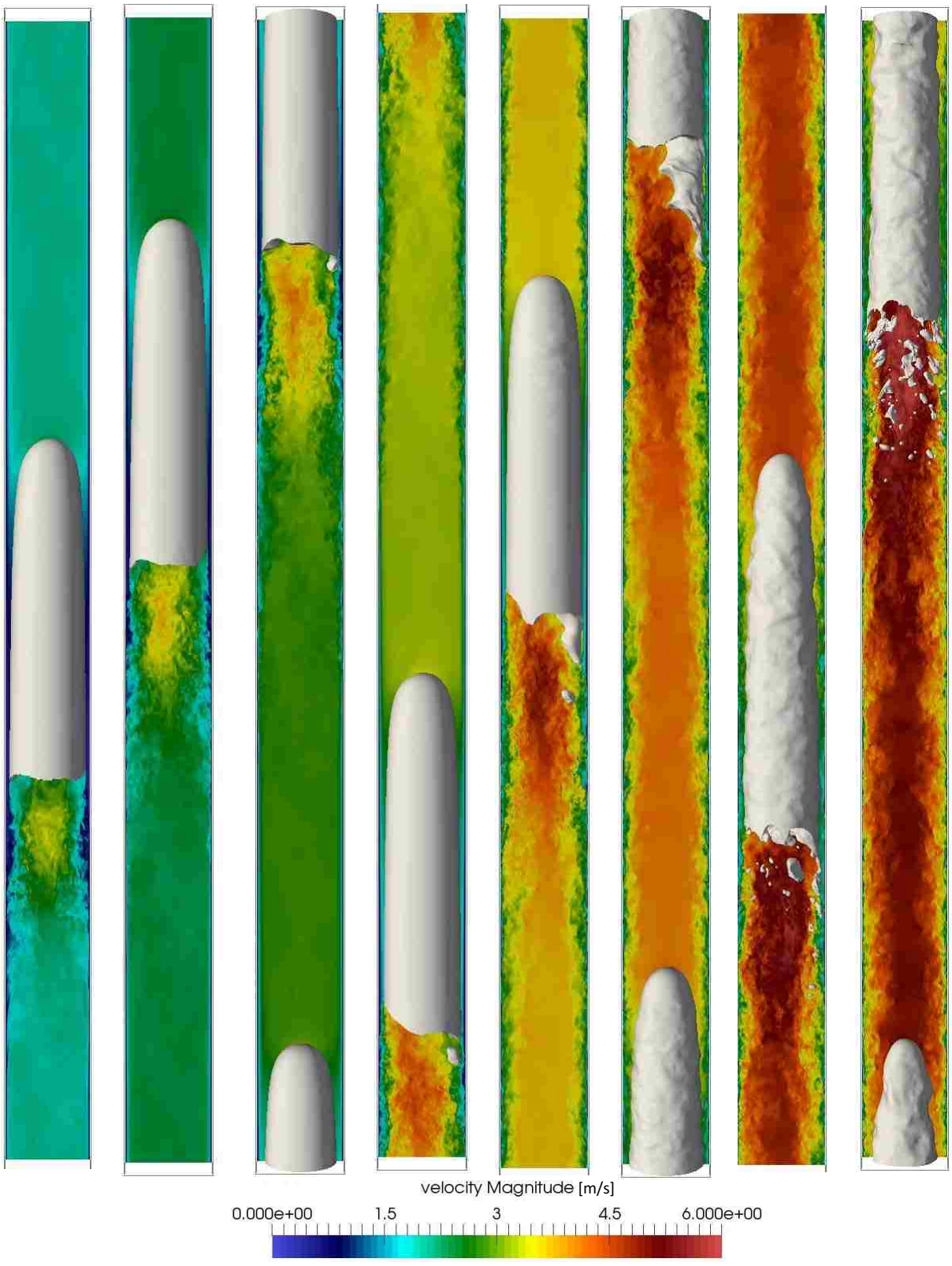
velocity Magnitude [m/s]
0.000e+00
1.5
3
4.5
6.000e+00

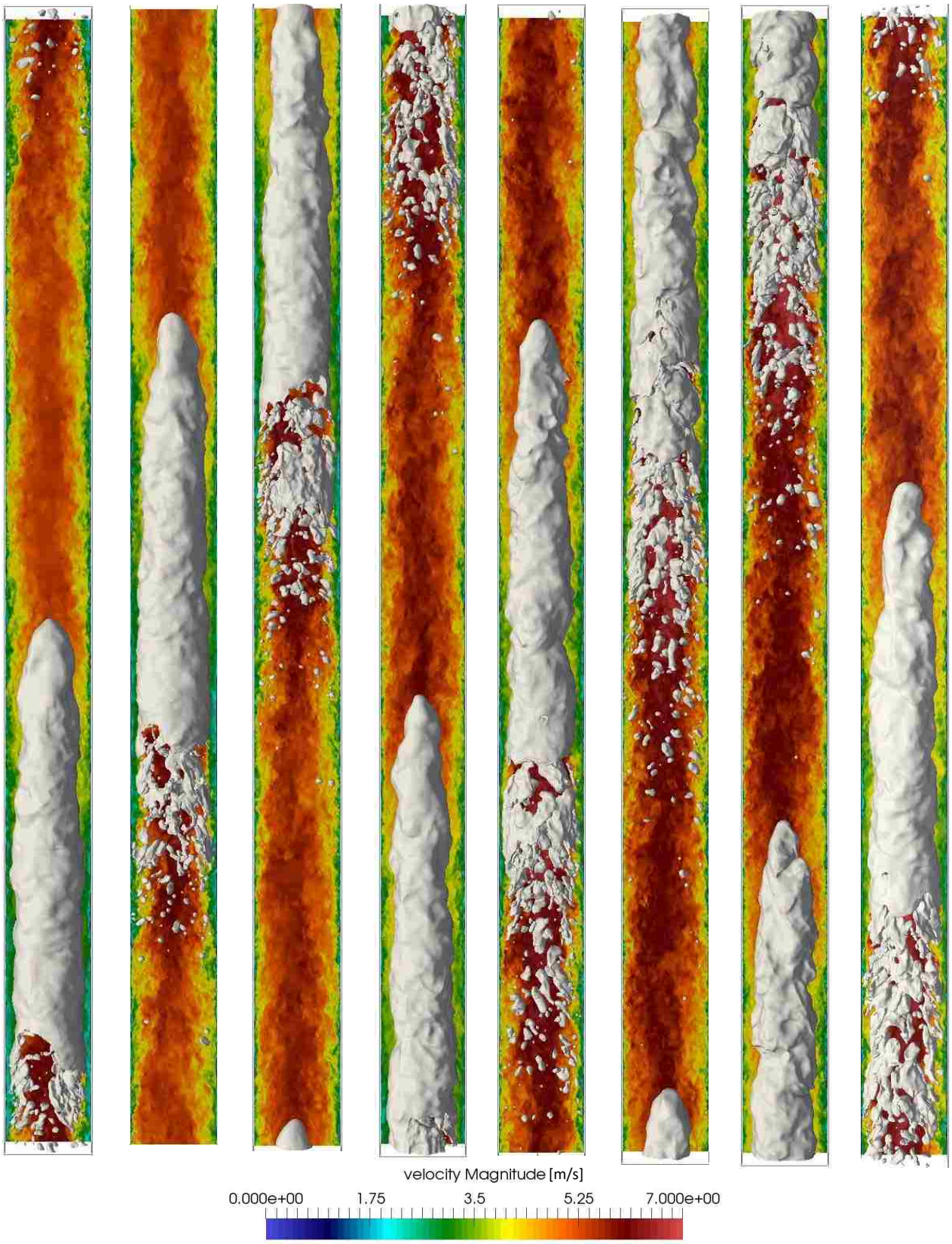
velocity Magnitude [m/s]
0.000e+00
1.75
3.5
5.25
7.000e+00

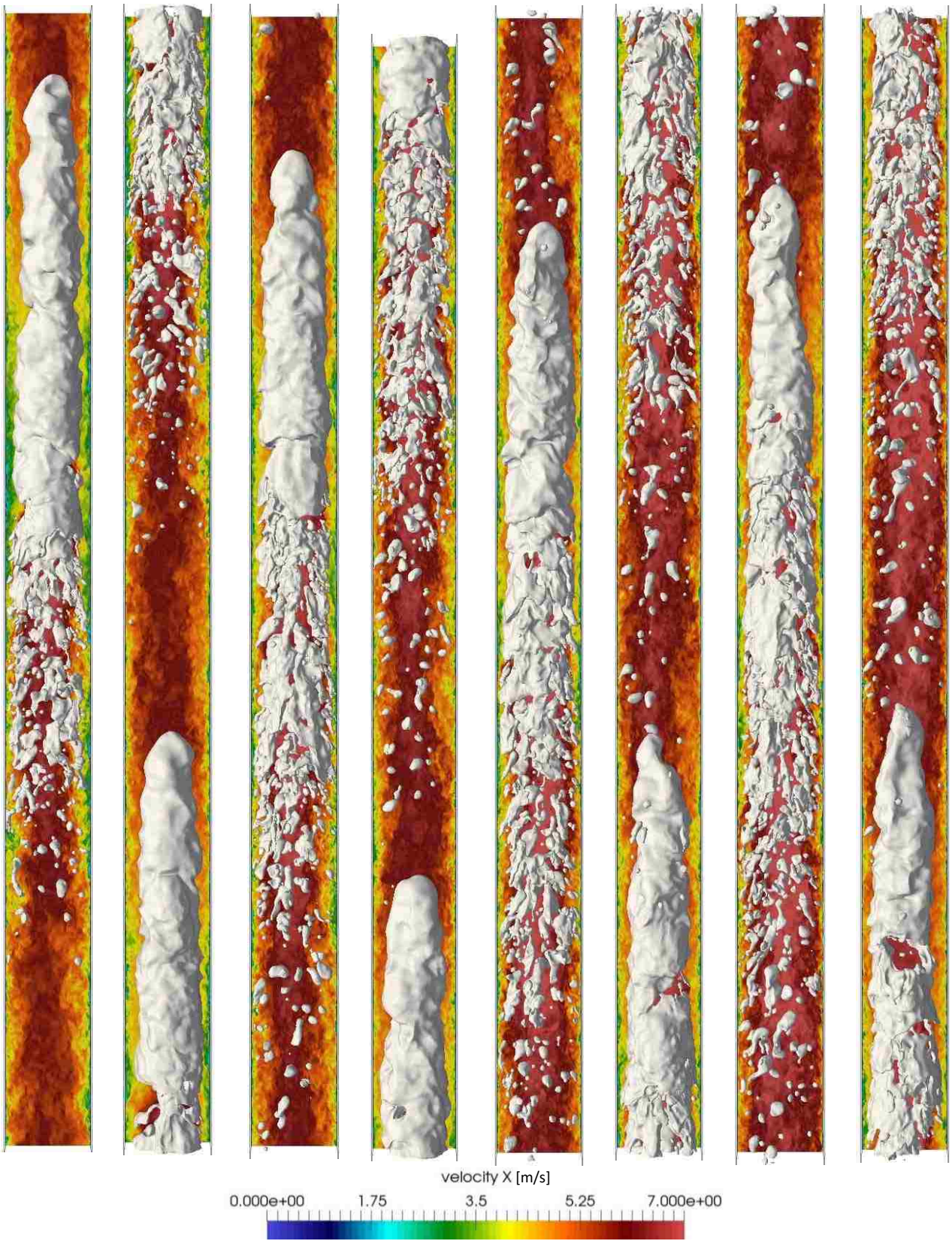
velocity X [m/s]
0.000e+00
1.75
3.5
5.25
7.000e+00


velocity X [m/s]
0.000e+00
2
4
6
8.000e+00

Appendix D

Time steps from the 10 cm long M2 reverse simulation. Surface tension is 0.0714 N/m.

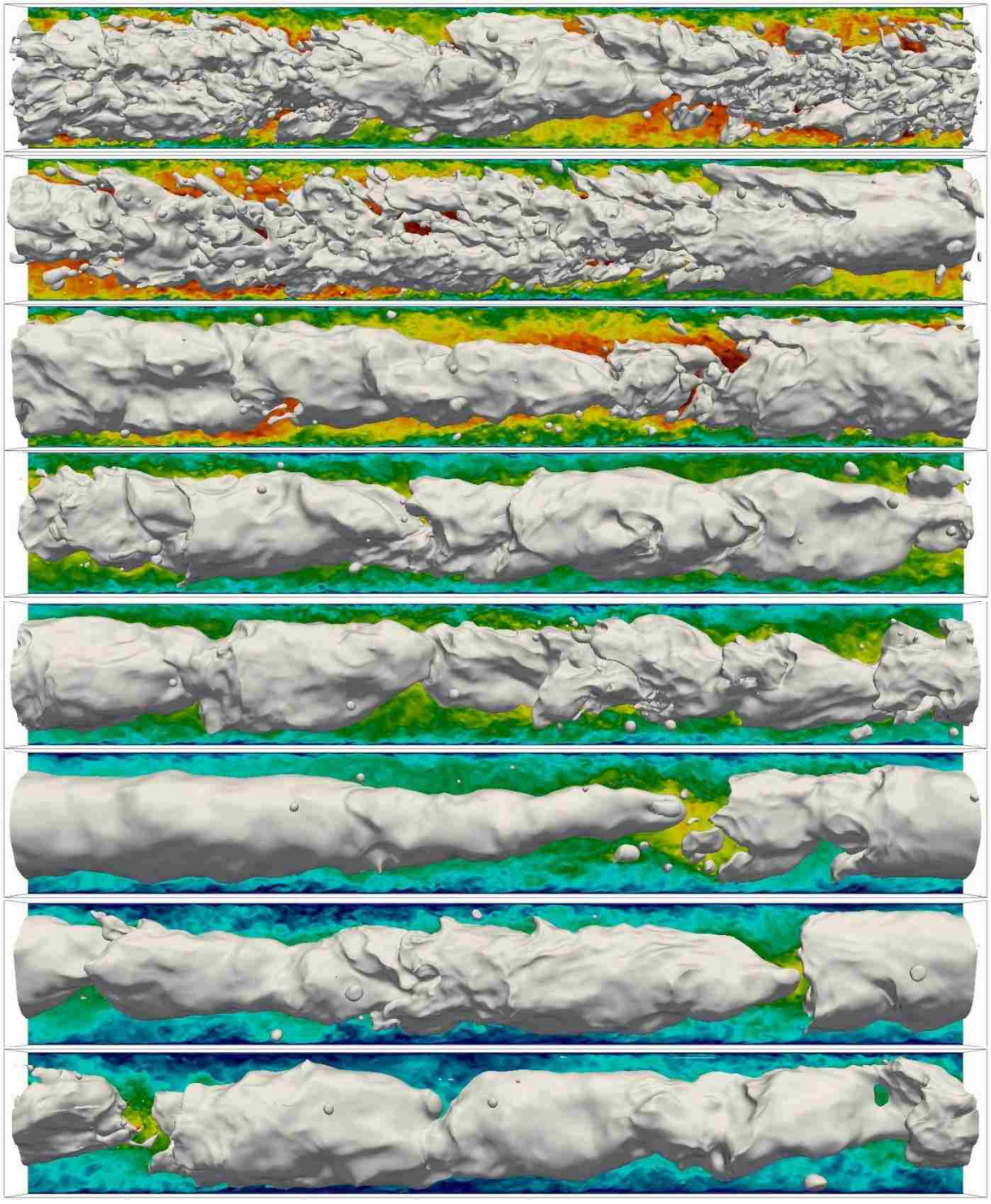

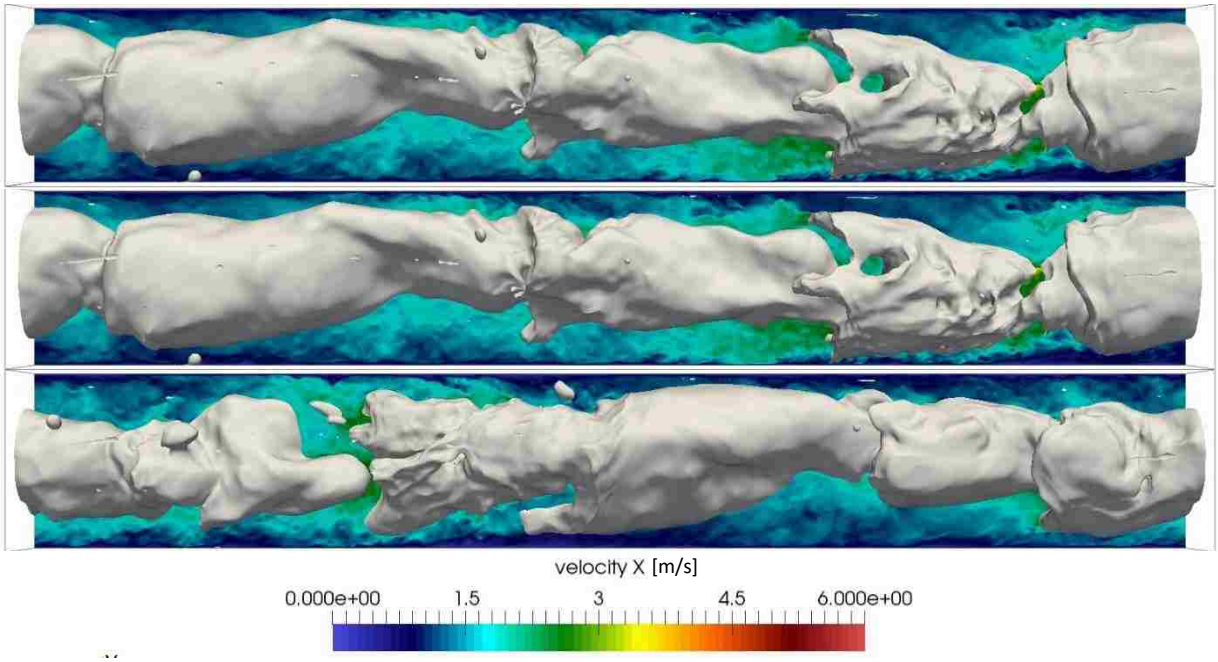
velocity X [m/s]
0.000e+00
1.5
3
4.5
6.000e+00

Appendix E

Time steps from the 20 cm long M1 reverse simulation. Surface tension is 0.0714 N/m.

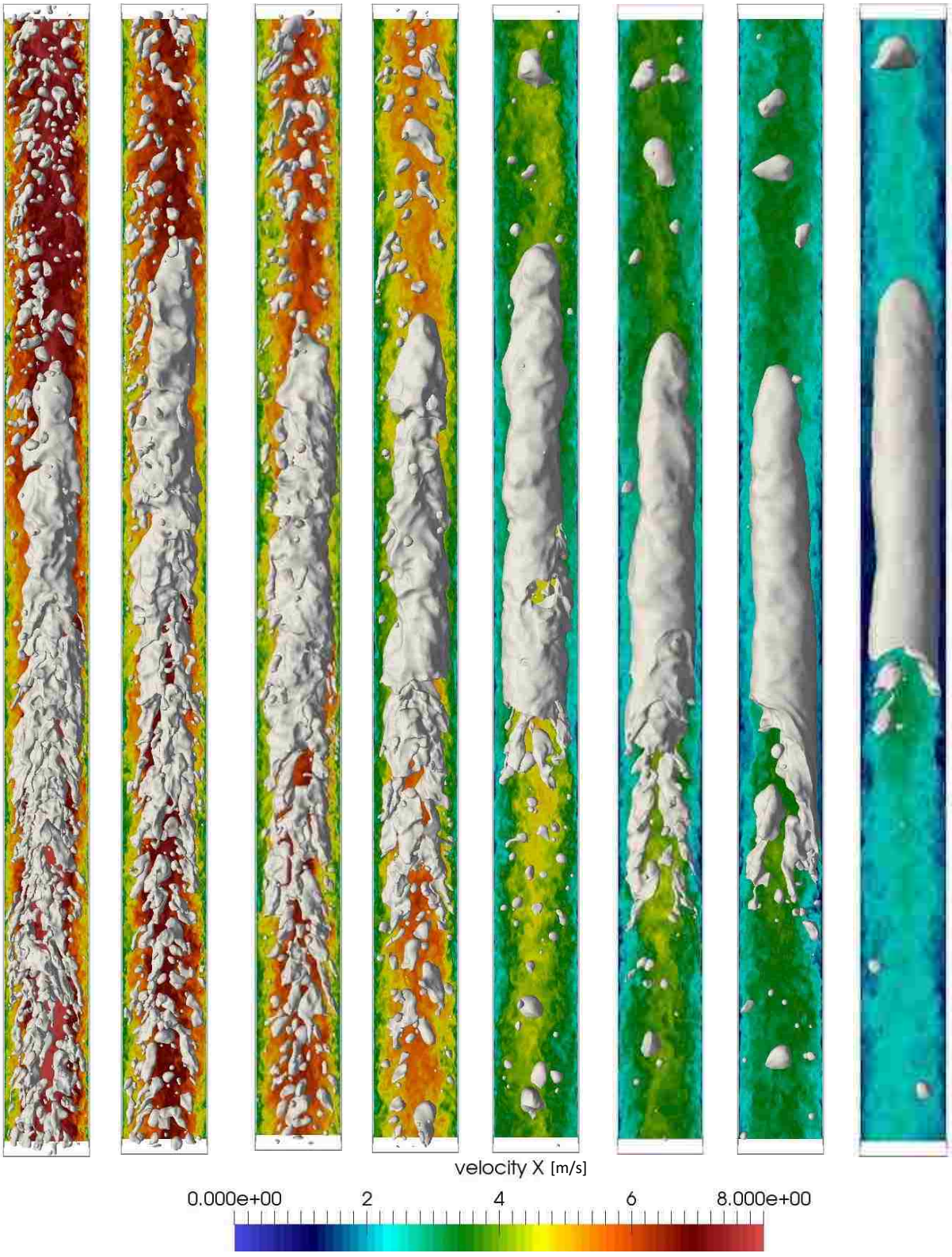


velocity X [m/s]
0.000e+00
1
2
3
4.000e+00

Appendix F

It is not unreasonable to be concerned that the pressure gradient jump causes numerical instabilities that are manifested in the interface of the bubble due to the manner by which the level set equation is formulated using the stabilized finite element method. The stabilized finite element method introduces two terms to the momentum equations. The first is the standard stabilization for the Galerkin form of the incompressible equations. The second is a two part term that corrects the lack of momentum conservation introduced by the first new term, and a second part that stabilizes term for the advective term introduced by the first part [64]. The concern is that by adding a significant amount of momentum to the domain through the jump in pressure gradient, the stabilized finite element method will react by manifesting large instabilities in the interface that break down the bubble. To test this theory, a low flow rate slug flow simulation was "slammed" by an extraordinarily large pressure gradient, 150,000 Pa/m, for 100 time steps (0.0025 seconds) before being reduced to the original value. This is an order of magnitude larger than the highest pressure gradient used in any other simulation presented. The bubble was then observed to see how the interface would react to this sudden change. Over the next 0.05 seconds, about 10 cm of flow by the bubble, no interface instabilities were observed. Some tail shearing began, but this is not surprising due to the sudden spike in interfacial shear that would be expected.

Appendix G

This appendix is a “video” appendix. Frames from the four major simulations are presented next to each other on the following pages. Flipping through the pages, starting at the last page, should provide a flipbook effect that animates the flows.